THE UNIVERSITY
of EDINBURGH

Characterising Large-Scale Chromatin Looping in Mouse Meiotic Prophase I

Isobel A. MacGregor

THE UNIVERSITY *of* EDINBURGH

Thesis Presented for the Degree of Doctor of Philosophy

The University of Edinburgh

September 2019

Declaration

I hereby declare that the work presented in this PhD thesis is the original work of the author, except where specific reference is made to other sources. This thesis has been composed solely by myself and has not been submitted for any other degree, diploma or qualification.

Isobel MacGregor

9th September 2019

This thesis is dedicated to Duncan MacGregor

who has been with me since the start

Acknowledgements

In the first instance, I would like to thank my supervisors Ian Adams and Nick Gilbert whose bountiful passion, experience and knowledge have proven invaluable from start to finish.

I would also like to thank all the members of the Adams and Gilbert labs, past and present, for creating such a warm and supportive environment in which to work. Adam Buckle, James Crichton, Catherine Naughton and Karen Dobie deserve special recognition for being the resilient sounding boards to my all too frequent waffles and wobbles. David Read, your nonsense and ice creams were always a much-needed pick-me-up and will always be greatly missed.

I am grateful to several people whose mice, reagents and expertise have helped to fuel my work: Jen Lawson (The mouse poet laureate), Shelagh Boyle (The FISH oracle), Harris Morrison and Matt Pearson for your microscopy expertise and Rolf Jessberger and Uddi Biswas for the *Smc1* mice.

I also owe a special thank you to my inspirational family for their unwavering love and support regardless of what 'challenge' I choose to throw in my path. You have taught me the value of diligence, determination and a good sense of fun, an arsenal which I could not have survived without. Thank you, Team MacGregor!

A mad and beautiful array of friends have also accompanied me throughout this endeavour including the Ladies of the Wizza, Winemergency, the best wee club in Edinburgh, the Godfamilies, STEAM pals, my Bruntsfield boys and the little one who ran away… and then came back again. A big thank you to each of you for being a constant source of perspective and relief from the working abyss.

Finally, I thank Laura. Thank you for your enduring patience, positivity and encouragement. You have kept me sane through the most testing of times with a happy heart and a smile on my face; I would not have made it without you. For all of this and so much more I will be forever grateful.

Abstract

Meiotic prophase I pachytene meiocytes exhibit a highly characteristic chromatin architecture. Running the length of every chromosome, the chromatin is packaged into sequential loop arrays emanating from a proteinaceous core, known as the synaptonemal complex (SC). The configuration of these chromatin loop arrays, including loop density and positioning, has been proposed to significantly impact on the distribution of meiotic recombination, a key process in the promotion of the faithful segregation of homologous chromosomes at the first meiotic division. This relationship is primarily based on observations made in lower-order organisms, therefore this thesis sought to characterise the fundamental principles of meiotic chromatin organisation at the level of individual chromatin loops in mice.

To investigate chromosome organisation in mouse meiosis, fluorescence *in situ* hybridisation (FISH) was conducted to map a single autosomal loop at the *HoxA* locus on chromosome 6 in pachytene spermatocytes. This approach defined a consistent ~1.3 Mb chromatin loop emanating from the SC. Higher resolution FISH analysis demonstrated that chromatids are tightly clustered when in proximity to the SC but become more separate as the chromatin extends into the loop. Furthermore, the topology of the *HoxA* loop was shown to be altered in cohesin mutant mice (*Smc1β-/-* and *Smc1β-/-,1α*), in which whole chromosome morphology is known to be disrupted, thus supporting the validity of the chromatin loop map and its cohesin-dependent regulation.

To understand the role of transcription in the maintenance of meiotic chromatin loop architecture in pachytene spermatocytes, FISH analyses were performed following acute transcriptional inhibition. Inhibition led to no significant change in SC length. However, the total nuclear area was substantially reduced as autosomal chromatin was drawn closer to the SC, with no significant change in chromatin compaction. A relatively subtle response was seen on the grossly transcriptionally silent sex chromosomes. On RNase treatment, a similar, yet less substantial, change in chromosome morphology was observed. Collectively, these findings demonstrate that chromatin loop organisation is dependent on a transcriptional component.

In mice, the frequency of meiotic crossovers (COs; a product of meiotic recombination) is sexually dimorphic, with an approximately two-fold reduction in male CO frequency relative to females. FISH-based analyses revealed that chromatin loop extensions are significantly longer and chromatid separation substantially greater in spermatocytes, relative to oocytes. Chromatid separation was also found to be significantly greater at two CO hotspots in juvenile males, which experience a reduction in inter-homolog interactions compared to their adult counterparts. Cumulatively, these data indicate that differences in the frequency of inter-homolog interactions and COs correspond with differences in the relative spatial positioning of chromatids.

Together, these findings advance present understanding of the fundamental features of meiotic chromatin architecture at the level of individual chromatin loops in murine meiocytes. Furthermore, this research provides insight into the nuclear environment in which meiotic recombination occurs, which ultimately has wide-reaching clinical implications relating to infertility, specific developmental disorders and spontaneous miscarriage, in which the legitimate segregation of meiotic chromosomes is perturbed.

Lay Abstract

Every living organism created through sexual reproduction possesses a paternal and a maternal copy of genetic information that makes an individual unique. This genetic information is encoded within a string-like molecule known as DNA. Importantly, it is not only the genetic sequence of DNA which can influence biological processes inside cells but also how the DNA is folded and packaged up.

To date, studies have shown that DNA folding differs between cell types, yet relatively little is known about DNA folding in the cells which go on to form eggs and sperm. Two copies of the paternal and maternal DNA are present inside these cells and microscopy techniques have shown that each of these four DNA strands folds back and forth to form loop arrays extending for a shared protein axis. However, the dimensions and genetic positions of these loops is not known in humans or mice. Advancing present understanding of these DNA loop structures is thought to be important, since the length of the loops and the protein axis appear to relate to a cellular process, which forms crossovers, where stretches of DNA are exchanged between the maternal and paternal DNA sequences. The principle focus of my PhD was to map these loop arrays in mouse cells, to improve understanding of the cellular mechanisms that manipulate DNA looping and to further explore how these loops relate to crossovers.

My research utilised fluorescent labels to highlight both the protein axis and specific DNA sequences, which could be visualised through a microscope. Using this technique, I demonstrated that the bases of the DNA loops were fixed at specific DNA sequences and were conserved between individual cells. This finding enabled me to map the entirety of a chromatin loop and establish the physical length of an individual DNA loop in micrometres. In addition, I also found that the two strands of paternal and maternal DNA did not pair with one another as they extended away from the protein axis. However, the extent of such pairing was dependent on the position of the sequence within the DNA loop and the extent to which the protein axis had assembled.

Following the initial characterisation of the DNA loop I next examined the mechanisms responsible for DNA loop formation and maintenance. Firstly, I revealed that a protein ring called cohesin reduces the length of individual DNA loops, potentially by influencing the amount and position of DNA which interacts with the protein axis. Additionally, I generated evidence to suggest that the maintenance of DNA loop length is also reliant on a motor protein, called DNA polymerase, which moves along the DNA.

Intriguingly, in humans and mice, females tend to form more crossovers than males. My research, in combination with that of others, has revealed that this increase in crossovers in females also corresponds with a longer protein axis, shorter DNA loops and less separation of the four DNA strands compared to males. To explore these relationships in more detail I compared DNA loop organisation between young and adult male mice, as young males are thought to experience fewer interactions between maternal and paternal DNA strands which are necessary for crossover formation. I found that fewer interactions between maternal and paternal DNA in young males did not correspond with the length of the protein axis or loops, but separation of the four DNA strands did appear greater, suggesting that this feature may influence the progression of crossover formation.

Taken together, the research conducted within this PhD has helped to elucidate the basic organisation of DNA loops and its relationship with crossovers in the cells that go on to form eggs and sperm. The importance of crossovers is twofold; firstly, it creates genetic diversity which evolutionary forces can act on and secondly, it reduces the likelihood of infertility, miscarriage and development disorders, such as Down syndrome. Consequently, this research may help to form the foundations from which further research can better appreciate specific clinical and evolutionary events.

Table of Contents

Declaration……i
Dedication……ii
Acknowledgments……iii
Abstract……iv
Lay Abstract……vi
Table of Contents……viii
List of Figures……xiv
List of Tables……xviii
Abbreviations……xix
Chapter 1 Introduction…… 2
1.1 Sexual Reproduction and Meiosis…… 2
1.2 Meiotic Prophase I…… 3
1.3 Meiotic Chromosome Organisation…… 6
1.3.1 The Synaptonemal Complex…… 6
1.3.2 Large-Scale Chromatin Organisation…… 8
1.4 Assembly of the Synaptonemal Complex……13
1.4.1 Axial Elements……13
1.4.2 Transverse Filaments……14
1.4.3 Central Elements……15
1.4.4 Synaptonemal complex maintenance factor……16
1.4.5 SC Components and Large-Scale Chromatin Organisation……17
1.5 The Cohesin Complex……19
1.5.1 The Cohesin Complex……19
1.5.2 The Cohesin Core……20
1.5.3 Meiotic Cohesin and Chromosome Organisation……21
1.5.4 Meiotic Cohesin-Mediated Chromatin Loop Formation……24

1.6 Additional Structural Factors....28
1.6.1 The Condensin Complex....28
1.6.2 Transcription and Meiotic Large-Scale Chromatin Architecture....29
1.6.3 Meiotic CTCF....32
1.7 Meiotic Recombination....34
1.7.1 Overview....34
1.7.2 SPO11 and DSB Formation....35
1.7.3 DSB hotspots....36
1.7.4 Early DSB Processing....37
1.7.5 Recombinases and the Homology Search....39
1.7.6 Inter-Sister versus Inter-Homolog Repair....41
1.7.7 The Inter-Homolog Repair Pathway....42
1.7.8 Recombination-Independent Repair....47
1.8 Meiotic Recombination and Large-Scale Chromatin Looping....48
1.8.1 The Spatial Organisation of Meiotic Recombination Relative to the Chromosome Axis....48
1.8.2 Covariance of CO Abundance and Chromatin Loop Density....50
1.9 Thesis Aims....55

Chapter 2 Materials and Methods....56
2.1 Animals Use and Sample Preparation....56
2.1.1 Animal Use....56
2.1.2 Testes Surface-Spread Preparation....57
2.1.3 Testis Section Preparation....58
2.1.4 Ovary Spread Preparation....58
2.2 Pachytene Cell Enrichment and Treatment....59
2.2.1 Testis Single Cell Solution Preparation....59
2.2.2 Centrifugal Elutriation....60
2.2.3 Drug Treatment....61

2.3 Preparation of Fluorescence *In Situ* Hybridisation (FISH) Probes 62
2.3.1 FISH Probes Utilised 62
2.3.2 Growth of BAC and Fosmid Clones 63
2.3.3 Bacterial Glycerol Stock.....63
2.3.4 Purification of BAC and Fosmid FISH Probe DNA 63
2.3.5 Nick Translation of BAC and Fosmid FISH Probe DNA 64
2.3.6 Quantification of Label Incorporation 65
2.4 Immunofluorescent-Fluorescent *In Situ* Hybridisation (IF-FISH) on Surface-Spreads 66
2.4.1 Immunofluorescent (IF) staining 66
2.4.2 FISH Probe Hybridisation 66
2.4.3 FISH Probe Detection.....68
2.5 Immunofluorescent-Fluorescent *In Situ* Hybridisation (IF-FISH) on Testes Sections.....69
2.5.1 Section Antigen Retrieval and Immunofluorescent (IF) Staining 69
2.5.2 FISH Probe Hybridisation and Detection in Testes Sections.....69
2.6 Image Capture.....70
2.7 Image Analysis 72
2.7.1 Meiocyte Staging and Purity 72
2.7.2 IF and FISH Analysis - 2D Data.....72
2.7.3 Inter-Chromatid Distance - 3D Data.....74
2.8 RNA Isolation and Quantification 74
2.9 Statistical Analysis.....75

Chapter 3 Mapping an Autosomal Chromatin Loop in Mouse Pachytene Spermatocytes 77

3.1 Introduction 77

3.2 Results 79

3.2.1 SC-Proximal and SC-Distal Chromatin Regions 79

3.2.2 Mapping a Single Autosomal Chromatin Loop 81

3.2.3 Examining Chromatid Organisation within a Chromatin Loop 85

3.2.4 Comparing Recombination and IF-FISH Maps 90

3.2.5 Extending the Autosomal Chromatin Loop Map 91

3.2.6 Investigating the Role of SMC1β and SMC1α on Whole Chromosome Organisation 92

3.2.7 Chromatin Loop Organisation in *Smc1β-/-* and *Smc1β-/-,1α* Spermatocytes 94

3.2.8 Inter-Chromatid Organisation in *Smc1β-/-* and *Smc1β-/-,1α* Spermatocytes 98

3.2.9 Chromatin Condensation in *Smc1β-/-* and *Smc1β-/-,1α* Spermatocytes 101

3.2.10 Comparing HiC and IF-FISH Maps 103

3.2.11 Chromatin Organisation in Testes Sections 105

3.3 Discussion 108

3.3.1 Visually Mapping a Single Chromatin Loop in Pachytene Spermatocytes 108

3.3.2 Reconciling Spermatocyte HiC and IF-FISH data 110

3.3.3 Chromatid Organisation 111

3.3.4 Technical Drawbacks of IF-FISH 112

3.3.5 Recombination Mapping in the IF-FISH-defined Chromatin Loop 113

3.3.6 SMC1 Variants Manipulate Pachytene Chromatin Loops 114

Chapter 4 Dynamics of Meiotic Chromatin Loops in Mouse Spermatocyte Prophase I 119

4.1 Introduction....119

4.2 Results....121

4.2.1 Changes in Chromatid Organisation during Prophase I....121

4.2.2 Maintenance of Chromatin Organisation during Pachytene....125

4.2.3 Nuclear Organisation on Transcription Inhibition....127

4.2.4 Chromosome Morphology on Transcription Inhibition....130

4.2.5 Local Chromatin Condensation on Transcription Inhibition....134

4.2.6 Chromatin Loop Organisation on Transcription Inhibition....136

4.2.7 Chromatid Organisation on Transcription Inhibition....138

4.2.8 Nuclear Organisation on RNase Treatment....139

4.2.9 Transcription and the Positioning of Chromatin Regions Relative to the SC 141

4.3 Discussion....145

4.3.1 Chromatin Organisation in Meiotic Prophase I....145

4.3.2 Transcription and Pachytene Chromatin Organisation....149

4.3.3 RNA and Pachytene Chromatin Organisation....152

Chapter 5 Chromatid Organisation and Meiotic Recombination in Mouse Meiocytes 155

5.1 Introduction....155

5.2 Results....156

5.2.1 Comparing Chromosome Loop Morphology in Male and Female Pachytene Meiocytes....156

5.2.2 Comparing Local Chromatin Condensation in Male and Female Pachytene Meiocytes....160

5.2.3 Comparing Chromatin Loop Axis-Association in Male and Female Pachytene Meiocytes....162

5.2.4 Comparing Chromatid Organisation in Male and Female Pachytene Meiocytes....164

5.2.5 Chromatid Organisation at Meiotic Hotspots....166
5.2.6 Chromosome Morphology in Juvenile Spermatocytes....169
5.2.7 Chromatid Organisation in Juvenile Spermatocytes....171
5.3 Discussion....177
5.3.1 Regulating Inter-Homolog versus Inter-Sister Interactions....177
5.3.2 Chromatid Organisation at DMC1-Defined Hotspots and Coldspots 182
5.3.3 Sexually Dimorphic Chromatin Loop Topology....182

Chapter 6 Conclusion....185
6.1 Summary....185
6.1.1 Mapping Meiotic Chromatin Loops in Mice....185
6.1.2 The Regulation of Meiotic Chromatin Loops....187
6.1.3 The Functional Significance of Meiotic Chromatin Loop Arrays....189
6.1.4 Extending IF-FISH Analyses Temporally and Spatially....193
6.2 Wider Perspectives....195

Chapter 7 Bibliography....196

List of Figures

Chapter 1: Introduction

Figure 1-1. Meiotic cell division 3

Figure 1-2. The progression of meiotic prophase I 5

Figure 1-3. Organisation of the pachytene synaptonemal complex.. 7

Figure 1-4. DNA organisation during pachytene……..10

Figure 1-5. Stepwise model of synaptonemal complex assembly…….. 17

Figure 1-6. Putative cohesin complexes in meiosis. 20

Figure 1-7. Present models of the effect of SYCP3 and SMC1β on the organisation of the meiotic chromosome axes and chromatin loops. 25

Figure 1-8. Proposed dynamic loop formation models in interphase cells 27

Figure 1-9. Double-strand break end processing. 40

Figure 1-10. Overview of the recombination repair pathways.....46

Figure 1-11. Tethered loop-axis complex model 49

Figure 1-12. A correlative relationship between chromosome axis length, chromatin loop length and CO abundance 51

Chapter 3: Mapping an Autosomal Chromatin Loop in Mouse Pachytene Spermatocytes

Figure 3-1. BAC FISH probe-based mapping of SC-proximal and SC-distal regions in pachytene spermatocytes. 80

Figure 3-2. BAC FISH probe-based mapping of a single chromatin loop in pachytene spermatocytes. 82

Figure 3-3. Fosmid FISH probe-based mapping of a single chromatin loop in pachytene spermatocytes. 84

Figure 3-4. Inter-chromatid distances along a single chromatin loop in pachytene spermatocytes 87

Figure 3-5. Chromatid pairing along a single chromatin loop in pachytene spermatocytes. 89

Figure 3-6. Comparing IF-FISH map to DSB hotspot maps. 90

Figure 3-7. BAC FISH probe-based mapping of 2.5 kb flanking regions either side of the mapped chromatin loop in pachytene spermatocytes.....91

Figure 3-8. Analysis of chromosome 6 SC length and chromatin area in Smc1 mutant pachytene spermatocytes. 93

Figure 3-9. BAC FISH probe-based mapping of SC-proximal and SC-distal regions in *Smc1* mutant pachytene spermatocytes 95

Figure 3-10. Fosmid FISH probe-based mapping of a single chromatin loop in Smc1 mutant pachytene spermatocytes. 97

Figure 3-11. Inter-chromatid distance along a single chromatin loop in Smc1 mutant pachytene spermatocytes.. 99

Figure 3-12. Inter-sister chromatid distance on the non-homologous X chromosome in Smc1 mutant pachytene spermatocytes.....100

Figure 3-13. Chromatin condensation in *Smc1* mutant pachytene spermatocytes 102

Figure 3-14. Comparing HiC and IF-FISH Maps. 104

Figure 3-15. Inter-chromatid distances in pachytene spermatocytes present in testicular tissue sections 107

Figure 3-16. Putative Alterations in Chromatin Organisation in Smc1β-/- spermatocytes 117

Chapter 4: Dynamics of Meiotic Chromatin Loops in Mouse Spermatocyte Prophase I

Figure 4-1. Organisation of SC-proximal and SC-distal chromatids in leptotene ...122

Figure 4-2. Organisation of presumptive sister chromatids at a SC-proximal and a SC-distal locus in pachytene.....123

Figure 4-3. Sister chromatid organisation at leptotene and pachytene on the non-homologous X chromosome 124

Figure 4-4. Chromatid organisation relative to SC length 126

Figure 4-5. Sister chromatid organisation relative to chromosome axis length 127

Figure 4-6. Changes to nuclear area after transcription inhibition 128

Figure 4-7. Effect of transcription inhibition on SC length.....129

Figure 4-8. Effect of transcription inhibition on autosomal chromosome morphology 131

Figure 4-9. Changes to sex chromosome morphology on transcription inhibition. .134

Figure 4-10. Changes to chromatin condensation on transcription inhibition.....135

Figure 4-11. BAC FISH probe-based mapping of SC-Proximal and SC-distal regions after transcription inhibition 137

Figure 4-12. Changes to chromatid organisation on transcription inhibition.....138

Figure 4-13. Changes to nuclear architecture on RNase treatment.....140

Figure 4-14. Transcription in the *HoxA* Defined Chromatin Loop. 142

Figure 4-15. The relative positioning of the pachytene SC and transcriptionally active genes.....144

Figure 4-16. Models of cohesin-dependent modulation of sister chromatid organisation at a SC-proximal and a SC-distal locus between leptotene and pachytene.....148

Figure 4-17. Model of transcription- and cohesin-dependent chromatin loop extension relative to the meiotic chromosome axis in yeast and murine meiocytes.....150

Chapter 5: Chromatid Organisation and Meiotic Recombination in Mouse Meiocytes

Figure 5-1. Differences in pachytene chromosome morphology between males and females.....157

Figure 5-2. Differences in the positioning of SC-proximal and SC-distal regions in male and female pachytene meiocytes.....159

Figure 5-3. Autosomal chromatin compaction in male and female pachytene meiocytes 160

Figure 5-4. Sex chromosome chromatin compaction in male and female pachytene meiocytes 161

Figure 5-5. Differences in the organisation of a single chromatin loop in male and female pachytene meiocytes 163

Figure 5-6. Inter-chromatid distances along a single chromatin loop in male and female pachytene meiocytes 166

Figure 5-7. Chromatid organisation at meiotic hotspots in pachytene spermatocytes 167

Figure 5-8. Chromatid organisation at meiotic hotspots in leptotene spermatocytes 168

Figure 5-9. Differences in chromosome morphology in juvenile and adult pachytene spermatocytes. 170

Figure 5-10. Differences in chromatid organisation at meiotic hotspots in juvenile and adult pachytene spermatocytes 172

Figure 5-11. Differences in sister chromatid organisation in juvenile and adult pachytene spermatocytes 173

Figure 5-12. Differences in chromatid organisation in juvenile and adult leptotene spermatocytes 176

Figure 5-13. Sister chromatid capture model 179

Chapter 6: Discussion

Figure 6-1. Chromatin loop organisation and repair template choice overtime in murine spermatocytes 192

List of Tables

Chapter 1: Introduction

Table 1-1. Summary table of the phenotypes recorded for SYCP1-null, SYCP3-null and SC-null spermatocytes 21
Table 1-2. Summary table of the phenotypes recorded for mutants of the meiosis-specific cohesin components 53

Chapter 2: Materials and Methods

Table 2-1. Drugs administered 61
Table 2-2. FISH probes 62
Table 2-3. Immunofluorescence antibodies 66
Table 2-4. Antibodies/Avidin for FISH probe detection 68

Abbreviations

3C: Chromosome conformation capture

AE: Axial element

BAC: Bacterial artificial chromosome

BSA: Bovine serum albumin

CE: Central element

ChIP: Chromatin immunoprecipitation

ChIP-seq: ChIP sequencing

CO: Crossover

COI: Crossover interference

Co-IP: Co-Immunoprecipitation

DAPI: 4,6-diamidino-2-phenylindole

dHJ: Double Holliday junction

D-Loop: Displacement-loop

DMEM: Dulbecco's modified Eagle's medium

DNA: Deoxyribonucleic acid

DPBS: Dulbecco's phosphate buffer saline

dpp: Days post-partum

DSB: Double-strand DNA break

dsDNA: Double-stranded DNA

DTT: Dithiothreitol

E: Embryonic day

EDTA: Ethylenediaminetetraacetic acid

EM: Electron microscopy

FCS: Foetal calf serum

FISH: Fluorescence *in situ* hybridisation

FITC: Fluorescein isothiocyanate

GTE: Glucose/Tris/EDTA

IF: Immunofluorescence

JM: Joint molecule

KO: Knockout

KRB: Krebs ringer buffer

LE: Lateral element

MSCI: Meiotic sex chromosome inactivation

MSUC: Meiotic silencing of unsynapsed chromatin

NCO: Non-crossover

NHEJ: Non-homologous end joining

PAR: Pseudoautosomal region

PFA: Paraformaldehyde

PMSF: Phenylmethylsulphonyl fluoride

Pol: Polymerase

RNA: Ribonucleic acid

ROI: Region of interest

RT-PCR: Quantitative reverse transcription PCR

SC: Synaptonemal complex

SDS: Sodium dodecyl sulphate

SDSA: Synthesis-dependent strand annealing

SINE: Short interspersed nuclear element

SSC: Saline sodium citrate

ssDNA: Single-stranded DNA

TAD: Topologically associated domain

TE: Tris/EDTA

UV: Ultraviolet

TF: Transverse filament

WT: Wild type

Chapter 1:

Introduction

Chapter 1 Introduction

1.1 Sexual Reproduction and Meiosis

Sexual reproduction can be defined as the creation of offspring, through the combining of genetic material from two individuals. Meiosis is a specialised cell division integral to the sexual lifecycle, which facilitates the generation of haploid gametes, that fuse on fertilisation to form a genetically distinct, diploid zygote. Meiosis commences with a complete round of DNA replication, which duplicates each chromosome to form two sister chromatids. In contrast to mitosis, in meiosis replication is followed by two successive rounds of chromosome segregation, which first separates the two homologous copies of each chromosome and then their constituent sister chromatids (Figure 1-1). The haploid daughter cells that arise from meiosis therefore contain half the number of chromosomes compared to their diploid progenitors, thus enabling the ploidy of sexually reproducing species to be maintained (Handel and Schimenti, 2010).

Prior to entering nuclear division, meiotic cells undergo a protracted stage referred to as prophase I. Several meiosis-specific events that occur during prophase I are critical for the successful completion of meiosis. These events include the establishment of physical interactions between homologous chromosomes, through the process of meiotic recombination, as well as the pairing and synapsis of homologous chromosomes. Defects within these key meiotic events can be highly detrimental, leading to infertility and miscarriage in humans (Handel and Schimenti, 2010; Geisinger and Benavente, 2017). This thesis examines the physical configuration of chromatin in mammalian prophase I to create further insight into the inter-play between chromosomal organisation and fertility.

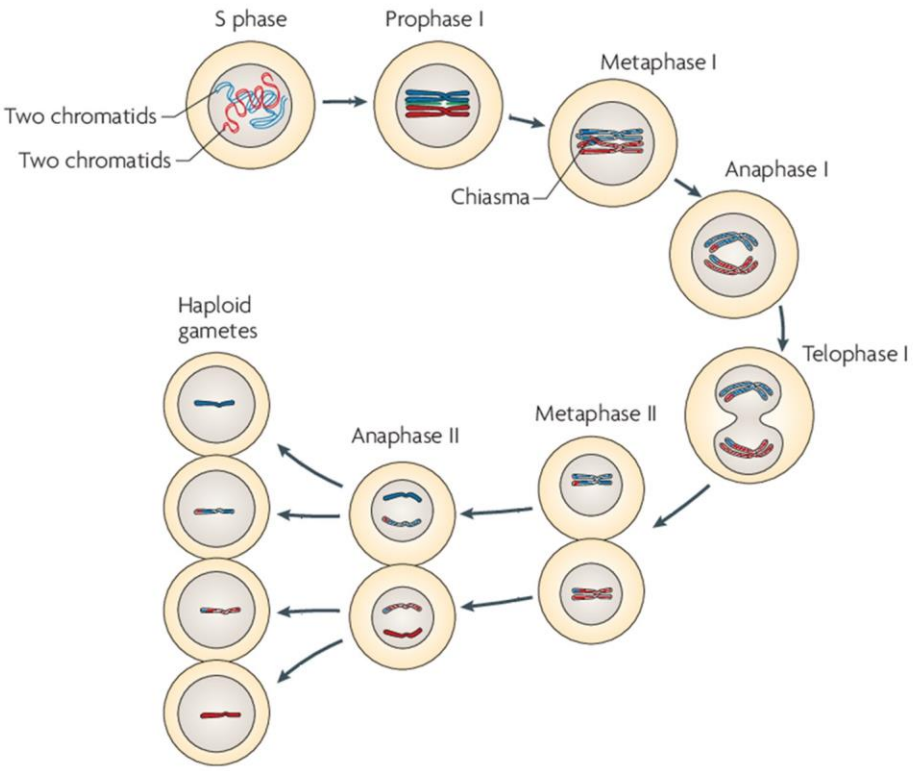

Figure 1-1. Meiotic cell division. Chromosomes are replicated during S phase to generate two sister chromatids per chromosome. During meiotic prophase I, genetic information is exchanged between homologous chromosomes through meiotic recombination, which results in the formation of chiasma that become cytologically evident in metaphase I. Following chiasma formation, homologous chromosomes are segregated during anaphase/telophase I. Sister chromatids are subsequently segregated in the second round of meiotic division. Image adapted from Handel and Schimenti, 2010.

1.2 Meiotic Prophase I

At the core of meiotic prophase I, is the assembly of the synaptonemal complex (SC), a meiosis-specific, protein structure which binds the axes of homologous chromosomes to one another. Prophase I can be broken down into four cytologically distinct substages, according to the status of SC assembly and the degree of inter-homolog interactions (Figure 1-2); leptotene (from the Greek for 'thin threads'), zygotene ('paired threads'), pachytene ('thick threads') and diplotene ('two threads'; Clermont, 1972; Page and Hawley, 2003). Meiotic recombination occurs concomitantly with the progression of prophase I, therefore the SC-defined

substaging of prophase I can assist in estimating the timing of recombinogenic events in wildtype meiocytes (Zickler and Kleckner, 1999).

In leptotene, formation of the SC begins with the generation of a fine, continuous protein core, referred to as the axial element (AE), which runs the length of individual chromosomes. The majority of meiotic recombination events simultaneously commence in leptotene, as hundreds of programmed double-strand breaks (DSBs) are formed throughout the genome (Bergerat *et al*., 1997; Keeney, Giroux, and Kleckner, 1997). Upon DNA cleavage, a DNA damage response cascade ensues, leading to the highly orchestrated recruitment of recombination repair proteins, which go on to initiate a homology search (Moens *et al.*, 2002). In combination, the homology search and rapid chromosomal movements, induced by force-generating machinery at the nuclear periphery, cause homologous chromosomes to be drawn into increasingly more intimate juxtaposition and to co-align in zygotene (Boateng *et al.,* 2013; Lee, Conrad and Dresser, 2012; Scherthan, 2001). On pairing of homologous chromosome axes, the AEs become known as lateral elements (LEs). Subsequent to homologous chromosome pairing, inter-homolog synapsis begins as sophisticated polymerisation reactions between transverse filament (TF) and central element (CE) proteins occur, causing homologous LEs to become bound to one another (Page and Hawley, 2003). Synapsis is completed in pachytene, as homologous LEs form two regular filamentous structures, which become synapsed along their entire length by a single SC (see Section 1.4). Unlike in females, synapsis of the heteromorphic sex chromosomes in male mice is constrained to a relatively short region of homology, known as the pseudoautosomal region (PAR). In mice, a single PAR extends ~700 kb at the XY telomere and provides the sequence identity necessary for synapsis and recombination between the X and Y chromosomes (Perry *et al.*, 2001). By the end of pachytene, DSBs are resolved typically by exploiting a homologous or sister chromatid as a recombinogenic repair template (Baudat and de Massy, 2007; Handel and Schimenti, 2010). In a fraction of instances (~10% in mice; Baudat and de Massy, 2007), the resolution of DSBs facilitates crossover (CO) formation, which is delineated by the reciprocal exchange of homologous chromosome arms flanking the break (Baudat, Imai and de Massy, 2013). Once cells enter diplotene, cyclin-dependent and aurora kinases work to promote the desynapsis of homologous chromosomes, as CE proteins and subsequently LE proteins are induced to dissociate from the SC (Sun and Handel, 2008). Consequently, the physical links between homologous chromosomes are largely disbanded, except for the CO sites. CO sites mature into

the inter-homolog bridges, referred to as chiasmata, which become cytologically visible at metaphase I. Chiasmata are essential for the appropriate bi-orientation of homologs on the metaphase I plate, which increases the likelihood of their faithful bipolar segregation in the first meiotic division and ultimately the successful generation of normal gametes (Petronczki, Siomos and Nasmyth, 2003).

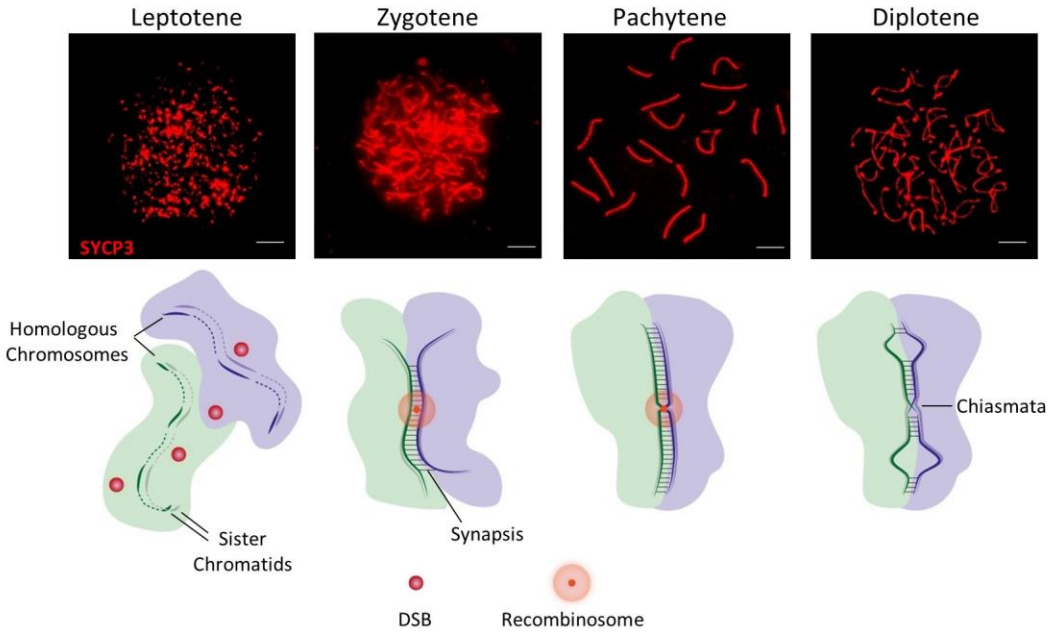

Figure 1-2. The progression of meiotic prophase I. Immunofluorescent staining of the axial element (AE) protein SYCP3 (red) on murine testes surface-spreads in leptotene, zygotene, pachytene and diplotene. Scale bar, 5 μm. The corresponding chromosomal organisation to each sub-stage is depicted below each image by a pair of homologous chromosomes (green and purple regions), each composed of two sister chromatids. In leptotene, DSBs are generated (red dot) whilst the chromosome axis running the length of each individual chromosome recruit structural component proteins (purple and green dashed/unbroken lines). In zygotene, axial element formation is complete (purple and green unbroken lines) and DSBs recruit recombination proteins that promote pairing and synapsis of homologous chromosomes, facilitated by the polymerisation of transverse filaments (TFs) and central elements (CEs) in the core of the synaptonemal complex (black bars). Complete SC assembly and synapsis are achieved in pachytene, during which a subset of DSBs may be resolved to form crossovers (COs) by a 'recombinosome' composed of recombinogenic machinery (orange dot). COs later mature into the cytologically visible chiasmata in diplotene as the SC disassembles.

1.3 Meiotic Chromosome Organisation

1.3.1 The Synaptonemal Complex

The synaptonemal complex (SC) is central to the progression of meiotic prophase I, forming a physical tether between homologous chromosomes and acting as the scaffold on which recombination machinery resides to process meiotic DSBs (Baudat *et al*., 2013; Zickler and Kleckner, 2015). Elegant electron microscopy (EM) analyses have demonstrated that each SC exhibits a ladder-like conformation; the rails align in parallel between each of the homologous chromosomes, with an inter-axis distance of approximately 100 nm in mice (Moses, 1968; Schücker *et al.*, 2015; Westergaard and von Wettstein, 1972; Schmekel *et al.* 1993). In mammals, the SC is composed of several meiosis-specific protein structural components: the LE proteins SYCP2 and SYCP3, which appear as the rail-like structures, and the core region elements SYCP1, SYCE1-3, TEX12 and SIX6OS1, which appear as the rung-like structures (Figure 1-3; Costa, 2005; de Vries *et al.*, 2005; Hamer, 2006; Bolcun-Filas *et al.*, 2007; Bolcun-Filas *et al.*, 2009; Schramm *et al.*, 2011; Gómez-H *et al.*, 2016). Notably, recent super-resolution microscopy investigations in *D. melanogaster* and mice have highlighted that the SC is composed of two layers that are suggested to connect two non-sister chromatids between homologs (Cahoon *et al*., 2017; Schücker *et al.*, 2015). Studies in *C. elegans* (Pattabiraman *et al.*, 2017; Rog, Köhler, and Dernburg, 2017) and mice (Enguita-marruedo *et al.,* 2018), also indicate that SC components are mobile and interact weakly, causing SC composition and organisation to be dynamic.

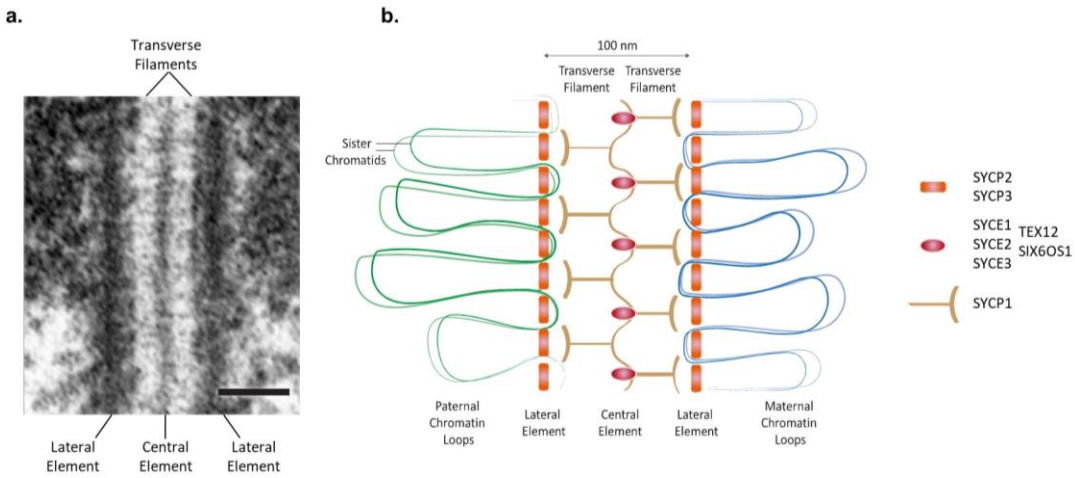

Figure 1-3. Organisation of the pachytene synaptonemal complex. **a.** The SC, visualised by EM (Scale bar, 100 nm; Kouznetsova, Benavente, Pastink, and Höög, 2011) and **b.** as a schematic. Meiotic chromosomes are organised into a sequential chromatin loop arrays. During pachytene, the base of which associates with a highly proteinaceous structure, referred to as the synaptonemal complex (SC). The SC is a tripartite structure, composed of 2 homologous lateral elements (SYCP2 and SYCP3) and a core region. The core is comprised of transverse filaments (SYCP1), which tether homologous chromosomes to one another, and central elements (SYCE1, SYCE2, SYCE3, SIX6OS1 and TEX12), which stabilise the SC and aid its extension.

1.3.2 Large-Scale Chromatin Organisation

To date, the most comprehensive characterisation of chromatin architecture has been conducted within the mitotic cell cycle, in which chromatin organisation is traditionally described to conform to a hierarchical structure. The hierarchical organisation of mammalian chromatin begins with a flexible chromatin fibre, composed of a nucleosomal array, in which adjacent nucleosomes are separated by 10-100 bp of 'linker' DNA (Alberts *et al*., 2002). The chromatin fibre is then decorated by multiple layers of regulatory adaptations, which cause the fibres to fold into secondary structures with a diameter of 5-24 nm, according to *in vivo* observations (Cai *et al.*, 2018; Eltsov *et al.*, 2008; McDowall, Smith, and Dubochet, 1986; Ou *et al*., 2017). Despite the exact topology of chromatin secondary structures currently being under scrutiny (Maeshima, Ide, and Babokhov, 2019), this level of chromatin organisation is the fundamental basis from which specific large-scale chromatin structures are formed.

The characterisation of large-scale chromatin structures has principally employed two fundamental techniques; fluorescent *in situ* hybridisation (FISH) and chromosome conformation capture (3C). In FISH, the hybridisation of fluorophore-labelled DNA probes in fixed cells, enables specific sequences of interest to be made cytologically visible. Thus, FISH permits the precise configuration of chromatin to be determined within individual cells. Chromosome conformation capture (3C) technologies, including genome-wide HiC and capture-3C, enable the 3D proximity of genomic loci to be assessed. This is achieved by quantifying the likelihood that two loci are in sufficient enough proximity to be cross-linked by a fixative agent, such as paraformaldehyde, inside a nucleus (Gibcus and Dekker, 2014).

The most comprehensive characterisations of chromatin architecture have been conducted in interphase and mitotic cells, producing a wealth of knowledge regarding basic large-scale chromatin organisation. The primary units of large-scale chromatin architecture in interphase cells are chromatin loops and topologically associated domains (TADs), which exhibit significant inter-cellular heterogeneity (Flyamer *et al*., 2017; Stevens *et al*., 2017). A chromatin loop is delineated by a pair of distal genomic sites, positioned in *cis*, which are more likely to interact with one another than with the intervening sequence (R*ao et al*., 2014). While TADs are 3C-defined self-associating chromatin regions, within which the chromatin exhibits a two- to three-fold interaction bias (Dixon *et al*., 2012), it is not clear how chromatin is physically arranged within

and between TADs. In addition to TAD and chromatin loops, larger structures acting at a multi-megabase scale, referred to as chromosome compartments and nuclear territories, have also been identified in interphase cells. Compartments are chromosomal regions of similar transcriptional activity, that coalesce in close nuclear proximity. 3C analyses tend to categorise nuclear compartments into two, A and B, which correspond to transcriptionally active and inactive chromatin, respectively (Lieberman-Aiden *et al*., 2009; Rao *et al*., 2014). Furthermore, extensive FISH and 3C investigations have demonstrated that individual chromosomes have a tendency to appear as discrete territories (Cremer and Cremer, 2010; Lieberman-Aiden *et al*., 2009). These data conform to basic thermodynamic principles, which predict that polymer chains possess a preferential bias towards *cis*, rather than *trans*, interactions.

Mitotic metaphase chromatin is compacted 10-fold more than within the average interphase nucleus (Ghosh and Jost, 2018). Recent studies have shown that such an increase in compaction is largely achieved through the manipulation of large-scale chromatin organisation (Daban, 2003; Naumova *et al*., 2013; Ou *et al*., 2017). Early structural analyses, utilising strategies such as transmission EM, highlighted that mitotic chromatin loop arrays emanate from a central, discontinuous scaffold (Paulson and Laemmli, 1977; Poirier and Marko, 2002), composed primarily of condensin and topoisomerase II alpha (Shintomi, Takahashi, and Hirano, 2015). According to HiC data from metaphase chicken DT40 cells, chromatin folds into chromatin loops arrays composed of ~80 kb inner loops, nested within ~400 kb outer loops (Chicano *et al*., 2019; Gibcus *et al*., 2018; Paulson and Laemmli, 1977). Moreover, over 95% of mitotic loops are not positioned at sequence-specific sites (Gibcus *et al*., 2018). Thus, mitotic loops are speculated to attach randomly to the core axis to form a chromatin network with great inter-cellular heterogeneity.

In both interphase and mitotic cells, large-scale chromatin organisation is frequently defined as structures greater than chromatin secondary structures (Merkenschlager and Nora, 2016). Importantly, the existence of such secondary structures in meiocytes has yet to be verified, therefore large-scale meiotic chromatin structures are herein defined as those which exhibit analogous features to those observed during the mitotic cell cycle. Cytological (Zickler and Kleckner, 1999), and more recently HiC (Schalbetter *et al.,* 2018; Alavattam *et al.*, 2019; Patel *et al.*, 2019; Vara *et al.*, 2019; Wang *et al.,* 2019), analyses have demonstrated that large-scale chromatin architecture undergoes significant alterations as early as meiotic prophase I. Historic

EM images are suggestive of prophase I chromatin not arranging into a simple linear fibre, lacking any organisational strategy. Instead, the chromatin appears to fold into relatively uniform sets of sequential loop arrays extending from the SC (Figure 1-3 and Figure 1-4; Zickler and Kleckner, 1999). Such configurations are indeed reminiscent of chromatin configuration reported in mitotic metaphase. The average length of meiotic chromatin loops is species-specific (Moens and Pearlman, 1988). In mice, predictions from EM, FISH and HiC studies suggest that the average meiotic loop may extend anywhere between 120 kb and 2 Mb (Ito *et al*., 2014; Moens and Pearlman, 1988; Patel *et al*., 2019). In pachytene, EM images indicate that each of the four chromatid copies forms a loop array emanating from a common SC. Both electron and conventional light microscopy have reported chromatid 'doubleness', predominantly in leptotene of lower order eukaryotes, suggesting that, at least during early prophase I, sister chromatids are arranged in distinct arrays (Zickler and Kleckner, 1999).

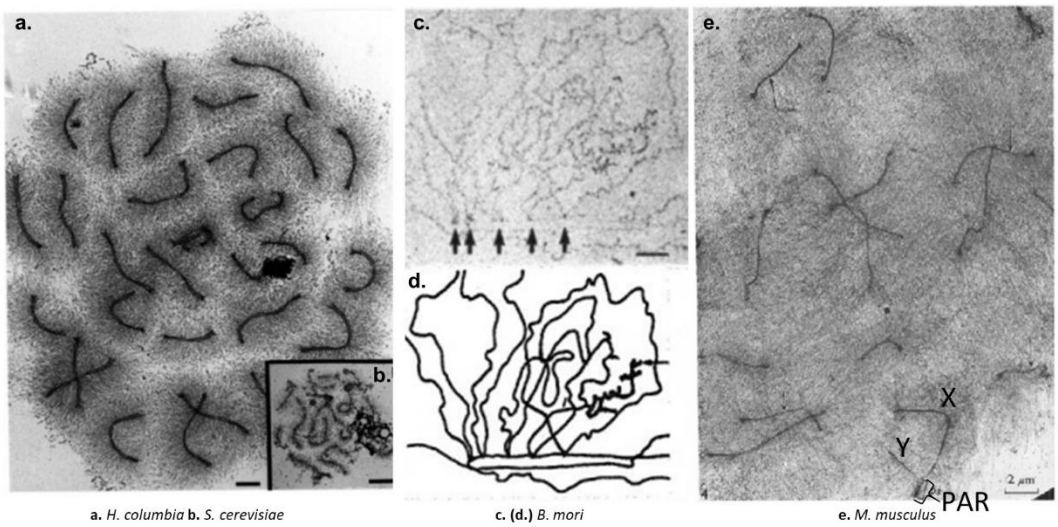

Figure 1-4. DNA organisation during pachytene. DNA spread pachytene nuclei from *H. columbia* (**a.**; Moens and Pearlman, 1988), *S. cerevisiae* (**b.**; Moens and Pearlman, 1988), *B. mori* (**c.**; Rattner, Goldsmith and Hamkalo, 1981; **d.** corresponding tracing) and *M. musculus* (**e.**; Tres, 1977) meiocytes, hypotonically decondensed and visualised by EM. DNA is visible extending from the pachytene SC. All scale bars, 2 μm. X and Y chromosomes and pseudoautosomal region (PAR) highlighted in **e.**

Meiotic chromatin loop arrays are most thoroughly annotated in *S. cerevisiae* and were originally mapped by a ChIP assay, which isolated chromatin interacting with the yeast AE protein, Red1. This investigation demonstrated that in budding yeast, chromatin associates with the chromosome axis in a sequence-specific manner, enabling axis-associated and loop-associated chromatin to be distinguished (Blat, Protacio, Hunter, and Kleckner, 2002). These patterns have recently been confirmed by HiC analyses in yeast, which have mapped loop-like chromatin contacts and have enabled variables, such as chromosome arm compaction, to be quantified (Schalbetter *et al*., 2018).

In contrast to yeast, attempts to isolate and sequence SC-associated chromatin in mammals, through ChIP for the AE protein SYCP3, have not resulted in the enrichment of unique genomic sequences (Johnson *et al*., 2013). Rather, repetitive sequences, including active SINE retrotransposons, were reported to be modestly enriched in the SYCP3 ChIP data from both rodent and primate spermatocytes (Johnson *et al*., 2013). These data also resonate with findings generated when nucleases were used to trim away peripheral loop-associated chromatin, enabling the residual axis-proximal chromatin to be isolated and sequenced (Li *et al.*, 1983; Moens and Pearlman, 1988; Pearlman, Tsao, and Moens, 1992). A number of transgenic mouse experiments have also shown that 'foreign' bacterial sequences, inserted within the immunoglobulin locus, do not visibly co-localise with the murine SC, but instead appear as loops, anchored to the SC by flanking endogenous chromatin (Heng, Tsui, and Moens, 1994; Kolas *et al*., 2004). However, it is not yet clear if there is a specific sequence or genomic feature, such as a particular arrangement of repetitive elements, within the immunoglobulin region that is responsible for this property. Intriguingly, a human-derived yeast artificial chromosome was found to adopt a similar axis/loop organisation to endogenous chromatin in meiotic yeast nuclei, with a 20-times reduction in chromatin compaction (Loidl *et al.*, 1995; Sears, Hegemann, and Hieter, 1992). In the future, it will therefore prove interesting to examine how DNA sequence and host genetic determinants inter-relate to manipulate loop organisation and whether such mechanisms are conserved between yeast and mammals.

It is only in recent months that HiC maps have been generated in mouse (Alavattam *et al.*, 2019; Patel *et al.*, 2019; Vara *et al.*, 2019; Wang *et al.,* 2019) and Rhesus monkey (Wang *et al*., 2019) spermatocytes, in prophase I. These HiC investigations

revealed that as mammalian spermatocytes progress through prophase I, interphase-defined TAD and compartment structures are reduced in frequency and smaller, more refined compartments, which extend up to 0.5-2 Mb in mouse pachytene, become apparent (Alavattam *et al.*, 2019; Patel *et al.*, 2019; Vara *et al.*, 2019; Wang *et al.,* 2019). One recent HiC study, suggested that chromatin compartmentalisation was lost all together, with a simultaneous 60% decline in TADs compared to spermatogonia (Vara *et al*., 2019). A marked loss of long-range interactions, exceeding 3-10 Mb, was also observed in mouse spermatocytes (Alavattam *et al*., 2019; Patel *et al*., 2019). This observation supports the concept that meiotic chromatin is organised around a chromosome axis. The chromosome compartments, defined in mammalian meiocytes, are distinct from the reproducible loop-like structures mapped in yeast (Schalbetter *et al.*, 2018; Alavattam *et al.*, 2019; Patel *et al.*, 2019). However, it is not known whether these differences reflect fundamental differences in the way that meiotic chromatin is organised and interacts with the SC between these species. Or, that interactions between meiotic chromatin and the SC exhibit more inter-cellular heterogeneity in mammals compared to yeast. It is also important to note, the potential of inter-sister and inter-homolog interactions being captured by 3C methodologies can complicate the identification of chromatin interactions occurring in *cis.* Moreover, many questions remain regarding how meiotic HiC maps correlate with axis-association sites and the cytologically visible chromatin loops.

1.4 Assembly of the Synaptonemal Complex

1.4.1 Axial Elements

SC assembly can be divided into three principle steps: Firstly, recruitment of SYCP2 and SYCP3 to the chromosome core. Secondly, the promotion of SYCP1-mediated inter-homolog synapsis. And finally, the stabilisation and extension of the core region along chromosomes axes, following the recruitment of CE proteins (Figure 1-5). During leptotene, SYCP2 and SYCP3 are recruited to the chromosome axis in an inter-dependent manner (Pelttari *et al*., 2001; Yang *et al*., 2006). Three principle lines of evidence support SYCP2 and SYCP3 as the key structural constituents of the AE: Firstly, by immuno-based microscopy, both proteins have been shown to co-localise along unsynapsed chromosome axes, where they are maintained through SC assembly until dissolution of the SC at diplotene (Dobson *et al.*, 1994; Offenberg *et al*., 1998). Secondly, when overexpressed in cultured somatic cells, and *in vitro*, full-length SYCP3 self-assembles into long filaments, reminiscent of endogenous AEs (Yuan *et al*., 1998). Although SYCP2 is incapable of self-assembly in isolation, on co-expression with SYCP3 the proteins form a stoichiometric complex, facilitated by interactions at their coiled coil-domains (Yang *et al.*, 2006; West *et al.*, 2019). On further assembly, the SYCP2-SYCP3 complex causes the SYCP3 homotypic filaments to form a dynamic scaffold (Pelttari *et al.*, 2001; West *et al.*, 2019). These observations are complemented by *in vivo* observations in *Sycp2−/−* spermatocytes and oocytes, in which SYCP3 forms large aggregates that fail to bind axial chromosomal cores (Yang *et al.*, 2006). And thirdly, genetic knockout studies, in *Sycp2-/-* and *Sycp3-/-* mice, show perturbations in chromosome synapsis (Yang *et al*., 2006; Yuan *et al*., 2002, 2000). These data demonstrate that both proteins are essential for inter-homolog synapsis and SC assembly. The structural aberrations imposed on *Sycp2-/-* and *Sycp3-/-* spermatocytes result in the triggering of the meiotic sex chromosome inactivation (MSCI) checkpoint, which induces apoptosis specifically in males (Turner *et al*., 2005; Yang *et al*., 2006; Yuan *et al*., 2000). Unlike their male counterparts, *Sycp3-/-* oocytes progress through meiotic prophase I, albeit the chromosomal axes undergo a 1.5-fold longitudinal decompaction, demonstrating that SYCP3 is required to promote the longitudinal compaction of the chromosomal axis (Novak *et al*., 2008).

1.4.2 Transverse Filaments

The classic model of SC assembly dictates that, following pairing of homologous chromosomes, SYCP1 interacts with homologous axial elements and the DNA backbone to promote SC assembly, chromosome synapsis and the strengthening of chromatin-axis interactions (Figure 1-5; Fraune *et al.*, 2012; Dunce *et al.,* 2018). Artificial expression of *Sycp1* in cultured somatic cells, in which additional SC components are absent, leads to the self-assembly of the protein into SC-like polycomplex structures (Öllinger, Alsheimer and Benavente, 2005). *In vitro* crystallographic and biophysical studies explain this may be achieved through the assembly of SYCP1 tetramers, whose interactions form a structure of intertwined lattices between homologous AEs (Dunce *et al.*, 2018). In addition, SYCP1 has DNA-binding interfaces, whose ability to interact with DNA has been confirmed by electrophoretic mobility shift assays (Dunce *et al.*, 2018). These findings therefore imply that SYCP1 acts as a linker between homologous LEs, while SYCP1-DNA interactions may reinforce the SYCP1 lattice. In *Sycp1-/-* mice, LEs appear to form normally, but homologous LEs fail to undergo synapsis along their entire length to form a complete SC (de Vries *et al*., 2005). Consequently, *Sycp1-/-* meiocytes undergo MSCI-mediated cell death and mice experience complete infertility (de Vries *et al*., 2005). In the absence of DSBs or specific recombination factors, such as DMC1, homolog synapsis is significantly perturbed in mice, as AEs still form but the assembly of a complete SC is disrupted and, in some instances, SC formation is observed between non-homologous chromosomes (eg. Pittman *et al.*, 1998; de Vries *et al.*, 1999; Baudat *et al.*, 2000; Romanienko and Camerini-Otero, 2000). Collectively, these genetic studies highlight that SYCP1-mediated synapsis between homologous chromosomes is recombination-dependent (discussed in further detail in Section 1.7).

1.4.3 Central Elements

In addition to SYCP1 recruitment, SC maturation is dependent on CE proteins (Figure 1-5), which are proposed to both stabilise nascent SYCP1-mediated synapsis and promote the longitudinal extension of the mature SC along the length of every bivalent (Dunce *et al.,* 2018). This leads to the CE proteins being described as either synaptic initiation factors or extension factors.

SYCE3, SYCE1 and SIX6OS1 are described as synaptic initiation factors, as their respective mouse knockouts exhibit short discontinuous SYCP1 assemblies between homologous axes, leading to the failure of complete SC maturation (Bolcun-Filas *et al.*, 2009; Schramm *et al.,* 2011; Gómez-H *et al.*, 2016). Accordingly, the mutant meiocytes undergo MSCI-mediated arrest, prompting apoptosis and infertility (Bolcun-Filas *et al.*, 2009; Schramm *et al.,* 2011; Gómez-H *et al.*, 2016). On completion of wildtype synapsis, the synaptic initiation factors localise along the length of each LE. Furthermore, co-immunoprecipitation studies in somatic cells have reported that SYCE3 interacts with SYCP1 and SYCE1, providing a physical link between transverse filaments and the core region (Costa, 2005; Schramm *et al.,* 2011; Lu *et al.*, 2014; Hernández-Hernández *et al.,* 2016). Similarly to other SC components, biophysical findings have shown SYCE3 undergoes self-assembly forming a discrete series of oligomers, which have the potential to extend indefinitely to support a SYCP1 lattice (Dunne and Davies, 2019a). Although SIX6OS1 has yet to undergo structural elucidation, the protein shares common sequence features with SYCE3, indicating the two proteins may share similar structural roles within the SC to structurally reinforce SYCP1 (Gómez-H *et al*., 2016). In *Syce3-/-* and *Six6os1-/-* mice, all other known CE proteins fail to recruit to the SC. Thus, leading to the conclusion that SYCE3 and SIX6OS1 facilitate loading of additional CE proteins, which subsequently promotes complete synapsis between homologous axes (Schramm *et al.*, 2011; Gómez-H *et al.*, 2016). In comparison to SYCE3, SYCE1 forms a non-assembling dimer, whose structure is compatible with a strut, responsible for physically linking multiple layers of SYCP1 together within the SC to promote synapsis (Dunne and Davies, 2019b). Cumulatively, present data indicates that SYCE3, SYCE1 and SIX6OS1 are required to promote short stretches of synapsis between chromosomes axes, by providing transverse and vertical structural supports to a nascent SYCP1 lattice (Bolcun-Filas *et al.*, 2009; Schramm *et al.,* 2011; Gómez-H *et al.*, 2016).

Biophysical studies have revealed that SYCE2 and TEX12 form a stable, constitutive 4:4 complex, supporting prior findings which suggested that the proteins co-localise and co-immunoprecipitate together in mouse testis lysate (Davies, Maman, and Pellegrini, 2012; Hamer, 2006). In *in vitro* biophysical analyses, the SYCE2-TEX12 complex forms long filamentous structures, which can extend to a micrometre scale (Davies *et al*., 2012). However, *in vivo*, SYCE2-TEX12 localise in a punctuate pattern along the wildtype SC (Hamer, 2006; Bolcun-Filas *et al.*, 2007; Hamer *et al.*, 2008). Disruption of these complexes, through *Syce2*-depletion, leads to synaptic failure, yet short stretches of SYCP1 filaments are evident (Bolcun-Filas *et al*., 2007). This suggests that the SYEC2-TEX12 complex is responsible for extending synapsis in discrete intervals along the chromosome axis. Similarly to the synapsis initiation proteins, the inability to form a complete SC leads to the initiation of the MSCI checkpoint in *Syce2*-/- mice (Bolcun-Filas *et al.*, 2007).

1.4.4 Synaptonemal complex maintenance factor

Recently, a novel protein, SCRE (Synaptonemal complex reinforcing element), was characterised (Liu *et al*., 2019). SCRE distributes itself in punctuate foci, 400-1,400 nm apart, along the SC in wildtype cells. This distribution indicates the protein is likely to be functionally distinct from previously reported SC components, which appear more regularly along the SC (Liu *et al*., 2019). In *Scre-/-* mice SYCP1 assemblies prematurely desynapse and the distribution of synapsis elongation factors becomes abnormal (Liu *et al*., 2019). Therefore, these data suggest that SCRE is responsible for maintaining the integrity of the initial SYCP1-mediated synapsis.

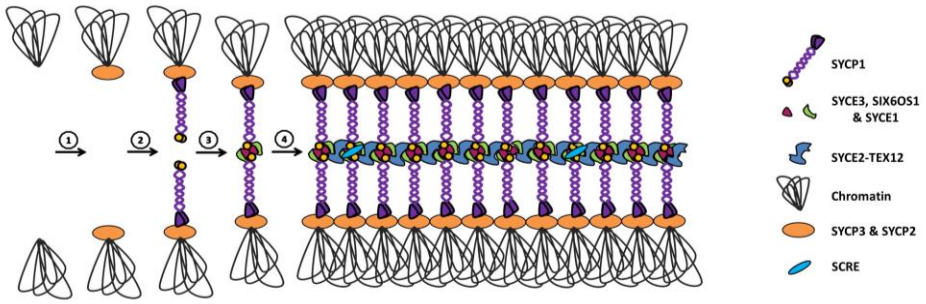

Figure 1-5. Stepwise model of synaptonemal complex assembly. 1. SYCP2 and SYCP3 are recruited to the chromosome axis at the base of chromatin loops. **2.** Homologous axes pair and SYCP1 associates with the axes. **3.** SYCE3, SYCE1 and SIX6OS1 are recruited to the sites of SYCP1-mediated synapsis initiation. **4.** SYCE1 and SCRE work to stabilise the initial synapsis initiation points and the SYCE2-TEX12 complex promotes synapsis elongation and the formation of a complete SC along the length of the homologous LEs. Image adapted from Fraune, 2012.

1.4.5 SC Components and Large-Scale Chromatin Organisation

Intriguingly, cytological analyses have shown that chromatin loop density frequently exhibits an intimate, inverse relationship with axis length (Baier *et al.*, 2014; Gruhn *et al.*, 2013; Kauppi *et al.*, 2011; Tease and Hultén, 2004; Zickler and Kleckner, 1999). Therefore, attention has been drawn towards how components of the SC act as meiosis-specific architectural factors. AE formation is aided through the recruitment and incorporation of SYCP2 and SYCP3, which create the initial platform on which the SC assembles and from which chromatin loops extend. Both AE proteins have been shown to possess putative DNA-binding domains (Offenberg *et al.*, 1998; Syrjänen, Pellegrini, and Davies, 2014). This observation has been explored to a greater depth with the SYCP3 protein, where large, homotypic SYCP3 oligomers have been reported to bind and condense plasmid DNA (Bollschweiler, Radu, and Pellegrini, 2018). Additionally, *in vitro* single-molecule analysis has demonstrated that SYCP3 tetramers coordinate linkage between distinct DNA regions, consequently bringing genetically distal loci into greater physical proximity (Baier, Alsheimer, and Benavente, 2007; Syrjänen *et al.*, 2017; Syrjänen, Pellegrini, and Davies, 2014). It is therefore possible that clusters of SYCP3 tetramers and SYCP2:SYCP3 complexes assist in the nucleation or stabilisation of chromatin loop structures, along the meiotic

AE. To interrogate this structural role of SYCP3 in an *in vivo* context, chromatin organisation was assessed in *Sycp3-/-* mouse spermatocytes (Kolas *et al.*, 2004; Novak *et al.*, 2008). Curiously, in the absence of SYCP3, the length of chromatin extensions from the SC (determined by the width of a chromosome paint and the length of a λ-phage insert extending from the chromosome axis) declines by ~50% in mouse spermatocytes (Kolas *et al.*, 2004). Furthermore, in wildtype spermatocytes, the λ-phage insert failed to attach to the SC. Yet, in the absence of SYCP3, the exogenous DNA appears to interact with the SC at multiple attachment sites (Figure 1-7; Kolas *et al.*, 2004). This indicates that SYCP3 may promote the extent to which chromatin extends from the SC, by reducing the number of axis-association sites and therefore the number of loops formed. For instance, it might be possible that the presence of SYCP3 creates stable axis-association sites at specific points along the chromosome axis, which improves the efficiency at which chromatin loops are extended. However, in *Sycp3-/-* mice, the axis-association structures become less stable, reducing chromatin loop extensions and enabling more axis-association sites to be established. Whether this effect is dependent on the DNA-binding abilities of SYCP3 observed *in vitro* and/or SYCP3-mediated chromosome axis compaction is not known. Additionally, interpreting analyses based on the organisation of a λ-phage insert should be done with caution, as it is not clear if the insert is capable of accurately recapitulating the endogenous chromatin. Furthermore, it remains to be determined if such defects result from the absence of SYCP3 or the pre-synaptic developmental arrest (Yuan *et al*., 2000), causing the differences in axis-chromatin interactions, observed in *Sycp3-/-* and *Sycp3*+/+ mice, to simply represent distinct stages of prophase I progression.

1.5 The Cohesin Complex

1.5.1 The Cohesin Complex

The core mammalian cohesin complex in interphase cells is composed of two SMC family members, SMC1α and SMC3, and a kleisin protein, RAD21 (Nasmyth and Haering, 2009). Each of the SMC subunits has a coiled-coil domain, that connects a globular hinge domain to an ATPase, nucleotide-binding domain. In the cohesin complex, SMC1α and SMC3 stably dimerise via their respective hinge domains (Haering *et al.*, 2002), with RAD21 completing the ring by binding the nucleotide-binding head domains of both SMC1 subunits (Anderson *et al.*, 2002; Gruber, Haering, and Nasmyth, 2003; Haering *et al*., 2002). RAD21 is also bound by additional accessory factors, including a stromal antigen group protein (either SA1 or SA2) and Kleckner, 1999; Wells *et al.*, 2017). During meiotic prophase I, the canonical cohesin subunits are supplemented with three meiosis-specific cohesin subunits, SMC1β, a paralog of SMC1α, and two kleisins, RAD21L and REC8 (Eijpe *et al.*, 2003; Ishiguro *et al.*, 2011), whilst SA1 and SA2 are supplemented by STAG3, a third stromal antigen protein (Pezzi *et al*., 2000; Prieto *et al*., 2001; Rankin, 2015). These additional, meiosis-specific subunits associate with the canonical cohesin subunits to create an enhanced range of cohesin complexes available to meiocytes. Results from several co-immunoprecipitation experiments have been combined to draw a list of putative cohesin complexes (Figure 1-6; Lee and Hirano, 2011). Importantly however, the complete range of meiotic cohesin complexes is yet to be fully verified in mouse spermatocytes.

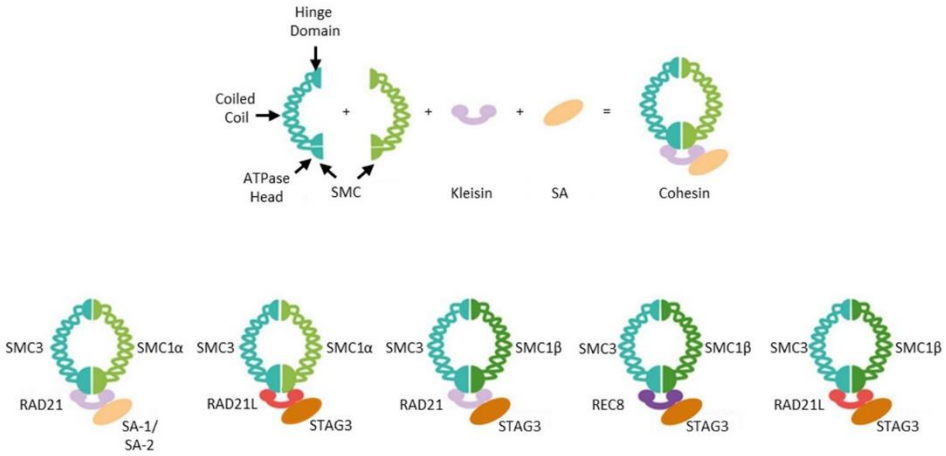

Figure 1-6. Putative cohesin complexes in meiosis. Cohesin is composed of four core subunits assembled as shown (top row), including two SMC1 proteins that connect at their hinge domain. The SMC dimer binds via the ATPase head domains to a kleisin subunit and a SA subunit. Bottom row - Proposed cohesin complex composition in mouse testes, as based on co-immunoprecipitation analyses (bottom Lee and Hirano, 2011). Figure adapted from (Rankin, 2015).

1.5.2 The Cohesin Core

Western blotting of isolated rat SCs has demonstrated that SCs are composed of an extensive number of components and/or protein variants, highlighting the possibility that further proteins may be present at the SC, in addition to the canonical SC proteins (Heyting *et al.*, 1985). Cytological analyses of the SC have demonstrated that cohesin complexes are enriched at the LE, while REC8 and STAG3 have also been shown through co-immunoprecipitation to interact with the SYCP3, in mammalian testis lysate (Eijpe *et al.*, 2000; Lee *et al.*, 2003; Pezzi *et al*., 2000). Immunofluorescent staining has shown that meiotic cohesin proteins begin to be expressed in S-phase in mammals. Then, during leptotene, the cohesin complexes of each replicated chromosome are aligned, to form the initial axial element/cohesin core, prior to SYCP2/SYCP3 recruitment (Eijpe *et al*., 2003; Uhlmann and Nasmyth, 1998). Electron microscopy (EM) studies in *Sycp3-/-* mice, which fail to recruit SYCP2 or SYCP3 to the chromosome axis, revealed that a SC-like chromosome core was still apparent (Liebe *et al*., 2004). Immunofluorescent staining has also confirmed that, in both *Sycp3*-null and *Sycp2*-null mice, SYCP1 recruitment is still possible and forms

SC-like structures (Pelttari *et al*., 2001). Notably, in *Sycp1-/-Sycp3-/-* (SC-null) mice, a chromosome axis enriched in cohesin subunits is maintained and capable of recruiting additional SC components. This indicates that cohesin is likely to be pivotal in SC assembly and chromosome synapsis (Meiotic phenotypes of the SC-null mice are summarised in Table 1-1; Kouznetsova *et al.*, 2011).

Table 1-1. Summary table of the phenotypes recorded for SYCP1-null, SYCP3-null and SC-null spermatocytes.

	SYCP1-null	**SYCP3-null**	**SC-null**
Synapsis	No	Partial	No
Cohesin Axis	Yes	Yes	Yes
Recombination	Delayed	Distribution disrupted	Delayed
Fertile	No	No	No

1.5.3 Meiotic Cohesin and Chromosome Organisation

In the mitotic cell cycle, the cohesin ring complex acts as an adherent force mediating sister chromatid cohesion, which is maintained until the timely bipolar segregation of sister chromatids, at the metaphase-to-anaphase transition during mitosis (Nasmyth, 2011; Uhlmann, Lottspeich, and Nasmyth, 1999). The principle model of cohesin-mediated chromatid cohesion is based on the fact that cohesin rings have a diameter approximately three times greater than an extended chromatin fibre (Huis in't Veld *et al*., 2014). Therefore, it is possible for the cohesin rings to topologically entrap sister chromatids, either through a single cohesin ring encircling both chromatids (Haering *et al.*, 2008) or the dimerization of two cohesin rings into 'handcuffs', enabling each monomer to constrain a single chromatid (Skibbens, 2016). Similarly to somatic cells, cohesin is essential for facilitating sister chromatid cohesion in meiocytes, which in turn is integral to CO formation and balanced meiotic segregation (Revenkova *et al*., 2004; Xu *et al*., 2005; Llano *et al*., 2014). However, in addition to its role in chromatid cohesion in prophase I, genetic knockout mouse models have demonstrated that cohesin is also intimately involved in the orchestration of gross chromosome organisation, influencing both the SC and the organisation of chromatin loops.

Throughout prophase I, the two most prominent kleisin proteins are REC8 and RAD21L (Lee and Hirano, 2011; Ishiguro *et al*., 2014). Both REC8 and RAD21L become detectable through immunostaining in S-phase and co-localise with chromosomes axes (Herrán *et al*., 2011; Ishiguro *et al*., 2011; Lee and Hirano, 2011). Super-resolution immunostaining has shown that within the SC, the two kleisins are discontinuously localised at the interface between the LEs and the core region and are not necessarily symmetric between homologous LEs (Rong *et al.*, 2016). Recent genome-wide ChIP-seq data has shown that RAD21L and REC8 are positioned approximately every 264.1 kb and 219.2 kb, respectively, in pachytene-enriched populations (Vara *et al*., 2019). However, the degree of inter-cellular heterogeneity of cohesin binding profiles is not presently known. *Rec8-Rad21l* double mutant murine meiocytes are incapable of assembling an AE, causing meiotic arrest in a leptotene-like state (Biswas *et al.,* 2016; Llano *et al*., 2012; Ward *et al.*, 2016). Less severe axial aberrations are observed in single knockout mice; in male mice axes partially or completely depleted of *Rec8* are shortened (Bannister *et al.*, 2004; Xu *et al.*, 2005). Furthermore, by comparing wildtype mouse strains with distinct levels of REC8, SC length was found to correlate with REC8 abundance (Vranis *et al.*, 2010). Direct genetic manipulation of *Rec8* expression will be required to verify this proposition. However, such alterations in gross chromosomal morphology, indicate that cohesin is integral to axis assembly. Consequently, since axis and chromatin loop topology are known to be intimately related (Zickler and Kleckner, 1999), it is plausible that both meiosis-specific kleisins are also involved in the manipulation of large-scale chromatin organisation.

The meiosis-specific stromal antigen protein STAG3 is expressed in mouse spermatocytes in pre-leptotene through to zygotene, where it is highly enriched on AEs (Fukuda *et al*., 2014). Deletion of *Stag3* in mice has the most striking mutant phenotype of all cohesin single knockout mice examined to date, which may be due to its association with the majority of meiosis-specific cohesin complexes (Eijpe *et al*., 2000). *Stag3-/-* spermatocytes can form complete AEs; however, they are shortened by over 50% and are unable to achieve full synapsis as SYCP3 forms protein aggregates. Similar phenotypes were also observed in *Stag3-/-Rec8-/-* and *Stag3-/-Rad21l-/-* mice (Fukuda *et al*., 2014; Hopkins *et al*., 2014; Llano *et al*., 2014; Ward *et al*., 2016; Winters, Mcnicoll, and Jessberger, 2014). Furthermore, although presently unquantified, chromosome paints increase in area following *Stag3* deletion,

suggesting that STAG3 is also important in the manipulation of chromatin extensions from the chromosome axis (Bhattacharyya *et al.,* 2019).

In mice, the relationship between cohesin and chromosome morphology has been most extensively examined using genetic analyses of *Smc1* mutants. *Smc1β*-null mouse spermatocytes and oocytes experience a two-fold reduction in SC length, relative to wildtype mice, indicating a role for SMC1β in the decompaction of the AE (Novak *et al*., 2008; Biswas, Stevense and Jessberger, 2018). The reduction in SC length in *Smc1β*-/- oocytes is accompanied by alterations in chromatin organisation, as the length of chromatin extensions from the SC appear highly heterogeneous, relative to wildtype chromatin topology (Novak *et al*., 2008). Novak *et al.* postulate this is due to chromatin being anchored to the SC by either SMC1β-dependent or SMC1β -independent mechanisms. This would cause only a subset of axis-association sites along the chromosome axis to be affected in *Smc1β*-/- oocytes, as only a subset of 'anchored' chromatin is released from the axis (Novak *et al.*, 2008). However, it is also feasible the SMC1β is involved in determining chromatin compaction and the physical length of chromatin loops, without altering axis-association density directly. Intriguingly, although *Smc1β-/-* oocytes only experience a subtle change in average chromatin loop length (Novak *et al.*, 2008), *Smc1β-/-* loops are 1.8-1.9 fold greater in spermatocytes (Revenkova *et al*., 2004), highlighting that SMC1β could have a putative sexually dimorphic role in the manipulation of chromatin structure. Notably, by placing the *Smc1α* gene under the control of a transgenic *Smc1β* promoter, in *Smc1β*-/- spermatocytes (*Smc1β-/-,1α*), a partial rescue in SC length is observed, demonstrating a degree of redundancy between the *Smc1* paralogs in the determination of SC length (Biswas, Stevense and Jessberger, 2018). The meiosis-specific role of SMC1α is yet to be interrogated independently of SMC1β, due to its involvement in the mitotic cell cycle. Thus, investigations utilising a conditional *Smc1α* knockout could shed light on the degree of redundancy between the SMC1 variants.

1.5.4 Meiotic Cohesin-Mediated Chromatin Loop Formation

It is evident that cohesin has the capacity to manipulate meiotic chromatin organisation. The exact underlying mechanism behind cohesin-mediated chromatin manipulation is presently unknown. However, it is interesting to consider how cohesin interrelates with SYCP3, as two key components of the AE (Figure 1-7). Axis length in *Sycp3-/-Smc1β-/-* mouse oocytes is elevated relative to wildtype axes, indicating that SYCP3 has a more significant impact on axis organisation than SMC1β, as one may expect from a key SC component (Novak *et al.*, 2008). The heterogeneity in chromatin loop length, as seen in *Smc1β-/-* mouse oocytes, is preserved in the *Sycp3-/-Smc1β-/-* mice (Novak *et al*., 2008). In this regard, SMC1β is epistatic to SYCP3 and acts upstream of the AE to dictate chromatin loop topology, whilst SYCP3 manipulates these structures further according to SC organisation. A comparable study is yet to be conducted in murine spermatocytes.

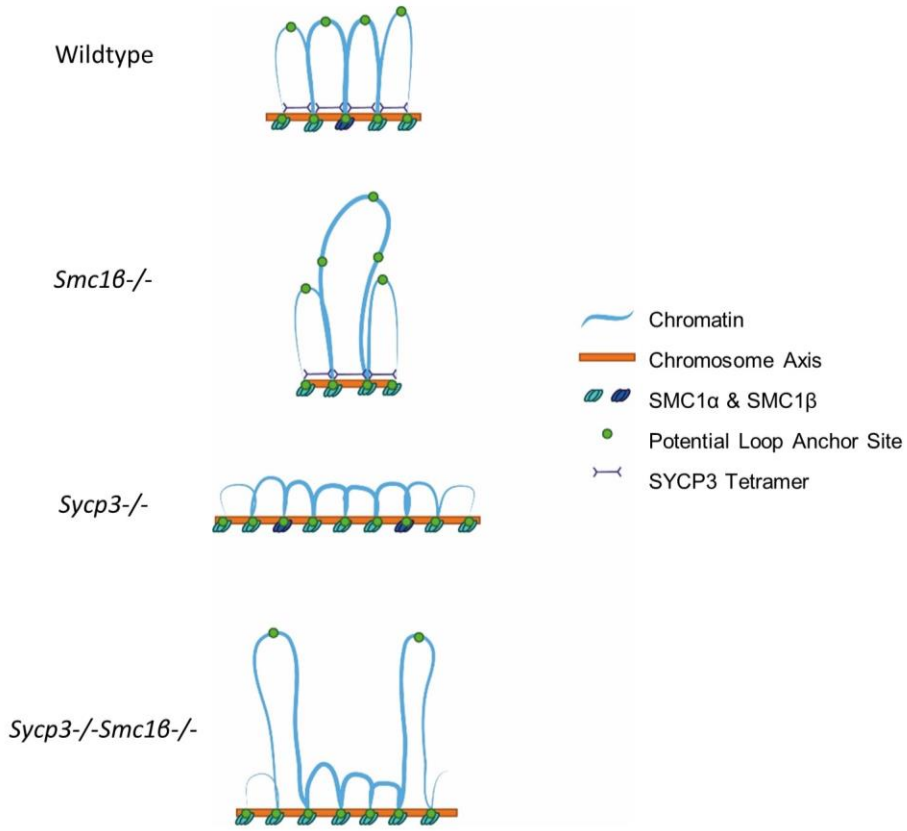

Figure 1-7. Present models of the effect of SYCP3 and SMC1β on the organisation of the meiotic chromosome axes and chromatin loops. Schematics depict the predicted behaviour of a single chromatid in relation to the chromosome axis in wildtype, *Smc1β-/-*, *Sycp3-/-* and *Sycp3-/-Smc1β-/-* pachytene meiocytes. In wildtype meiocytes, chromatin loop and axis length is known to be manipulated by cohesin and SYCP3. Cohesin complexes tether a subset of potential axis-association sites to the chromosome axis, while SYCP3 tetramers act to stabilise the adjacent loop anchors. In *Smc1β-/-* meiocytes, a specific subset of loop anchor points is released from the chromosome axis, causing adjacent wildtype loops to merge and the chromosome axis to compact. In *Sycp3-/-* meiocytes, an increase in axis-associated sites occurs while the chromosome axis decompacts in a concertina-like manner. In *Sycp3-/-Smc1β-/-* meiocytes, potential axis-association sites are tethered to the chromosome axis, except for a subset whose axis-association was mediated by SMC1β, while the chromosome axis decompacts, due to the absence of SYCP3. Image adapted from Novak *et al*., 2008.

A HiC analysis conducted in *rec8*-defective *S. cerevisiae* has demonstrated the absolute requirement of cohesin for the formation of HiC-defined loop formation and chromosome arm compaction in yeast meiosis (Schalbetter *et al*., 2018). Despite comparable HiC analyses not yet being conducted in mammalian meiocytes, chromosome-wide FISH based data in mice has shown that meiotic cohesin is involved in the organisation of chromatin extensions from the chromosome axis, as described in Section 1.5.3 (Revenkova *et al.*, 2004; Novak *et al.*, 2008; Bhattacharyya *et al.,* 2019). Cohesin-dependent modulation of chromatin loop length could feasibly result from the gain/loss of specific axis-association sites at fixed sequences (as proposed in Novak *et al.*, 2008; Figure 1-7) and/or the dynamic movement of a cohesin complex bridging two genomic loci. In interphase cells, the artificial manipulation of cohesin abundance, both positively and negatively, has proven the importance of cohesin in the large-scale organisation of interphase chromatin (Covo *et al.*, 2010; Haarhuis *et al*., 2017; Rao *et al*., 2017). This cohesin-dependent modulation is linked to the dynamic movement of cohesin, as the HiC-defined loop contact points enriched in cohesin are distal from predicted cohesin loading sites (Wendt *et al*., 2008). Furthermore, *in vitro* single-molecule imaging and structural biology studies have shown that cohesin can migrate in a stepwise manner, in the presence of ATP, along chromatin fibres from its loading origin, until it dissociates from the chromatin or a specific obstacle impedes its path (Davidson *et al*., 2017; Diebold-Durand *et al*., 2017; Stigler *et al.*, 2016). The ability of cohesin to bridge genomic loci and translocate along chromatin fibres has been applied to several models, including the two described in Figure 1-8, which attempt to explain the dynamic formation of chromatin loops in interphase cells. These models have largely been substantiated through polymer simulations, based on the predicted kinetics of structural protein components, such as cohesin, and the biophysical properties of chromatin. Reassuringly, such simulations can accurately recapitulate genome-wide chromatin contact maps, generated *in vivo* (Nora *et al*., 2012; Sanborn *et al*., 2015). The majority of evidence to support cohesin-dependent dynamic chromatin loop organisation in interphase cells, is dependent on accurate maps of HiC-defined large-scale chromatin structures and the distribution structural factors, such as cohesin, as defined by ChIP-seq. However, although HiC maps have been generated (Alavattam *et al.*, 2019; Patel *et al.*, 2019; Vara *et al.*, 2019; Wang *et al.,* 2019), the relationship between HiC-defined contact points and axis-associated structural factors including cohesin are not known. Therefore, the dynamic nature of axis-associated chromatin

and its effects on large-scale chromatin looping cannot presently be confirmed, nor denied.

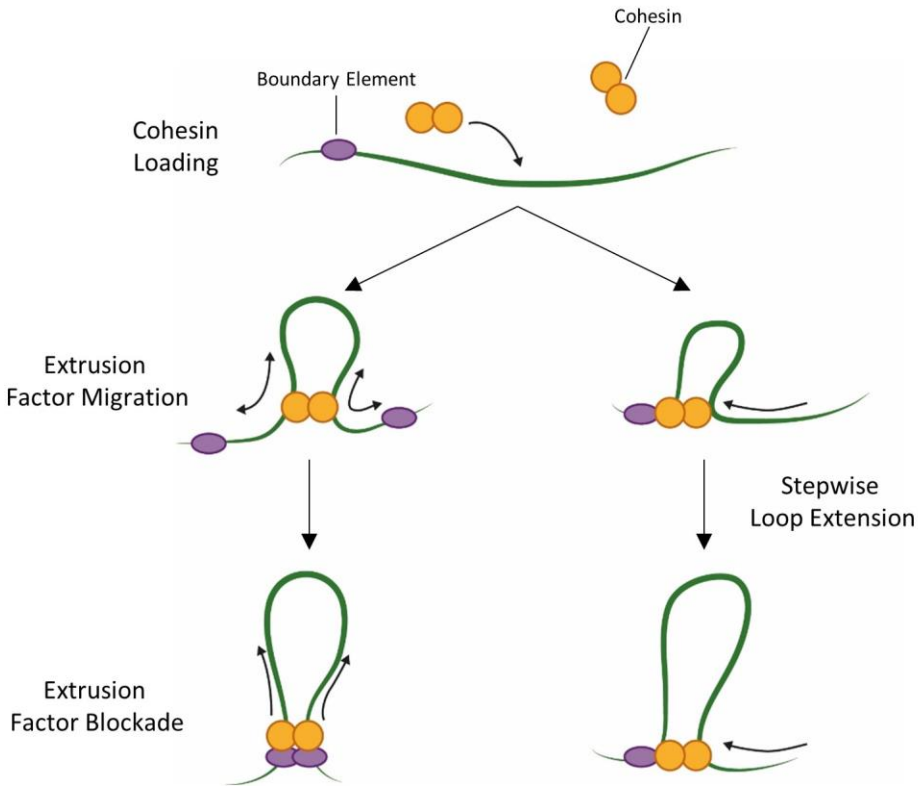

Figure 1-8. Proposed dynamic loop formation models in interphase cells. A cohesin complex is loaded onto chromatin and topologically entraps two adjacent chromatin sites. Pathway 1 (left) – Cohesin then actively or passively migrates along the chromatin, causing the intervening chromatin loop to rise and fall in length, depending on the directionality of the extrusion factor's migratory path. Ultimately, extrusion is impeded by the dissociation of the cohesin and/or the presence of a boundary element creating an extrusion factor blockade (Alipour and Marko, 2012; Nasmyth, 2001). Pathway 2 (right) – Cohesin acts as a 'stepping motor' that 'reels' along the chromatin to/from a fixed point. As cohesin 'reels' along a linear chromatin fibre, the intervening chromatin is forced to form a growing cluster until cohesin dissociates, or its movement is impeded (Lawrimore *et al.*, 2017).

1.6 Additional Structural Factors

1.6.1 The Condensin Complex

Cohesin is a member of the structural maintenance of chromosome (SMC) protein family. The SMC protein family is highly conserved and in vertebrates includes cohesin, condensin and the SMC5/6 complex (Uhlmann, 2016). All eukaryotic SMC proteins act in SMC homo- and heterodimers, with specialised non-SMC proteins to create multi-protein complexes, which are capable of entrapping chromatin fibres (Nasmyth and Haering, 2009). Although, it is not clear whether SMC5/6 complexes are capable of manipulating large-scale chromatin structures (Aragon, 2018), condensin is strongly implicated in the manipulation of mitotic chromatin architecture (Nasmyth and Haering, 2009; Nishiyama, 2019).

Condensin has two variants, condensin I and condensin II. The two SMC family members, SMC2 and SMC4, are shared between the two variant complexes, whilst the condensin holocomplexes are completed by a unique set of non-SMC subunits: CAP-G, CAP-D2 and CAP-H for condensin I and CAP-G2, CAP-D3 and CAP-H2 for condensin II (Hirano, 2012). With common and distinct subunits, the condensin I and II complexes execute complementary, yet independent roles, in somatic cells (Hirano, 2012). Similarly to cohesin, condensin has the capacity to topologically link chromatin duplexes (Cuylen, Metz, and Haering, 2011) and has DNA translocase activity (Terakawa *et al*., 2017), producing a means by which condensin may migrate relative to DNA and facilitate loop formation (Hirano, Kobayashi, and Hirano, 1997; Hirano and Mitchison, 1994). Real-time imaging of λ-DNA has produced convincing visual evidence for the condensin-mediated formation and processive extrusion of DNA loops (Figure 1-8; Ganji *et al.*, 2018). More specifically, this study revealed that a single condensin complex anchors itself at one side of the loop, while reeling the DNA at the other, to extrude a DNA loop, in an ATP-dependent manner (Ganji *et al*., 2018). Despite the intimately related structural composition of cohesin and condensin, cohesin was unable to promote DNA loop formation or extrusion in an equivalent *in vitro* context (Ganji *et al*., 2018). Thus, it is likely that cohesin and condensin act through distinct mechanisms to manipulate chromatin configuration. In part, this may be accounted for the coiled-coil domains of the SMC family members tending to display different conformations (Anderson *et al*., 2002). Recently, real-time imaging has also revealed that condensin complexes can traverse one another to create intricate secondary looping structures (Kim *et al.*, 2019).

Considering the morphological similarities between the sequential chromatin loop arrays of mitotic and meiotic prophase I, it is plausible that the condensin-mediated chromosomal rearrangements are conserved between cell states. Studies in *S. cerevisiae* (Yu and Koshland, 2003) and *C. elegans* (Chan, Severson, and Meyer, 2004; Mets and Meyer, 2009) have shown that chromosome axis length and synapsis are reliant on condensin, providing evidence to support the proposition that condensin is important for meiotic chromosome architecture during meiotic prophase I in lower-order organisms. Relative to lower-order organisms, information regarding the function on condensin in mammalian meiosis is scarce. Conditional deletions of condensin I and II in growing mouse oocytes, following meiotic prophase I, results in metaphase I chromosomes acquiring morphogenic abnormalities, as chromosomes appear fuzzier and thicker, with more significant deformations being evident in condensin II-deficient mice (Houlard *et al*., 2015). These findings are consistent with condensin I and condensin II having a role in metaphase chromosome condensation, as has been observed in mitosis. However, the role of condensin in manipulation of chromatin in mammalian meiotic prophase I is yet to be examined.

1.6.2 Transcription and Meiotic Large-Scale Chromatin Architecture

The transcriptional profile of murine meiocytes during prophase I is dynamic; RNA-seq data indicates that spermatocytes are transcriptionally active throughout prophase I (da Cruz *et al*., 2016; Fallahi *et al.*, 2010). According to the incorporation of tritiated-RNA analogs and the absence of immunofluorescently labelled phosphorylated RNA Pol II and transcription-associated epigenetic marks, transcriptional activity is relatively greater following mid-pachytene, compared to earlier stages (Monesi, 1964; Page *et al*., 2012). In addition, throughout prophase I the transcription profile of the XY chromosomes in males is highly distinct from the autosomes, as XY protein-coding genes are silenced through meiotic sex chromosome inhibition (MSCI) within a peripheral nuclear subdomain, known as the sex body (McKee and Handel, 1993; Solari, 1974; Song *et al*., 2009).

Several descriptive studies have revealed a correlative relationship between transcription and large-scale chromatin organisation in murine meiocytes: Firstly, single-molecule localisation microscopy has demonstrated that H3K4me3, an

epigenetic mark indicative of open, active chromatin and hotspots, extends radially from the SC, with a morphology compatible with chromatin loops. While H3K27me3, an epigenetic mark indicative of transcriptional repression, forms periodic clusters within 40-50 nm of the pachytene SC (Prakash *et al*., 2015). Therefore, the distribution of transcriptionally active and silent epigenetic marks is spatially distinct relative to the chromosome axis. Whether this relationship is of structural or functional relevance is not known. A second cytological study, generated EM images to reveal that transcriptional inhibition, mediated through actinomycin D treatment, causes chromatin to significantly condense around the murine pachytene SC (Handel, Caldwell, and Wiltshire, 1995). This finding demonstrates that a transcriptional component is involved in the maintenance of the length of chromatin extensions from the chromatin axis, which is dynamically regulated during pachytene in mouse spermatocytes.

HiC investigations in mouse and *Rhesus macaque* spermatocytes have demonstrated that the loci present within HiC-defined 'refined compartments' correspond with RNA polymerase II-bound loci and clusters of active transcription (Alavattam *et al.*, 2019; Patel *et al.*, 2019; Vara *et al.*, 2019; Wang *et al.,* 2019). In addition, HiC investigations have shown that the large-scale chromatin organisation of the X chromosome undergoes a profound transformation, in parallel with the gross shutdown of X-linked gene expression in mouse spermatocytes; during the transformation, chromatin compartments and precise chromatin contact points are lost along the length of the X chromosome, although the basic sequential loop configuration is thought to be preserved (Alavattam *et al*., 2019; Patel *et al*., 2019; Vara *et al*., 2019; Wang *et al*., 2019). Conversely to endogenous systems of gene silencing on the X chromosome, treatment with the transcription inhibitor, α-amanitin, induced no significant effect on the refined chromatin compartments observed in mammalian HiC analyses of autosomal chromosomes (Wang *et al.*, 2019). This finding suggests that the relative strength of chromatin contacts between specific loci remains constant on transcription inhibition. Notably, although such HiC contact maps provide evidence of relative chromatin proximity, without a comprehensive map of axis-association sites it is presently unclear how the distribution of transcriptionally active genes and HiC-defined changes in chromatin architecture correspond to the cytologically visible chromatin loops extending from the chromosome axis.

Despite numerous studies producing descriptive evidence to relate transcription and large-scale chromatin organisation to one another in murine meiocytes, no functional explanation to link transcription to the length of chromatin extensions in pachytene spermatocytes has been established in mammals. Insight into this relationship might be gained from studies conducted in yeast meiocytes. A series of ChIP-seq experiments conducted in *S. cerevisiae* have demonstrated that axis-association sites, defined by Rec8 and Red1 (yeast AE marker) binding, are preferentially positioned at the 3' end of actively transcribing convergent genes (Schalbetter *et al.*, 2018; Sun *et al.,* 2015). These axis-association sites are not fixed and can be refocussed, according to the expression ratio of the convergent genes flanking an anchorage point (Sun *et al*., 2015). This transcription-dependent axis-association patterning is completely eradicated on deletion of *rec8* (Sun *et al*., 2015). Thus, refocusing of chromatin-axis association could either result from a transcription-dependent sliding motion of cohesin, or the repeated recruitment of cohesin to a specific chromatin modification or structure positioned at the end of transcription bubbles. Although neither of these two possibilities can be discounted, it is of interest to note that *in vitro*, single molecule analysis has demonstrated that the DNA motor protein Ftsk, which acts as a proxy for transcription machinery, is sufficient to push a cohesin ring along a linear strand of DNA (Stigler *et al*., 2016). A comparable role for transcription in the manipulation of cohesin-dependent axis-association is yet to be directly interrogated in higher-order organisms. >80% of REC8/RAD21L-associated cohesin binding sites are within 2kb of transcriptional start sites in mouse prophase I (Vara *et al*., 2019). Intriguingly, this finding indicates the existence of a correlative relationship between cohesin distribution and transcription in mice. However, due to the disparate enrichment of cohesin at mouse transcriptional start sites and at the 3' end of genes in yeast, the spatial relationship between cohesin and transcription may not be comparable between the two species.

1.6.3 Meiotic CTCF

Dynamic chromatin loop formation models, such as those depicted in Figure 1-8, tend to not only involve a motor protein, but also boundary elements, which insulate neighbouring loops from one another. CTCF is a highly conserved architectural protein, which binds as a homodimer to thousands of sites throughout the mammalian genome in a sequence-specific manner, through its high-affinity zinc finger array (Feinauer *et al*., 2013; Saldaña-Meyer *et al*., 2014). In mammalian cells, CTCF is enriched at TAD boundaries and loop contact points (Rao *et al.*, 2014; Sanborn *et al.*, 2015; Narendra *et al.*, 2015). These binding patterns make CTCF a top candidate as an interphase boundary element, responsible for chromatin loop stabilisation. The acute depletion of functional CTCF genome-wide results in the loss of chromatin looping between CTCF sites and causes contiguous TADs to merge together (Lupiáñez *et al*., 2015; Nora *et al*., 2017; Zuin *et al*., 2014). Consistently, removal of specific CTCF sites abolishes CTCF-binding, interferes with cohesin recruitment and perturbs the distribution of chromatin loops and TADs (de Wit *et al*., 2015; Guo *et al*., 2015; Narendra *et al*., 2015; Rodríguez-Carballo *et al*., 2017; Williamson *et al*., 2019). ChIP studies have also found cohesin subunits to be heavily enriched at CTCF sites. For instance, in HeLa cells, 89% of cohesin binding sites (as defined by RAD21 ChIP) co-localise with CTCF sites across the genome (Wendt *et al*., 2008). In the context of the loop extrusion model (Figure 1-8), the spatial relationship between cohesin and CTCF can be explained by the progression of cohesin (loop extrusion factor) along a chromatin fibre being perturbed by the canonical boundary element, CTCF. Such a proposition is reinforced by *in vitro* single-molecule imaging, which indicates that the translocation of cohesin along DNA can be impeded by CTCF binding (Davidson *et al*., 2017; Stigler *et al*., 2016).

CTCF has an undoubtable role in the assembly of the majority of interphase chromatin loops and TADs (Nora *et al*., 2017); however, CTCF is dispensable for long-range chromatin contact domains in numerous organisms, including yeast and *C. elegans* (Heger *et al.*, 2012; Heger, Marin, and Schierenberg, 2009) and during mammalian mitosis (Oomen *et al*., 2019). Therefore, the question of whether meiotic chromatin loop formation acts in a CTCF-dependent or -independent manner now stands. CTCF-ChIP has verified the presence of CTCF in prophase I mouse spermatocytes and revealed over 19,000 CTCF-binding sites in late prophase I (Vara *et al*., 2019). It is curious to note, meiotic recombination, SC formation and cohesin localisation in

Ctcf knock-out mice all remain grossly unperturbed during meiotic prophase I, indicating that CTCF is not solely responsible for the control of such integral meiotic features (Hernández-Hernández *et al.*, 2016).

An evolutionary duplication of the canonical *Ctcf* gene has led to the creation of *Ctcfl* (or *Boris*), a paralog of *Ctcf*, whose normal expression is restricted to the male germline (Jabbari *et al*., 2018). The two paralogs have evolved overlapping, yet distinct, binding specificities and protein interactomes (Loukinov *et al*., 2002; Sleutels *et al*., 2012). It is therefore probable that CTCF and CTCFL function largely independently of one another. Although, in scenarios where binding sites are shared the two paralogs may promote, compete or interfere with their respective roles. Yet, the role of CTCFL in relation to large-scale chromatin organisation is not understood. CTCFL is predominantly expressed in spermatogonia and pre-leptotene spermatocytes (Loukinov *et al*., 2002; Sleutels *et al*., 2012), whilst *Ctcfl*-null male mice exhibit a mild fertility defect characterised by aberrations in post-meiotic stages of spermatogenesis (Sleutels *et al*., 2012; Suzuki *et al*., 2010). Accordingly, there is currently no published evidence to support the postulation that either CTCF or CTCFL have a direct influence on large-scale chromatin organisation, during mouse meiotic prophase I. However, it is feasible they may influence such structures prior to entry in prophase I. The creation of conditional *Ctcf/Ctcfl* double knock-out mice, where both paralogs are deleted on meiotic entry, may assist in ascertaining the significance of both paralogs in the modulation of chromatin structure during prophase I. It is also important to acknowledge, since dynamic loop formation/maintenance has not been verified in mammalian meiocytes, it is possible that such canonical ‘boundary elements’ are not required to constrain meiotic chromatin loops, either because alternate or redundant elements are present, or chromatin loops are fixed.

1.7 Meiotic Recombination

1.7.1 Overview

Prior to the first meiotic division, the genome undergoes a highly specialised process in prophase I, referred to as meiotic recombination (Cohen, Pollack and Pollard, 2006; Handel and Schimenti, 2010). In brief, meiotic recombination is initiated by the formation of hundreds of programmed double-strand breaks (DSBs). DSBs do not occur randomly throughout the genome, but instead are enriched at specific sites, known as meiotic hotspots (Smagulo*va et al*., 2011; Khil *et al.,* 2012; Pratto *et al.,* 2014). Meiotic DSBs are principally repaired through recombination, during which the sister or homologous chromatid is utilised as a reparative template. In homology-based repair, DSBs are processed into 3' ssDNA tails, which triggers a homology search, promoting pre-synaptic alignment of homologous chromosomes, following which the intact homolog is invaded and exploited for repair. In a fraction of instances (~10% in mice; Baudat and de Massy, 2007), the resolution of meiotic DSBs facilitates the formation of crossovers (COs), where the DNA positioned downstream of the DSB is reciprocally exchanged between the maternally- and paternally-derived homologous chromosomes (Baudat *et al*., 2013). COs go on to establish the physical connections between homologous chromosomes, known as chiasmata. Failure to generate chiasmata gives rise to achiasmate chromosomes, which significantly increase the risk of chromosome missegregation, during the first meiotic division, and the creation of aneuploid gametes (discussed in Handel and Schimenti, 2010). Consequently, meiotic recombination is essential for the balanced segregation of meiotic chromosomes to generate healthy, haploid gametes. Furthermore, the genetic exchange between maternally- and paternally-derived chromosomes, promotes genetic diversification, as novel allelic combinations are created that can influence the direction of evolutionary change within a population (Webster and Hurst, 2012).

1.7.2 SPO11 and DSB Formation

Meiotic recombination is initiated by the formation of DSBs catalysed by the highly conserved transesterase enzyme, SPO11 (Figure 1-9; Keeney *et al.*, 1999). The mouse *Spo11* gene spans 13 exons and alternative splicing generates two principle isoforms, SPO11β (all exons incorporated) and SPO11α (exon 2 excluded; Keeney *et al*., 1999; Neale, Pan, and Keeney, 2005; Romanienko and Camerini-Otero, 2000). Both isoforms possess homology with the archaeal topoisomerase VI A (TopoVIA) protein, which exerts its catalytic activity in a heterotetrametric complex with a meiotic topoisomerase VIB-like protein (MTOPVIB; Nichols, DeAngelis and Berger, 1999; Vrielynck *et al.*, 2016). Although SPO11-mediated cleavage is yet to be directly demonstrated *in vitro,* it is likely that SPO11 cleaves DNA in a similar manner to canonical class II TopoVIA proteins, as both are reliant on a conserved scissile tyrosine residue attacking a phosphorus group in the DNA for cleavage of the DNA backbone (Neale *et al*., 2005). The majority of *Spo11-/-* spermatocytes and oocytes tend to undergo prophase I arrest and do not complete the first meiotic division, due to synaptic failure (Baudat *et al*., 2000; Metzler-Guillemain and de Massy, 2000; Rinaldi *et al.*, 2017; Romanienko and Camerini-Otero, 2000). This mutant phenotype can be partially rescued by cisplatin-generated DSBs, which create an up to 10-fold increase in nuclei displaying significant synapsis (Romanienko and Camerini-Otero, 2000). SPO11's DSB forming activity is therefore responsible for promoting chromosome synapsis and facilitating the progression of meiotic prophase I. In addition, ATM, the DNA damage-responsive kinase, is implicated in the fine-tuned control of DSB formation; mice experience a 10-fold increase in DSB formation on *Atm* deletion compared to wildtype mice, as large domains on a Mb-scale become sensitized to DSB machinery (Lange *et al*., 2016; Yamada *et al*., 2017).

1.7.3 DSB hotspots

SPO11-mediated DSBs are not randomly distributed throughout the meiotic genome, but are instead enriched at permissive regions, known as hotspots (de Massy, 2013; Lam and Keeney, 2014; Lichten and Goldman, 1995). Recent advances in hotspot mapping have led to the development of two genome-wide, high resolution mapping techniques: SPO11-oligo mapping, which involves SPO11 immunoprecipitation and the sequencing of SPO11-bound oligonucleotides (described in Section 1.7.4; Neale, Pan and Keeney, 2005), and DMC1 ssDNA sequencing (DMC1 SSDS), which utilises ChIP-seq of ssDNA bound by the recombinase protein DMC1 (described in Section 1.7.5; Khil *et al.*, 2012). Over 20,000 hotspots were identified in two mouse genomes by DMC1 SSDS mapping (Brick *et al.,* 2018). Yet, within any given meiotic cell, only a limited portion of hotspots are targeted by SPO11, in a phenomenon referred to as hotspot designation (Barlow *et al*., 1997; Brick *et al*., 2012; Cole *et al*., 2012).

When attempting to identify the unique traits of meiotic hotspots, one of the first aspects to consider is the underlying DNA sequence. In most mammals, the distribution of hotspots is heavily influenced by the binding of the *trans*-acting, zinc-finger histone methyltransferase, PR domain-containing protein 9 (PRDM9) (Baudat *et al*., 2010; Brick *et al*., 2012; Myers *et al*., 2010; Parvanov, Petkov, and Paigen, 2010). Through its zinc-finger array, PRDM9 binds specific sequence motifs and deposits methyl groups on H3K4 and H3K36 through its PR/SET domain (Brick *et al*., 2012; Grey *et al*., 2011; Imai *et al*., 2017; Powers *et al*., 2016). Although the dependency on PRDM9 for fertility varies between mouse strains, DMC1 SSDS has revealed that meiotic DSBs accumulate at ectopic loci, with a marked increase at gene promoters, in *Prdm9-/-* mice (Brick *et al*., 2012; Mihola *et al*., 2019). This highlights a role for PRDM9 in determining the distribution of meiotic DSBs. In mice, PRDM9 binding actively redistributes nucleosomes to create an extended nucleosomal-depleted region, centred on the PRDM9 binding motif in which SPO11-oligo reads are enriched (Baker *et al.*, 2014; Lange *et al*., 2016). Although a direct relationship between SPO11 recruitment and nucleosome positioning has yet to be demonstrated in mice, yeast studies have shown that SPO11 is only capable of accessing DNA in an “open”, nucleosome-depleted state, indicating a partial means by which PRDM9 might determine DSB distribution across the mouse genome (Berchowitz *et al.*, 2009; Pan *et al*., 2011; Shenkar, Shen, and Arnheim, 1991).

Experimental evidence indicates that the distribution of meiotic hotspots is not solely determined by the underlying sequence. In support of sequence-independent determination of meiotic hotspots, investigations in *S. cerevisiae* revealed that the artificial insertion of hotspot sequences, within 'cold' genomic regions, can considerably lower the recombinogenic potential of the sequence, according to DSB frequency and the extent of allelic exchange (Borde, Wu, and Lichten, 1999). Inversely, targeting SPO11 to 'coldspots', through Gal4-mediated recruitment, is insufficient to elevate the inherently low DSB activity of the coldspot region (Robine *et al*., 2007). Retargeting hotspot sequences, or SPO11, to canonical 'coldspots' is therefore insufficient to instigate DSB formation and recombination at ectopic loci within the yeast genome. Whether comparable sequence-independent controls are active in PRDM9-dependent more complex species is yet to be explored. However, genome-wide mapping of PRDM9 binding motifs has indicated that, at least in humans, these motifs are neither sufficient nor necessary for the prediction of PRDM9 binding and recombination events (Altemose *et al*., 2017; Walker *et al*., 2015), suggesting that alternate chromatin features working in *cis* might govern hotspot designation.

1.7.4 Early DSB Processing

Following the formation of SPO11-mediated DSBs, a highly orchestrated DNA damage repair pathway is triggered, spearheaded by ATM/ATR-mediated phosphorylation of histone H2AX serine 139 (γH2AX; Figure 1-9; Rogakou *et al.*, 1999; Celeste *et al.*, 2002; Bellani, 2005). As SPO11 cleaves the DNA backbone to form DSBs, it becomes covalently bound to the newly exposed 5' nucleotides at its catalytic tyrosine residue (Keeney, 2008). SPO11 is subsequently liberated from the DSB through single-stranded nucleolytic cleavage, resulting in the release of SPO11 covalently bound to a short oligonucleotide (SPO11-oligo), which are detectable in a range of organisms from yeast to mice (Bergerat *et al*., 1997; Keeney *et al*., 1997; Neale *et al*., 2005).

The endonuclease Mre11 is heavily implicated in Spo11 liberation in *S. cerevisiae,* where nuclease-defective alleles of *mre11* are incapable of SPO11 liberation (Cannavo and Cejka, 2014; Garcia *et al.*, 2011; Neale *et al*., 2005). Consistent with the genetic deletion of other recombination machinery, targeted deletion of *Mre11*

results in embryonic lethality in mice (Buis *et al*., 2008). Viable mice, harbouring specific hypomorphic mutations in *Mre11*, generate normal levels of the early recombination marker, RAD51, which persist for an abnormal length of time. These observations suggest that initial DSB resection is unlikely to be defective in *Mre11* hypomorphs, but DSB repair occurs inefficiently (Theunissen *et al*., 2003). Collectively, these data indicate that MRE11 is important during meiotic recombination yet its precise role is presently unknown.

Following SPO11 liberation in yeast, the resultant single-stranded DNA overhangs formed are further resected bidirectionally in the 5'-3' direction away from the DSB (Zakharyevich *et al.,* 2010; Mimitou, Yamada and Keeney, 2017). Combined SPO11-oligo and strand-specific SSDS data in mice predict that DSB end resection extends an average of ~900 nt (Lange *et al*., 2016). Direct molecular analyses have demonstrated that the exonuclease Exo1 is responsible for completing resection in *S. cerevisiae*. However, whether resectioning is of biological significance is questionable, since CO formation was unperturbed in nuclease-defective *exo1* mutants (Zakharyevich *et al.*, 2010; Keelagher *et al.*, 2011). Furthermore, in *Exo1*-null and *Exo1*-nuclease defective mice, the recruitment of recombination machinery and progression of prophase I is not perturbed (Schaetzlein *et al*., 2013; Wei *et al*., 2003). Therefore, although resectioning is a conserved feature of meiotic recombination, its functional purpose and its underlying mechanism remains elusive in mice.

Intriguingly, two meiosis-specific HORMA-domain proteins, HORMAD1 and HORMAD2, intimately relate chromosomal synapsis and the processing of meiotic DSBs. The HORMAD proteins preferentially associate with unsynapsed axes and recruit the DNA damage-responsive kinase, ATR, to unsynapsed chromatin, promoting DSB resolution and synapsis, whereupon HORMADs are evicted from the LE (Kogo *et al*., 2012; Shin *et al*., 2010; Wojtasz *et al*., 2009). ATR is recruited to DSB-associated ssDNA and is responsible for coordinating downstream DSB repair (Pacheco *et al*., 2018). In the absence of either HORMAD protein, the distribution of ATR is significantly perturbed, as the kinase is forced to form punctuate foci along axes, rather than spreading along the length of unsynapsed axes. These findings suggest that the recruitment of the HORMAD proteins to asynapsed axes, results in the co-recruitment of ATR and the resultant promotion of synapsis at these sites (Daniel *et al*., 2011; Wojtasz *et al*., 2012). Thus, it has been postulated that the two HORMAD proteins act in a negative feedback loop at the interface between meiotic

recombination and SC assembly, as their binding promotes SC formation, while SC assembly and DSB formation cause HORMADs to dissociate from the chromosome axes and enable meiosis to progress (Daniel *et al*., 2011; Kauppi *et al*., 2013; Kogo *et al*., 2012; Shin, McGuire, and Rajkovic, 2013).

1.7.5 Recombinases and the Homology Search

The resultant 3' single-stranded DSB ends act as substrates for the assembly of nucleoprotein filaments, composed of protein factors including the replication protein A (RPA) complex (Figure 1-9). The complex is composed of RPA1, RPA2 and RPA3 in a heterotrimer, with RPA1 acting as the principle DNA binding subunit (Wold, 1997). *In vitro* investigations have demonstrated that RPA binding of ssDNA protects the exposed DNA from premature degradation and prevents the formation of secondary structures, which may interfere with subsequent protein-DNA interaction required for recombination *in vivo* (Chen, Lisby, and Symington, 2013). A recent study utilised a tamoxifen-inducible inactivation strategy in mice (Shi *et al*., 2019), in which RPA1 abundance declines on the tamoxifen-dependent induction of Cre-Lox recombination, targeted to the *Rpa1* gene. *Rpa1*-depleted spermatocytes undergo a zygotene-like arrest in which γH2AX levels are elevated and the direct recruitment of recombination machinery is completely abrogated, compared to untreated mice (Golub *et al.*, 1998; Shi *et al*., 2019), demonstrating that RPA is essential for the recruitment of recombinase proteins to meiotic DSBs.

In most eukaryotes, RPA is displaced from ssDNA at meiotic DSBs by the ubiquitous recombinase RAD51 and the meiosis-specific recombinase DMC1 (Figure 1-9; Yang *et al.*, 2008). Both RAD51 and DMC1 are homologous to RecA and polymerise on the single-stranded DNA (Aboussekhra *et al.*, 2015; Bishop *et al.*, 1992). The resultant nucleoprotein filaments facilitate a homology search, to identify an intact DNA duplex template for recombination-based repair. It is not clear why two recombinases are present in meiotic cells. An *in vitro* binding assay revealed that RAD51 and DMC1 are distinct in the stringency in which they drive the homology search; DMC1 can tolerate base triplets which encode single, double or triple mismatches, without disrupting the formation and stability of the resultant heteroduplex. Whereas, the stability of RAD51-dependent heteroduplexes is sensitive to a single mismatch between DNA sequences (Lee *et al*., 2017). However, whether this is indeed the case *in vivo* is yet to be verified.

Furthermore, perturbed DMC1 and RAD51 activity confer distinct phenotypes; *Dmc1* knockout and knockdown mouse meiocytes exhibit elevated levels of unrepaired DSBs, marked by RAD51, and a lack of chromosomal pairing, indicating that RAD51 is incapable of facilitating DSB repair in the absence of DMC1 (Dai *et al.*, 2017; Pittman *et al*., 1998; Yoshida *et al*., 1998), while *Rad51* knockdown spermatocytes experience a substantial rise in apoptosis during leptotene/zygotene, effecting earlier stages of prophase I progression (Dai *et al*., 2017).

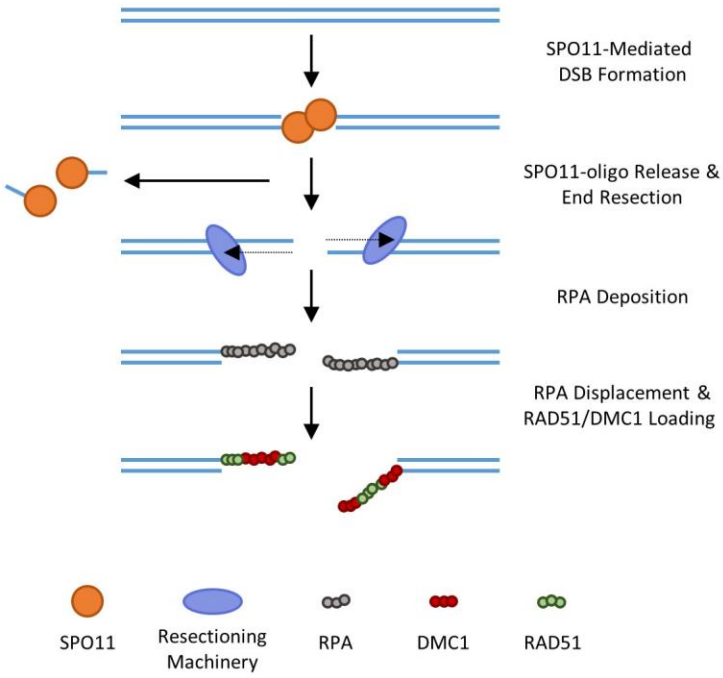

Figure 1-9. Double-strand break end processing. SPO11 cleaves a DNA duplex to create a double-strand break (DSB) and becomes covalently bound to the exposed ends of the DSB. SPO11 is subsequently liberated from the DNA, through nucleolytic cleavage, leading to the generation of SPO11-oligos, in which SPO11 is covalently bound to a short oligonucleotide. The resultant overhangs are further resected and RPA is deposited on the ssDNA to stabilise and protect the exposed overhangs. RPA is displaced by the ubiquitous recombinase RAD51 and the meiosis-specific recombinase DMC1, in preparation for the homology search and strand invasion.

1.7.6 Inter-Sister versus Inter-Homolog Repair

Following RAD51/DMC1 loading, homologous chromosomes are drawn into increasingly intimate juxtaposition, as the recombinase enzymes drive a homology search and the formation of a displacement-loop as intact chromatids undergo single-end invasion (Szostak *et al.*, 1983). Importantly, meiotic recombination occurs subsequently to complete DNA replication, meaning that three intact templates (two homologous chromatids and one sister chromatid) are available as potential repair templates. The study of inter-sister versus inter-homolog recombination in meiosis is relatively unexplored, since sister chromatids are identical and therefore it is challenging to identify the occurrence of inter-sister exchange. To date, the only direct assay to quantify template choice has been developed in yeast (Bell and Byers, 1983). The assay relies on the incorporation of known restriction fragment length polymorphisms into the genome, which after cleavage and southern blotting of a 2D electrophoresis gel, can distinguish between inter-sister and inter-homolog repair, based on the migration behaviour of the products (Bell and Byers, 1983). This assay facilitates the semi-quantification of inter-homolog versus inter-sister events and has highlighted that recombination is heavily biased towards inter-homolog repair, with an estimated ratio of inter-homolog to inter-sister interactions of approximately 5:1 (Kim *et al*., 2010; Lao and Hunter, 2010; Schwacha and Kleckner, 1997). The presence of an inter-homolog bias is yet to be verified in mammalian meiocytes. Importantly, any bias which may exist must occur to a sufficient level to enable the generation of an appropriate number of chiasmata.

In *S. cerevisiae*, inter-homolog bias has been postulated to occur through a 'kinetic impediment' of inter-sister recombination, in which multiple protein factors reduce the rate of inter-sister recombination (Goldfarb and Lichten, 2010). 2D gel electrophoresis has facilitated the identification of several factors capable of manipulating inter-homolog repair bias, which include recombination machinery and modulatory phosphokinases (Cao, Alani, and Kleckner, 1990; Cromie *et al.*, 2006; Schwacha and Kleckner, 1994). Of interest, is the balance between RAD51 and DMC1, as DMC1 is suggested to be more efficient for inter-homolog recombination, relative to RAD51. For instance, inter-homolog recombination is promoted through the dimerization of the AE meiotic kinase I (Mek1). The Mek1 dimer inhibits Rad51-mediated inter-homolog repair, through direct phosphorylation of Rad51 (Niu *et al*., 2005, 2009), causing Dmc1 activity to be favoured and a 3-fold decrease in inter-sister exchange

(Goldfarb and Lichten, 2010). Furthermore, single-molecule biophysical analyses have demonstrated that Rad51 activity is also disrupted by the meiosis-specific Rad51-binding protein Hed1. Hed1 directly competes with the Rad51 activating protein Rad54 for Rad51 binding and thus provides a second opportunity to down-regulate Rad51 recombinase activity (Crickard *et al*., 2018; Liu *et al*., 2014; Niu *et al*., 2009). Such pro-inter-homolog activity is counteracted by Rec8-mediated sister chromatid cohesion at chromosome axes, since in the absence of Rec8, inter-homolog bias declines, creating a 1:1 ratio between inter-homolog and inter-sister mediated repair (Kim *et al*., 2010). Importantly, it is not yet known how such modulatory mechanisms are able to differentiate between sister and homologous chromatids, particularly in isogenic strains in which each chromatid encodes an identical sequence.

1.7.7 The Inter-Homolog Repair Pathway

Once an inter-homolog D-loop has been established, two forms of recombination product can be generated. If the entirety of the homologous chromosome arms downstream of the original DSB are exchanged, the event is designated as a CO. If the original configuration of the homologous chromosomes is maintained and genetic exchange is confined to the sequences contiguous to the DSB, the event is designated as a non-CO (NCO; Figure 1-10; Schwacha and Kleckner, 1995; Bishop and Zickler, 2004). In mice, approximately 10% of DSBs mature into COs, the remainder are expected to result in NCOs, or exchanges between sister chromatids, despite the fact that it is only the COs that form the chiasmata needed from chromosome segregation (Baudat and de Massy, 2007; Co*le et al*., 2012).

Subsequent to D-loop formation, the ssDNA overhang is extended as DNA polymerases exploit the homolog as a reparative template. The extended D-loop becomes long enough to undergo second-end capture, as the invading strand returns to the opposite side of the DSB to create a joint molecule (JM). If the JM remains stable, a double Holliday junction (dHJ) forms and is repaired through either resolution, leading to a CO, or dissolution, which results in an NCO or a CO, depending on the directionality of the cleavage (Figure 1-10; Schwacha and Kleckner, 1995; Hunter and Kleckner, 2001). COs which result from such DSB repair may form through one of two principle pathways, referred to as class I or class II. The two classes are distinguished based on distinct genetic controls and affiliated processing machinery. Class I COs are subject to a phenomenon known as CO interference

(COI), in which the formation of contiguous COs is impeded causing COs to appear to evenly distribute along a meiotic chromosome, while class II COs are exempt from such forces (Holloway *et al.*, 2008). In mice, 90-95% of COs are affiliated with the class I CO pathway, whilst the remainder are accounted for by an alternate, class II, CO pathway (Guillon *et al.*, 2005; Svetlanov *et al.*, 2008).

Class I Crossovers

The class I CO pathway is associated with the sequential loading of two heterodimeric mismatch repair protein complexes; firstly, the MutSγ (MSH4-MSH5) complex is recruited and replaces RAD51/DMC1, in combination with RPA and BLM helicase to mark inter-homolog interactions (Moens *et al.*, 2007). In mice, immunostaining of *Msh4-/-* and *Msh5-/-* meiocytes has revealed that although the initiation of recombination occurs successfully, with no disruption to RAD51 foci, chromosome synapsis is significantly impaired. Approximately 30% and 90% of *Msh4-/-* and *Msh5-/-* spermatocytes exhibiting absolutely no pairing, respectively (de Vries *et al*., 1999; Edelmann *et al*., 1999; Kneitz *et al*., 2000). This might result due to issues in dHJ stability, as *in vitro* studies have shown that the human MutSγ complex topologically entraps dHJ substrates and mediates dHJ stability (Milano *et al*., 2019). In addition to dHJ stability, the MutSγ complex in mice has been shown to co-localise and interact with the MutLγ complex, composed of MLH1 and MLH3, at 20-25 discrete foci, consistent with the number of chiasmata (Kolas *et al*., 2005; Lipkin *et al*., 2002; Santucci-Darmanin *et al*., 2000). MLH1 and MLH3 are critical in the generation of class I COs, as loss of either protein results in the almost complete elimination of chiasmata in murine spermatocytes and premature segregation of homologous chromosomes (Anderson *et al.*, 1999; Baker *et al*., 1996; Lipkin *et al*., 2002). *In vitro*, MutLγ possesses endonuclease activity capable of creating single-stranded nicks in the supercoiled DNA, speculated to be similar to that at dHJs (Rogacheva *et al*., 2014). To interrogate the catalytic role of the MutLγ complex in mice, a point mutation was generated in the endonuclease domain of MLH3 (Toledo *et al*., 2019). DSB formation, early recombination events, synapsis and MutLγ recruitment were unperturbed in the mutant mice. However, the point mutant caused more than a 4-fold reduction in chiasmata, relative to wildtype mice, thus demonstrating that endonuclease activity of MLH3 is important in the creation of class I COs (Toledo *et al*., 2019).

Class II Crossovers

Unlike class I COs, class II COs form independently of MLH1 and MLH3 and are instead reliant on the MUS81-EME1 complex, which can cleave dHJs in a nuclease-dependent manner (Boddy *et al*., 2001). In *mus81*-null *S. cerevisiae,* COs are reduced and the mutant phenotype can be rescued by expression of a bacterial resolvase (Boddy *et al*., 2001) This indicates that the Mus81 resolvase is involved in CO formation. Importantly, loss of MUS81 in mice does not disrupt overall CO frequency, as the number of Class I COs compensates for the loss of Class II COs (Holloway *et al*., 2008). The rise in Class I COs occurs without a rise in MSH4/MSH5 abundance, which suggests that an integrated regulatory event occurs between the two CO pathways following MSH4/MSH5 loading (Holloway *et al*., 2008).

Synthesis-Dependent Strand Annealing

Historically, it was postulated that both COs and NCOs are generated through the repair of dHJs (Szostak *et al*., 1983). However, the formation of COs and a subset of NCOs is temporally distinct in *S. cerevisiae*, as a portion of NCO heteroduplex products are created simultaneously to dHJ intermediates and therefore prior to dHJ repair (Allers and Lichten, 2001). Additionally, in *S. cerevisiae*, defective dHJ repair, induced by a *ndt80* mutation, caused a marked decline in COs without any significant impact on NCO abundance (Allers and Lichten, 2001). Collectively, these findings demonstrate that, at least in these lower-order organisms, NCOs and COs are generated by two temporally distinct processes. This conclusion led to investigations into a conserved synthesis-dependent strand annealing (SDSA) pathway, as a means of NCO formation (Figure 1-10). SDSA is reliant on the disruption of interactions between the sampling nucleoprotein filament and the intact homolog prior to second-end capture and JM formation. The ultimate product of SDSA is an NCO, since the invading strand dissociates from the D-loop and the newly synthesised sequence re-anneals to the other side of the original DSB, without the involvement of a dHJ intermediate or extensive reciprocal exchange of genetic information between homologous chromosomes. The physical disruption of the sampling nucleofilament may occur passively through relatively weak and transient DNA-DNA interactions, or actively through the action of specific proteins. For instance, DNA helicases are pro-SDSA candidates proposed to supress CO formation and thus encourage SDSA. In *S. cerevisiae*, deletion of the helicase Sgs1 results in a 2-3 fold rise in COs (Ira,

Malkova, Liberi, Foiani, and James, 2003), this is thought to occur as Sgs1 acts with Topoisomerase III in a conserved complex to topologically disrupt the invading nucleofilament, which prompts the disassembly of early invasion intermediates (de Muyt *et al*., 2012; Forget and Kowalczykowski, 2012; Kaur, de Muyt, and Lichten, 2015). It is possible that the topological manipulation of chromatin mediated by Topoisomerase III and Sgs1 may be sufficient to disrupt the invading nucleoprotein complex, causing it to dissociate (Forget and Kowalczykowski, 2012). Furthermore, it is also plausible that the mammalian homolog of Sgs1, BLM, may possess similar pro-SDSA behaviour. Intriguingly, although no significant difference in class I CO markers, MSH4 and MLH1, was observed in *Blm-/-* mouse spermatocytes, the abundance of chiasmata-like structures was elevated (Holloway *et al.*, 2010). This observation indicates that BLM is responsible for supressing class II CO formation and presumably up-regulating SDSA or sister chromatid-mediated repair.

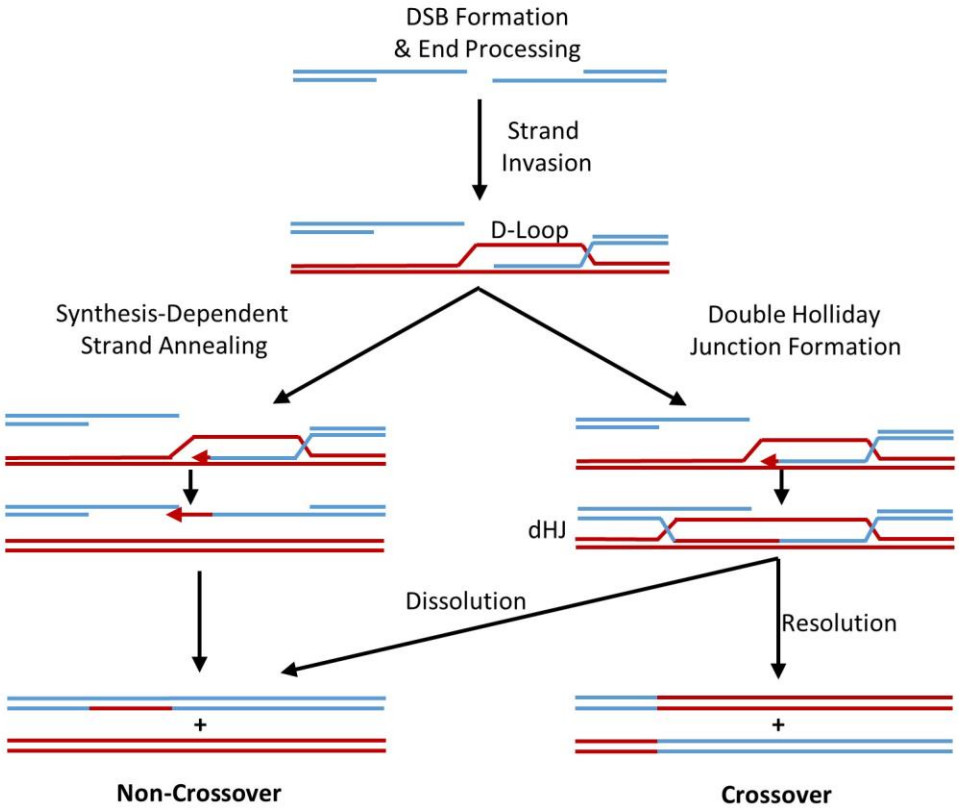

Figure 1-10. Overview of the recombination repair pathways. Following SPO11-mediated DSB formation and DSB end processing, the 3' ssDNA overhang undergoes a homology search. The intact, homologous DNA duplex experiences single end invasion to form a D-loop. In both synthesis-dependent strand annealing (SDSA) and double Holliday junction (dHJ) formation the 3' end of the invading strand is used to prime DNA synthesis, to stabilise the invasion. In the SDSA pathway, the strand invasion is displaced from the homologous duplex and repair is completed with the second processed DSB end to yield a non-crossover (NCO) product. In the second pathway, extension of the invading strand enables second end capture, resulting in the assembly of a dHJ. The dHJ can then be resolved to create a crossover (CO) or dissolved to yield a non-crossover (NCO).

1.7.8 Recombination-Independent Repair

In somatic cells, DSBs can be resolved by homologous recombination or non-homologous end joining (NHEJ). NHEJ mediates the direct re-ligation of DSBs and therefore occurs independently of DNA sequence and throughout the mitotic cell cycle, without the need for a reparative template. Classical NHEJ is initiated by the Ku70-Ku80 heterodimer (Ku complex), which binds the exposed ends of DSBs to form a Ku:DNA complex that consequently prevents further DSB resection. The Ku complex also mediates the recruitment of NHEJ machinery. In vertebrates, initially the nucleases and polymerases, in combination with the DNA-dependent protein kinase catalytic subunit (DNA-PKcs), are recruited to process the lesions. This protein recruitment ensures the DSBs are suitably primed for the ligase complex, composed of DNA ligase IV and XRCC4, to mediate DSB end-joining (reviewed in Chang *et al.*, 2017). Interestingly, Ku70 is present in mouse pachytene spermatocytes, where the majority of the detectable protein through immunostaining is confined to the sex body (Goedecke *et al.*, 1999). Furthermore, the NHEJ markers, Ku70 and XRCC4, become constitutively expressed in mouse spermatocytes exposed to γ-radiation in mid-pachytene to diplotene (Enguita-marruedo *et al*., 2019). Cumulatively, these findings suggest that during prophase I, both NHEJ and recombination repair pathways are active and may compete with one another to resolve meiotic DSB in murine spermatocytes. It is also possible that an alternate 'error-prone' repair pathway, known as single-strand annealing (SSA), is also active in meiocytes. SSA occurs through the annealing of complementary single strands, typically involving repetitive elements, which flank a DSB and become exposed on resectioning. However, although this pathway is relatively well defined in somatic cells (Bhargava, Onyango, and Stark, 2016) its involvement in meiosis remains elusive.

1.8 Meiotic Recombination and Large-Scale Chromatin Looping

1.8.1 The Spatial Organisation of Meiotic Recombination Relative to the Chromosome Axis

In *S. cerevisiae*, the ChIP-seq-based mapping of AE marker, Red1, has enabled loop- and axis-associated regions to be distinguished and their physical distribution compared to that of DMC1. The binding of the CO marker and axis-associated regions were found to be largely mutually exclusive, implying that CO sites occur in chromatin loops (Blat *et al*., 2002). Interestingly, EM serial section studies revealed that recombination machinery form prominent nodules, known as recombinosomes, along the length of the pachytene SC (Carpenter, 1981). Combining these data led to the proposition of the tethered loop-axis complex (TLAC; Figure 1-11) model, in which the DNA sequence at a meiotic hotspot must be recruited to the axis and 'tethered' to its corresponding recombinosome (Blat *et al.*, 2002; Panizza *et al.*, 2011). In *S. cerevisiae*, the Spp1 protein has been recognised as an important 'tethering' factor. Both yeast two-hybrid and ChIP co-localisation studies revealed chromatin loop tethering is mediated by Spp1, interacting with H3K4me3, at loop-associated hotspots, and recombination machinery positioned on chromosome axes (Acquaviva *et al*., 2013; Panizza *et al*., 2011; Sommermeyer *et al.*, 2013). Although a clear spatial pattern is evident between recombination machinery and meiotic hotspots, many questions regarding the functional purpose of this relationship must now be addressed.

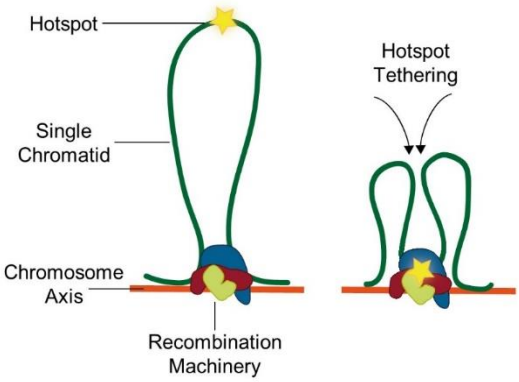

Figure 1-11. Tethered loop-axis complex model. Hotspot-associated sequences are positioned in between axis-associated sites, while recombination machinery physically associates with the chromosome axis. This implies that hotspot sequences must be indirectly recruited to the chromosome axis, in order to undergo DSB formation and recombination.

Despite a clear spatial pattern of both meiotic hotspots and recombination machinery being evident in *S. cerevisiae*, the distribution of hotspot sequences and recombination machinery, relative to the chromosome axis, is yet to be determined in higher-order organisms, including mice and humans. Immunostaining has shown a profound enrichment of recombination machinery at the chromosome axis in murine spermatocytes (Grey, Baudat, and de Massy, 2009; Kumar *et al*., 2015; Kumar, Bourbon, and de Massy, 2010; Stanzione *et al*., 2016). However, since chromatin looping, in relation to the chromosome axis, is yet to be comprehensively mapped, a preferential enrichment for hotspot sequences in loop-associated regions cannot be conclusively confirmed in mammals. Notably, the TLAC model is also heavily dependent on the assumption that the positioning of meiotic hotspots and axis-associated sequence are fixed relative to the axis but, this is not necessarily true. Therefore, the completion of live-cell FISH could prove valuable in the interrogation of such assumptions in higher-order organisms.

1.8.2 Covariance of CO Abundance and Chromatin Loop Density

The organisation of large-scale chromatin architecture in prophase I meiocytes has been attributed to a role in the global modulation of meiotic recombination and CO frequency (Gruhn *et al*., 2013; Heng *et al*., 1996; Kauppi *et al*., 2011). One piece of evidence, which sparked this suggestion, was that the spacing of chromatin loops along pachytene axes appears to be evolutionarily conserved (~20 loops per µm; Kleckner *et al.*, 2011), causing loop and axis length to be inversely correlated. A prime example of this can be appreciated when comparing male and female meiocytes, where a 2-fold increase in axis length is compensated by a ~2-fold decline in loop length (chromosome paint width) in human females, relative to males (Gruhn *et al*., 2013; Lynn *et al*., 2002; Tease and Hultén, 2004). Intriguingly, global CO frequency is also sexually dimorphic (Haldane, 1922; Lynn *et al.*, 2005), as both murine and human females experience a 2-fold increase in CO abundance compared to their males counterparts, with concomitant changes in axis and chromatin loop length (Bojko, 1985; Petkov *et al.*, 2007; Rasmussen and Holm, 1978). Consequently, the sexually dimorphic levels of COs covaries with the length of chromatin extensions and chromosome axes. Furthermore, recent super-resolution microscopy has shown that the width of the SC in mouse oocytes is approximately 10% less than that of the spermatocyte SC (Agostinho *et al*., 2018).

The correlation between CO frequency and chromatin organisation has not been observed in isolation. For instance, a similar relationship has been observed at the mouse pseudoautosomal region (PAR). In male mice, the ~7 fold increase in CO formation at PAR loci (Soriano *et al*., 1987) coincides with a 4-fold increase in SC length (µm per Mb) and 3-7-fold reduction in chromatin-SC extension length, relative to autosomal loci (Kauppi *et al*., 2011; Lange *et al*., 2016). Although CO rates are not equivalently high at autosomal telomeres, compared to the PAR in male meiosis, a 1.5-2-fold increase in CO abundance is observed at these regions relative to non-telomeric autosomal regions (Liu *et al.*, 2014; Pratto *et al.*, 2014). FISH data has confirmed that chromatin is in greater proximity to the chromosome axis at autosomal telomeres (Heng *et al*., 1996). Furthermore, a study of three mouse strains exhibiting distinct levels of COs (marked by MLH1 foci), again corroborated an inverse correlation between CO frequency and SC length, and between SC length and chromatin loop length (measured by chromosome paint width; Baier *et al.*, 2014). Taken together, these observations demonstrate that CO abundance, SC length and

chromatin extension length are seen to frequently correlate with one another in wildtype meiocytes (Figure 1-12). It might be of value to also note recombination at the PAR occurs independently of PRDM9 (Brick *et al*., 2012), while autosomal telomeric regions (<15 Mb from telomere) in humans also experience a decline in the occurrence of DMC1-PRDM9 overlap (Altemose *et al*., 2017). Moreover, it is possible that the three strains of mice exhibiting distinct CO frequencies might also possess distinct PRDM9 alleles. Whether PRDM9 binding functionally relates to chromatin organisation and CO abundance is not presently clear. One means by which this could be assessed, in addition to comparing chromatin structure locally at PRDM9-dependent and -independent sites (Brick *et al.*, 2012; Grey *et al.*, 2017), is to examine chromatin structure in domesticated dogs, wolves and coyotes, which are known to function independently of PRDM9 (Muñoz-Fuentes, Rienzo, and Vilà, 2011).

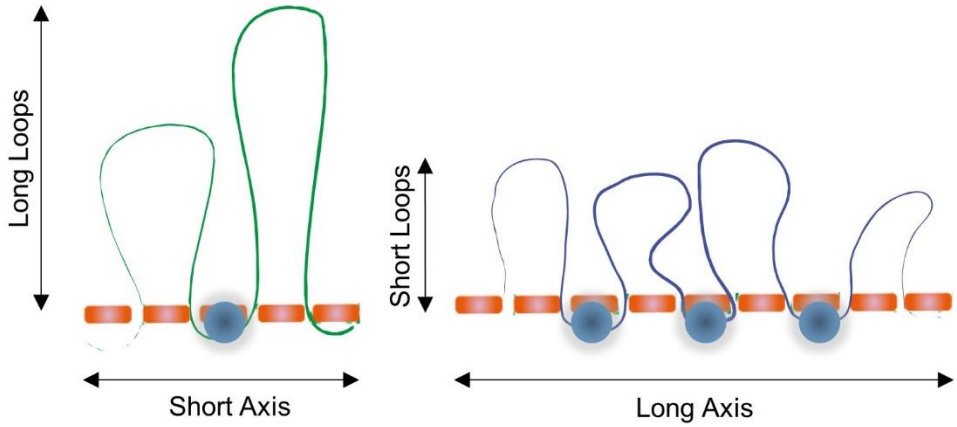

Figure 1-12. A correlative relationship between chromosome axis length, chromatin loop length and CO abundance. A single chromatin loop array is depicted. The bases of the chromatin loops interacts with the chromosome axis. An inverse correlation has been proposed between the length of chromosome axis and chromatin loop extensions, suggesting that a shorter axis/SC is associated with fewer and longer loops. Chromatin organised into more and shorter loops is proposed to experience more recombination events (blue dots), compared with chromatin organised into fewer and longer loops.

CO abundance is determined by the combined effects of DSB formation, inter-sister versus inter-homolog template choice and the ratio of CO:NCO events. Thus, the relationship between chromosome morphology and CO abundance could be determined by any one of these stages of recombination. Importantly, although heterozygotes for a null *Spo11* allele exhibited a 25% decline in early recombination markers (RAD51 foci), no change in MLH1-associated COs, SC length or chromatin loop length (according to chromosome paint width) was observed, while no apparent difference in axis length was observed in *Spo11-/-* spermatocytes (Baudat *et al*., 2000; Baier *et al*., 2014). Therefore, CO abundance, SC length and chromatin loop length appear to be regulated independently of the extent of early recombination events, indicating that CO abundance might instead be influenced by a relationship between chromosome structure and DSB repair fate, although this relationship is yet to be directly interrogated.

To substantiate a functional link between the topology of meiotic chromosomes and CO abundance, chromatin organisation could be experimentally perturbed to determine its effects on CO formation. However, genetic manipulation of chromosome architecture, for instance through the deletion of SC components and cohesin subunits, frequently results in impaired synapsis of homologous AEs (Table 1-1 and Table 1-2). During pachytene, detection of autosomal asynapsis induces the meiotic sex chromosome inactivation pathway (MSCI; Turner *et al.*, 2005). In wildtype spermatocytes, meiotic silencing of unsynapsed chromosomes (MSUC) is affiliated with the non-homologous sex chromosomes, which leads to the silencing of sex-linked genes and the formation of the sex body (Solari, 1974; Turner *et al*., 2004). However, on aberrant asynapsis of autosomal chromosomes the MSUC machinery is drawn away from the sex chromosomes, leading to the deleterious up-regulation of sex-linked genes and ultimately cell death. Thus, such events prevent the effect of disrupted chromosome morphology on CO formation being determined (Barchi *et al*., 2005; Mahadevaiah *et al*., 2008).

Table 1-2. Summary table of the phenotypes recorded for mutants of the meiosis-specific cohesin components. Axis/SC length and MLH1 foci counts are shown relative to wildtype. *Axis length analysed by (Hopkins *et al*., 2014). Table adapted from Hopkins *et al.*, 2014 and Biswas, Stevense and Jessberger, 2018.

	Arrest Stage	Homolog Asynapsis	Axis/SC Length	MLH1	References
Smc1β-/-	Early Pachytene	Yes	~50% shorter	Absent	Revenkova *et al.*, 2004 Novak *et al.*, 2008; Biswas *et al.*, 2013
Smc1β-/-,1α	Late Pachytene	No	~15% shorter	Reduced	Biswas *et al.*, 2018
Rec8-/-	Late Zygotene	Yes	~50% shorter*	Absent	Bannister *et al.*, 2004; Xu *et al.*, 2005; Bhattacharyya *et al.*, 2019
Rad21l-/-	Mid Zygotene	Yes	NA	Absent	Herrán *et al.*, 2011
Stag3-/-	Leptotene/ Mid Zygotene	Yes	~66% shorter	Absent	*Hopkins et al., 2014;* Llano *et al.*, 2014*;* Winters *et al.*, 2014; Fukuda *et al.*, 2014*;* Bhattacharyya *et al.*, 2019
Rad21l-/- Rec8-/-	Mid Leptotene	Yes	Absent	NA	Llano *et al.*, 2012
Stag3-/- Rad21l-/-	Mid Zygotene	Yes	Absent/ Shortened	NA	Ward *et al.*, 2016
Stag3-/- Rec8-/-	Mid Zygotene	Yes	Absent/ Shortened	NA	Ward *et al.*, 2016

Notably, despite chromosome synapsis being impaired and MLH1 foci being absent in *Smc1β-/-* spermatocytes, the artificial up-regulation of *Smc1α* in *Smc1β-/-,1α* mice appears to rescue the synapsis defect (Biswas, Stevense and Jessberger, 2018). Moreover, *Smc1β-/-,1α* exhibit a 1.1 µm reduction in average SC length, relative to wildtype spermatocytes (Biswas, Stevense and Jessberger, 2018). Therefore, in this instance the relationship between chromosome architecture can be examined, while evading MSUC-mediated apoptosis. As expected from the wildtype comparative analyses described above, the loss of *Smc1β* and concomitant up-regulation of *Smc1α* in *Smc1β-/-,1α* spermatocytes caused a decline in average SC length and a simultaneous 1.3-fold fall in MLH1 foci counts (Biswas, Stevense and Jessberger, 2018). A similar conclusion was also drawn from studies in heterozygote cohesin-deficient mice, in which both MLH1 foci counts and SC length were shown to be copy number dependent (Murdoch *et al*., 2013). Collectively, these data indicate cohesin-mediated changes in meiotic chromosome architecture might manipulate CO abundance. However, it is presently unclear whether this effect occurs directly or indirectly. For instance, through alterations in the expression of key recombination machinery, or the promotion of interactions between meiotic hotspots and recombination machinery, independently of their relative position to the chromosome

axis (Bhattacharyya *et al.,* 2019). Future investigations are therefore required to fully substantiate the role of cohesin in the manipulation of meiotic chromosome morphology and CO formation.

Presently, no experimental evidence explains how chromatin loop/axis length and CO are related, although a cohesin-dependent component is evident. One hypothesis might be that the length of chromatin loops improves the efficiency at which loop-associated meiotic hotspots are tethered to axis-associated recombinosomes, in accordance with the TLAC model. However, it is conceivable that CO abundance is determined independently of the relative positioning of hotspot sequences and recombination machinery within chromatin loops. An alternate model of CO abundance modulation could consider the phenomenon of CO interference (COI). COI refers to the observation that the likelihood of two COs occurring in close genetic proximity is less than would be expected if CO positioning occurred stochastically (Muller, 1916; Sturtevant, 1914). Thus, COI has the capacity to influence the distribution and number of COs which may form. COI is dependent on the ability of a preliminary CO event to 'interfere' with a secondary CO event, therefore a means to communicate this information between loci must be active (Kleckner *et al.*, 2004; Zhang *et al.*, 2014). It is feasible that chromatin loop density may influence the abundance of mature COs by influencing the mechanical stresses imposed along meiotic chromatin and consequently the ability of COI to dictate the number of COs which form. Alternate models linking the meiotic chromosome organisation to CO abundance are also plausible in mammalian systems. Distinguishing between such possibilities is crucially reliant on a greater understanding of chromatin organisation, relative to the chromosome axis and recombination machinery.

1.9 Thesis Aims

The highly conserved looping of chromatin evident in meiocytes, remains a remarkable example of the complexities of large-scale chromatin architecture, distinct from that observed in interphase or mitotic cells. However, despite the great extent of mapping investigations conducted in lower-order organisms, meiotic chromatin structures have not been thoroughly characterised in complex species. To date, most structural studies have exploited genome-wide mapping strategies in such organisms. However, these studies have shed little insight on inter-cellular heterogeneity of chromatin topology, the spatial relationship of chromatin relative to the synaptonemal complex, or the conservation of loop structures throughout prophase I. The absence of such structural detail has also prevented examination of firstly, the regulatory mechanisms which underlie large-scale chromatin architecture, such as the involvement of cohesin and transcriptional machinery, as seen in yeast. And secondly, the putative functional link between chromatin loops and the extent and distribution of meiotic COs. Therefore, the principle focus of this thesis was to utilise a single-cellular, cytological approach, to characterise chromatin loop topology in murine meiocytes. This would then facilitate the dissection of both the structural mechanisms underlying chromatin loops and their potential functional relationship with meiotic recombination pathways. Accordingly, the main aims of my thesis were specified as follows:

- To generate and validate a comprehensive map of a single autosomal chromatin loop using IF-FISH in mouse pachytene spermatocytes
- To compare chromatin organisation between leptotene and pachytene spermatocytes, in order to further elucidate the temporal dynamics of chromatin organisation during prophase I
- To examine the role of transcription in the maintenance of pachytene chromatin loop architecture in mouse spermatocytes
- To compare chromatin loop organisation in prophase I meiocytes with distinct CO abundances and inter-homolog biases, in order to generate insight into the correlative relationships between large-scale chromatin architecture and key events during meiotic recombination

Chapter 2:

Materials and Methods

Chapter 2 Materials and Methods

2.1 Animals Use and Sample Preparation

2.1.1 Animal Use

Animal housing and dissection, including euthanasia and organ removal, were conducted according to UK Home Office regulations and approved institutional guidelines for animal welfare (The University of Edinburgh, Edinburgh). Adult and juvenile mice were culled using cervical dislocation. Late gestation embryos were culled using decapitation.

Adult C57BL/6 wildtype mice were procured from Charles River Laboratories. Embryonic and juvenile C57BL/6 wild type mice were generated in house through wildtype C57BL/6 x C57BL/6 matings.

Smc1β+/+, *Smc1β-/-* and *Smc1β-/-,1α* testes surface-spreads were generated from mice created on a C57BL/6 genetic background (Biswas, Stevense, and Jessberger, 2018) and were kindly prepared and gifted by Rolf Jessberger and Uddi Biswas (Institute of Physiological Chemistry, Dresden).

2.1.2 Testes Surface-Spread Preparation

Testes surface-spreads were prepared for immunofluorescence (IF) and fluorescent *in situ* hybridisation (FISH) using the Speed preparation protocol, developed by Robert Speed (Speed, 1982). Plain glass slides for cell spreading were sterilised by boiling in dH_2O and air drying. Adult testes were isolated from 2-6-month-old wild type C57BL/6 mice. Juvenile testes were isolated from 16-day-old (16 dpp) wild type C57BL/6 mice. Testes were dissected from each animal and stored in Dulbecco's phosphate buffered saline (DPBS; 0.137 M NaCl, 3 mM KCl, 8 mM Na_2HPO_4, 1.5 mM KH_2PO_4, pH7.3) prior to the removal of the tunica albuginea and the release of the seminiferous tubules with forceps. The seminiferous tubules were macerated with razor blades into a cloudy cell suspension in 500 µl DMEM (Thermo Fisher Scientific, #41966029). The resultant suspension was made up to 4 ml with DMEM and transferred to a 15 ml tube which was left to stand at room temperature for 10 mins until larger clumps of tissue had settled. The supernatant was then transferred to a fresh 15 ml tube and centrifuged at 1000 rpm (Sorvall Legend RT, 75006445 rotor), for 5 mins at 4°C to pellet the cells. After centrifugation the pellet was resuspended in 1 ml fresh DMEM per pair of testes. Twenty sterilised slides per pair of testes were placed in a humid chamber, five drops of 4.5% sucrose (Sigma) solution were then added to each slide using a Pasteur pipette. Using a fresh Pasteur pipette a single drop (~25 µl) of the cell suspension was added to the centre of each slide from a height of ~15 cm, followed by a single drop 0.05% Triton-X-100 (Amersham Bioscience). Slides were left to stand at room temperature for 10 mins in a sealed humid chamber. Eight drops of 2% paraformaldehyde (PFA), pH8 (Sigma), with 0.02% SDS (Sigma), was then added to the slides by Pasteur pipette and the samples left to stand at room temperature for 20 mins in a sealed humid chamber to fix the nuclei. The fixative was subsequently removed by gently washing each slide in dH_2O, following which the slides were air dried. If not used immediately slides were stored at -80°C.

2.1.3 Testis Section Preparation

Testicular tissue for sectioning was isolated from 2-6-month-old wildtype C57BL/6 mice. Testes were halved using a surgical scalpel, fixed in 4% PFA overnight and stored in 70% ethanol at 4°C until embedding. In preparation for embedding testes halves were dehydrated in an ethanol series, followed by a xylene series and subsequently paraffin-embedded (Tissue-Tek VIP 5 Jr. and Tissue-Tek Embedding Center, Sakura). 5 µm sections were cut using a microtome (HistoCore BIOCUT, Leica), quickly laid on Superfrost+ glass slides at 46°C and stored at room temperature until further use.

2.1.4 Ovary Spread Preparation

The procedure used to prepare oocyte cell spreads for IF and FISH was modified from methodologies published by Peters *et al*. (Peters, Plug, Annemieke, van Vugt, and De Boer, 1997). To obtain pachytene oocytes, embryonic ovaries were isolated at E17.5. Females found plugged after mating were classed as E0.5 the morning the plug was observed. At the appropriate litter age, the pregnant dams were culled and the uterine sack containing the embryos was isolated. Individual embryos were extracted from the uterine sack and ovaries isolated using forceps into DPBS at 4°C. Ovaries were transferred into 500 µl hypotonic extraction buffer (30 mM Tris, 50 mM sucrose (Sigma), 17 mM trisodium citrate dehydrate (Sigma), 5 mM EDTA (Roche), 0.5 mM DTT (Sigma), 0.5 mM PMSF (Sigma), pH8.2) and were left to stand at room temperature for 15-30 mins. Each pair of ovaries was then added to 20 µl 500 mM sucrose solution in a 0.2 ml tube and the tissue was homogenised with a sterile needle for 5 mins. One plain glass slide was prepared per ovary by sterilising in boiling dH_2O, air drying and soaking in 1% PFA (pH 9.2, pH set using 10 mM sodium borate), with 0.15% Triton-X-100. 10 µl of the sucrose cell suspension was added to the top corner of the fix-soaked slide and zig-zagged down the slide. Cells were then incubated overnight in a warm, humid chamber whereupon the slides were left to air dry prior to storage at -80°C.

2.2 Pachytene Cell Enrichment and Treatment

2.2.1 Testis Single Cell Solution Preparation

The preparation of a single cell solution from testicular tissue was based on a protocol previously described by Gaysinskaya *et al*. (Gaysinskaya, Soh, van der Heijden, and Bortvin, 2014; Handel, Caldwell, and Wiltshire, 1995). Adult testes were isolated from 2-6-month-old wild type C57BL/6 mice and stored in DPBS prior to the removal of the tunica albuginea with forceps and the release of the seminiferous tubules. The seminiferous tubules were placed in 500 µl of Krebs-Ringer bicarbonate (KRB) solution (120 mM NaCl, 3.4 mM KCl, 25.2 mM $NaHCO_3$, 1.2 mM KH_2PO_4, 1.2 mM $MgSO_4.7H_2O$, 1.3 mM $CaCl_2$, 2 mg/ml Dextrose), supplemented with 0.4% bovine serum albumin (BSA; Sigma) and large clumps of tubules were gently teased apart using forceps. The seminiferous tubules were then transferred into a 50 ml glass beaker containing 15 ml of KRB solution, supplemented with 0.4% BSA, 5 µg/ml DNaseI (Invitrogen) and 200 U/ml collagenase (Type I, prepared from *Cl. histolyticumI*; Gibco), which was then shaken at 60 strokes per minute in a 32°C water bath for 5 mins to separate individual tubules. The somatic interstitial cells were then removed by washing the tubules twice in KRB solution, 0.4% BSA. Residual buffer was removed and replaced with 8.4 ml KRB, supplemented with 0.4% BSA, 5 µg/ml DNase I and 2.5% trypsin (Type IX-S, from porcine pancreas; Sigma) to digest the seminiferous tubules. A single cell suspension was then generated by shaking the suspension at 60 strokes per minute in a 32°C water bath for 10 mins until a cloudy suspension was created. The cells were further dissociated by mixing the suspension using a wide bore Pasteur pipette for 4 mins. 1 ml newborn calf serum (Hyclone; GE Life Sciences) was added to the suspension to neutralise the trypsin. The resulting suspension was passed through a 70-µm cell strainer (Fisherbrand), to remove large pieces of debris which may disrupt elutriation.

2.2.2 Centrifugal Elutriation

Pachytene spermatocyte cells were fractionated from the testicular single cell suspension by centrifugal elutriation (Avanti J-26 XP Centrifuge, JE-5.0 Elutriator Rotor, 5 ml Elutriator Chamber; Beckman Coulter). The elutriator was prepared by flushing with 70% ethanol for 2 mins, followed by sterile distilled water for 3 mins at a flow rate of 60 ml/min at 2,700 rpm, 15°C. The elutriator was then set to spin at 2,700 rpm at a flow rate of 60 ml/minute as KRB solution (supplemented with 0.4% BSA and 5% foetal calf serum (FCS)) was flushed through. The single cell suspension was then loaded into the elutriator via the reservoir and a 10 ml syringe for 5 mins under the above conditions to allow cells to gather in the centrifugation chamber. The flow rate was gradually increased from 60 to 100 ml/min over 5 mins in order to elute unrequired small cells, including sperm and round spermatids. The flow rate was increased to 120, 130, 140 and 150 ml/min, and 50 ml was collected for each flow rate to harvest the pachytene-enriched cell population. The pachytene-enriched flow through was immediately centrifuged at 1,200 rpm (Sorvall Legend RT, 75006445 rotor) at 15°C, for 15 mins. The resultant pellet was resuspended into 2 ml KRB solution supplemented with 0.4% BSA and 5% FCS.

The cells within the pachytene-enriched suspension were stained with 0.4% Hyclone Trypan Blue (Fischer Scientific), to conduct a Trypan blue exclusion test to quantify cell viability and were counted using a haemocytometer. To determine the purity of the pachytene-enriched suspension testes spreads were prepared (Section 2.1.2) and were stained with 4,6-diamoidino-2-phenylidole (DAPI) and IF, using anti-SYCP3, as described in Section 2.4.1, and the proportion of testes SYCP3-positive and -negative cell types and prophase I stages was determined as described in Section 2.7.1.

2.2.3 Drug Treatment

Pachytene-enriched cell suspensions were treated with actinomycin D, α-amanitin, Flavopiridol hydrochloride hydrate or RNase A under the conditions specified in Table 2-1. For RNase A treatment cells were permeabilised with 0.2% Triton X-100. Drug treatments were conducted in a total volume of 1 ml in a 1.5 ml tube incubated in a shaking incubator at 32°C, 75 rpm (Innova 4230, New Brunswick Scientific, Edison, NJ, USA).

Table 2-1. Drugs administered

Drug	Concentration	Time Period	Supplier
Actinomycin D	50 µg/ml	1 hr	Sigma (A4262)
α-amanitin	75 µg/ml	3 hrs	Sigma (A2263)
Flavopiridol Hydrochloride	100 µM	1 hr	Sigma (F3055)
RNase A (PureLink)	1 mg/ml	10 + 30 mins	Invitrogen (12091021)

2.3 Preparation of Fluorescence *In Situ* Hybridisation (FISH) Probes

2.3.1 FISH Probes Utilised

Table 2-2. FISH probes.

Probe	Probe Name in Text	Genomic Location (mm9)	Probe Type
RP23-421K19	B-A	chr6:51946668-52152698	BAC
RP24-103E20	BAC-1 or B-B	chr6:52155315-52324369	BAC
RP24-75L23	BAC-2 or B-C	chr6:52330643-52558894	BAC
RP24-120P24	B-D	chr6:52548577-52716439	BAC
RP23-314F10	B-E	chr6:52723098-52885978	BAC
RP23-361A8	B-F	chr6:52881717-53063069	BAC
RP23-398L22	B-G	chr6:53099840-53266110	BAC
RP23-285F21	B-H	chr6:53271997-53505028	BAC
RP23-201K15	B-I	chr6:53506262-53704283	BAC
RP23-184I21	B-J	chr6:53706992-53927135	BAC
RP24-283B15	B-K	chr6:53925146-54096067	BAC
RP24-299P12	B+500	chr6:54402197-54568318	BAC
RP24-372L21	B+1000	chr6:54939597-55127024	BAC
RP24-272M2	B+1500	chr6:55440649-55603442	BAC
RP23-222F6	B+2000	chr6:55889295-56091187	BAC
RP24-62O20	B+2500	chr6:56380961-56612866	BAC
RP24-263L11	B-500	chr6:51316802-51495336	BAC
RP23-410E12	B-1000	chr6:50860277-51024081	BAC
RP23-245D10	B-1500	chr6:50342043-50573777	BAC
RP23-55C1	B-2000	chr6:49907793-50081317	BAC
RP24-252F16	B-2500	chr6:49409053-49577966	BAC
RP23-414F5	Gtf2e2 G	chr8:34756321-34934615	BAC
RP23-135N4	Gtf2e2 F1	chr8:33928612-34128993	BAC
RP24-370O24	Gtf2e2 G2	chr8:35502185-35646689	BAC
RP24-82O23	Spata4 G	chr8:55492998-55737483	BAC
RP24-274D4	Spata4 F1	chr8:54935921-55076581	BAC
RP23-349P11	Spata4 F2	chr8:56122154-56200749	BAC
RP24-500I4	PAR	chrY:90698547-90844698	BAC
WIBR1-1277H09	F-A	chr6:52117094-52154575	Fosmid
WIBR1-2289F08	F-B	chr6:52354007-52391254	Fosmid
WIBR1-2730H09	F-C	chr6:52868608-52908281	Fosmid
WIBR1-1192B16	F-D	chr6:53155783-53191192	Fosmid
WIBR1-1997N10	F-E	chr6:53568343-53602318	Fosmid
WIBR1-0326P16	F-F	chr6:53770711-53813004	Fosmid
WIBR1-2622M05	F-G	chr6:53934473-53978292	Fosmid
WIBR1-0872E17	A3 Hotspot	chr1:161936661-161974457	Fosmid
WIBR1-1095D24	59.5 Hotspot	chr19:59492514-59533114	Fosmid
WIBR1-0640J10	Female-Biased Hotspot A	chr10:82186262-82225317	Fosmid
WIBR1-2306C22	Female-Biased Hotspot B	chr19:55407528-55445660	Fosmid
WIBR1-2079G06	Male-Biased Hotspot A	chr10:51769679-82225317	Fosmid

WIBR1-2471L08	Male-Biased Hotspot B	chr19:25677845-25714849	Fosmid
WIBR1-2669H19	Common Coldspot A	chr10:48968759-49006376	Fosmid
WIBR1-1549I14	Common Coldspot B	chr19:30989440-31025530	Fosmid
WIBR1-2660H22	Common Hotspot A	chr10:47517034-47557541	Fosmid
WIBR1-1309N18	Common Hotspot B	chr19:24818441-24855700	Fosmid
WI1-1274C8	Non-Homologous A	chrX:96070005-96104303	Fosmid
WI1-1165M1	Non-Homologous B	chrX:96648345-96687318	Fosmid

2.3.2 Growth of BAC and Fosmid Clones

BAC and fosmid clones, detailed in Table 2-2, were purchased from BACPAC Resources Centre and were delivered as agar stabs. DH10B bacterial cells harbouring the BAC or fosmid DNA were streaked on agar plates supplemented with 34 µg/ml chloramphenicol (Sigma) and grown overnight at 37°C to enable single colonies to be isolated. Individual bacterial colonies were picked and grown in 5 ml sterile L-broth (IGMM Technical Services), supplemented with 34 µg/ml chloramphenicol, in a 50 ml tube, at 37°C in a shaking incubator (250 rpm; Innova 4230, New Brunswick Scientific, Edison, NJ, USA) overnight.

2.3.3 Bacterial Glycerol Stock

For long-term storage of BAC and fosmid clones, glycerol stocks were prepared in which 500 µl of the overnight liquid culture was combined with sterile glycerol (IGMM Technical Services) to a final concentration of 20% v/v and stored at -80°C.

2.3.4 Purification of BAC and Fosmid FISH Probe DNA

BAC and fosmid DNA was extracted from bacteria from the overnight liquid culture using an alkaline lysis mini prep. 1.5 ml of the overnight culture was added to a 1.5 ml tube and cells were collected by centrifugation (30 secs, 21,130 g, 4°C). The supernatant was subsequently discarded, and an additional 1.5 ml of overnight culture was added and centrifuged as above. In preparation for lysis the pellet was resuspended in 200 µl GTE buffer (50 mM Glucose, 25 mM Tris pH8, 10 mM EDTA), supplemented with 5 mg/ml lysozyme (Sigma) and 20 mg/ml RNase A/T1 (ThermoFisher Scientific), and left to stand at room temperature for 5 mins. Cells were

lysed using 400 µl lysis buffer (0.1 M NaOH, 1% SDS), mixed by inversion and left to stand at room temperature for 5 mins. To precipitate cellular debris, 300 µl acetate buffer (5M potassium acetate, 11.5% glacial acetic acid) was added to the lysate, inverted to mix and then stood on ice for 5 mins. Samples were centrifuged at 15,871 g for 5 mins at 4°C, supernatants were collected, and DNA purified using an equal volume of phenol-chloroform-isoamyl alcohol mixture (Sigma), mixed by gentle inversion, and centrifuged at 15,871 g for 5 mins at 4°C. The upper aqueous phase was recovered, and residual phenol-chloroform removed by adding an equal volume of chloroform (Sigma), mixing by gentle inversion and centrifugation at 15,871 g for 5 mins at 4°C. The aqueous phase was collected, and the DNA precipitated with an equal volume of isopropanol (Sigma) on dry ice for a minimum of 30 mins. The DNA was then recovered by centrifugation at 15,871 g for 20 mins at 4°C and washed with 70% ethanol and centrifuged at 15,871 g for 5 mins at 4°C. Residual ethanol was allowed to evaporate at room temperature and the pellet was resuspended in 20 µl Tris/EDTA (TE; IGMM Technical Services) and stored at room temperature.

2.3.5 Nick Translation of BAC and Fosmid FISH Probe DNA

Following the purification of BAC and fosmid FISH DNA the probes were labelled with the uridine analogue digoxigenin-11-dUTP (Roche) or biotin-16-dUTP (Roche) using a nick translation reaction. A 20 µl nick translation mix was prepared for each reaction; each mix contained ~1 µg DNA, 2.5 µl each of 0.5 mM of dATP, dGTP and dCTP, either 1.5 µl 1 mM digoxigenin-11-dUTP plus 1 µl 0.5mM dTTP or 2.5 µl 1 mM bioton-16-dUTP, DNase I (Roche) to a final concentration of 1 U/ml, DNA polymerase I (Invitrogen) to a final concertation of 0.5 U/ml, in 1x nick translation salts buffer (0.5 M Tris pH 7.5, 0.1 M $MgSO_4$, 1 mM DTT, 0.5 mg/ml BSA, Sigma). The nick translation reaction was conducted by incubating the mix at 16°C for 90 mins. 2 µl 20% SDS, 3 µl 0.5 M EDTA and 65 µl TE were added to the mix to stop the reaction in a final volume of 90 µl. Unincorporated nucleotides were removed by passing the nick translation mix through a Sephadex G50 quick spin column (Roche) centrifuged at 2,500 rpm (Sorvall Legend RT, 75006445 rotor) for 2 mins and the flow through was collected. Labelled probes were stored at room temperature.

2.3.6 Quantification of Label Incorporation

To ensure BAC and fosmid FISH probe DNA had successfully incorporated a sufficient amount of digoxigenin-11-dUTP or biotin-16-dUTP nucleotides, biotin or digoxigenin was quantified using an alkaline phosphatase-based dot-blot assay. Gridded nitrocellulose membranes (Protan BA 85, Whatman) were prepared by soaking the membranes in 20x saline sodium citrate buffer (SSC; 3M NaCl, 0.3M tri-sodium citrate, pH7.4, IGMM Technical Services) for 10 mins, allowed to air dry and stored at room temperature before use. Labelled DNA samples were prepared by diluting each sample by 1 in 500, 1 in 1,000, 1 in 5,000 and 1 in 10,000 in TE. A 1 µl spot for each probe dilution was applied to the nitrocellulose membrane. Probes previously confirmed to be effectively labelled were spotted on the nitrocellulose membrane in the same dilution series as a positive control. The DNA was crosslinked to the nitrocellulose membranes using 150 mJ UV cross-linker set at 254 nm (CL-1000 Ultraviolet Crosslinker, UVP). Following crosslinking the membrane was washed briefly using Buffer I (0.1 M Tris pH 7.5, 0.5 M NaCl) and then blocked in 3% BSA, Buffer I for 15-30 mins at 60°C. After blocking, the labelled DNA was detected by applying 75 mU/ml streptavidin-alkaline phosphatase (Roche) and/or 75 mU/ml anti-digoxigenin-alkaline phosphatase Fab fragments (Roche) in 10 ml Buffer I for 15 mins at room temperature. Excess detection probe was removed by performing two 15 mins in Buffer I. The membrane was then equilibrated in Buffer II (0.1 M Tris pH 9.5). The alkaline phosphatase-associated probes were then detected using the alkaline phosphatase substrate kit according to the manufacturer's protocol (Vector Labs). The kit contains the chromogen 5-bromo-4-chloro-3-idolyl phosphate and nitroblue tetrazolium that forms an indigo reaction product in the presence of alkaline phosphatase and enables visual quantification of digoxigenin-11-dUTP or biotin-16-dUTP nucleotide incorporation after a 1 hour incubation at room temperature.

2.4 Immunofluorescent-Fluorescent *In Situ* Hybridisation (IF-FISH) on Surface-Spreads

2.4.1 Immunofluorescent (IF) staining

IF staining was performed as described by Ollinger *et al.* (Ollinger *et al*., 2008). All antibodies used for IF staining are detailed in Table 2-3. If stored at -80°C testes and ovary surface-spreads were thawed in DPBS for 5 mins at room temperature prior to blocking. Testes and ovary surface-spreads were blocked for 30 mins at room temperature with 50 µl blocking solution (0.15% BSA, 0.1% Tween-20, 5% goat serum) covered by a plastic coverslip in a humid chamber. Blocking solution was drained from the slides and 50 µl primary antibody diluted in blocking solution to the appropriate concentration (Table 2-3) was added to the slides with a new plastic coverslip and incubated in a humid chamber for two hours at room temperature or overnight at 4°C. Unbound primary antibody was removed by 3x 5 min DPBS washes at room temperature following which 50 µl secondary antibody and 85 ng/ml DAPI diluted in blocking solution to the appropriate concentration (Table 2-3) was added with a fresh plastic coverslip and incubated in a dark, humid chamber for one hour at room temperature. Unbound secondary antibody and excess DAPI was removed by 3x 5 min DPBS washes. Following the removal of the secondary antibody the bound primary and secondary antibodies were fixed with 2% PFA (pH8) for 20 mins at room temperature. Fixative was then removed by 2x dH_2O washes. FISH was then performed as described in 2.4.2.

Table 2-3. Immunofluorescence antibodies

Antibody	Species	Source	Concentration
Anti-SYCP3	Mouse	Abcam, ab97672	1:500
Anti-Mouse Alexa Fluor 594	Goat	Invitrogen, A-11005	1:500

2.4.2 FISH Probe Hybridisation

Testes and ovary surface-spreads generated, IF-stained and fixed as in 2.1 and 2.4.1 were prepared for hybridisation of BAC and fosmid FISH probes by incubating the slides with 100 µg/ml RNaseA (PureLink RNaseA, Thermo Fischer Scientific) in 2x SSC at 37°C for ~1 hour. Slides were then washed in 2x SSC and dehydrated through a 70%, 90% and 100% ethanol series for 2 mins at each concentration. The slides were then air dried and warmed at 70°C for 5 mins in preparation for DNA

denaturation. The DNA on the slides was denatured in a 70% formamide, 2x SSC pH 7.5 solution for 30 mins at 80°C. Slides were then transferred for 2 mins into ice-cold 70% ethanol and 90% and 100% ethanol at room temperature to dehydrate each sample.

The biotinylated-16-dUTP and/or digoxigenin-11-dUTP labelled FISH probes were prepared for hybridisation simultaneously to the spreads/sections. For each slide ~100 ng of each labelled probe was combined with 5 µg mouse C_0t1 DNA (Invitrogen) and 10 µg salmon sperm (Ambion) competitor and precipitated with two volumes of 100% ethanol using a DNA SpeedVac Concentrator (Savant). For each slide probes were resuspended in 20 µl hybridisation mix composed of 50% deionised formamide (v/v, Sigma), 1% Tween-20 (Sigma) and 10% dextran sulphate (Sigma) in 2x SSC. In order to form a homogeneous mixture, the probes were left to dissolve in the hybridisation mix at room temperature for 30-60 mins with regular agitation. The probes were then denatured at 70°C for 5 mins and the mouse C_0t1 allowed to reanneal at 37°C for 15 mins.

Three directly labelled whole chromosome paints were purchased from Metasystems probes: Xcyting mouse chromosome painting probe XMP X Green, XMP Y Green and XMP 6 Green. The manufacturer's protocol for paint hybridisation was utilised with minor alterations: An equal volume of hybridisation mix, composition described above, was added to the chromosome paint. Chromosome paints were denatured at 75°C for 5 mins and reannealed at 37°C for 15 mins prior to hybridisation.

On completion of spread and FISH probe preparation 20 µl of the probe-hybridisation mix or chromosome paint-hybridisation mix was pipetted onto a 20x50 mm glass coverslip on a hot plate at 37°C. The coverslip was then gently placed on the surface of the sample and attached to the slides using a rubber sealant (TipTop). The hybridisation of labelled FISH probes was then performed on an enamel tray at 37°C overnight in a water bath.

2.4.3 FISH Probe Detection

The FISH probes were immediately detected after overnight hybridisation. The rubber sealant was gently removed, and the coverslip was allowed to float off in 2x SSC at 45°C for 3 mins. To remove unbound probes slides were washed: 3x 3 min washes in 2x SSC at 45°C, 4x 3 min washes in 0.1x SSC at 60°C. The slides were then prepared for blocking by dipping in 4x SSC, 0.1% Tween-20 at room temperature. Slides were then covered with blocking buffer (5% dried milk powder (Marvel), 4x SSC) for 5 mins at room temperature under a 22x50 mm glass coverslip in a humid chamber. Blocking buffer was drained from the slides and a sequential series of antibodies and avidin were applied to the slides according to the FISH probes utilised on each slide. Digoxigenin-labelled probes were detected by sequential application of FITC-conjugated anti-digoxigenin and FITC-conjugated anti-sheep IgG. Biotin-labelled probes were detected by the sequential application of Cy5-conjugated avidin, biotinylated anti-avidin and finally a second application of Cy5-conjugated avidin. All antibodies and detection probes were diluted to the required concentration in 5% dried milk powder, 4x SSC and centrifuged at 15,871 g for 15 mins at 4°C to move undissolved clumps of milk powder. Information regarding the antibodies and avidin, including required concentrations and suppliers, are detailed in Table 2-4. 50ul of each antibody/avidin was incubated with the sample for 30 mins at 37°C in a humid chamber. Between each antibody/avidin application 4x 3 min washes with 4x SSC, 0.1% Tween-20 were conducted at 37°C. Following the final antibody/avidin incubation the samples were washed twice in 4x SSC with 0.1% Tween-20 for 3 mins at 37°C, after which the slides were stained with 50 µg/ml DAPI in 4x SSC with 0.1% Tween-20 for 3 mins before a final wash in 4x SSC with 0.1% Tween-20. 22x50 mm glass coverslips were mounted using Vectashield mounting medium and sealed with nail varnish.

Table 2-4. Antibodies/Avidin for FISH probe detection

Antibody/Avidin	Species	Source	Concentration
Anti-Digoxigenin-Fluorescein Fab	Sheep	Vector Labs	1:20
Fluorescein Anti-Sheep IgG (H+L)	Rabbit	Roche	1:100
Cy5-Streptavidin		Invitrogen	1:10
Biotinylated Anti-Avidin	Goat	Vector Labs	1:100

2.5 Immunofluorescent-Fluorescent *In Situ* Hybridisation (IF-FISH) on Testes Sections

2.5.1 Section Antigen Retrieval and Immunofluorescent (IF) Staining

Embedded testes (2.1.3) were prepared for cytological analysis by melting the wax at 60°C for 20 mins, followed by 3x 10 min xylene (Sigma) washes to dewax the sections. The sections were rehydrated through a 100% (3x 10 min), 90% (2x 5 min) and 70% (2x 5 min) ethanol series, followed by 3x DPBS washes. Antigen retrieval was conducted by boiling sections for 30 mins in 1 L 0.1 M citrate buffer (pH 6; BDH Chemicals Ltd.) and allowed to cool to room temperature for approximately 30 mins. Antibody staining and fixation were conducted immediately after antigen retrieval using the same protocol as described in 2.4.1.

2.5.2 FISH Probe Hybridisation and Detection in Testes Sections

Following IF staining and antibody fixation testes sections were incubated in 2x SSC at 75°C in preparation for denaturation. The sections were denatured in a 70% formamide, 2x SSC pH 7.5 solution for 3 mins at 75°C. Slides were then transferred for 2 mins into ice-cold 70% ethanol and 90% and 100% ethanol at room temperature to dehydrate each sample. FISH probes were preparation, hybridisation and detection were conducted as described in sections 2.4.2 and 2.4.3.

2.6 Image Capture

Typical three and four channel images were captured using the following three imaging systems:

- The first imaging system was employed to image and capture three channel images with triple emitters. Epifluorescent images were acquired using a Photometrics Coolsnap HQ2 CCD camera and a Zeiss Axioplan II fluorescence microscope with Plan-neofluar objectives (Carl Zeiss, Cambridge, UK), a Mercury Halide fluorescent light source (Exfo Excite 120, Excelitas Technologies) and Chroma #83000 triple band pass filter set (Chroma Technology Corp., Rockingham, VT) with the excitation filters installed in a motorised filter wheel (Ludl Electronic Products, Hawthorne, NY). Image capture was performed using a Plan-APOCHROMAT 100x/1.4011, ∞/0.17 lens and Micromanager software with 1x1 binning. In order to measure the area of FISH probe and DAPI signals a common exposure time was used throughout image capture.
- The second imaging system was employed to image and capture four channel images with single emission filters. Epifluorescent images were acquired using a Photometrics Coolsnap HQ2 CCD camera or a Photometrics Prime BSI CMOS camera and a Zeiss AxioImager A2 fluorescence microscope with Plan-neofluar objectives (Carl Zeiss, Cambridge, UK), a Mercury Halide fluorescent light source (Exfo Excite 120, Excelitas Technologies) and Chroma #89000ET four colour filter set (Chroma Technology Corp., Rockingham, VT) with the single excitation and emission filters installed in motorised filter wheels (Prior Scientific Instruments, Cambridge, UK). Image capture was performed using a Plan-APOCHROMAT 100x/1.4011, ∞/0.17 lens and Micromanager software with 1x1 binning.

- The third imaging system was used to image three channel images with single emission filters in 3D. Epifluorescent images were acquired using a Photometrics Coolsnap HQ2 CCD camera and a Zeiss AxioImager A1 fluorescence microscope with a Plan Apochromat 100x 1.4NA objective, a Lumen 200W metal halide light source (Prior Scientific Instruments, Cambridge, UK) and Chroma #89014ET single excitation and emission filters (Chroma Technology Corp., Rockingham, VT) with the excitation and emission filters installed in Prior motorised filter wheels. A piezoelectrically driven objective mount (PIFOC model P-721, Physik Instrumente GmbH and Co, Karlsruhe) was used to control movement in the z dimension. Hardware control, image capture and analysis were performed using a Plan-APOCHROMAT, 100x/1.4011, 440780-9904 lens and NIS Elements software.

2.7 Image Analysis

2.7.1 Meiocyte Staging and Purity

Primary spermatocytes and oocytes were distinguished from alternate cell types by their SYCP3-positive signal. Prophase I spermatocyte and oocytes were staged according to axial element organisation, visualised by anti-SYCP3 IF. Leptotene nuclei were identified by incomplete axial element formation with numerous short SYCP3 fragments with no apparent synapsis, whilst zygotene nuclei showed extensive formation of the AE and incomplete synapsis of homologous chromosomes. Pachytene nuclei were identified by complete synapsis of all 20 homologous chromosomes in oocytes or all 19 autosomal chromosome and synapsis between the sex chromosomes at the PAR in spermatocytes.

2.7.2 IF and FISH Analysis - 2D Data

Total autosomal SC length or total axis length in pachytene were quantified by measuring the length of SYCP3-positive axes using the ImageJ plugin NeuronJ (Meijering *et al*., 2004). In order to compare SC length between individual spermatocytes the sex chromosomes were excluded from analysis. Sex chromosomes can be identified by their characteristic morphology, where a short region of synapsis at the PAR is evident between the heteromorphic X and Y chromosomes, highlighted by SYCP3. If the sex chromosomes were not distinguishable from the autosomes in a spermatocyte image the image was discarded from analysis. The sex chromosomes cannot be distinguished from autosomes in oocytes by anti-SYCP3 IF staining. Therefore, when comparing male and female axis lengths all 20 SCs in oocytes and all 19 autosomal SCs, plus the X chromosome axis, in spermatocytes were measured.

Images were taken at a constant exposure for FISH/DAPI area comparisons. DAPI and BAC probe area were calculated by segmenting the appropriate channels and using the pre-defined ImageJ area tool. Chromosome paint area was calculated using a custom script written by Nick Gilbert using ImageJ software.

Inter-chromatid and inter-sister chromatid distances was measured using fosmid FISH probes, which provided sufficient resolution to determine the position of each of the four individual chromatids. In order to measure inter-chromatid distance, the position of each chromatid was first identified. ImageJ software was used to segment the FISH probe channels and identify the XY coordinates of the centroid of each FISH probe signal. For autosomal loci, if more than four fosmid foci were visible in a nucleus, or for non-homologous loci if more than two fosmid foci were visible in a nucleus, the nuclei were excluded from analysis. If fewer than four discrete fosmid foci at an autosomal locus were visible the position of all four chromatids was determined manually by considering the intensity and/or area of the fosmid foci, if this could not be accurately achieved the nucleus was excluded from analysis. If only one fosmid foci was visible at non-homologous loci it was assumed both chromatids were present but undistinguishable. Once the XY centroid coordinates for all four autosomal chromatids or two non-homologous chromatids were determined the inter-chromatid and inter-sister chromatid distances were calculated by trigonometric equations for each nucleus. Presumptive inter-sister chromatid distances at autosomal loci in leptotene was determined by calculating the mean of the two shortest inter-chromatid distance in nuclei where the two shortest distances were over 2x less than the mean of the remaining four inter-chromatid distances. The minimal inter-sister chromatid distances at autosomal loci in pachytene were determined by calculating the mean of the two shortest inter-chromatid distances. Inter-chromatid and presumptive and minimal inter-sister chromatid distances were typically expressed as the mean of the respective inter-chromatid distances.

The BAC-SC overlap frequency was generated manually by calculating the percentage of nuclei in which the BAC FISH probe visibly overlapped with the SC, marked by anti-SYCP3 IF signal. Chromatin regions were categorised into SC-proximal and SC-distal region according to whether the associated BAC-SC overlap frequency was >80% or <80%, respectively.

The mean tether-to-fosmid distance was calculated per pachytene nucleus by conducting IF-FISH in which both a BAC and fosmid probe was utilised. A consistent SC-proximal BAC probe with a BAC-SC overlap score of 98%, identified as described above, was selected to act as a proxy for an axis-association site. A fosmid probe was selected to highlight the position of the four chromatids at a specific genomic region. The XY centroid coordinates of the four chromatids were recorded per fosmid and the

XY coordinates of the BAC-SC overlap point were identified and recorded. The tether-to-fosmid distance was calculated through trigonometric equations for each of the four chromatids and the mean tether-to-fosmid distance per nucleus was calculated by taking the mean value from the four individual distances.

Analyses typically aimed to score 20-30 nuclei per biological replicate, though some experiments where slides of specific genotypes or prophase I substages were limiting, fewer nuclei were scored. The number of nuclei scored is indicated in each analysis.

2.7.3 Inter-Chromatid Distance - 3D Data

For 3D analysis of tissue sections, images were deconvolved using a calculated point spread function (PSF) with the Fast algorithm of Volocity (Perkinelmer Inc, Waltham MA). Image analysis was carried out using the Quantitation module of Volocity (Perkinelmer Inc, Waltham MA), in which the XYZ coordinates of the centroid of each probe signal was recorded. The inter-chromatid distance was calculated by trigonometric equations and the mean of all six inter-chromatid distances per nucleus was calculated. For all 3D analyses approximately 30 nuclei were scored per biological replicate.

2.8 RNA Isolation and Quantification

RNA was isolated from pachytene-enriched cells in suspension using the RNeasy Mini Plus kit (Qiagen), in combination with an RNase-free DNase set (Qiagen) to digest any genomic DNA contaminants, according to the manufacturer's protocol. RNA was eluted from the RNeasy columns in 30 µl RNase-free water.

The concentration and purity (260/280) of the RNA and cDNA product were determined by NanoDrop analysis (NanoDrop-1000, Thermo Fisher).

2.9 Statistical Analysis

The Fisher's exact test was used to assess the significance of a non-random association occurring between two categorical variables, using the null hypothesis that the relative proportions of one variable are distinct from the second. The Fisher's exact test was therefore used to assess the difference in chromatin-SC overlap and non-overlap between two distinct FISH probes.

The Mann Whitney-U test was selected to assess whether continuous variables from two independent samples were significantly different from one another, without the presumption of a normal distribution, using the null hypothesis that it is equally likely that a randomly selected value from one sample will be distinct from a randomly selected value from the second sample. The Mann-Whitney-U test was therefore used to compare quantitative variables, principally including distances and areas, between different genotypes, treatment group and FISH probes.

One-tailed t-tests were conducted to assess whether one independent sample was significantly less than another independent sample, using the null hypothesis that there is no significant difference between the two data sets. The one tail T-test was therefore used to assess whether significantly less RNA was present on transcription inhibition or following RNase treatments.

Linear regression analyses were performed to establish whether a linear relationship occurred between two quantitative variables, therefore enabling one independent variable to predict the value of a second variable. The significance of the relationship was measured against the null hypothesis that the correlation coefficient is equal to zero. Linear regression was therefore employed to assess the relationship between quantitative variable such as SC length and inter-fosmid distances.

Chapter 3:

Mapping an Autosomal Chromatin Loop in Mouse Pachytene Spermatocytes

Chapter 3 Mapping an Autosomal Chromatin Loop in Mouse Pachytene Spermatocytes

3.1 Introduction

The fundamental principles of large-scale chromatin organisation in pachytene spermatocytes have been known for several decades. Electron microscopy (EM)-led investigations originally revealed that chromatin formed sequential loop arrays (Figure 1-4), in which sister chromatids are postulated to emanate perpendicularly from the SC in a co-oriented manner (reviewed in Zickler and Kleckner, 1999). Several HiC-based studies have recently attempted to map these cytologically visible chromatin structures in mammals. These studies have reported the loss of interphase-associated chromatin configurations, including TADs, loops and compartments, and their replacement with refined, meiosis-specific compartments in pachytene-enriched populations of primate and rodent spermatocytes (Alavattam *et al*., 2019; Patel *et al*., 2019; Vara *et al*., 2019; Wang *et al*., 2019). However, it is not presently clear how these HiC-defined structures physically manifest inside meiotic nuclei, particularly in relationship to the SC, as SC-DNA interactions have yet to be comprehensively mapped in mammals. Moreover, the extent to which chromatin organisation varies between chromatids within a single nucleus, between nuclei and between mice has not been addressed.

The aim of this chapter was to develop IF-FISH based methods to visualise the path of chromatin within pachytene spermatocytes relative to the SC, to ascertain whether chromatin loops can be consistently mapped on a single cell basis. In addition, the IF-FISH assays produced unique data regarding the organisation of individual chromatids and inter-cellular homogeneity, which could not be extracted from whole chromosome cytological assays or population-based HiC approaches.

A region surrounding the *HoxA* gene cluster on 6qB3 was chosen for analysis, since extensive characterisation has been conducted at *Hox* gene family loci in regard to their 3D chromatin architecture in interphase cells, which creates a basis of knowledge and resources to build on for my own investigations (Montavon and Duboule, 2013; Narendra *et al*., 2015; Rodríguez-Carballo *et al*., 2017). IF-FISH on surface-spread pachytene spermatocytes categorised chromatin regions into SC-proximal and SC-distal regions, enabling a ~1.3 Mb chromatin loop, extending up to

~3 μm from the SC, to be mapped. Higher resolution FISH analysis was also performed to interrogate the relative spatial positioning of individual chromatids. Additionally, the validity of this newly defined chromatin loop was tested by assessing the change in chromatin loop organisation in cohesin mutant spermatocytes, in which chromosome morphology is known to appear abnormal (Biswas, Stevense, and Jessberger, 2018; Novak *et al*., 2008; Revenkova *et al*., 2004).

The single cell IF-FISH strategies developed in this chapter provide an effective tool to interrogate the spatial organisation of large-scale chromatin structures, relative to the pachytene SC. Cumulatively, the resultant findings have provided a comprehensive insight into the consistent topological organisation of autosomal chromatin loops, as well as the modulatory role of cohesin complexes, which ultimately provides a basis from which the functional importance of such structures can be examined.

3.2 Results

3.2.1 SC-Proximal and SC-Distal Chromatin Regions

Investigations into large-scale chromatin looping were begun by assessing whether chromatin-SC association was sequence-dependent and therefore caused specific genomic regions to be consistently in close proximity to the pachytene SC in individual nuclei and mice. To test this, IF-FISH was performed on mouse surface-spread spermatocytes, to assess the spatial relationship between specific genomic sequences and the SC (Figure 3-1). The proximity of specific chromatin regions to the SC was measured by determining the frequency at which individual BAC FISH probes (~150-200 kb) visibly overlapped with the SC (anti-SYCP3 IF); a greater frequency of visible BAC-SC overlap is indicative of greater physical proximity to the SC. Two adjacent BAC probes were selected on chromosome 6 (Figure 3-1b), the first of which (BAC-1) lies over the *HoxA* cluster and the second (BAC-2) adjacent to the first. On average, BAC-1 was significantly more likely to overlap with the SC than BAC-2 ($p<0.0001$, Fischer's exact test), with 98% and 59% of nuclei exhibiting BAC-SC overlap, respectively (Figure 3-1e). By comparing the frequency of BAC-SC overlap, the underlying chromatin was categorised into two discrete regions; a SC-proximal region (BAC-1), with a consistently high BAC-SC overlap frequency, and a SC-distal region (BAC-2), with a relatively low BAC-SC overlap frequency. The BAC-SC overlap frequency did not significantly alter between individual mice ($p=0.3-1$, Fisher's exact test), indicating that SC-proximal and SC-distal regions were conserved between animals (Figure 3-1e). By combining the same two adjacent BAC probes on surface-spread spermatocytes, the path of the chromatin over ~400 kb was visualised (Figure 3-1d). The chromatin was observed extending away from an SC-proximal 'tether point' towards the SC-distal region in a loop-like manner. Collectively, these data demonstrate that, at least at the *HoxA* locus, specific genomic regions are consistently in proximity to the pachytene SC, supporting the existence of a conserved axis-association sequence or region.

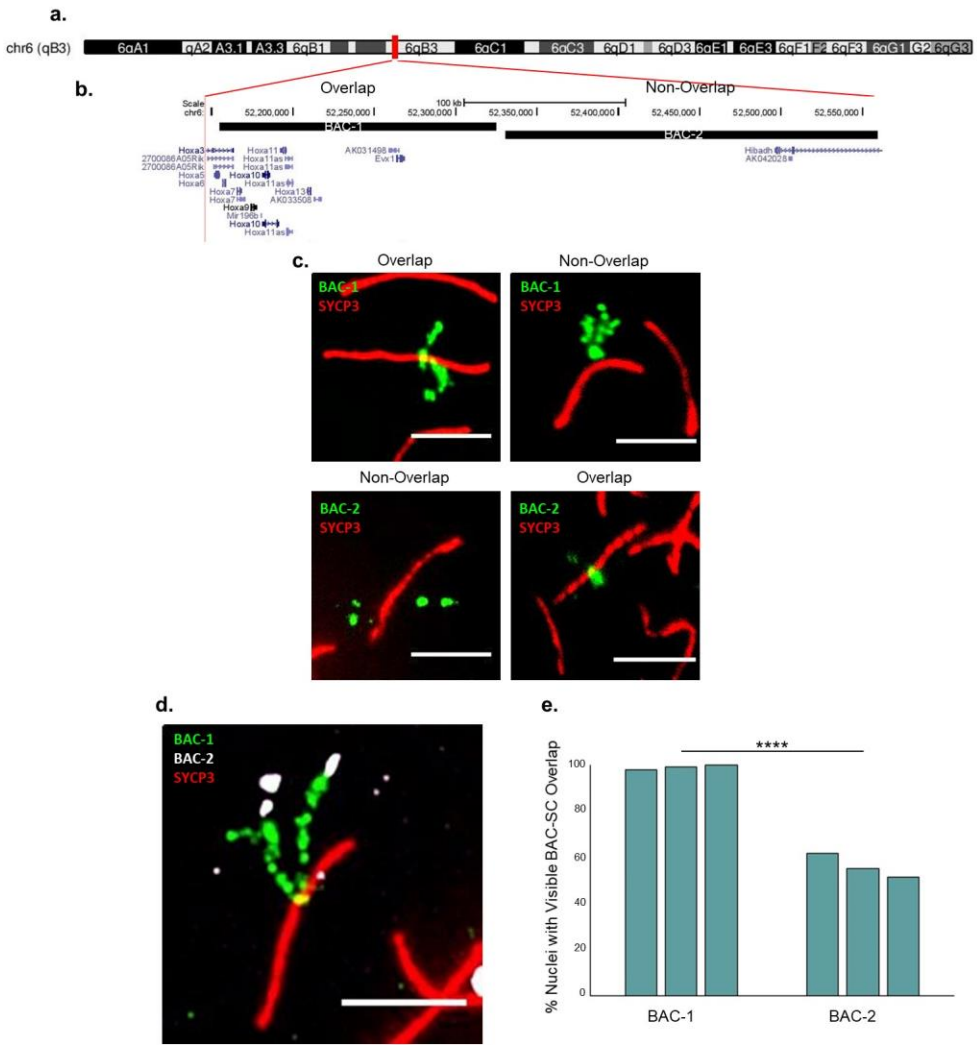

Figure 3-1. BAC FISH probe-based mapping of SC-proximal and SC-distal regions in pachytene spermatocytes. a. Chromosome 6 ideogram. Red box and lines show the location of the FISH probes. **b.** Genomic location of BAC FISH probes (mm9 assembly) with RefSeq genes. **c.** Representative images of BAC-SC overlap and non-overlap at BAC-1 and BAC-2. BAC FISH, green. Anti-SYCP3 IF, red. 5 µm scale bar. **d.** Representative image of two adjacent FISH probes, BAC-1 (green) and BAC-2 (white), extending from a single point of the SC. Anti-SYCP3 IF, red. 5 µm scale bar. **e.** The percent of pachytene spermatocyte nuclei where the BAC probe visibly overlaps with the SC (anti-SYCP3 IF). Three individual bars, individual mice. ****, $p<0.0001$ (Fisher's exact test). BAC-1 nuclei counts per mouse 110, 105, 25. BAC-2 nuclei counts per mouse 110, 87, 33.

3.2.2 Mapping a Single Autosomal Chromatin Loop

The BAC-1 region at the *HoxA* cluster, which is consistently positioned close to the pachytene SC (98% BAC-SC overlap), potentially represents one end of a chromatin loop. Therefore, I next sought to determine the length of this putative loop by performing a 'chromatin walk' experiment. The experiment exploited the BAC-SC overlap assay, described in section 3.2.1, using nine adjacent BAC probes, surrounding the previously defined SC-proximal and SC-distal regions, referred to as BAC-B (BAC-1) and BAC-C (BAC-2) respectively in Figure 3-2. A threshold of 80% was used to distinguish SC-proximal and SC-distal regions; a mean BAC-SC score >80% is indicative of a SC-proximal region and a BAC-SC score <80% is indicative of a SC-distal region. A ~1.3 Mb region of low-frequency BAC-SC overlap was identified (BAC-SC mean overlap score <80%, BAC-C to BAC-H), which appeared sandwiched between two regions of high-frequency SC overlap (BAC-SC mean overlap score >80%, BAC-A to BAC-B and BAC-I to BAC-K; Figure 3-2c). These measures indicate that a single SC-distal region can extend ~1.3 Mb, before returning to the SC and effectively closing the chromatin loop.

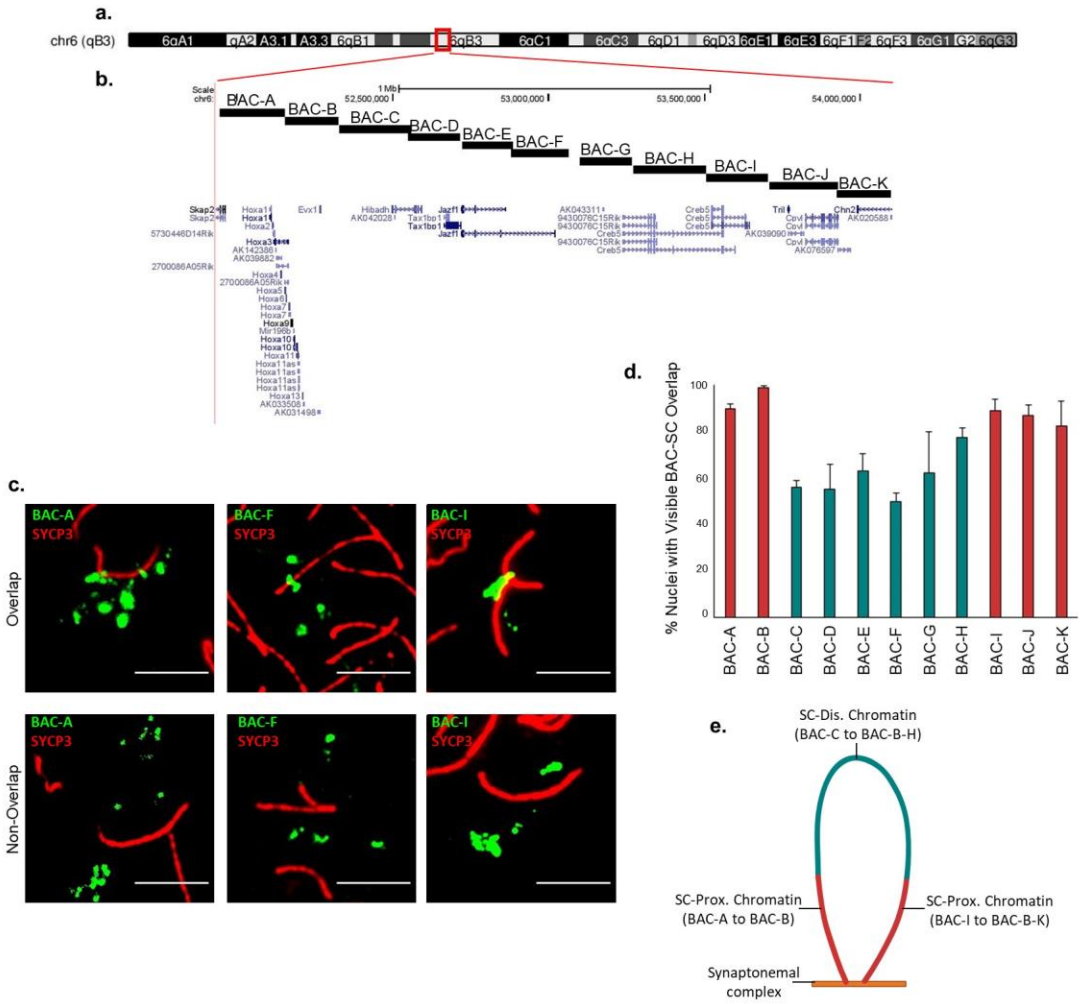

Figure 3-2. BAC FISH probe-based mapping of a single chromatin loop in pachytene spermatocytes. a. Chromosome 6 ideogram. Red box and lines show the location of the FISH probes. **b.** Genomic location of BAC FISH probes (mm9 assembly) including RefSeq genes. **c.** Representative images of BAC-SC overlap and non-overlap at BAC-A (SC-proximal), BAC-F (SC-distal) and BAC-I (SC-proximal). BAC FISH, green. Anti-SYCP3 IF, red. 5 µm scale bar. **d.** The percent of pachytene spermatocyte nuclei where the BAC probe visibly overlaps with the SC (SYCP3) signal. Blue bars, SC-distal, average <80%. Red bars, SC-proximal, average >80%. 3 mice analysed per BAC probe. Error bars, standard error. Nuclei scored: BAC-A, 79; BAC-B, 241; BAC-C, 230; BAC-D, 114; BAC-E, 147; BAC-F, 117; BAC-G, 70; BAC-H, 71; BAC-I, 107; BAC-J, 70; BAC-K, 85. ***e.*** Schematic of a single chromatid and its possible physical organisation relative to the synaptonemal complex between BAC-A and BAC-K. Blue line, SC-distal chromatin (SC-dis.). Red line, SC-proximal chromatin (SC-prox.). Orange bar, synaptonemal complex.

To enhance the resolution at which the chromatin loop was mapped, smaller fosmid FISH probes (~40 kb) were used to enable the physical distance between the SC and specific loci along the chromatin loop to be measured. Seven fosmid FISH probes (F-A to F-G, Figure 3-3b) were selected at discrete sites along the pre-defined chromatin loop (Figure 3-2), in order to generate representative measurements throughout the chromatin loop. A tether-to-fosmid assay was performed by combining a BAC probe, which acted as a proxy for the SC 'tether' point due to its high incidence of SC overlap (BAC-1, 98% BAC-SC overlap, Figure 3-1e), with one of the selected fosmid FISH probes and anti-SYCP3 IF to mark the pachytene SC. The coordinates of the SC 'tether' point at the base of the chromatin loop were firstly recorded at the site at which the BAC 'tether' probe visibly overlapped with the anti-SYCP3 IF signal. Following which, the centroid coordinates of each of the four chromatids highlighted by the fosmid probe were recorded. The mean tether-to-fosmid distance was then calculated per nucleus. The distance from the SC tether point increased from probe F-A (0.93 ± 0.09 µm) to F-C (2.81 ± 0.15 µm) and declined between F-C and F-F (1.31 ± 0.09 µm), before extending away from the SC again at F-F to F-G (2.98 ± 0.18 µm). These data thus refine the loop topology predicted in Figure 3-2, while demonstrating that a single chromatin loop can extend at least ~3 µm from the pachytene SC in surface-spread spermatocytes.

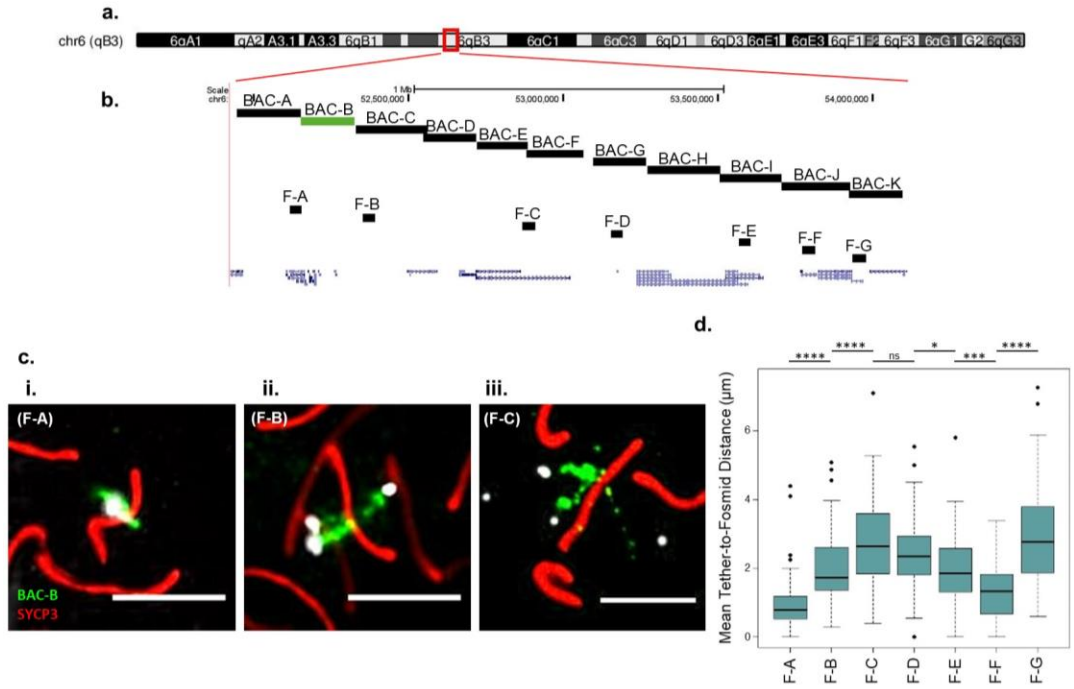

Figure 3-3. Fosmid FISH probe-based mapping of a single chromatin loop in pachytene spermatocytes. a. Chromosome 6 ideogram. The red box and lines show the location of the FISH probes. **b.** Genomic location of BAC and fosmid FISH probes (mm9 assembly) with RefSeq genes. 'Tether' BAC probe (BAC-B), green. **c.** Representative images of chromatid separation from the SC for **i)** F-A (SC-proximal), **ii)** F-B (intermediate) and **iii)** F-C (SC-distal). 'Tether' BAC probe (BAC-B), green. Fosmid, white. Anti-SYCP3 IF, red. 5 µm scale bar. **d.** Boxplots of the mean tether-to-fosmid distance (µm) per nucleus. 3 mice analysed per fosmid. Nuclei scored: F-A, 73; F-B, 93; F-C, 72; F-D, 50; F-E, 61; F-F, 75; F-G, 69. ****, $p<0.0001$; ***, $p<0.001$; *, $p<0.05$; ns, $p>0.05$ (Mann Whitney U test).

3.2.3 Examining Chromatid Organisation within a Chromatin Loop

Subsequently to defining a chromatin loop, the organisation of the four chromatids relative to SC were determined to establish whether homologous and sister chromatids attach to the pachytene SC at the same genomic regions. To assess the relative organisation of the four chromatids and the SC, IF-FISH was performed using fosmid FISH probes to distinguish individual chromatids. Following imaging of the processed spermatocytes, the centroid coordinates of each of the four chromatids was recorded and the mean of the six inter-chromatid distances per nucleus was calculated. This was conducted using seven fosmid FISH probes (F-A to F-G; Figure 3-4b) distributed along the length of the pre-defined chromatin loop (Figure 3-2). This enabled the relationship between distance from the SC and the extent of chromatid separation to be examined (Figure 3-4d). The extent of chromatid separation followed a strikingly comparable trend to the tether-to-fosmid distances (Figure 3-3), as the inter-chromatid distance increased from probe F-A (0.97 ± 0.09 µm) to F-C (3.06 ± 0.20 µm) and subsequently declined between F-C and F-F (1.27 ± 0.13 µm), before increasing again from F-F to F-G (3.40 ± 0.23 µm). At all seven loci examined, the inter-chromatid distance exhibits a strong, positive relationship with distance from the SC (average linear regression ~0.6, Figure 3-4e). Taken together, these findings demonstrate that the four chromatids tend to cluster in proximity to the SC at a common genetic region and then physically separate as they extend away from it.

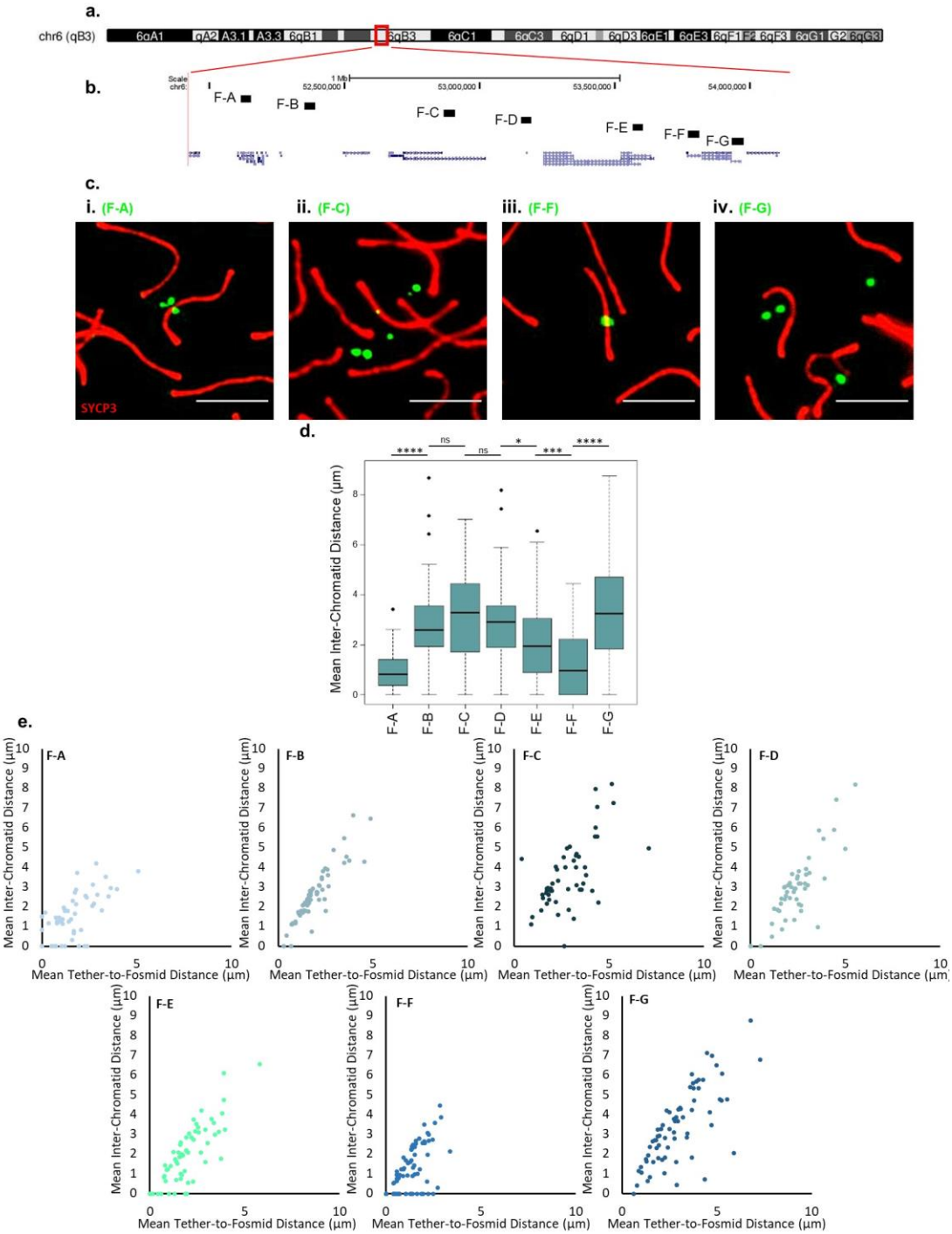
a.
chr6 (qB3)
b.
F-A
F-B
F-C
F-D
F-E
F-F
F-G
c.
i. (F-A)
ii. (F-C)
iii. (F-F)
iv. (F-G)
SYCP3
d.
Mean Inter-Chromatid Distance (µm)
ns
****
*
***
e.
Mean Tether-to-Fosmid Distance (µm)

Figure 3-4. Inter-chromatid distances along a single chromatin loop in pachytene spermatocytes. a. Chromosome 6 ideogram, the red box and lines show the location of the FISH probes. **b.** Genomic location of fosmid FISH probes including RefSeq genes (mm9 assembly). **c.** Representative images of inter-chromatid distance and chromatid separation from the SC for **i)** F-A (SC-proximal), **ii)** F-C (SC-distal), **iii)** F-F (SC-proximal) and **iv)** F-G (SC-distal). Fosmid, green. Anti-SYCP3 IF, red. 5 µm scale bar. **d.** Boxplots of the mean inter-chromatid distance per nucleus for fosmids F-A to F-G. 3 mice analysed per fosmid. ****, $p<0.0001$; ***, $p<0.001$, *, $p<0.05$; ns, $p>0.05$ (Mann Whitney U test). **e.** Scatterplots of mean tether-to-fosmid distance (µm) per nucleus against mean inter-chromatid distance (µm) for fosmids F-A to F-G. All show strong positive correlations (F-A, 0.62; F-B, 0.64; F- C, 0.61; F-D, 0.56; F-E, 0.61; F-F, 0.40; F-G, 0.58; $p<0.0001$, Linear regression model). Nuclei scored: F-A, 74; F-B, 73; F-C, 74; F-D, 50; F-E, 61; F-F, 75; F-G, 69.

Sister chromatids are often described as being tightly conjoined (eg. Kleckner, 2006), therefore the prevalence of sister chromatid pairing in pachytene spermatocytes was next examined. Homologous and sister chromatids are of identical genetic composition in the C57BL/6 mice used, meaning homologous and sister chromatids could not be distinguished from one another by the sequence-specific fosmid FISH probes. To overcome this limitation, a presumption was made that if sister chromatid pairing occurred within a nucleus, two of the inter-chromatid distances would be significantly less than the remaining four inter-chromatid distances. To test this hypothesis, the centroid coordinates of the four chromatids were recorded and the corresponding six inter-chromatid distances were calculated. The inter-chromatid distances belonging to each of the two potential chromatids pairs were then determined, by firstly identifying the shortest inter-chromatid distance and presuming that this value was representative of the first ‘pair’ of chromatids. The inter-chromatid distance, corresponding to the second ‘pair’, was subsequently established by identifying the inter-chromatid distance belonging to the two chromatids which were not involved in the first pair. The remaining four inter-chromatid distances were then presumed to be the inter-pair distances (Figure 3-5c). The two presumptive ‘pair’ distances (S1 and S2) and the presumptive four ‘inter-pair’ distances (H1-H4) were then ranked and the nuclear averages per rank were plotted. These plots were compared to simulations generated from when i) six random inter-chromatid values were sampled from a normal distribution similar to that of experimental inter-chromatid data, to model the null hypothesis that no chromatid pairing occurs and ii) four

presumptive ‘inter-pair’ distances were generated, from the same normal distribution, which were 4x, 2x and 1.5x the length of the two ‘pair’ distances, to model the alternate hypothesis that chromatid pairing occurs. The six inter-chromatid values generated from each simulated nucleus were then ranked 1 to 6 and the mean of 50 simulated nuclei per rank was plotted (Figure 3-5a). In the simulations of the alternate hypothesis a ‘step’ is evident between the two shortest distances and the remaining four longer distances, which becomes greater in size as the extent of pairing becomes more extreme (Figure 3-5ai to iii). However, simulations of the null hypothesis (Figure 3-5aiv) represent a single population as the gradient between the six inter-chromatid values is similar throughout the data. None of the experimentally generated inter-chromatid distances, at the seven loci examined, corresponded to the ‘step’ model, simulated by the alternate hypothesis, in which the two inter-sister chromatid distances are considerably shorter than the four remaining inter-homolog distances (Figure 3-5b). Taken together, these data suggest that on surface-spread spermatocytes chromatids do not tend to pair with one another during pachytene.

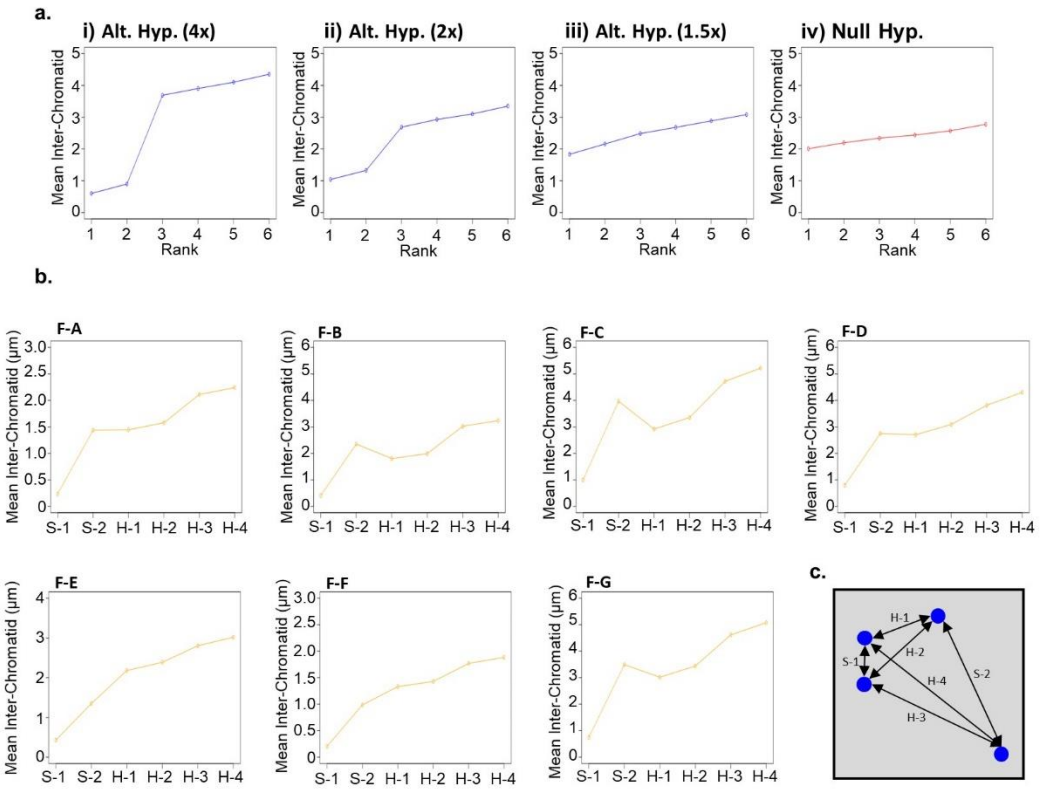

Figure 3-5. Chromatid pairing along a single chromatin loop in pachytene spermatocytes. a. Simulations of the alternate hypothesis where inter-pair distances are **i)** 4x, **ii)** 2x, **iii)** 1.5x the two paired inter-chromatid distance and **iv)** the null hypothesis that all chromatid distances (paired and inter-pair) are the same and no pairing is evident. **b.** Assessing chromatid pairing at fosmids F-A to F-G. The mean of each of the two presumptive paired inter-chromatid distances (S-1 to S-2) and the four inter-pair distances (H-1 to H-4) were ranked in each nucleus, the mean inter-chromatid distance is shown for each rank. Nuclei scored: F-A, 74; F-B, 73; F-C, 74; F-D, 50; F-E, 61; F-F, 75; F-G, 69. **c.** Example schematic of the organisation of the four chromatids, highlighted by fosmid FISH probes (blue dots) ranked according to the two inter-chromatid distances at each presumptive pair (S-1 to S-2) and the four inter-pair inter-chromatid distances (H-1 to H-2).

3.2.4 Comparing Recombination and IF-FISH Maps

After mapping SC-proximal and SC-distal regions across a ~2.2 Mb region, in Section 3.2.2, the relationship between SC proximity and recombinogenic activity was examined by comparing the IF-FISH chromatin maps to a SPO11-oligo map (Lange *et al*., 2016) and a DMC1 ssDNA sequencing (SSDS) map (Brick *et al*., 2012; Figure 3-6). In accordance with the tethered loop-axis complex (TLAC) model, both SPO11-oligo peaks and DMC1 SSDS peaks were enriched in the SC-distal, loop region, defined by a relatively low frequency of visible BAC-SC overlap.

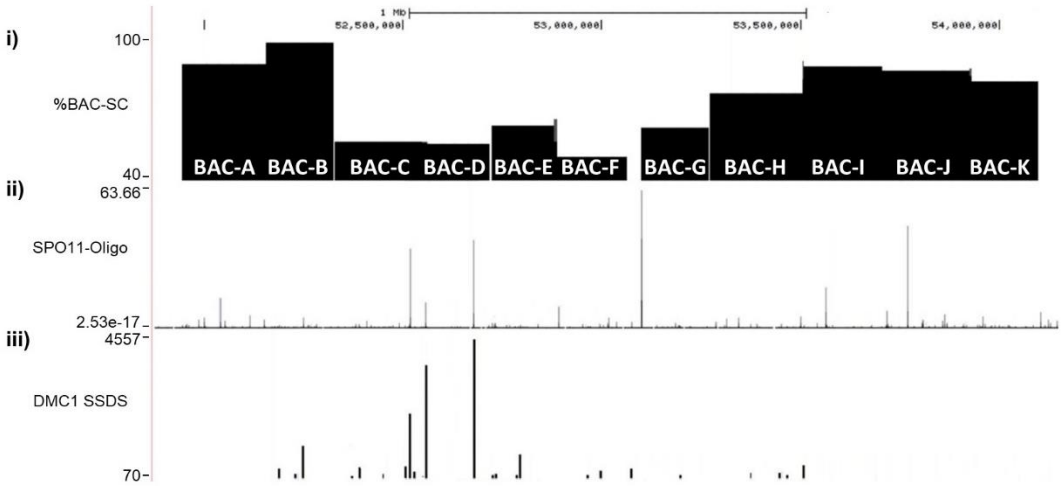

Figure 3-6. Comparing IF-FISH map to DSB hotspot maps. Browser tracks (mm9 assembly) depict: **i)** The percent of pachytene spermatocyte nuclei where the BAC probe visibly overlaps with the SC (anti-SYCP3 IF), as presented in Figure 3-2. **ii)**. SPO11-Oligo map (C57BL/6 wildtype; Lange *et al*., 2016 - GSE84689). **iii)** DMC1 SSDS (ssDNA sequencing; C57BL/6 wildtype; Brick *et al*., 2012 - GSE35498).

3.2.5 Extending the Autosomal Chromatin Loop Map

In order to ascertain more about the context in which the previously defined chromatin loop (Section 3.2.2) is present, the BAC-SC overlap map was extended to survey chromatin-SC proximity 2.5 Mb either side of the loop at ~500 kb intervals (Figure 3-7b). Blocks of both SC-proximal (>80% BAC-SC overlap) and SC-distal (<80% BAC-SC overlap) regions were identified in the flanking regions (Figure 3-7c). Notably, the length of each of the SC-proximal and SC-distal regions reported did not appear to be consistent. Thus, indicating that the originally mapped chromatin loop is not a unit of a uniform, sequential loop array which may be defined through this cytological approach.

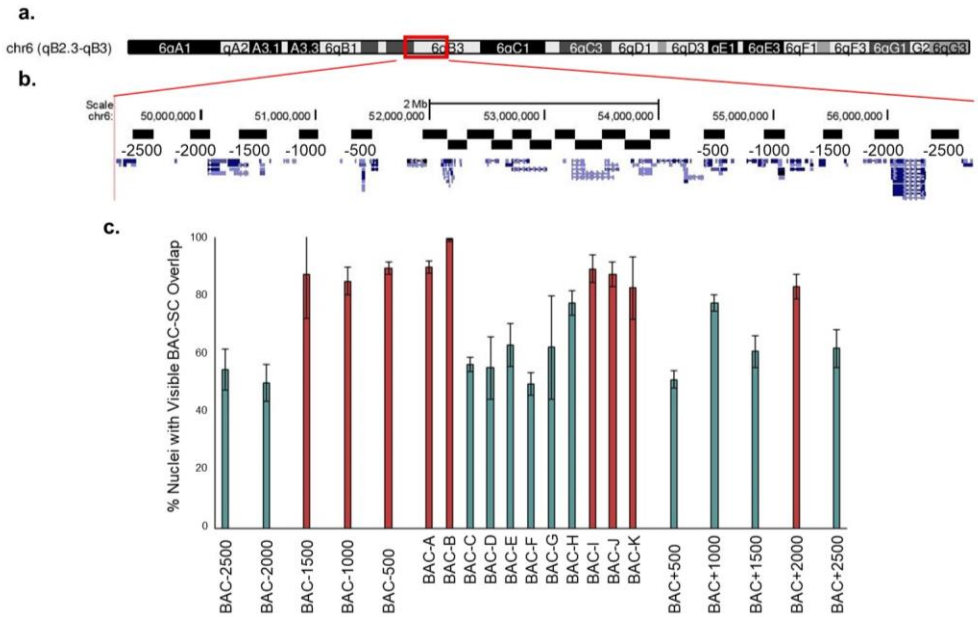

Figure 3-7. BAC FISH probe-based mapping of 2.5 kb flanking regions either side of the mapped chromatin loop in pachytene spermatocytes. a. Chromosome 6 ideogram with the red box and lines indicating the location of the FISH probes. **b.** Genomic location of BAC FISH probes (mm9 assembly) with RefSeq genes. **c.** Percent of pachytene spermatocyte nuclei where the BAC probe visibly overlaps with the SC (anti-SYCP3 IF). Blue bars, SC-distal, average <80%. Red bars, SC-proximal, average >80%. 3 mice analysed per BAC. Error bars, standard error. Nuclei scored: BAC-2500, 87; BAC-2000, 72; BAC-1500, 77; BAC-1000, 73; BAC-500, 84; BAC+500, 83; BAC+1000, 76; BAC+1500, 84; BAC+2000, 83; BAC+2500, 85.

3.2.6 Investigating the Role of SMC1β and SMC1α on Whole Chromosome Organisation

The core cohesin complex is composed of a SMC1-SMC3 heterodimer. In mammalian meiocytes two SMC1 variants, SMC1β and SMC1α, are present (Revenkova, Eijpe, Heyting, and Gross, 2001). A relatively new study revealed that the two SMC1 variants exhibit partial redundancy in their ability to manipulate chromosome morphology. Intriguingly, *Smc1β*-/- mice exhibit a 2-fold decline in SC length, which undergoes a partial rescue on the artificial up-regulation of *Smc1α* under the control of the *Smc1β* promoter, in *Smc1β-/-,1α* mice (Biswas, Stevense and Jessberger, 2018; Novak *et al*., 2008; Revenkova *et al*., 2004). Therefore, both SMC1β and SMC1α can determine the length of meiotic chromosome axes. Moreover, SMC1β has been directly shown to manipulate the morphology of chromatin emanating from the SC (Novak *et al*., 2008; Revenkova *et al*., 2004). I chose to exploit the known modulatory effects of SMC1β and SMC1α on meiotic chromosome organisation, to validate the autosomal chromatin loop previously defined on chromosome 6 and further explore the role of cohesin on a chromatin loop level.

Considering the impact of SMC1β and SMC1α on axis length, the total area of a chromosome territory (chromosome 6) was compared between *Smc1β+/+*, *Smc1β-/-* and *Smc1β-/-,1α* pachytene spermatocytes, to assess their influence on the extent to which chromatin extends away from the SC on a gross chromosomal level (Figure 3-8). Chromosome 6 was selected for analysis, since the previously defined chromatin loop (Section 3.2.2) resides on the chromosome, enabling the behaviour of the bulk chromosome and individual chromatin loop to be compared in the *Smc1* mutants. A chromosome 6 FISH paint was combined with anti-SYCP3 IF staining, to sub-stage the spermatocytes and measure chromosome SC length (Figure 3-8a). Loss of SMC1β resulted in a ~2-fold reduction in the SC length of chromosome 6 (3.61 µm) and a corresponding 2.4-fold increase in chromosome territory area (121.96 μm^2), relative to in *Smc1β+/+* spermatocytes (7.79 µm and 51.27 μm^2; Figure 3-8b and c). Thus, proving consistent with previously published findings (Revenkova *et al*., 2004). Moreover, in agreement with observations made by Biswas *et al*., increased expression of *Smc1α* led to the partial rescue of chromosome 6 SC length in *Smc1β-/-* spermatocytes (5.88 µm; Biswas, Stevense and Jessberger, 2018). In addition, I found that increased expression of *Smc1α*, in *Smc1β-/-,1α* spermatocytes, resulted in a corresponding partial rescue in chromosome 6 territory area to 109.06

μm^2 (Figure 3-8b). Taken together, these findings indicate that SMC1β and SMC1α work with a degree of redundancy to manipulate the gross morphology of the SC and chromatin extensions on chromosome 6.

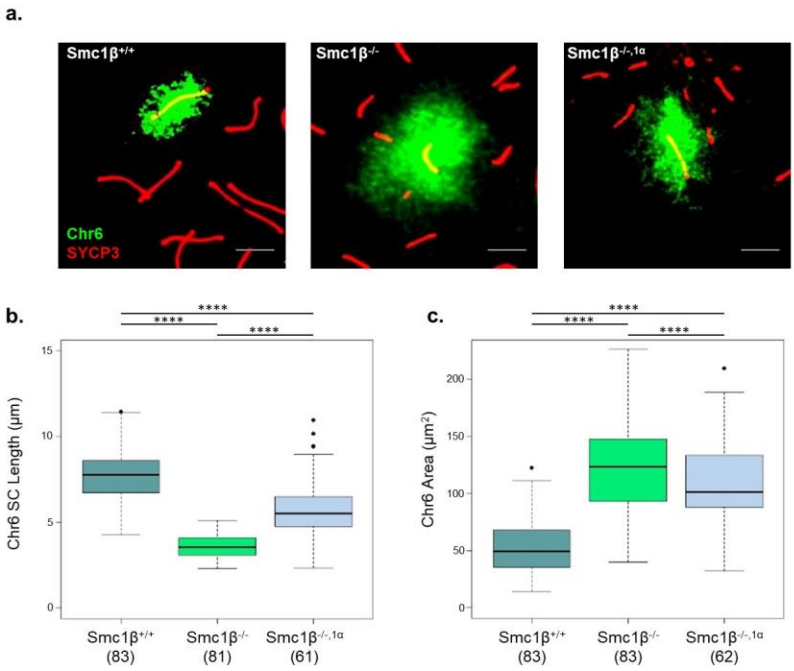

Figure 3-8. Analysis of chromosome 6 SC length and chromatin area in *Smc1* mutant pachytene spermatocytes. a. Representative images of chromosome 6 SC length (anti-SYCP3 IF, red) and chromatin area (Chr6 paint, green) in the three genotypes, *Smc1β+/+, Smc1β-/-* and *Smc1β-/-,1α*. 5 μm scale bar. **b.** Boxplots of chromosome 6 SC length (μm) in Smc1β+/+, Smc1β-/- and *Smc1β-/-,1α*. **c.** Boxplots of chromosome 6 paint territory area (μm^2) in *Smc1β+/+, Smc1β-/-* and *Smc1β-/-,1α*. 3 mice analysed per genotype. Bracketed values, number of nuclei scored. ****, p<0.0001 (Mann Whitney U test).

3.2.7 Chromatin Loop Organisation in *Smc1β-/-* and *Smc1β-/-,1α* Spermatocytes

SMC1-dependent changes in chromosomal area imply that SMC1β and SMC1α influence the organisation of individual chromatin loops. I conducted the previously described BAC-SC overlap assay (Section 3.2.2) to ascertain how the SMC1 variants effect the positioning of SC-proximal and SC-distal chromatin, defined in wildtype cells. Two BAC probes were selected for analysis, the first representative of a SC-proximal region (BAC-B, Figure 3-2) and the second representative of a SC-distal region (BAC-D, Figure 3-2), in wildtype spermatocytes. In all three SMC1 genotypes assessed (*Smc1β+/+, Smc1β-/-* and *Smc1β-/-,1α*), the SC-distal region was significantly less likely to overlap with the pachytene SC than the SC-proximal region ($p<0.0001$, Fisher's exact test; Figure 3-9). Indicating that the positioning of the SC-proximal and SC-distal chromatin regions, relative to the SC, was conserved in the absence of SMC1β and on increased expression of SMC1α, in *Smc1β-/-* spermatocytes.

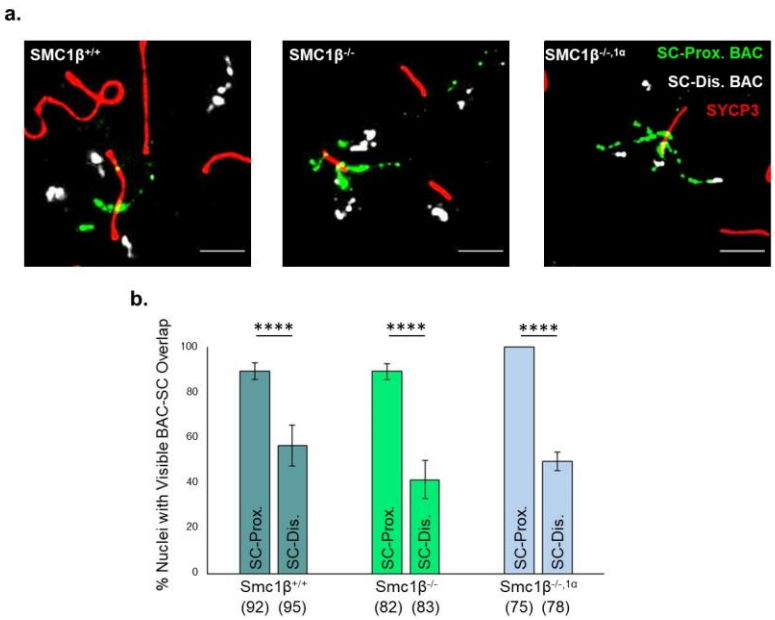

Figure 3-9. BAC FISH probe-based mapping of SC-proximal and SC-distal regions in *Smc1* mutant pachytene spermatocytes. a. Representative images of the visible BAC-SC overlap of a SC-proximal BAC probe (SC-Prox., green) and a SC-distal BAC probe (SC-Dis., white), originally defined in wildtype mice, in the three genotypes *Smc1β+/+, Smc1β-/-* and *Smc1β-/-,1α*. Anti-SYCP3 IF, red. 5 µm scale bar. **b.** Bar chart of the percent of pachytene spermatocyte nuclei where each BAC probe, SC-Proximal and SC-distal, visibly overlaps with the SC (SYCP3) signal in *Smc1β+/+, Smc1β-/-* and *Smc1β-/-,1α*. 3 mice analysed per genotype and per probe. Error bars, standard error. Bracketed values, number of nuclei scored. ****, p<0.0001 (Fisher's exact test).

In order to assess how the distance of specific chromatin regions differs according to the loss SMC1β and up-regulation of *Smc1α*, the tether-to-fosmid assay, previously described in Section 3.2.2**,** was performed on *Smc1β+/+, Smc1β-/-* and *Smc1β-/-,1α* spermatocytes (Figure 3-10). Three fosmids were selected for analysis, to represent consecutive SC-proximal (F-A), SC-distal (F-C) and SC-proximal (F-F) regions along a single chromatin loop (Figure 3-3). On deletion of *Smc1β*, all three loci experienced an ~2-fold increase in distance from the SC, relative to in *Smc1β+/+* spermatocytes, coincidently with a reduction in inter-locus variation (F-A, 3.01 ± 0.19 µm to 6.08 ± 0.89 µm; F-C, 3.85 ±0.21 µm to 6.17 ± 2.29 µm; F-F, 2.03 ± 0.11 µm to 4.85 ± 0.33 µm; Figure 3-10). Each locus exhibited a distinct response following the up-regulation of *Smc1α* in *Smc1β-/-* spermatocytes; at the first SC-proximal fosmid (F-A) chromatin experienced complete rescue back to the *Smc1β+/+* tether-to-fosmid distance (3.58 ± 0.40 µm), while the second SC-proximal fosmid (F-F) underwent a partial rescue (3.60 ± 0.120 µm) and the SC-distal fosmid (F-C) experienced no significant change from the *Smc1β-/-* mice (5.76± 0.0.43 µm). Together, these data indicate that loss of SMC1β causes SC-proximal and SC-distal regions to increase from ~3 to 5-6 µm from the SC. Yet, SMC1α does not have a comparable effect on all SC-proximal and SC-distal loci.

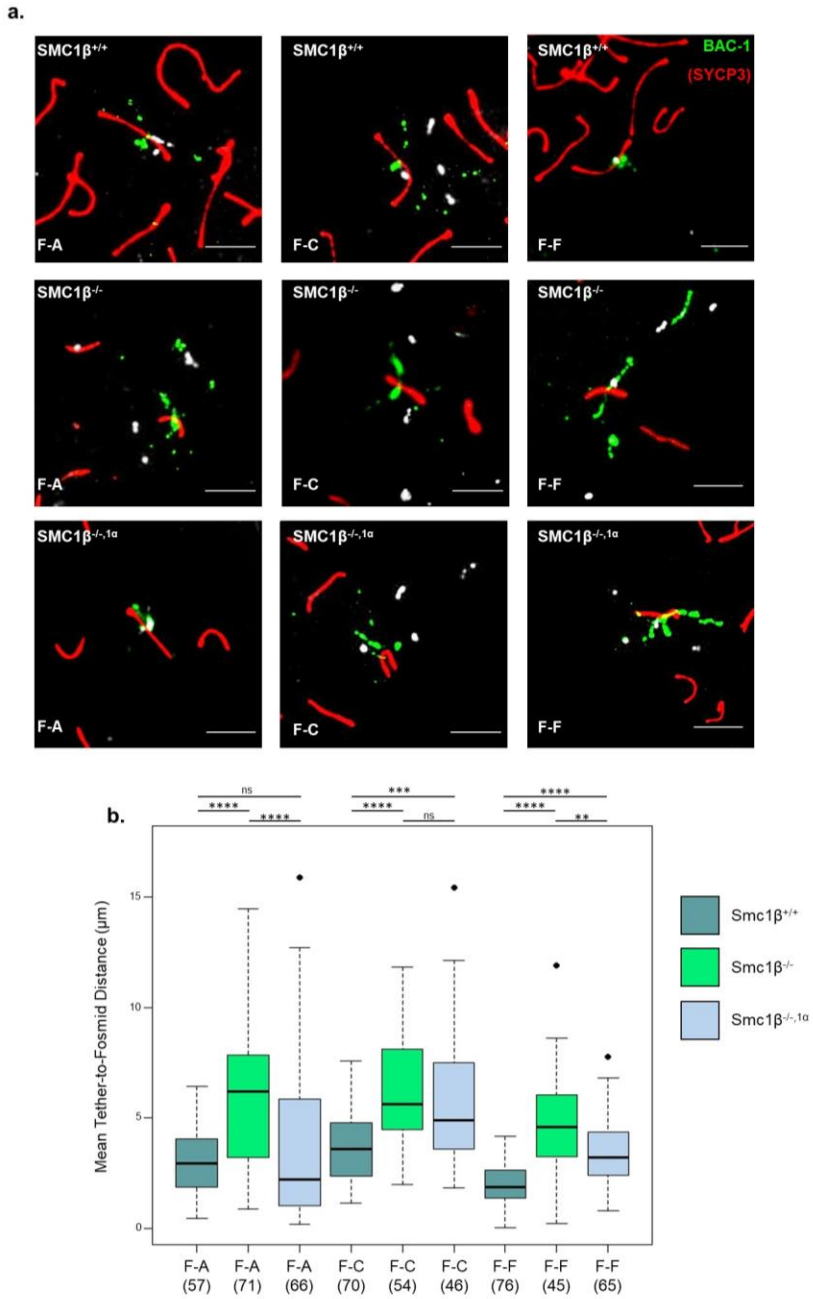

Figure 3-10. Fosmid FISH probe-based mapping of a single chromatin loop in *Smc1* mutant pachytene spermatocytes. a. Representative images of chromatid separation from the SC for F-A (SC-proximal), F-C (SC-distal) and F-F (SC-proximal) in the three genotypes *Smc1β+/+, Smc1β-/-* and *Smc1β-/-,1α*. 'Tether' BAC probe (BAC-1/BAC-B), green. Fosmid, white. Anti-SYCP3 IF, red. 5 µm scale bar. **b.** Boxplots of the mean tether-to-fosmid distance per nucleus (µm) for fosmids F-A, F-C and F-F in *Smc1β+/+, Smc1β-/-* and *Smc1β-/-,1α*. 3 mice analysed per genotype and per probe. Bracketed values, number of nuclei scored. ****, p<0.0001; ***, p<0.001; **, p<0.01; ns, p>0.05 (Mann Whitney U test).

3.2.8 Inter-Chromatid Organisation in *Smc1β-/-* and *Smc1β-/-,1α* Spermatocytes

In wildtype spermatocytes, a strong, positive correlation was observed between distance from the SC and inter-chromatid distance (Figure 3-4). Based on the impact of SMC1β and SCM1α on chromatin organisation, relative to the SC, the inter-chromatid distance was measured in response to *Smc1β-/-* and *Smc1β-/-,1α*, relative to *Smc1β+/+*, at the same loci as in Section 3.2.7. The mean inter-chromatid distance was measured by recording the XY coordinates of each of the four foci, generated by a single fosmid and calculating the mean of the six inter-foci distances. Inter-chromatid distance was seen to increase at all three loci by ~2-fold in the absence of SMC1β, with a reduction in inter-chromatid variation (Figure 3-11), relative to *Smc1β+/+* spermatocytes (F-A, 3.14 ± 0.26 µm to 8.37 ± 0.55 µm; F-C, 4.88 ± 0.32 µm to 7.44 ± 0.46 µm; F-F, 2.32 ± 0.18 µm to 6.79 ± 0.49 µm). This observation demonstrates that SMC1β reduces inter-chromatid distances throughout a chromatin loop by ~2-fold. In *Smc1β-/-,1α* spermatocytes, a partial rescue in inter-chromatid was observed at all three loci (F-A, 5.12 ± 0.26 µm; F-C, 6.29 ± 0.66 µm; F-F, 4.30 ± 0.27 µm). Thus, SMC1α can partially substitute SMC1β in the spatial manipulation of individual chromatids. However, their role in this respect are not fully overlapping, since a complete rescue was not observed.

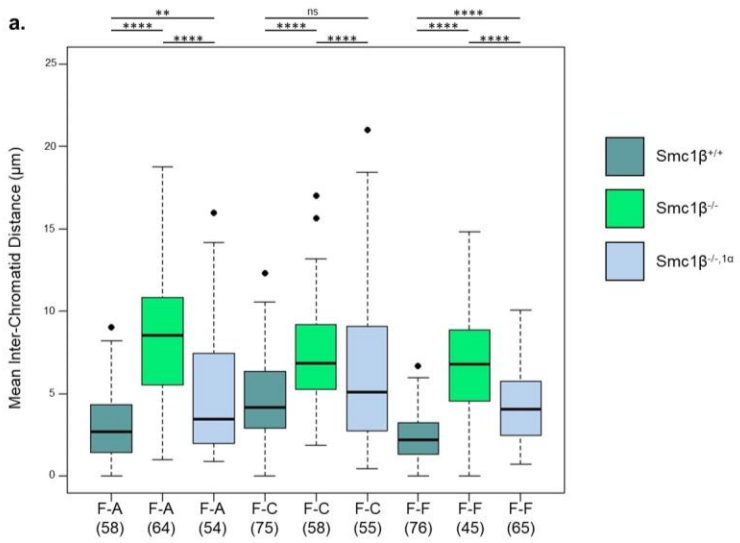

Figure 3-11. Inter-chromatid distance along a single chromatin loop in *Smc1* mutant pachytene spermatocytes. a. Boxplots of the nuclear mean inter-chromatid distance (µm) for fosmids F-A, F-C and F-F in *Smc1β+/+, Smc1β-/-* and *Smc1β-/-,1α*. 3 mice analysed per genotype and per probe. Bracketed values, number of nuclei scored. ****, p<0.0001; ***, p<0.001; **, p<0.01; ns, p>0.05 (Mann Whitney U test).

Next, inter-sister chromatid distance in pachytene spermatocytes was compared between *Smc1β+/+, Smc1β-/-* and *Smc1β-/-,1α* mice. FISH cannot distinguish between autosomal sister chromatids and homologous chromatids in inbred C57BL/6 mice. Therefore inter-sister chromatid organisation was assessed by using two fosmid FISH probes, A and B, positioned ~500 kb apart on the non-homologous region of the X chromosome (Figure 3-12). Inter-sister chromatid distance was measured by taking the (X,Y) coordinates of the centroid of the two foci produced by each of the fosmids and calculating the inter-centroid distance. Similarly to the autosomal loci, *Smc1β*-deletion elevated inter-sister chromatid distance by over 2.5-3-fold (A, 1.64 ± 0.21 µm to 4.93 ± 0.54 µm; B, 1.63 ± 0.61 µm to 4.02 ± 0.39 µm; Figure 3-12). On increased expression of *Smc1α* in *Smc1β-/-* spermatocytes inter-sister chromatid distance underwent a partial rescue at both loci (A, 3.30 ± 0.93 µm; B, 2.38 ± 0.29 µm). In summary, these data demonstrate that both SMC1α and SMC1β are responsible for promoting inter-sister chromatid proximity on the non-homologous X chromosome, presumably through their ability to mediate chromatid cohesion.

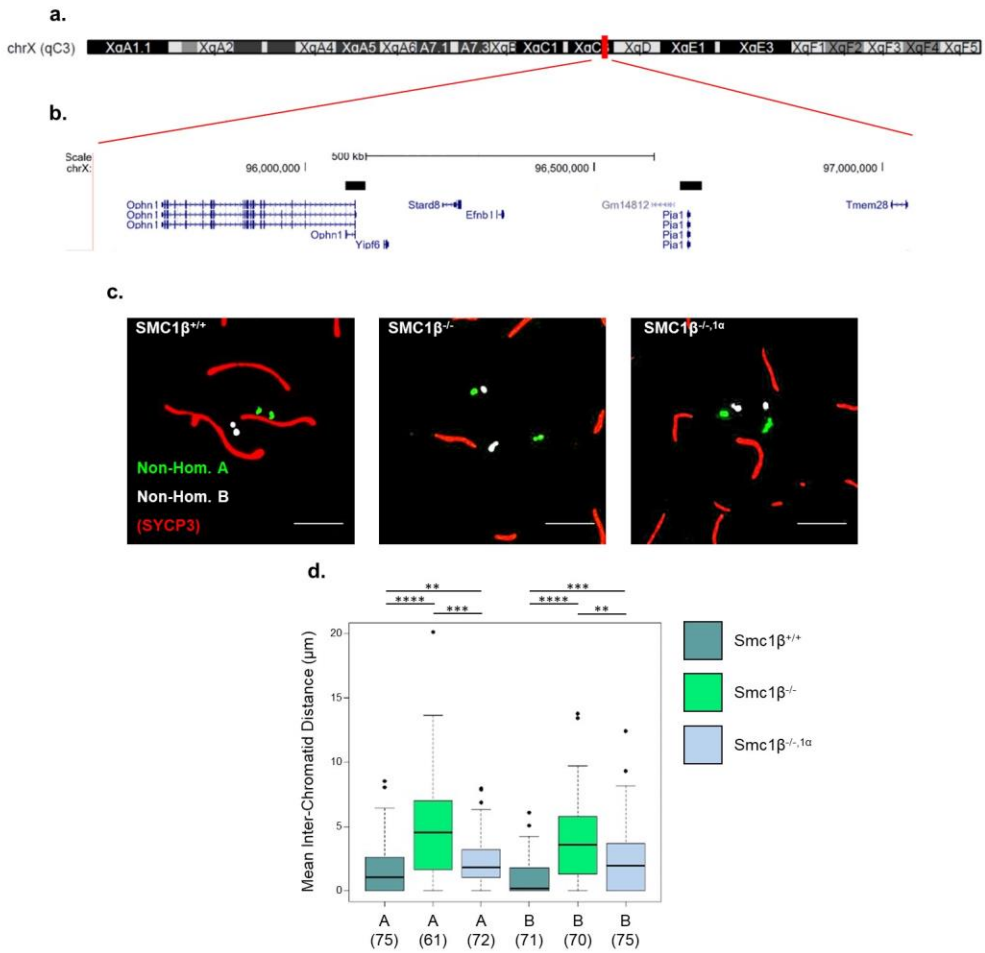

Figure 3-12. Inter-sister chromatid distance on the non-homologous X chromosome in *Smc1* mutant pachytene spermatocytes. a. Chromosome X ideogram. The red box and lines show the location of the FISH probes. **b.** Schematic of the genomic location of fosmid FISH probes including RefSeq genes (mm9 assembly). **c.** Representative images of inter-sister chromatid distance for two fosmids, A (green) and B (white), on the non-homologous X chromosomes in the three genotypes *Smc1β+/+, Smc1β-/-* and *Smc1β-/-,1α*. Anti-SYCP3 IF, red. 5 µm scale bar. **d.** Boxplots of the nuclear mean inter-chromatid distance (µm) for fosmids A and B in *Smc1β+/+, Smc1β-/-* and *Smc1β-/-,1α*. 3 mice analysed per genotype and per probe. Bracketed values, number of nuclei scored. ****, p<0.0001; ***, p<0.001; **, p<0.01 (Mann Whitney U test).

3.2.9 Chromatin Condensation in *Smc1β-/-* and *Smc1β-/-,1α* Spermatocytes

Once changes in large-scale organisation had been verified at chromosome-wide and individual loop level in *Smc1β-/-* and *Smc1β-/-,1α* spermatocytes (Sections 3.2.6 and 3.2.7), the local impact on chromatin condensation, which I define as the compaction and/or clustering of chromatin fibres, was next assessed on a local level. To examine how SMC1β and SMC1α manipulates chromatin condensation, the area of a SC-proximal BAC probe (BAC-B; 169 kb) and a SC-distal BAC probe (BAC-D; 167 kb) was measured; a larger BAC probe area is indicative of chromatin decompaction and/or less chromatid clustering, while a smaller BAC probe area is indicative of more chromatin compaction and/or more chromatid clustering (Figure 3-13). The area of the SC-distal BAC probe did not significantly change, relative to *Smc1β+/+* spermatocytes (3.20 ± 0.16 μm^2), in *Smc1β-/-* (3.57 ± 0.22 μm^2), or *Smc1β-/-,1α* mice (3.13 ± 0.20 µm2). However, the BAC probe area of the SC-proximal region increased in the absence of SMC1β, in both *Smc1β-/-* (4.03 ± 0.21 μm^2) and *Smc1β-/-,1α* (3.93 ± 0.20 μm^2) spermatocytes, compared to *Smc1β+/+* spermatocytes (2.38 ± 0.13 μm^2). This suggests that neither SMC1 variant influences chromatin condensation of SC-distal chromatin, whereas SMC1β can promote condensation of SC-proximal chromatin, through a rise in chromatin compaction and/or clustering of individual chromatids, which is not rescued through the up-regulation of *Smc1α* expression.

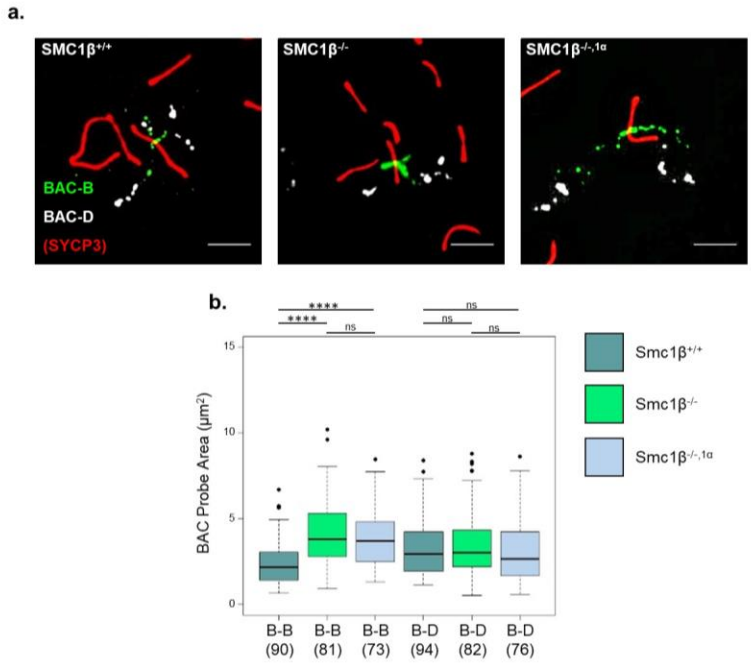

Figure 3-13. Chromatin condensation in *Smc1* mutant pachytene spermatocytes. a. Representative images of the SC-proximal BAC-B probe (B-B, green) and a SC-distal BAC-D probe (B-D, white), originally defined in wildtype mice, in the three genotypes *Smc1β+/+, Smc1β-/-* and *Smc1β-/-,1α*. Anti-SYCP3 IF, red. 5 µm scale bar. **b.** Boxplots of the area (µm^2) of a SC-proximal BAC probe (BAC-B) and a SC-distal BAC probe (BAC-D) in *Smc1β+/+, Smc1β-/-* and *Smc1β-/-,1α*. 3 mice analysed per genotype and per probe. Bracketed values, number of nuclei scored. ****, p<0.0001 (Mann Whitney U test).

3.2.10 Comparing HiC and IF-FISH Maps

During the course of my PhD, HiC studies of meiotic chromatin organisation in mouse spermatocytes were published that encompass the *HoxA* chromatin loop, which I defined by IF-FISH. HiC provides a genome-wide map of contact frequencies, which infer spatial proximity between loci, by assuming that contact frequency is inversely proportional to the spatial proximity of the loci in a native state. One may therefore expect the chromatin loop, defined through IF-FISH, to appear as a loop-like structure in a HiC heatmap, where the two loci at the base of the loop exhibit an elevated contact frequency positioned in parallel to the diagonal. Within the IF-FISH defined chromatin loop region, the HiC heatmaps generated from four independent investigations varied (Figure 3-14a). In two HiC studies, faint TAD-like structures coincide with the IF-FISH defined loop, where a square block of elevated contact frequencies centres along the diagonal of the region of interest (Figure 3-14 ai and iii). While a subtle loop-like contact point was apparent at the base of the IF-FISH-defined loop in the third and fourth studies (Figure 3-14 aii and iv). Comparisons between IF-FISH and HiC data indicate that, although HiC heatmaps subtly conform to IF-FISH-based loop mapping, the contact frequencies generated through HiC are not nearly as striking as I would expect from the highly consistent chromatin loop map generated through IF-FISH.

The pachytene IF-FISH chromatin loop map was also compared with a published HiC heatmap generated in mouse embryonic stem cells (Bonev *et al*., 2017), to determine how large-scale chromatin organisation corresponds between pachytene spermatocytes and interphase cells (Figure 3-14b). Intriguingly, the IF-FISH-mapped chromatin loop appears to co-localise with a TAD-like interphase structure, composed of at least two smaller, nested TADs. Although such large-scale chromatin structures are not identical, the interphase HiC heatmaps appear more comparable to the IF-FISH pachytene loop, than the pachytene HiC heatmaps. This suggests that at the region examined, specific chromatin interaction points are preserved between somatic and pachytene cells. In this instance, it is possible that the boundary between the two TADs confined within the pachytene loop is lost, while the outer boundaries are preserved to create a single pachytene loop.

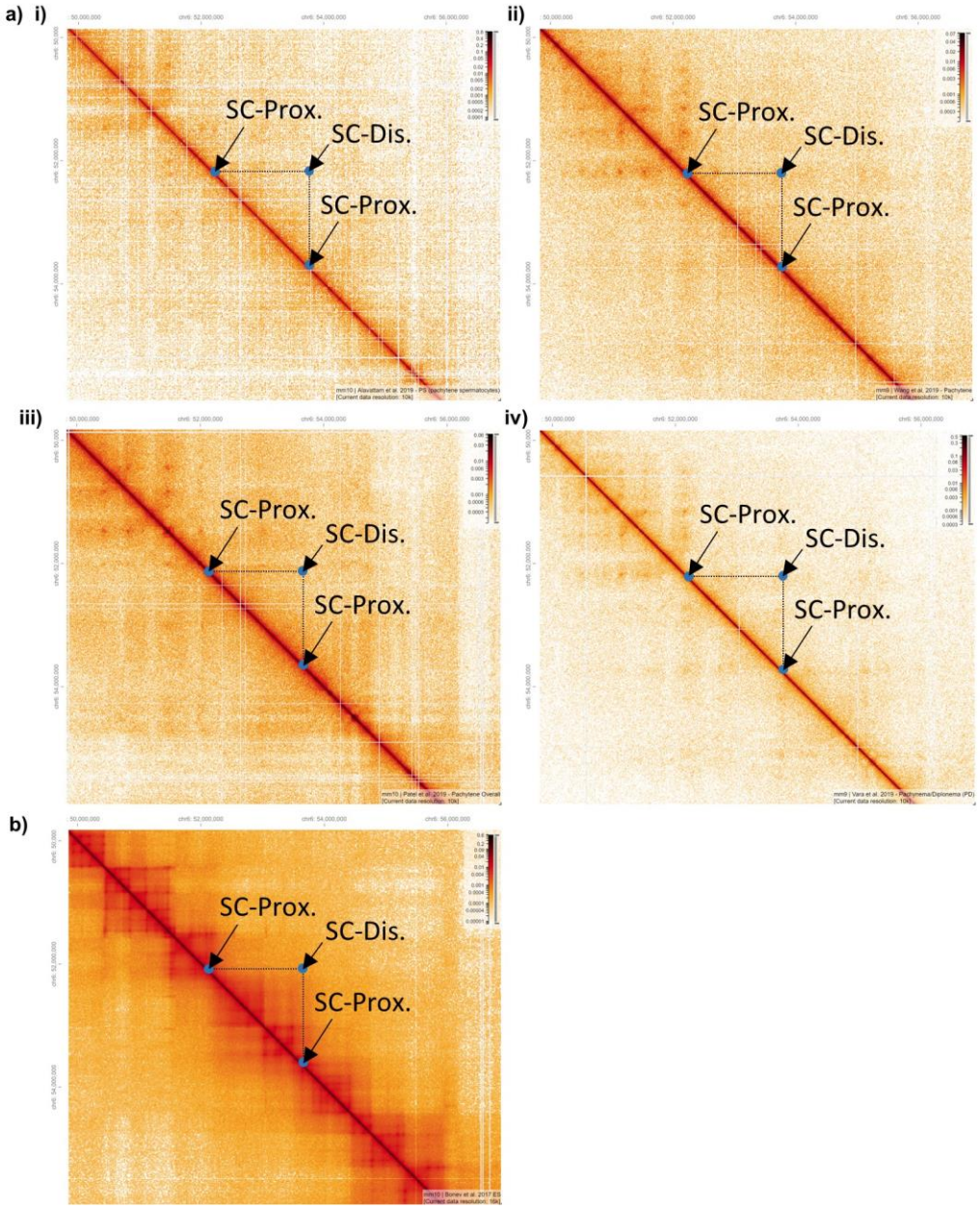

Figure 3-14. Comparing HiC and IF-FISH Maps. a. Heatmaps showing the normalised HiC interaction frequencies (10 kb bins, chr6:50,562,290-57,614,241 mm10, chr6:49,819,284-56,871,235 mm9). **i)** Alavattam *et al.*, 2019 (mm10). **ii)** Wang *et al*., 2019 (mm9). **iii)** Patel *et al.,* 2019 (mm10). **iv)** Vara *et al.*, 2019 (mm9) **b.** Heatmap showing the normalised HiC frequencies (16 kb bins, chr6:50,562,290-57,614,241 mm10) in mouse embryonic stem cells. Bonev *et al.*, 2017. Dashed line, range of IF-FISH loop. Arrows and blue dots, SC-proximal (SC-prox.) and SC-distal (SC-dis.) sites, as defined by IF-FISH.

3.2.11 Chromatin Organisation in Testes Sections

One possible reason why the IF-FISH loop map and HiC heatmap generated in pachytene spermatocytes only subtly complement one another, is that surface-spreading was used for IF-FISH, while HiC analyses examined fixed, intact spermatocytes. Surface-spreading improves the ease by which individual chromosomes and affiliated structures can be visually distinguished. Furthermore, the preservation and accessibility of nuclear protein structures, necessitated by IF, are considered excellent. However, one drawback of using surface-spreading is the risk of disrupting native chromatin organisation prior to fixation. To ensure the IF-FISH-mapped chromatin structures were not an artefact of surface-spreading, inter-chromatid distances were measured in paraffin-embedded testicular sections, in which the chromatin is thought to adhere to a near-native state. In the testicular sections, IF-FISH was conducted using an anti-SYCP3 antibody for spermatocyte sub-staging and one of two fosmid FISH probes: F-A, as a representative SC-proximal probe, and F-C, as a representative SC-distal probe (Figure 3-15). The tether-to-fosmid distance is challenging to measure in intact nuclei, due to a lack of spreading of individual chromosome axes, therefore inter-chromatid measurements were used to assess if the organisation determined in surface-spread spermatocyte also exists in sections. Similarly to surface-spread spermatocytes, the mean inter-chromatid distance was significantly greater at the SC-distal locus than at the SC-proximal locus in testicular sections, increasing by over 10-fold from 0.38 ± 0.04 µm to 5.43 ± 0.29 µm (Figure 3-15b). Since inter-chromatid distance and distance from the SC are strongly correlated on surface-spreads, inter-chromatid distances would suggest that the positioning of the SC-distal and SC-proximal regions, relative to the SC, were conserved in a near-native state. Chromatid pairing was also assessed by ranking the inter-chromatid distances, as described in Section 3.2.3. In accordance with surface-spread spermatocytes (Figure 3-5), there was no evidence of chromatid pairing at the SC-distal locus (F-C) in testes sections (Figure 3-15c). However, a pairing-like trend was evident in the testes sections at the SC-proximal locus (F-A; Figure 3-15c), as the ranked inter-chromatid distances were comparable with the simulated alternate hypothesis, in which chromatid pairing is evident. Interestingly, no such evidence of a pairing-like trend at the SC-proximal locus was observed in surface-spread spermatocytes (Figure 3-5). Taken together these findings demonstrate that the organisation of total inter-chromatid distances, and presumably distance from the SC, between SC-proximal and SC-distal loci is conserved between surface-spread and

near-native state spermatocytes. Thus, showing that surface-spreads act as a reliable representation of native chromatin configurations and the chromatin-loop maps produced through IF-FISH are accurate. However, chromatid pairing may be disrupted on surface-spreading, therefore predictions of chromatid pairing should be treated with caution, when generated through surface-spreading.

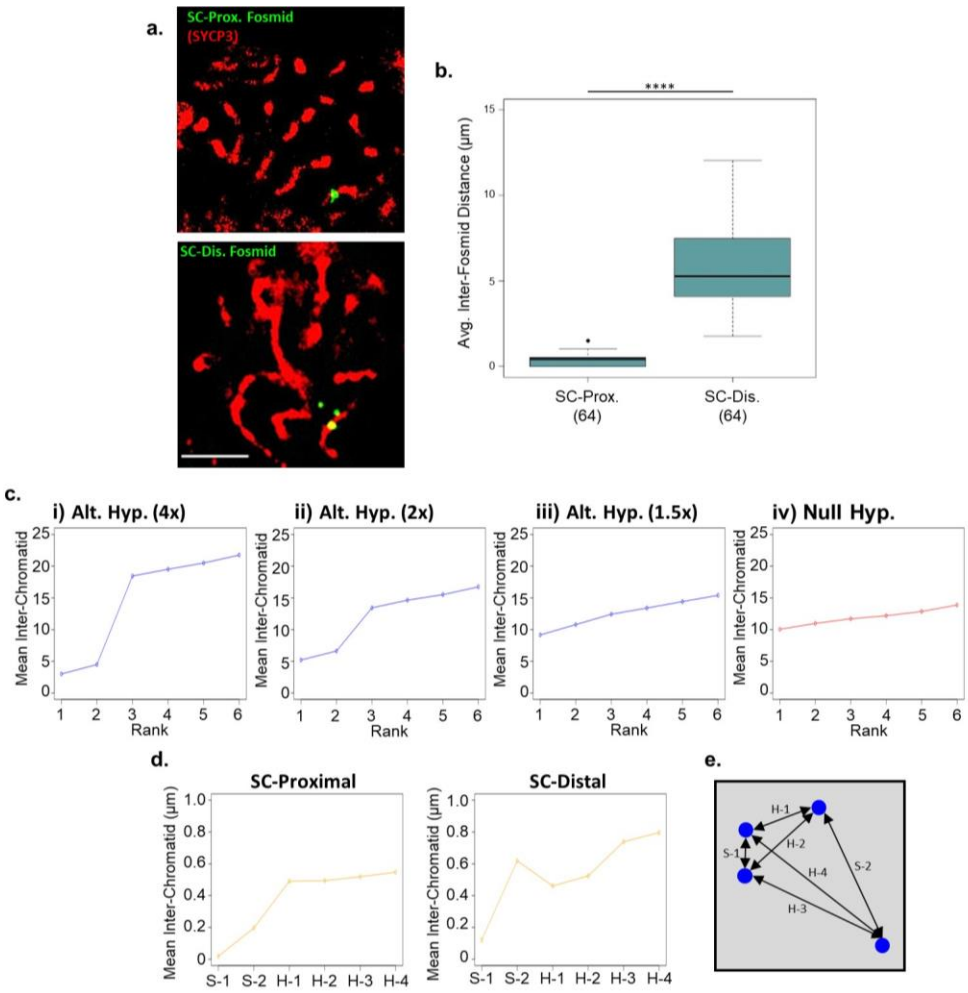

Figure 3-15. Inter-chromatid distances in pachytene spermatocytes present in testicular tissue sections. a. Representative cross-sections of inter-chromatid distance for an SC-proximal fosmid (SC-Prox., F-A) and SC-distal fosmid (SC-Dis., F-C) in pachytene spermatocytes in tissue sections. Fosmid, green. Anti-SYCP3 IF, red. 6 µm scale bar. **b.** Boxplot of the mean inter-chromatid distance per nucleus for fosmids F-A (SC-prox.) and F-C (SC-dis.). 3 mice analysed per fosmid. Bracketed values, number of nuclei scored. ****, $p<0.0001$ (Mann Whitney U test). **c.** Simulations of the alternate hypothesis where inter-pair distances are **i)** 4x, **ii)** 2x, **iii)** 1.5x the two paired inter-chromatid distance and **iv)** the null hypothesis that all chromatid distances (paired and inter-pair) are the same and no pairing is evident. **d.** Assessing chromatid pairing at a SC-proximal locus (F-A) and a SC-distal loci (F-C) in testes sections. The mean of each of the two presumptive paired inter-chromatid distances (S-1 to S-2) and the four inter-pair distances (H-1 to H-4) were ranked in each nucleus, the mean inter-chromatid distance is shown for each rank. Nuclei scored: SC-proximal, 64; SC-distal, 64. **e.** Example schematic of the organisation of the four chromatids, highlighted by fosmid probes ranked according to the two inter-chromatid distances at each presumptive pair (S-1 to S-2) and the four inter-pair inter-chromatid distances (H-1 to H-2).

3.3 Discussion

3.3.1 Visually Mapping a Single Chromatin Loop in Pachytene Spermatocytes

Unlike in yeast, where chromatin-SC interactions can be mapped genome-wide by HiC and ChIP-seq (Blat *et al.*, 2002; Schalbetter *et al.*, 2018), comparable approaches in mice have proven challenging to interpret (Alavattam *et al*., 2019; Johnson *et al*., 2013; Patel *et al*., 2019; Wang *et al*., 2019). Therefore, an alternate mapping strategy using IF-FISH was developed to comprehensively examine the organisation of specific chromatin loop arrays, relative to the pachytene SC, on a single cell level.

In this chapter, an effective, IF-FISH-based technique was developed to differentiate SC-proximal and SC-distal regions in mouse pachytene spermatocytes. The assay highlighted that the relative positioning between the SC and specific chromatin regions (150-200 kb in length) was consistent between individual mice. These patterns are compliant with HiC observations, which suggest that specific pachytene chromatin contact points can arise at fixed positions from a central axis in murine spermatocytes and meiotic *S. cerevisiae* (Alavattam *et al*., 2019; Patel *et al*., 2019; Schalbetter *et al.*, 2018; Wang *et al*., 2019). In addition, such conservation in loop organisation between animals, implies that the spatial distribution of the mechanisms responsible for forming and maintaining pachytene chromatin loop arrays is also conserved. These mechanisms must depend on a sequence specific component, directly or indirectly, in order to differentiate SC-proximal and SC-distal regions.

By combining adjacent BAC FISH probes, chromatin extensions from the SC conformed to a loop-like structure, enabling an entire ~1.3 Mb loop to be mapped. This finding supports the established meiotic loop model and complements HiC-based studies, in which the average loop length was predicted to be 1.5-2 Mb in late prophase (Patel *et al*., 2019). The relationship between HiC- and IF-FISH-based chromatin mapping is discussed in further detail in Section 3.3.2. Admittedly, the length of this specific chromatin loop at the *HoxA* cluster is over 2-fold greater than previous FISH-based predictions, in which chromosome paints were used to calculate an average loop length (Ito *et al*., 2014). Furthermore, historic EM images were interpreted to suggest that loop sizes are strikingly uniform, with no obvious regional disruptions, along the length of individual SCs. However, chromosome-wide analyses are prone to individual loops being obscured by overlapping chromatin (discussed in

Zickler and Kleckner, 1999). Therefore, by examining relatively shorter genomic distances, IF-FISH can yield more informative results, regarding the precise length of individual chromatin loops and loop length heterogeneity along a chromatin loop array.

An important point to consider when categorising genomic regions into SC-proximal and SC-distal positions, is that a chromatin loop is a continuum, running from two minima to an intervening maximal point. This topology, therefore, does not lend itself easily to such binary categorisation. Consequently, despite an 80% BAC-SC score being set as a threshold to discriminate the two groups, as this value appeared to represent a divide in the data, there were a number of regions with a percent BAC-SC score close to the threshold that could have been categorised into a third intermediate group between SC-proximal and SC-distal sites.

Notably, the BAC-SC overlap assay cannot distinguish between direct chromatin-SC tethering interactions, or simply the cytologically visible overlap of the two structures in three-dimensional space. This caveat is of particular relevance when considering long SC-proximal regions, as seen in Figure 3-7, within which loop topology cannot be accurately interpreted. For instance, multiple small loops may be present within an SC-proximal region, or the entirety of the region may be bound to the SC or confined to a single shallow loop. Reassuringly, the fosmid-based mapping of the *HoxA* chromatin loop largely agreed with the patterns produced by the BAC-SC overlap assay. The use of fosmid FISH probes also improved the resolution at which the positioning of chromatin, relative to the SC, could be mapped. Notably, since consecutive fosmids were separated by up to ~500 kb, the exact loci associated with the loop maxima and minima are not necessarily accounted for and may require further fosmid FISH probes to be utilised for identification. *In vitro* analyses have shown that the AE protein, SYCP3, is capable of bridging DNA molecules, creating a potential means by which chromatin looping is formed and/or maintained (Syrjänen *et al*., 2017; Syrjänen, Pellegrini, and Davies, 2014). Thus, it would be interesting to assess whether SYCP3 and other SC components, such as SYCP1, which is predicted to bear a putative DNA-binding domain (Dunce *et al.,* 2018), could discriminate between SC-distal and SC-proximal sequences presently identified.

3.3.2 Reconciling Spermatocyte HiC and IF-FISH data

FISH is increasingly being exploited as a validatory tool in interphase 3C studies. However, although HiC analysis hinted at chromatin loop interactions corresponding to those observed through FISH, the contact frequencies were considerably less than one may expect based on the consistent configurations identified in FISH. Several factors may account for this disparity including: i) the technical distinction between FISH and HiC readouts ii) the single cellular versus multicellular nature of FISH and HiC analyses, respectively and iii) the technical biases incurred by each technique. It is interesting to note, there appears to be more similarities between the IF-FISH pachytene loop map and the HiC heatmap generated from mouse embryonic stem cells, than with the pachytene HiC heatmaps. This suggests that large-scale chromatin in pachytene meiocytes may be more conserved from interphase-like states, than is presently predicted by HiC analyses.

Typically, when HiC and FISH based data are compared the spatial proximity between two loci is measured through FISH and compared to contact frequencies, generated by 3C analyses. However, in pachytene spermatocytes, such inter-locus FISH measurements proved considerably more challenging to perform, due to the presence of four chromatids, which hindered the ability to accurately differentiate loci arranged in *cis*. Hence, an alternative FISH strategy was employed, in which the SC was used as a reference point to map chromatin loops, with the presumption that distance from the SC would be inversely proportional to contact frequency. However, although HiC and FISH are considered complementary techniques, multiple studies have cautioned that the two strategies do not completely reconcile with one another and in some instances the two readouts can appear paradoxical (Bickmore and Van Steensel, 2013; Nora *et al*., 2012; Williamson *et al*., 2014). These differences may be accounted for by the two techniques having distinct readouts, IF-FISH measures spatial distance and HiC generates contact frequencies, based on the capture radius of a cross-linker. One study demonstrated that HiC and FISH data were compliant over short distances, but often opposing over larger distances. Thus, demonstrating that *in vivo* chromatin organisation may account for differences in HiC and FISH outcomes (Fudenberg and Imakaev, 2017). Furthermore, according to *in silico* simulations the processivity, separation and speed of loop extrusion can cause contact frequency and physical distance to fall into disagreement (Fudenberg and Imakaev, 2017). Chromatin loop topology and dynamics could therefore account for a lack of a definitive relationship

between HiC and IF-FISH data in spermatocytes. Additionally, it is possible that HiC and FISH are assessing different levels and/or types of chromatin architecture in meiotic chromosomes, and that integrating information from both types of analysis may be required to fully understand this phenomenon.

3.3.3 Chromatid Organisation

Despite bulk chromatin often appearing as a single morphological unit, ultrastructural analyses have demonstrated that each chromatid forms a physically distinct chromatin loop array. These data support a dual loop model in which sister chromatids form co-oriented, parallel loop arrays stacked on top of one another (Zickler and Kleckner, 1999). Presently, the relative positioning of all four chromatids along the length of an autosomal pachytene chromatin loop was examined using IF-FISH. The principle finding of such analyses was that in pachytene, inter-chromatid distance exhibits a strong, positive correlation with distance from the SC, with a surprising absence of chromatid contiguity at SC-distal regions. Considering that the relative spatial positioning of specific chromatin regions and the SC occurs in a non-random manner (discussed in Section 3.3.1), it is not surprising that in proximity to the SC all four chromatids are clustered together, as they interact with components enriched at the SC, such as cohesin, which is known to increase chromatid proximity and cohesion (Ishiguro, 2018). These findings are also complemented by super-resolution images of DNA, which demonstrated that chromatin forms condensed clusters at regular intervals along the pachytene SC (Prakash *et al*., 2015). Intriguingly, IF-FISH analysis showed that chromatids separate with distance from the SC. This implies that mechanisms promoting chromatid contiguity are absent, or are out-competed, in SC-distal chromatin by either an active or passive means of chromatid separation, which has yet to be identified. Recent genome-wide cohesin ChIP-seq has suggested that cohesin is present within chromatin loops (Vara *et al*., 2019). However, my findings indicate cohesin does not consistently mediate chromatid cohesion within chromatin loops, it is plausible instead that a potentially less cohesive population of cohesin complexes are present on loop-associated chromatin. One means by which this could be experimentally examined is through the deletion of the cohesin release factor gene, *Wapl*, to establish whether retainment of chromatin-associate cohesin impacts on the relative positioning of chromatids.

Importantly, although no evidence of chromatid pairing was apparent in surface-spread spermatocytes, the extent of chromatid pairing was shown to be distinct between a SC-proximal and a SC-distal locus in testes sections. In sections, SC-proximal chromatids adopted a paired-like trend on inter-chromatid ranking, while SC-distal chromatids were stochastically positioned relative to one another in pachytene spermatocytes. This data can be considered plausible, considering the striking enrichment of the cohesion-mediating cohesin complex at the pachytene SC detected by IF staining (Eijpe *et al*, 2003). These findings may also warrant the conclusion that this spatial patterning of chromatid pairing may be important for this stage of meiotic prophase I. For instance, during pachytene a shift in DSB repair fate, from homolog-mediated repair to alternate repair approaches, is thought to occur, as persistent DSBs and DSBs on the non-homologous X chromosome must be repaired (Enguita-Marruedo *et al.*, 2019). Therefore, one possible explanation for this specific patterning, is that the apparent lack of sister chromatid pairing at SC-distal loci and pairing at SC-proximal loci promotes sister-mediated repair and/or supresses homologous-mediated repair. To interrogate this proposition, inter-chromatid distances should firstly be assessed at additional loci. In addition, if possible, it may prove valuable to attempt to assess this putative relationship, in mice in which DSB repair fate or chromatid organisation have been perturbed.

3.3.4 Technical Drawbacks of IF-FISH

This chapter was heavily reliant on the use of IF-FISH on surface-spread spermatocytes, to interrogate chromatin organisation in a spatial cellular context. This approach provides a powerful method of cytological analysis, allowing clear visualisation of chromatin structures relative to the chromosome axis, without the challenges of analyses affiliated with imaging in testicular sections in which nuclei are compact. However, it is important to acknowledge the time consuming and low throughput nature of these assays. Furthermore, this technique is associated with technical caveats. For instance, these analyses make the presumption that surface-spreading of nuclei impacts chromatin organisation to an equivalent extent throughout the entire genome, for instance between SC-distal and SC-proximal loci, without the disruption of the potentially unstable or weak structures on experimental manipulation prior to fixation. Investigations in interphase cells have demonstrated that, although FISH measurements generated through hypotonic swelling (2D specimens) are

distinct from those produced through formaldehyde fixation (3D specimens), the results were suggestive of a general swelling effect, but no reorganisation of sequences relative to each other (Mahy *et al.*, 2002; Volpi *et al*., 2000). Furthermore, it was reassuring to report that the IF-FISH verification experiment conducted in testes sections, largely mirrored patterns of chromatin organisation observed on surface-spreads. This indicates that the presumed positioning of specific loci, relative to the pachytene SC and the overall extent of chromatid separation, appeared to be preserved on surface-spreading between SC-proximal and SC-distal loci. However, comparisons of IF-FISH data generated through surface-spreading and testes sections, highlighted that spreading can disrupt inter-chromatid arrangements, as pairing of chromatids at an SC-proximal locus was only evident in testes sections. Analyses of chromatid pairing at SC-proximal loci on surface-spreading should therefore be considered with caution. In addition, in testes sections the ability to distinguish individual chromatids, and thus determine inter-chromatid distance, was limited by the resolution of the equipment used to capture the image, as many chromatids were in too greater proximity to be differentiated. More sophisticated imaging technologies may therefore shed further light on chromatin arrangements, particularly at loci near the SC, where individual chromatids are more challenging to discriminate.

3.3.5 Recombination Mapping in the IF-FISH-defined Chromatin Loop

The concept of the tethered loop-axis complex (TLAC) model is based on observations that recombinogenic machinery localises to the chromosome axis while, meiotic hotspots sequences map to positions in between axis-associated sites. Therefore, hotspot sequences must be recruited to the axes, to overcome this apparent spatial paradox and undergo recombination (Blat *et al*., 2002; Kleckner, 2006; Panizza *et al*., 2011). These observations are largely based on studies performed in *S. cerevisiae,* in which both axis-associated sequences and meiotic hotspots have been mapped. In mammals, the mutually exclusive positioning of hotspots and axis-associated points has yet to be directly confirmed, since no chromatin-axis maps were available. Therefore, following the successful mapping of a chromatin loop in this chapter, the loop map was compared to the distribution of SPO11-oligos and DMC1 binding, as markers of early recombination. In support of

the TLAC model, both SPO11-oligos and DMC1 binding were enriched between two SC-proximal regions, within the intervening SC-distal region. These findings therefore help to corroborate the existence of the TLAC model in mammals.

Importantly, SPO11-oligos and DMC1-binding are not entirely excluded from SC-proximal sites. This may be explained by i) the limited resolution of the IF-FISH, defining the chromatin loops, ii) the possibility that not all hotspots are enriched at the loop-associated sequences and iii) the fact that there is a temporal disparity, between the initiation of recombination during leptotene and the pachytene-defined chromatin loop map. Importantly, it is possible that chromatin looping undergoes a transition between leptotene and pachytene, causing the looping and recombination maps to be asynchronous. In order to address this temporal discrepancy chromatin loop mapping should be conducted in early prophase I.

3.3.6 SMC1 Variants Manipulate Pachytene Chromatin Loops

Published data has elegantly described the ability of the two SMC1 variants, SMC1β and SMC1α, to manipulate meiotic chromosome morphology in mouse spermatocytes (Biswas, Stevense and Jessberger, 2018; Revenkova *et al*., 2004). *Smc1* mutant mice were exploited to validate the autosomal chromatin loop, defined in Section 3.2.2, by comparing the observed chromatin loop topology with that predicted from previously published findings.

Through IF-FISH analyses, the behaviour of the autosomal chromatin loop was shown to largely complement whole chromosome morphology changes in *Smc1β-/-* and *Smc1β-/-,1α* mice, relative to control *Smc1β+/+* mice (Biswas, Stevense and Jessberger, 2018; Revenkova *et al*., 2004); as specific loci increased in distance from the SC by ~2-fold in *Smc1β-/-* spermatocytes and underwent a partial rescue in *Smc1β-/-,1α* spermatocytes. Interestingly, the ability of *Smc1α* up-regulation to reduce the tether-to-fosmid distance was locus specific, indicating that SMC1α may be recruited and manipulate chromatin organisation differently at distinct axis-association sites. In accordance with a strong, positive relationship between distance from the SC and chromatid separation, inter-chromatid distance also increased ~2-fold following *Smc1β* deletion and was partially rescued on up-regulation of *Smc1α* (~1.5-fold reduction relative to *Smc1β-/-*). I demonstrated that SMC1 variants are therefore necessary for increasing sister chromatid proximity on the X chromosome.

However, due to FISH probe limitations, I cannot presently comment on the extent to which the variants manipulate inter-homolog proximity. Previous studies have shown that the sex chromosomes exhibit significantly more variation in axis morphology and synapsis, relative to the autosomes, in *Smc1β-/-* and *Smc1β-/-,1α* mice (Biswas, Stevense and Jessberger, 2018). Therefore, the observations made on the X chromosome may not directly translate to autosomes. Interestingly, the difference in inter-chromatin-SC falls between the three loci. This implies that they all lie at a similar distance from the SC and a nuclear limiting factor may be at play, to restrict further extension from the SC beyond this point. Together, these data conform to the behaviour of chromatin loops predicted from whole chromosomes analyses of SMC1 mutant spermatocytes and therefore help to validate the mapped chromatin loop.

The IF-FISH data described, can also provide novel insight into the relationship between cohesin and the manipulation of large-scale meiotic chromatin looping. It is intriguing to note, loss of cohesin components has disparate effects on chromatin in interphase and pachytene cells. High-resolution HiC data has revealed that the down-regulation of the cohesin subunit *Rec8*, in HCT-116, cells results in the majority of loop domains being lost (Rao *et al*., 2017). Meanwhile, down-regulation of the cohesin release factor WAPL, in HAP1 cells, increases median chromatin loop length (Haarhuis *et al*., 2017). These interphase observations led to the proposition that cohesin is necessary for the maintenance of chromatin loops, while cohesin turnover restricts their processive enlargement. However, in pachytene this is unlikely to be the case, as IF-FISH has demonstrated that chromatin loops are likely to be maintained and increase in length in the absence of *Smc1β* in pachytene spermatocytes (Novak *et al*., 2008; Revenkova *et al*., 2004). These data therefore highlight that a meiosis-specific mechanism causes meiotic cohesin to restrict, rather than promote, the extension of individual chromatin loops. For instance, the binding of SC components may disrupt cohesin's loop extrusion activity, causing cohesin to instead accumulate at axis-association sites along the SC.

Changes in two factors may account for the changes in tether-to-fosmid distances observed in *Smc1β-/-* and *Smc1β-/- ,1α* spermatocytes; firstly, the state of chromatin compaction and secondly, the positioning of chromatin-SC attachment sites. According to the area of BAC FISH probes, which was used as a proxy for chromatin compaction and/or chromatid clustering, SMC1β is responsible for promoting the condensation of SC-proximal chromatin. This finding may correspond with

observations made in *S. cerevisiae*, which demonstrated that the yeast paralog of REC8 is not only involved in mitotic sister chromatid cohesion, but also chromosome compaction (Guacci, Koshland, and Strunnikov, 1997). Interestingly however, the up-regulation of *Smc1α* was incapable of inducing chromatin compaction and/or reducing the chromatid clustering at either the SC-distal or SC-proximal region. This highlighting, incomplete redundancy between SMC1β and SMC1α and the fact that changes in SC-proximal chromatin compaction cannot solely account for changes in chromosome morphology, seen in both *Smc1β-/-* and *Smc1β-/-,1α* spermatocytes. This implies that the changes in chromatin loop length could also be driven by changes in chromatin-SC attachment points. It has previously been proposed that SMC1β is responsible for mediating a specific subset of chromatin-attachment points (Novak *et al*., 2008). In *Smc1β-/-* spermatocytes, all three loci examined by fosmid FISH probes, two SC-proximal and one SC-distal, exhibited a tether-to-fosmid distance greater than observed in *Smc1β+/+* spermatocytes. Assuming the basic chromatin loop array configuration is maintained, these findings imply that the wildtype SC-proximal loci are replaced by alternate SC-proximal sequences. Further IF-FISH based mapping is therefore required to identify these putative alternate sequences and ascertain whether alterations in loop topology, result from the loss of a specific combination of wildtype axis-association points and/or the adoption of novel chromatin-SC attachment points, for instance through alterations in the extent of loop extrusion (Figure 3-16). A change in the abundance of cohesin may affect the 'strength' of axis-association sites acting as an obstacle to loop extrusion, where a decline in cohesin increases the mobility of the chromatin fibre relative to the SC, enabling a chromatin loop to extrude further. It is also important to mention, during this interpretation, the length of axis-associated regions in *Smc1β+/+, Smc1β-/-* and *Smc1β-/-,1α* mice is not known. Therefore, it is feasible that more chromatin is 'released' from the axis-associated regions in the *Smc1* mutants, rather than the adoption of completely novel axis-association sites from previously loop-associated sequences, through loop extrusion or the complete loss of specific axis-association sites (Figure 3-16).

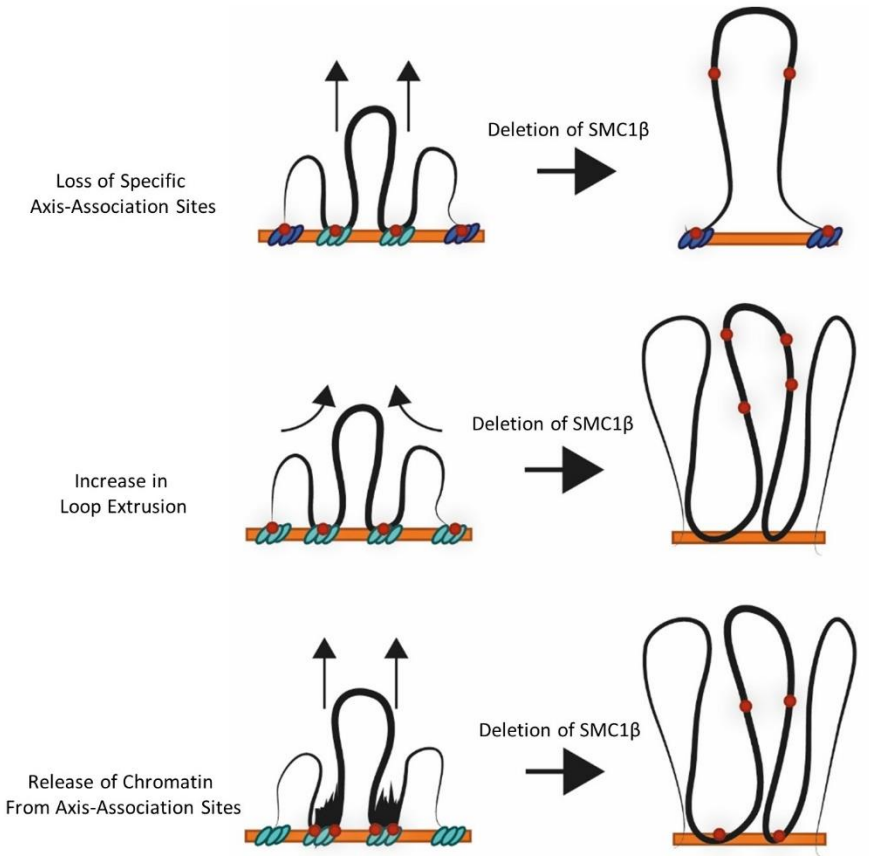

Figure 3-16. Putative Alterations in Chromatin Organisation in *Smc1β-/-* spermatocytes. A single chromatid depicting the different outcomes in chromatin organisation following the deletion of *Smc1β*, relative to the chromosome axis (orange bar). Red dots depict original chromatin-SC tether points. Blue ellipse, SMC1β-dependent attachment. Purple ellipse, SMC1β-independent attachment.

Chapter 4:

Dynamics of Meiotic Chromatin Loops in Mouse Spermatocyte Prophase I

Chapter 4 Dynamics of Meiotic Chromatin Loops in Mouse Spermatocyte Prophase I

4.1 Introduction

In male mice, meiotic prophase I extends over the course of ~10 days (Goetz, Chandley, and Speed, 1984), during which time the physical organisation of the entire genome undergoes a remarkable reconfiguration, as homologous chromosomes pair and synapse to facilitate crossover (CO) formation. In leptotene, chromosomes become individualised and chromatin loop arrays are observed emanating from the proteinaceous chromosome axes (Zickler and Kleckner, 1999). Homologous chromosomes begin to pair and synapse in zygotene, as the homology search ensues and attachment to force-generating machinery at the nuclear periphery creates a chromosome 'bouquet' (Boateng *et al*., 2013; Lee *et al*., 2012; Scherthan, 2001). Subsequently, in pachytene, the complete SC assembles to establish bivalent structures on which recombination events can generate COs (Grey *et al*., 2009; Kumar *et al*., 2015; Stanzione *et al*., 2016). Finally, in diplotene, the SC starts to disassemble, enabling homologous chromosomes to start to separate (Sun and Handel, 2008).

To date, the majority of meiotic chromosomal dynamics have been characterised cytologically according to the morphological appearance of the chromosome axes. Intriguingly, recent HiC studies have revealed striking conformational changes to large-scale chromatin contacts during meiotic progression; as prophase I is initiated, interphase-associated structures including chromatin loops and topological associated domains (TADs) are largely lost. These structures are replaced with attenuated compartments and 'hubs' formed through the clustering of transcriptionally active genomic elements (Alavattam *et al*., 2019; Patel *et al*., 2019; Vara *et al*., 2019; Wang *et al.,* 2019). Furthermore, progression from leptotene/zygotene to pachytene corresponds with a decline in HiC-defined inter-chromosome interactions, as bouqueting is disbanded, concomitant with an increase in *cis* inter-contact distances, implying that chromatin loops continue to extend from early to late prophase I (Patel *et al*., 2019; Vara *et al*., 2019). These findings are in agreement with immunofluorescence-fluorescent *in situ* hybridisation (IF-FISH) data, which showed a rise in chromatin extension length over prophase I (Kauppi *et al*., 2011). Intriguingly,

how these temporally dynamic changes in chromatin organisation relate to the formation of the cytologically visible chromatin loop structures and the relative positioning of individual chromatids remains unknown.

In this chapter, I firstly performed IF-FISH to examine the organisation of pachytene-defined SC-proximal and SC-distal region in leptotene. These analyses demonstrated that the two regions are cytologically distinguishable in leptotene and thus mechanisms acting to spatially discriminate these structures are likely at play prior to, or during leptotene. Furthermore, IF-FISH data indicates that once pachytene is reached, chromatin organisation is robustly maintained. I subsequently sought to investigate the relationship between transcription and the maintenance of pachytene chromatin organisation. Both RNA polymerase activity and the presence of RNA were found to influence large-scale chromatin organisation in pachytene. On transcription inhibition, chromatin loops were drawn into closer proximity with the SC, without compromising the relative positioning of large SC-proximal and SC-distal regions. In addition, I demonstrate that transcriptionally active loci are positioned distally from the SC, while silent flanking regions are in relatively greater physical proximity to the SC. Cumulatively, these findings provide increased descriptive detail, regarding the spatial relationship between meiotic chromatin organisation and transcription.

4.2 Results

4.2.1 Changes in Chromatid Organisation during Prophase I

The initial aim of this chapter was to examine the spatial relationship of pachytene-defined SC-proximal and SC-distal regions in leptotene. The pachytene loop mapping approaches employed in Chapter 3 were reliant on exploiting the highly distinctive pachytene SC as a reference point marking the base of chromatin loops. However, these strategies could not be performed in leptotene, as immunostaining of the chromosome axes (anti-SYCP3 IF) generates short, punctuate signals, making the identification of the axis corresponding to a specific chromatin loop challenging and prone to subjective interpretation. Consequently, it was not possible to determine the positioning of the genomic regions of interest relative to leptotene chromosome axes. To compare the pachytene-defined SC-proximal and SC-distal regions in leptotene, I examined inter-chromatid distances. In leptotene, homologous chromosomes are yet to synapse, therefore I made the assumption that, if the two shortest inter-chromatid distances were at least 2-fold less than the average of the remaining four inter-chromatid distances, these distances could be used as presumptive inter-sister chromatid distances (Figure 4-1). The mean presumptive inter-sister chromatid distance per nucleus was compared using two fosmid FISH probes; the first representing a pachytene-defined SC-proximal (A) and the second a SC-distal (B) region within the *HoxA* chromatin loop on chromosome six (Figure 3-3; F-A and F-C respectively). In leptotene, the average inter-sister chromatid distance was greater at the pachytene-defined SC-proximal fosmid A (1.80 ± 0.10 µm), relative to the pachytene-defined SC-distal fosmid B (1.27 ± 0.16 µm; $p<0.0001$, Mann Whitney U test; Figure 4-1), indicating that the two regions can be distinguished from one another through the relative organisation of presumptive sister chromatids. This observation suggests that during the first stage of prophase I, the structural organisation of chromatin at pachytene-defined SC-proximal and SC-distal regions are distinctly regulated, or differentially sensitive to the same regulatory mechanisms. Highlighting that the mechanisms, which initially establish this distinction, are active prior to or during leptotene.

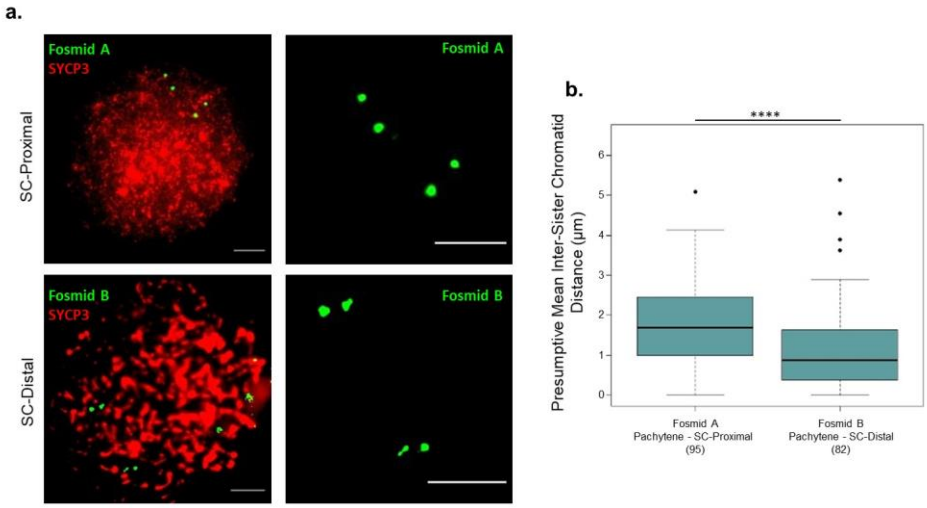

Figure 4-1. Organisation of SC-proximal and SC-distal chromatids in leptotene. a. Representative images of inter-chromatid distance for a Fosmid A (Pachytene-defined SC-proximal) and Fosmid B (Pachytene-defined SC-distal) in leptotene spermatocytes. Fosmids, green. Anti-SYCP3 IF, red. 5 µm scale bar. **b.** Boxplot of the mean presumptive inter-sister chromatid distance (µm) per nucleus for the pachytene-defined SC-distal and SC-proximal loci in leptotene nuclei. 3 mice analysed per probe. Bracketed values, number of nuclei scored. ****, p<0.0001 (Mann Whitney U test).

I next compared the mean of the two smallest inter-chromatid distances from pachytene at the same SC-proximal and SC-distal loci previously examined in leptotene (Figure 4-2). The resultant number generated in pachytene represents the smallest possible value that inter-sister chromatid distances could be for each locus in pachytene and therefore enabled a crude comparison of chromatid organisation to be conducted between leptotene and pachytene. As would be expected from the mean of all six inter-chromatid distances in pachytene (Figure 3-4), the mean of the two shortest inter-chromatid distances was significantly greater at the SC-distal locus, relative to the SC-proximal locus ($p=1.16x10^{-5}$, Mann Whitney U test; Figure 4-2). A comparison of the mean presumptive inter-sister chromatid distances in leptotene and pachytene showed that, between leptotene and pachytene, inter-sister chromatid distance may not significantly change at the SC-distal locus, from 1.27 ± 0.16 µm to 1.23 ± 0.14 µm (p=0.93, Mann Whitney U test). However, the presumptive inter-sister chromatid distance could decline between leptotene and pachytene from 1.80 ± 0.10 µm to 0.20 ± 0.04 µm at the SC-proximal locus (p=0.0029, Mann Whitney U test). These findings indicate that the relative positioning of presumptive sister chromatids

at the pachytene-defined SC-proximal and SC-distal loci could be regulated differently as prophase I advances.

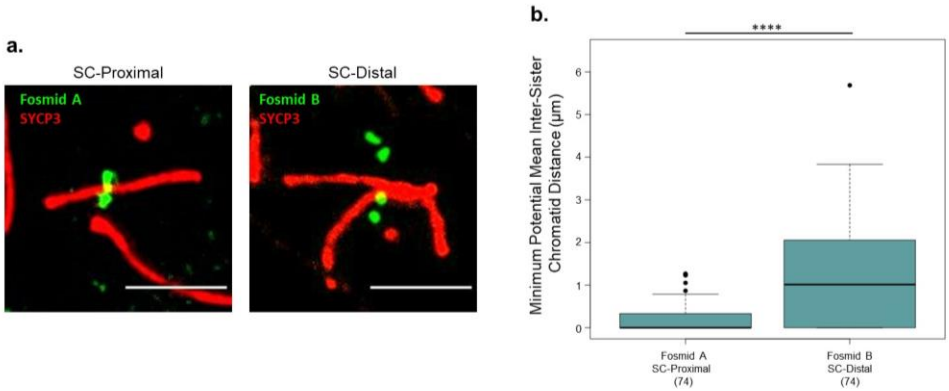

Figure 4-2. Organisation of presumptive sister chromatids at a SC-proximal and a SC-distal locus in pachytene. a. Representative images of inter-chromatid distance for a Fosmid A (SC-proximal) and Fosmid B (SC-distal) in pachytene spermatocytes. Fosmids, green. Anti-SYCP3 IF, red. 5 µm scale bar. **b.** Boxplot of the minimum potential mean inter-sister chromatid distance (µm) per nucleus for a SC-distal and a SC-proximal locus in pachytene nuclei. 3 mice analysed per probe. Bracketed values, number of nuclei scored. ****, $p<0.0001$ (Mann Whitney U test).

Without definitively distinguishing homologous and sister chromatids, I am unable to conclusively compare inter-sister chromatid distances between leptotene and pachytene. To overcome this limitation, inter-sister chromatid organisation was compared between leptotene and pachytene using two fosmid FISH probes, positioned ~500 kb apart on the non-homologous region of the X chromosome (Non-Hom. A and B; Figure 4-3). Inter-sister chromatid distance was measured by taking the centroid coordinates of the two foci created by each of the fosmids and calculating the inter-centroid distance. No significant change in inter-sister chromatid distance was observed at either of the two non-homologous loci examined between leptotene and pachytene (A, $p= 0.88$; B, $p=0.70$, Mann Whitney U test), with all inter-sister chromatid distances averaging ~1.2 µm (Figure 4-3). These data suggest that no change in inter-sister chromatid distance occurs between leptotene and pachytene, at these two non-homologous loci. Intriguingly, inter-sister distances at the two loci on the non-homologous X chromosome, and the presumptive inter-sister chromatid distance at the autosomal SC-distal loci, appear to behave comparably. Yet, without mapping the relative positioning of the loci on the non-homologous X chromosome, I cannot definitively conclude whether they both can be classified as SC-distal.

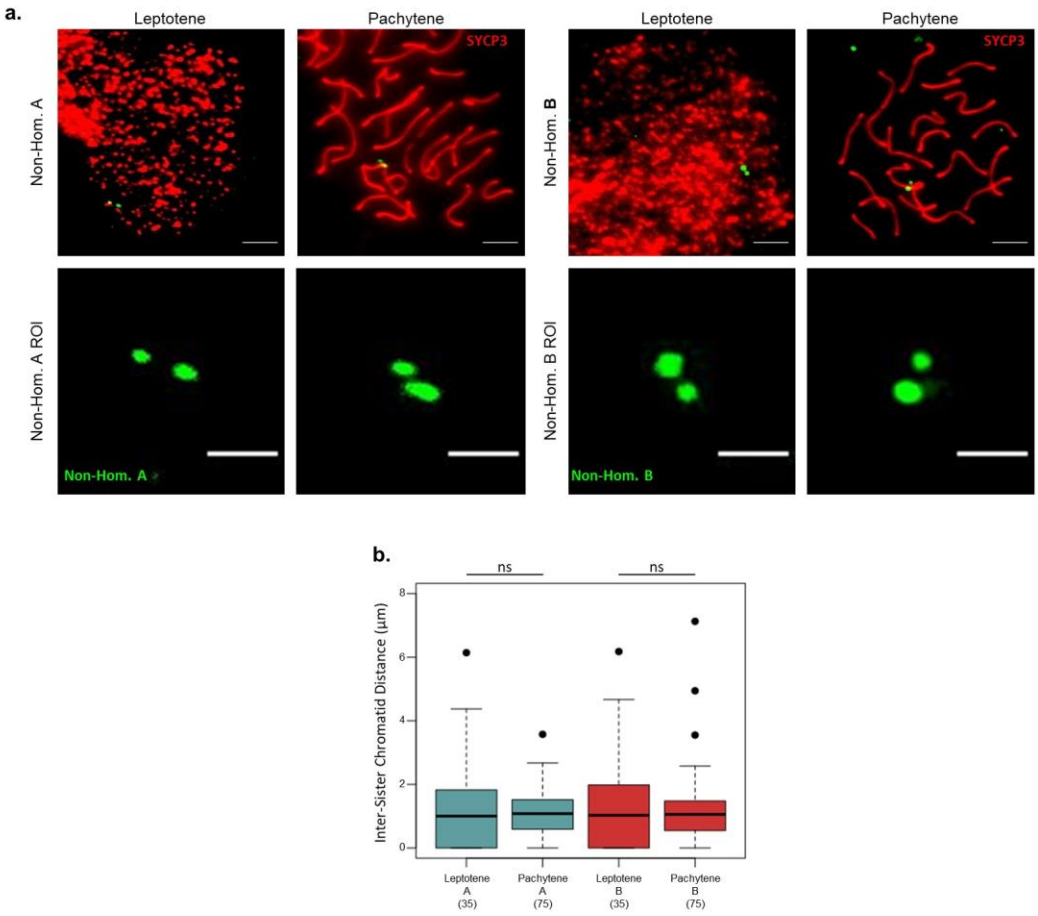

Figure 4-3. Sister chromatid organisation at leptotene and pachytene on the non-homologous X chromosome. a. Representative images of inter-sister chromatid distance at two loci on the non-homologous X chromosome (Non-Hom. A and Non-Hom. B) in leptotene and pachytene spermatocytes. Fosmid FISH probes, green. Anti-SYCP3 IF, red. 5 µm scale bar (2 µm scale bar in ROI). **b.** Boxplots of inter-sister chromatid distances (µm) for fosmids A and B in leptotene and pachytene spermatocytes. 3 mice analysed per substage and per probe. Bracketed values, number of nuclei score. ns, p>0.05 (Mann Whitney U test).

4.2.2 Maintenance of Chromatin Organisation during Pachytene

Measures of inter-chromatid distances indicate that as prophase I progresses, changes in the structural organisation of chromatin occurs in a locus-specific manner. I subsequently examined whether chromatin organisation is temporally dynamic, specifically within pachytene. The progression of pachytene can be measured according to the length of the SC complex, since SC length increases as pachytene progresses (Vranis *et al.*, 2010). The mean tether-to-fosmid distance and mean inter-chromatid distance were compared with SC length (anti-SYCP3 IF), to establish whether the length of chromatin extensions, or the extent of chromatid separation differed synchronously with the advances of pachytene (Figure 4-4). Tether-to-fosmid distance was determined by calculating the nuclear mean distance between the coordinates of the 'tether' BAC-SC overlap and the centroid coordinates of the fosmid foci marking the four chromatids (data generated in Figure 3-3). Mean inter-chromatid distance was established per nucleus by calculating the mean of the six inter-chromatid distances measured between all fosmid foci marking the four chromatids (data generated in Figure 3-4). The chromosome 6 SC was identified according to its relatively greater proximity to the chromosome 6-specific fosmid FISH probes. The behaviour of three fosmids probes representative of a pachytene-defined SC-proximal (F-A), SC-distal (F-C) and intermediate (F-B) loci were compared, to determine whether temporal relationships were dependent on the positioning of loci within a chromatin loop. No significant correlative relationship was observed between SC length and tether-to-fosmid distance (Figure 4-4a; F-A, $p=0.31$; F-B, $p=0.26$; F-C, $p=0.14$, Linear regression model), or inter-chromatid distance (Figure 4-4b; F-A, $p=0.31$; F-B, $p=0.26$; F-C, $p=0.72$, Linear regression model) at any of three fosmids examined. Therefore, these data demonstrate that the length of chromatin loops and the extent of chromatid separation do not correlate with the temporal advances of spermatocyte pachytene.

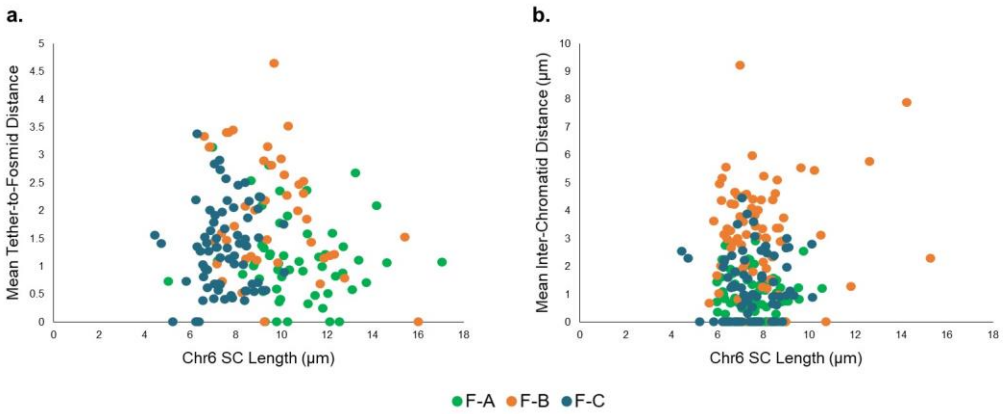

Figure 4-4. Chromatid organisation relative to SC length. a. Scatterplot of chromosome 6 (Chr6) SC length (µm) against mean tether-to-fosmid distance (µm) per nucleus for a SC-proximal (F-A), a SC-distal (F-C) and an intermediate locus (F-B). No significant correlations were observed, p>0.05 (Linear regression model). Nuclei scored: F-A 53; F-B 43; F-C 74. **b.** Scatterplot of Chr6 SC length (µm) against mean inter-chromatid distance (µm) per nucleus for a SC-proximal, a SC-distal and an intermediate locus. No significant correlations were observed, p>0.05 (Linear regression model). Nuclei scored: F-A 73; F-B 66; F-C 73.

The stability of inter-sister chromatid organisation in pachytene was also examined at the same two loci previously utilised in Figure 4-3, on the non-homologous X chromosome (Figure 4-5). Inter-sister chromatid distance was determined by calculating the distance between the fosmid foci generated by the two non-homologous chromatids (data generated in Figure 4-3). The X chromosome axis (anti-SYCP3 IF) was identified according to its proximity to the chromosome X-specific fosmid FISH probes and its characteristic partial synapsis with the shorter Y chromosome axis. Inter-sister chromatid distance exhibited no significant correlation with the length of the X chromosome axis (Non-Hom. A, p=0.46; Non-Hom. B, p=0.68, Linear regression model). This finding indicates that inter-sister chromatid distance is not dependent on the length of the X chromosome axis, or the progression of pachytene, similarly to autosomal loci.

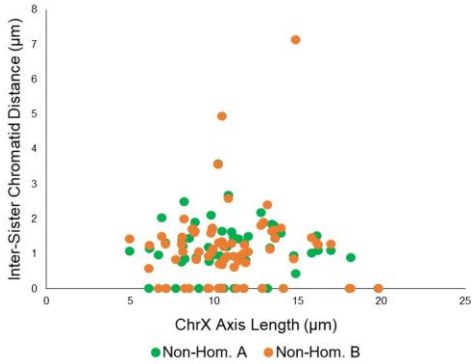

Figure 4-5. Sister chromatid organisation relative to chromosome axis length. Scatterplot of chromosome X (ChrX) axis length (µm) against inter-sister chromatid distance (µm) for two loci on the non-homologous X chromosome, Non-Hom. A and Non-Hom. B. No significant correlations were observed, $p>0.05$ (Linear regression model). Nuclei scored: Non-Hom. A, 75; Non-Hom. B, 75.

4.2.3 Nuclear Organisation on Transcription Inhibition

A historic electron microscopy (EM) study has previously shown that global inhibition of RNA polymerase causes meiotic autosomes to appear highly condensed (Handel, Caldwell and Wiltshire, 1995); this relationship was further explored by initially determining the role of transcription on the gross organisation of the meiotic nucleus, by measuring nuclear area following transcription inhibition (Figure 4-6). Three transcriptional inhibitors were employed to compare how differing mechanisms of inhibition impact on nuclear organisation: the DNA intercalator actinomycin D (1 hr), which inhibits the polymerase I, II and II migration, α-amanitin (3 hrs), which prevents nucleotide incorporation and induces degradation of polymerase II and III and finally Flavopiridol (1 hr), which impedes transcriptional initiation of paused polymerase II and III (Bensaude, 2011). Each treatment was administered to a pachytene-enriched cell population (average purity ~82%), in order to enable the inhibition of transcription to be assessed specifically within the pachytene population. Transcription inhibition was determined by measuring total RNA abundance per cell and comparing the concentration with the untreated sample (Figure 4-6c). All three inhibitors induced an >50% decline in RNA abundance, with actinomycin D producing the greatest decline in RNA production by an average of 70% (Figure 4-6c). After transcription inhibition,

the nuclear area, defined by DAPI staining, experienced a significant reduction, proportional to the extent of transcription inhibition induced by each treatment (Untreated, 1315 ± 90 μm^2; actinomycin D, 191 ± 11 μm^2; α-amanitin, 519 ± 27 μm^2; Flavopiridol, 272 ± 20 μm^2; Figure 4-6b). Together, these findings suggest that nuclear chromatin organisation is affected by ongoing transcription.

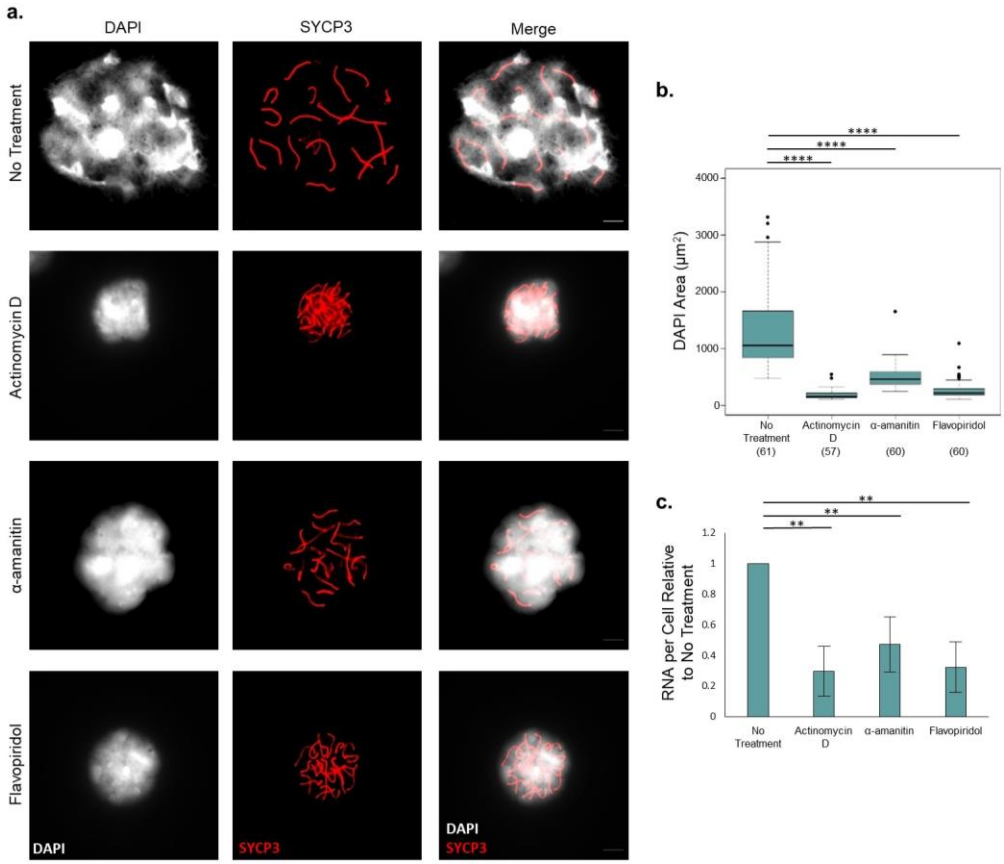

Figure 4-6. Changes to nuclear area after transcription inhibition. a. Representative images of pachytene spermatocytes following no treatment or actinomycin D (50 μg/ml, 1hr), α-amanitin (75 μg/ml, 3 hrs) and Flavopiridol (100 μM, 1hr) treatments. DAPI, white. Anti-SYCP3 IF, red. 5 μm scale bar. **b.** Boxplot of DAPI area (μm^2) following no treatment or actinomycin D, α-amanitin and Flavopiridol treatments. 3 mice analysed per treatment class. Bracketed values, number of nuclei score. ****, p<0.0001 (Mann Whitney U test). **c.** Bar chart of RNA concentration per cell relative to no treatment. Error bars, standard deviation. **, p <0.01 (One-tailed T-test).

In wildtype systems, the length of the pachytene SC is frequently found to be inversely proportional to the length of chromatin extensions (e.g. Baier, Hunt, Broman, and Hassold, 2014; Gruhn *et al.*, 2013; Kauppi *et al.*, 2011). Given that the nucleus appears grossly compacted on transcription inhibition, the effect of the strongest inhibitor, actinomycin D, on total autosomal SC length was tested (anti-SYCP3 IF; Figure 4-7). The total length of the autosomal SCs did not differ between treated (143.6 ± 2.2 µm) and untreated cells (139.8 ± 2.7 µm, p=0.182, Mann Whitney U test), suggesting that, despite the striking effect on nuclear area, transcription inhibition has no impact on SC organisation during a one-hour actinomycin D treatment.

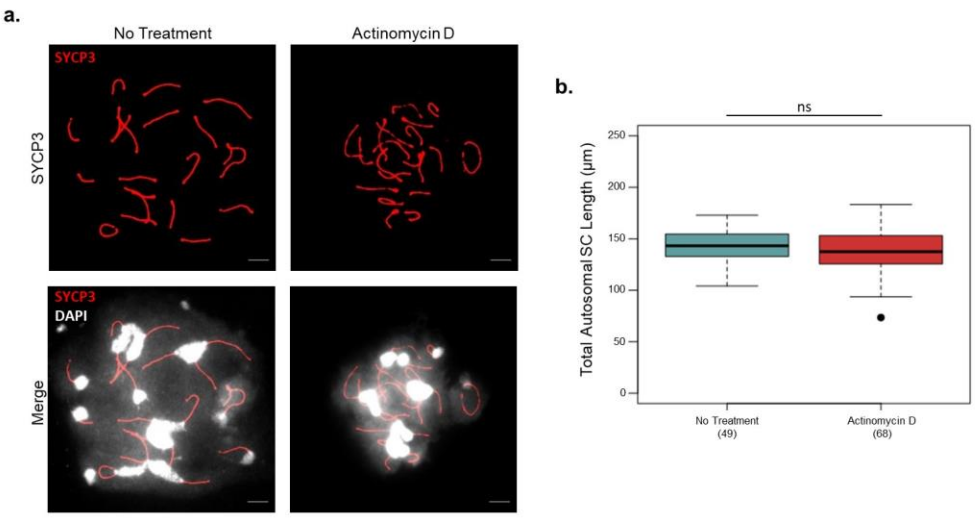

Figure 4-7. Effect of transcription inhibition on SC length. a. Representative images of pachytene spermatocytes following no treatment or actinomycin D treatment (50 µg/ml, 1hr). DAPI, white. Anti-SYCP3 IF, red. 5 µm scale bar. **b.** Boxplots of the total autosomal SC length (µm) following no treatment or actinomycin D treatment. 3 mice analysed per treatment class. Bracketed values, number of nuclei score. ns, p>0.05 (Mann Whitney U test).

4.2.4 Chromosome Morphology on Transcription Inhibition

After observing a significant decline in nuclear area after transcription inhibition, I next investigated its effect on a chromosomal level, by considering the morphology of chromosome 6, which contains the *HoxA* chromatin loop previously characterised in wildtype cells (Figure 3-2 and 3-3). As expected from total nuclear SC lengths (Figure 4-7), no change in the length of the chromosome 6 SC (~7.6 µm) was observed, following administration of actinomycin D (Figure 4-8b; p=0.25, Mann Whitney U test). Furthermore, the overall area of the chromosome 6 territory, highlighted by a chromosome 6 specific FISH paint, was significantly reduced from 90.8 ± 4.0 μm^2 to 33.8 ± 4.3 μm^2 (Figure 4-8c; $p<2.2x10^{-16}$, Mann Whitney U test). Thus, autosomal chromosome morphology closely corresponds to patterns observed on a nucleus-wide scale (Figure 4-6).

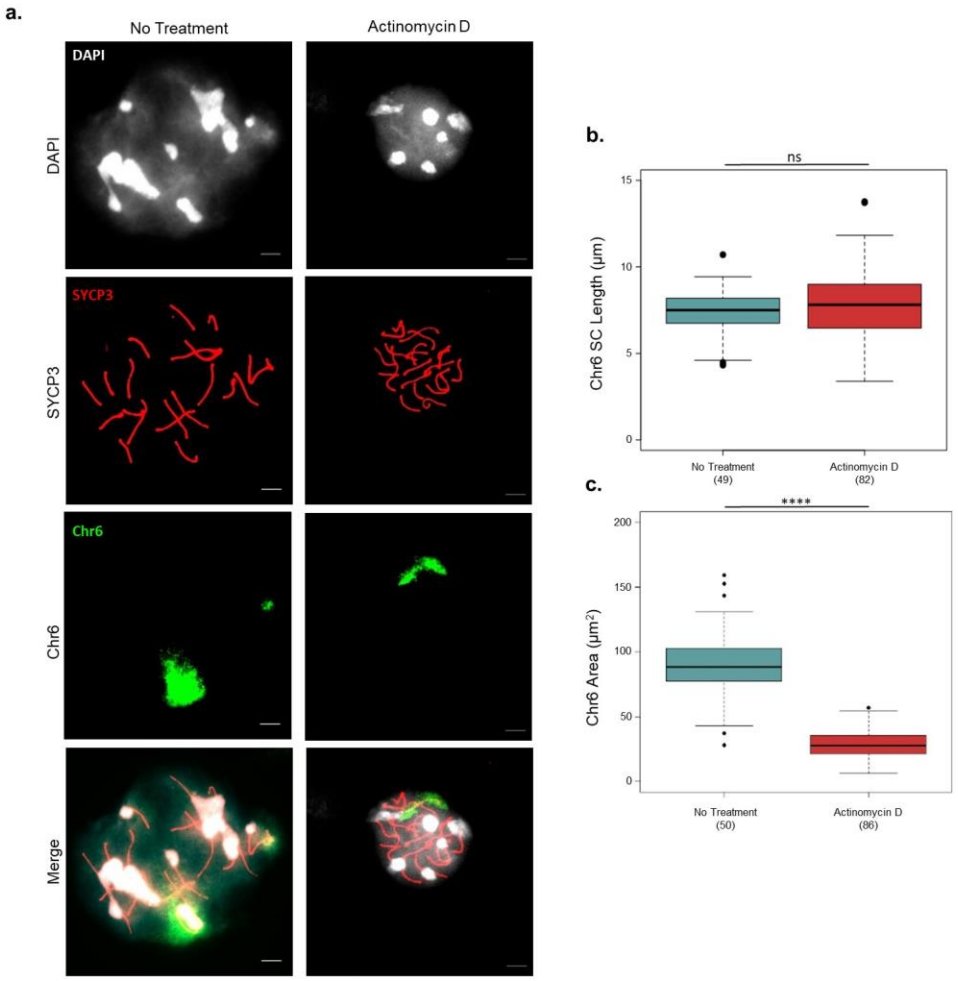

Figure 4-8. Effect of transcription inhibition on autosomal chromosome morphology. a. Representative images of chromosome 6 (Chr6) SC length and chromatin area following no treatment or actinomycin D treatment (50 µg/ml, 1hr). DAPI, white. Anti-SYCP3 IF, red. Chr6 paint, green. 5 µm scale bar. **b.** Boxplots of Chr6 SC length (µm) following no treatment or actinomycin D treatment. **c.** Boxplots of Chr6 territory area (μm^2) following no treatment or actinomycin D treatment. 3 mice analysed per treatment group. Bracketed values, number of nuclei scored. ****, $p<0.0001$; ns, $p>0.05$ (Mann Whitney U test).

At the zygotene-to-pachytene transition in males, the sex chromosomes spatially segregate to form the sex body (Handel, 2004), in which the unsynapsed region of the sex chromosomes are subject to large-scale transcriptional silencing (Turner, 2007). The effect of actinomycin D transcription inhibition on sex chromosome morphology was assessed, using chromosome paints specific to each sex chromosome (Figure 4-9). The area of both the X and Y chromosomes was significantly reduced following transcription inhibition by ~20% (X, $p=1.3x10^{-4}$; Y, p=0.019, Mann Whitney U test; Figure 4-9c and d). These results indicate that maintenance of sex chromosome morphology is dependent on a transcription-dependent component. Although the grossly silent sex chromosomes underwent an unexpected decline in overall area, considering their largely transcriptionally silent state (Turner, 2007), it is notable that the proportion of the total nucleus covered by the X chromosome increased >2-fold after transcription inhibition ($p=<2.2x10^{-16}$, Mann Whitney U test; Figure 4-9e). This finding indicates that the autosomes are likely to experience more compaction, compared with the sex chromosomes, on transcription inhibition.

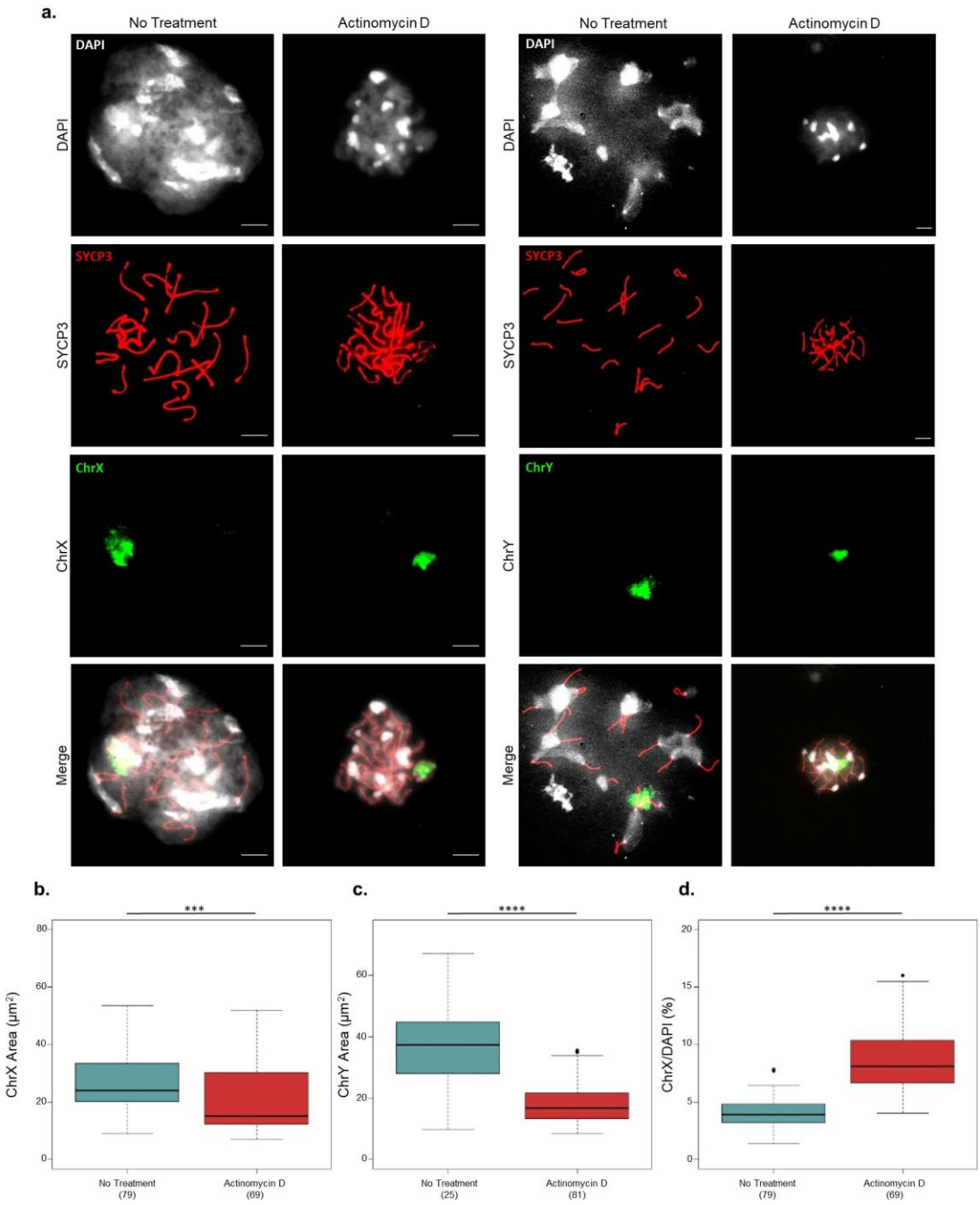
a.
No Treatment
Actinomycin D
No Treatment
Actinomycin D
DAPI
SYCP3
ChrX
ChrY
Merge
b.
ChrX Area (µm²)
No Treatment (79)
Actinomycin D (69)
***
c.
ChrY Area (µm²)
No Treatment (25)
Actinomycin D (81)
****
d.
ChrX/DAPI (%)
No Treatment (79)
Actinomycin D (69)
****

Figure 4-9. Changes to sex chromosome morphology on transcription inhibition. a. Representative images of the X chromosome (ChrX) and Y chromosome (ChrY) chromatin area following no treatment or actinomycin D treatment (50 µg/ml, 1hr). DAPI, white. Anti-SYCP3 IF, red. ChrX paint, green. 5 µm scale bar. **b.** Boxplots of ChrX territory area (μm^2) following no treatment or actinomycin D treatment. **c.** Boxplots of ChrY territory area (μm^2) following no treatment or actinomycin D treatment. **d.** Boxplots of percentage of the nuclear area (DAPI) covered by ChrX following no treatment or actinomycin D treatment. 3 mice analysed per treatment group. Bracketed values, number of nuclei scored. ****, $p<0.0001$; ***, $p<0.001$ (Mann Whitney U test).

4.2.5 Local Chromatin Condensation on Transcription Inhibition

Once chromatin compaction on transcription inhibition was confirmed on a chromosome wide scale, its impact on a local level was next assessed. The area occupied by a SC-proximal (BAC-B; 169 kb) and a SC-distal BAC probe (BAC-D; 167 kb) on chromosome 6 were used as indicators of local chromatin condensation, which I presently define as the combination of chromatin compaction and clustering of chromatids (Figure 4-10). After transcription inhibition, the area of the SC-proximal region declined by ~1.4-fold ($p=0.0002$, Mann Whitney U test; Figure 4-10). However, no significant change was experienced at the SC-distal region which remained at ~1.4 μm^2 ($p=0.63$, Mann Whitney U test, Figure 4-10). These results suggest that transcription inhibition does not influence chromatin organisation uniformly across the genome. Since BAC FISH probe area is dependent on both overall chromatin compaction and/or the clustering of individual chromatin fibres, the SC-proximal locus may have experienced an increase in chromatin compaction and/or the clustering of individual chromatids on transcription inhibition.

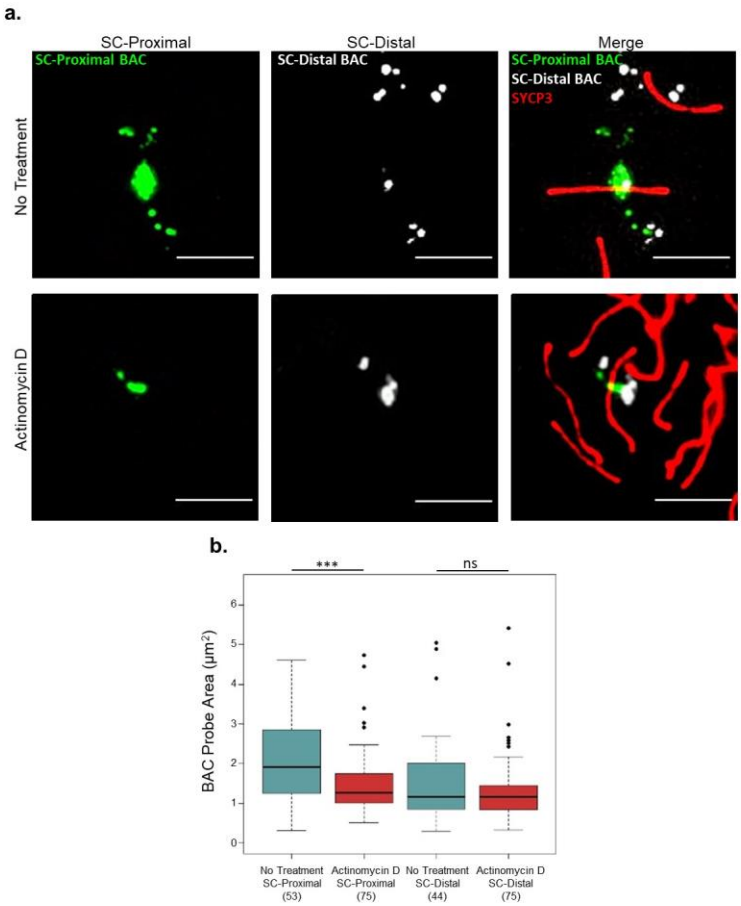

Figure 4-10. Changes to chromatin condensation on transcription inhibition. a. Representative images of the SC-proximal BAC probe (BAC-B) and a SC-distal BAC probe (BAC-D) following no treatment or actinomycin D treatment (50 µg/ml, 1hr). SC-proximal probe, green. SC-distal probe, white. Anti-SYCP3 IF, red. 5 µm scale bar. **b.** Boxplots of the area (μm^2) of a SC-proximal BAC probe and a SC-distal BAC probe following no treatment or actinomycin D treatment. 3 mice analysed per genotype and per probe. Bracketed values, number of nuclei scored. ***, $p<0.001$; ns, $p>0.05$ (Mann Whitney U test).

4.2.6 Chromatin Loop Organisation on Transcription Inhibition

After demonstrating that chromosome morphology was transcription dependent, the effect of transcription on individual chromatin loops was analysed. This was first examined by determining how the relative proximity of specific chromatin regions to the pachytene SC changed after transcription inhibition, through the administration of actinomycin D. The relative positioning of a SC-proximal (BAC-B) and a SC-distal region (BAC-D), within the chromatin loop defined in Chapter 3 (Figure 3-2), were examined using two specific BAC FISH probes (Figure 4-11). The positioning of the two chromatin regions relative to the SC was determined by assessing the frequency at which each BAC FISH probe visibly overlapped with the SC (anti-SYCP3 IF). The likelihood of BAC-SC overlap did not significantly change following transcription inhibition at the SC-proximal region (SC-proximal, $p=0.16$, Fisher's exact test). The SC-distal region increased in overlap frequency by ~20% (SC-distal, $p=0.049$, Fisher's exact test). These findings indicate that both regions were in proximity to the SC on transcription inhibition (Figure 4-11b). However, transcription inhibition did not affect the positioning of the two FISH probes relative to one another, as the SC-distal region remained significantly less likely to visibly overlap with the SC compared to the SC-proximal region ($p<0.0001$, Fisher's exact test; Figure 4-11b). This analysis revealed that transcription inhibition does not significantly disrupt the sequential path of chromatin away from the SC, at least at the resolution presently assessed.

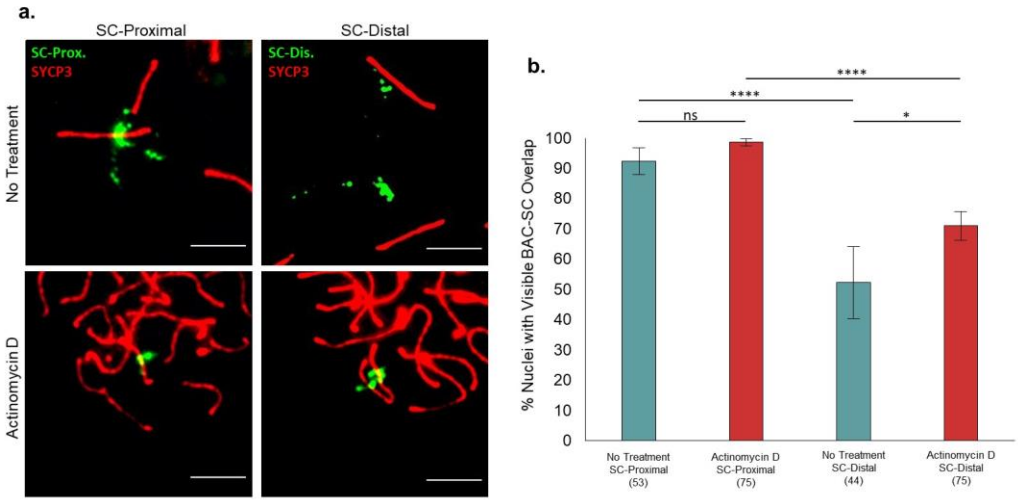

Figure 4-11. BAC FISH probe-based mapping of SC-Proximal and SC-distal regions after transcription inhibition. a. Representative images in spermatocytes of the visible BAC-SC overlap of two BAC probes defined as SC-proximal (BAC-B) and SC-distal (BAC-D) in wildtype spermatocytes following no treatment or actinomycin D treatment (50 µg/ml, 1hr). BAC probes, green. Anti-SYCP3 IF, red. 5 µm scale bar. **b.** Bar chart of the percent of pachytene meiocytes where each BAC probe visibly overlaps with the SC (anti-SYCP3 IF) following no treatment or actinomycin D treatment. 3 mice analysed per treatment group and per probe. Error bars, standard error. Bracketed values, number of nuclei scored. ****, p<0.0001 (Fisher's exact test).

4.2.7 Chromatid Organisation on Transcription Inhibition

As I had previously shown that chromatin extension from the pachytene SC is positively correlated with inter-chromatid distance (Figure 3-4), I next investigated whether chromatid organisation is affected by transcription inhibition (Figure 4-12). Inter-chromatid distance was determined by measuring the mean distance between the centroid coordinates of all four foci produced by a specific fosmid probe. Two fosmid probes were selected for analysis, the first representative of an SC-proximal locus (F-A) and the second representative of an SC-distal locus (F-C) on the chromosome 6 *HoxA* loop in untreated spermatocytes (Figure 3-3). On transcription inhibition, the mean inter-chromatid distance reduced by ~2-fold at the SC-proximal locus, from 2.4 ± 0.26 µm to 1.3 ± 0.096 µm ($p<0.0001$, Mann Whitney U test), and ~3-fold at the SC-distal locus, from 5.4 ± 0.42 µm to 1.8 ± 0.11 µm ($p<0.0001$, Mann Whitney U test). Therefore, chromatid separation and tether-to-fosmid distance, presuming no change in the positive correlation between chromatid separation and tether-to-fosmid distance, was considerably reduced after transcription inhibition.

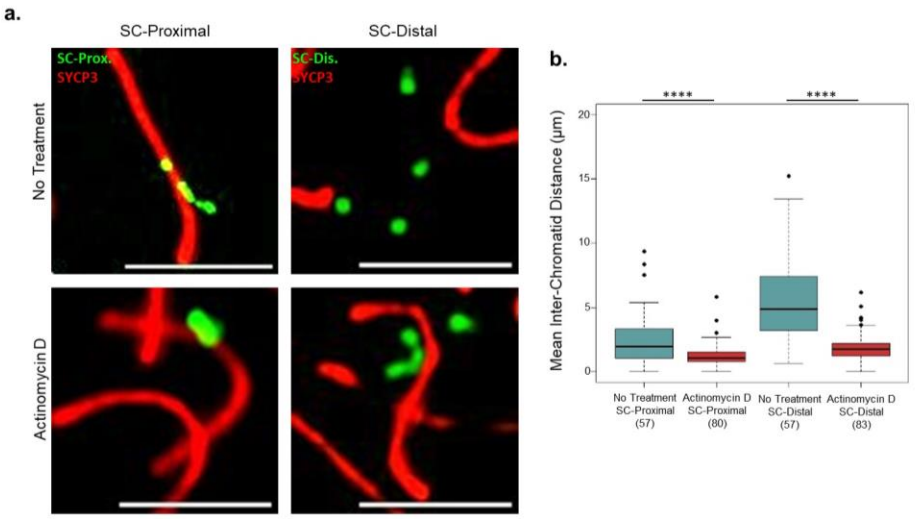

Figure 4-12. Changes to chromatid organisation on transcription inhibition. a. Representative images of inter-chromatid distance for a SC-proximal locus and a SC-distal locus following no treatment or actinomycin D treatment (50 µg/ml, 1hr). Fosmid FISH probe, green. Anti-SYCP3 IF, red. 5 µm scale bar. **b.** Boxplots of the average inter-fosmid distance (µm) per nucleus for the SC-proximal and the SC-distal fosmids following no treatment or actinomycin D treatment (50 µg/ml, 1hr). 3 mice analysed per genotype and per probe. Bracketed values, number of nuclei scored. ****, $p<0.0001$ (Mann Whitney U test).

4.2.8 Nuclear Organisation on RNase Treatment

Emerging evidence has indicated that an RNA component has the capacity to manipulate chromatin structure in interphase cells (Maison *et al*., 2002; Nozawa and Gilbert, 2019). I subsequently examined whether the maintenance and stability of pachytene chromatin structures was reliant on an RNA component. To investigate this idea, I assessed the effect of RNA degradation on the nuclear organisation of pachytene spermatocytes. Triton X-100-permeabilised spermatocytes were treated with RNase for ten minutes and one hour, to compare its effects acutely and over a time period comparable to the previous actinomycin D treatments. Each treatment was administered to a pachytene-enriched cell population, to enable the effect of RNA degradation to be assessed specifically within the pachytene population. Over both time-periods an >90% reduction in RNA was observed (Figure 4-13b). RNA degradation induced a 1.5-2-fold decline DAPI area after ten minutes and one hour (Figure 4-13c; 10 mins, p=<0.0001; 60 mins, p=0.00014, Mann Whitney U test). Together these findings indicate that an RNA component is required for the maintenance of chromatin morphology, causing the DNA to undergo considerable compaction after the removal of RNA. Intriguingly, RNase-induced nuclear compaction was ~1.5-2-fold less than that induced by RNA polymerase inhibition (Figure 4-6), implying the effect of transcription inhibition is not solely dependent on RNA synthesis.

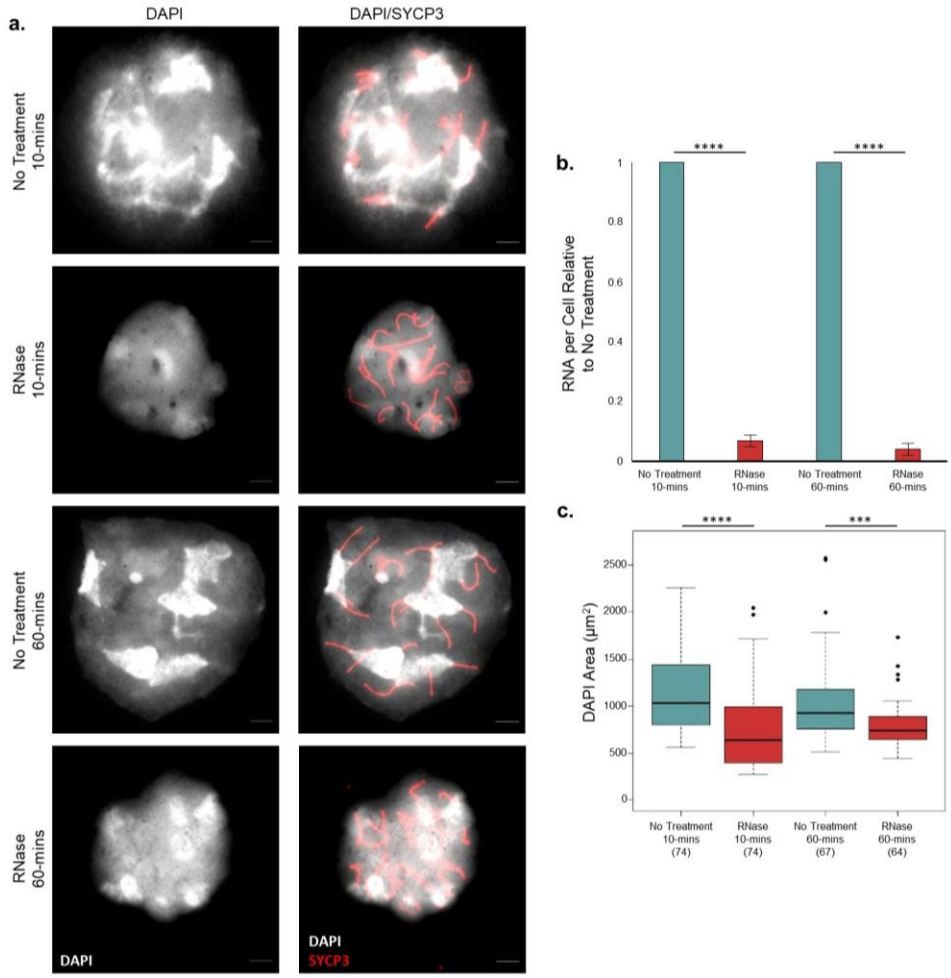

Figure 4-13. Changes to nuclear architecture on RNase treatment. a. Representative images of Triton X-100 permeabilised pachytene spermatocytes following no treatment and RNase (1 mg/ml) treatment for 10 minutes and 60 minutes. DAPI, white. Anti-SYCP3 IF, red. 5 µm scale bar. **b.** Bar chart of RNA concentration per cell relative to no treatment following 10- and 60-minutes RNase treatment. Error bars, standard deviation. ****, p <0.0001 (One-tailed T-test). **c.** Boxplots of DAPI area (µm^2) following no treatment and RNase treatment for 10- and 60-minutes. 3 mice analysed per treatment class. Bracketed values, number of nuclei score. ****, p<0.0001; ***, p<0.001 (Mann Whitney U test).

4.2.9 Transcription and the Positioning of Chromatin Regions Relative to the SC

After recognising that transcription has a significant role in the manipulation of chromatin organisation at nuclear, chromosomal and individual chromatin loop level in meiotic prophase I, I examined how transcriptional activity corresponds with the positioning of specific genes relative to the SC. In the first instance, I compared the *HoxA* chromatin loop maps, previously defined in Chapter 3 in the IF-FISH BAC-SC overlap assay(Fig 3-2), with pachytene RNA polymerase 2 and H3K4me3 ChIP-seq and RNA-seq signals, as markers of transcriptional activity (Figure 4-14). Intriguingly, RNA polymerase 2 ChIP-seq and RNA-Seq peaks were enriched in the SC-distal region, defined by a relatively lower BAC-SC overlap frequency (Figure 4-14). H3K4me3 ChIP-seq signals did colocalise with RNA polymerase 2 ChIP-seq and RNA-seq signals in the SC-distal region but they were also present in SC-proximal regions. This disparity is likely due to transcription-independent H3K4me3 signals occurring at SC-proximal regions. These data indicate that the large-scale chromatin loop at the *HoxA* locus is spatially associated with gene activation, leading to the enrichment of transcriptionally active signals in loop-associated sequences.

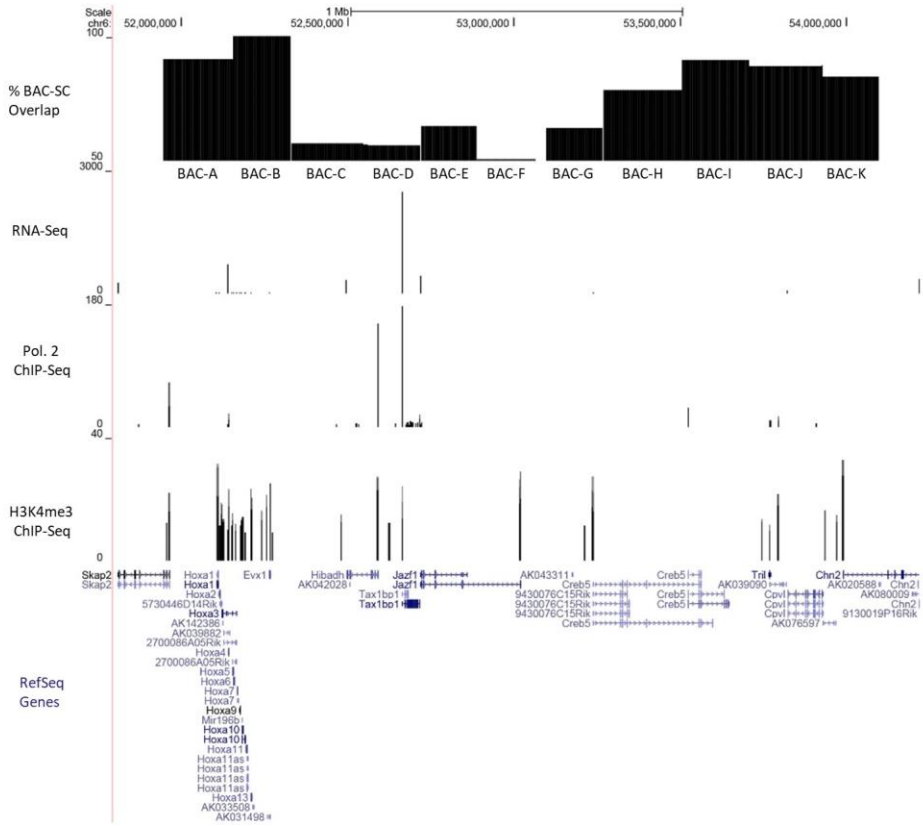

Figure 4-14. Transcription in the *HoxA* Defined Chromatin Loop. The frequency of BAC-SC overlap (%) acts an indicator of the positioning of the chromatin region, highlighted by the BAC FISH probe, relative to the pachytene SC (Figure 3-2). A relatively higher BAC-SC overlap score indicates greater SC proximity. Black tracks: pachytene RNA-Seq signal (GEO: GSE83264), pachytene RNA polymerase 2 (Pol2) ChIP-Seq (GEO: GSM1083638) and pachytene H3K4me3 ChIP-Seq (GEO: GSM2374727) generated from C57BL/6 mice (mm9). Purple track, RefSeq genes.

To determine whether the apparent enrichment of transcriptional activity in meiotic chromatin loops observed at the *HoxA* (Figure 4-14) is a conserved phenomenon, two additional genes were selected for the same analysis: *Spata4*, which has a relatively high transcriptional activity (8,131 FPKM) and *Gtf2e2,* which has a relatively lower transcriptional activity (2,046 FPKM) in pachytene according to RNA-seq data (GEO: GSE83264). The relative positioning of each gene and two regions flanking (± ~500 kb) regions to the SC were assessed. At the *Spata4* gene, the gene BAC probe was significantly less likely to overlap with the SC than the two flanking regions (F1 and F2 p<0.0001, Fisher's exact test, Figure 4-15). While at the *Gtf2e2* gene, only one of the flanking BAC probes was more likely to overlap with the SC than the gene BAC probe (F1, p=0.73; F2, p<0.0001, Fisher's exact test, Figure 4-15). Furthermore, pachytene RNA polymerase 2 and H3K4me3 ChIP-seq and RNA-seq signals were largely enriched in the SC-distal 'gene' regions, confirming its transcriptional activity. Together, these results demonstrate that transcriptionally active loci co-localise with SC-distal loop regions.

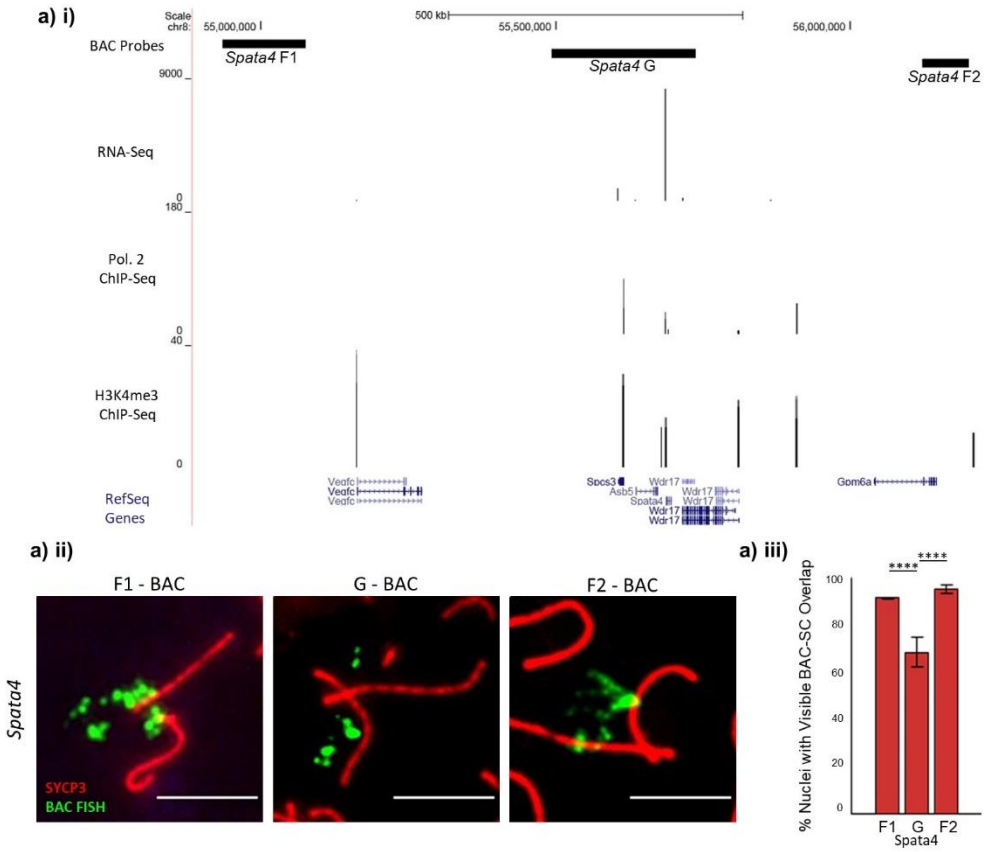

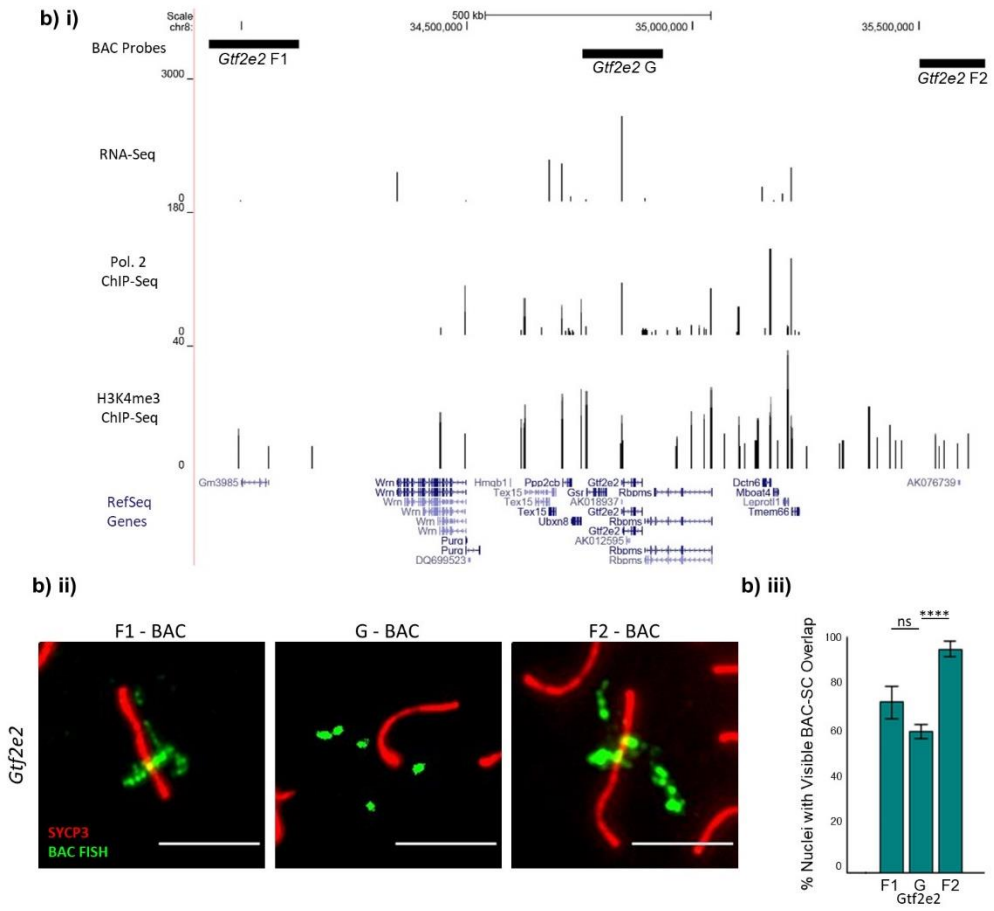

Figure 4-15. The relative positioning of the pachytene SC and transcriptionally active genes. Genomic locations of BAC FISH probes at *Spata4* **(a)** and *Gtf2e2* **(b)**. **i)** Three BAC FISH probes were used per gene: G, located over gene of interest; F1 and F2, located at flanking regions ± ~500 kb. Black tracks: pachytene RNA-Seq signal (GEO: GSE83264), pachytene RNA polymerase 2 (Pol2) ChIP-Seq (GEO: GSM1083638) and pachytene H3K4me3 ChIP-Seq (GEO: GSM2374727) generated from C57BL/6 mice (mm9). Purple track, RefSeq genes. **ii)** Representative images in spermatocytes of the visible BAC-SC overlap of three BAC probes F1, G and F2. BAC probe, green. Anti-SYCP3 IF, red. 5 µm scale bar. iii) The percent of pachytene spermatocyte nuclei where the BAC probe visibly overlaps with the SC (SYCP3) signal for flanking (F1 and F2) and gene (G) BAC FISH probes at *Spata4* ***(a)*** and *Gtf2e2* ***(b)***. ****, p<0.0001; ns, p>0.05 (Fisher's exact test). 3 mice analysed per BAC. Error bars, standard error. Nuclei scored: *Spata4* F1, 84; G, 79; F2, 87; *Gtf2e2* F1, 80; G, 85; F2, 82.

4.3 Discussion

4.3.1 Chromatin Organisation in Meiotic Prophase I

Chromosomes are dynamically regulated throughout meiotic prophase I, as homologs undergo pairing, synapsis and desynapsis, while the length of specific chromatin extensions increases from leptotene through to pachytene (Kauppi *et al*., 2011; Patel *et al*., 2019). Such striking organisational procedures occur in the context of sequential chromatin loop arrays. However, evidence regarding the temporal formation and maintenance of chromatin looping during mammalian meiotic prophase I is scarce.

In Chapter 3, a single chromatin loop was mapped relative to the pachytene SC (Figure 3-2 and 3-3). Importantly, such approaches are hindered in earlier stages of prophase I, as axis assembly, pairing and synapsis prevents corresponding chromosome axes and chromatin regions being reliably identified through IF-FISH. Consequently, complete loop topology could not be delineated in leptotene using an equivalent IF-FISH approach to that performed in pachytene. In order to gain further insight into meiotic chromatin loop dynamics between leptotene and pachytene, alternate loop mapping strategies must be explored. One means by which this may be achieved is through heightening the resolution of the FISH-based analysis. For instance, by utilising fosmid or oligonucleotide FISH probes to assess the frequency at which specific chromatin regions overlap with IF markers of chromosome axes, to identify putative axis-association sites. However, the interpretation of the data generated by such a strategy may prove challenging, since it is presently not clear whether axis-association sites are conserved between cells or individual chromatids during leptotene.

To advance current understanding of chromatin organisation in early prophase I, without relying on the relative positioning of loci to the chromosome axis, the mean presumptive inter-sister chromatid distances were compared between a pachytene-defined SC-proximal and a SC-distal region in leptotene. This analysis demonstrated that the two regions are cytologically distinguishable in leptotene, as presumptive inter-sister chromatid distances were greater at the SC-proximal locus (~1.8 µm), compared to those at the SC-distal locus (~1.3 µm). Surprisingly, these values are considerably greater than those observed during the mitotic cell cycle (~500 nm in G2

and ~750 nm in mitosis), although this may be accounted for by the surface-spreading of spermatocytes.

Intriguingly, since the SC-distal and SC-proximal loci exhibit distinct presumptive inter-sister chromatid distances, the underlying mechanisms responsible for this difference are likely to act in a site-specific manner. One potential means by which sister chromatid separation is differentially regulated between loci is through their relative proximity to cohesive cohesin complexes, which would imply that in leptotene the SC-distal locus is in greater proximity to cohesive cohesin than the SC-proximal locus (Figure 4-16). Furthermore, during the mammalian mitotic cell cycle, sister chromatid separation is reliant not only on the distribution of cohesin, but also transcriptional activity (Azuara *et al*., 2003; Mlynarczyk-Evans *et al*., 2006; Stanyte *et al*., 2018). Loci residing in the vicinity of actively transcribed chromatin exhibited sister chromatid separation more frequently than those in silent regions during G2 (Stanyte *et al*., 2018). Therefore, inter-sister distance may be reliant on the combined influence of cohesin and transcriptional activity. Future comparative investigations are now required to establish whether a correlative relationship exists in mammalian meiocytes, between sister chromatid separation and the distribution of candidate regulatory factors, such as cohesin or transcriptional machinery, in leptotene.

Between leptotene and pachytene, homologous chromosomes become increasingly more intimately juxtaposed, preventing total inter-chromatid distance being directly comparable between leptotene and pachytene. To overcome this issue, the mean of the two shortest inter-chromatid distances was used as a proxy for the minimal possible inter-sister chromatid distance in pachytene, permitting a crude comparison of chromatid organisation, between leptotene and pachytene, to be performed. It was interesting to find that presumptive inter-sister chromatid distances declined at the SC-proximal locus. However, no change was observed at the SC-distal locus, or the two loci on the non-homologous X chromosome. Importantly, although the autosomal loci and loci on the non-homologous X chromosome behave comparably, it is possible that the relative positioning of sister chromatids might be subject to distinct modulatory mechanisms. Notably, one HiC study demonstrated that once pachytene is reached, sex chromosomes undergo a unique and dramatic organisational change (Patel *et al*., 2019). Thus, the maintenance of definite inter-sister chromatid distances generated at X-linked loci are not necessarily a faithful representation of sister chromatid behaviour at autosomal loci.

Considering the putative site-specific changes in chromatid organisation at autosomal loci over time, it is tempting to question whether the same loop structure is present in both leptotene and pachytene. Presumably, the only way the same pachytene loop structure exists in leptotene would be if the chromosome axes affiliated with each sister chromatid are far apart from one other. However, this proposition conflicts with EM imaging of the axes in leptotene where the axes are shown to in proximity with one another (Zickler and Kleckner, 1999). Instead, I propose an alternate hypothesis in which sister chromosome axes are coaligned in leptotene and chromatin loop topology is distinct from pachytene. Although the mechanisms behind such rearrangements are not known, it is interesting to consider how the relative positioning of specific loci to cohesive machinery, such as cohesin, change over time (Figure 4-16a and b). Such models suggest that the SC-proximal locus increases in proximity to a cohesive cohesin complex between leptotene and pachytene. Cohesin is highly enriched at the chromosome axis, thus the above models could infer that the SC-proximal locus increases in proximity to the chromosome axis as prophase I progresses, while the relative positioning of the SC-distal locus is conserved. This proposition would appear to juxtapose observations, which have indicated that chromatin loops extend over time, as inferred by an increase in BAC FISH probe area (Kauppi *et al*., 2011) and in the inter-contact distances defined by HiC (Patel *et al*., 2019). This juxtaposition could be overcome if SC-proximal sister chromatids become more intimately co-aligned at cohesin enriched sites, as spermatocytes transition from leptotene to pachytene (Figure 4-16c). Furthermore, it is crucial during the interpretation of such analyses, to acknowledge the caveat that presumptive inter-sister chromatid distances cannot act as definitive representations of inter-sister chromatid distances, which could be considerably greater than the minimal possible values presently discussed.

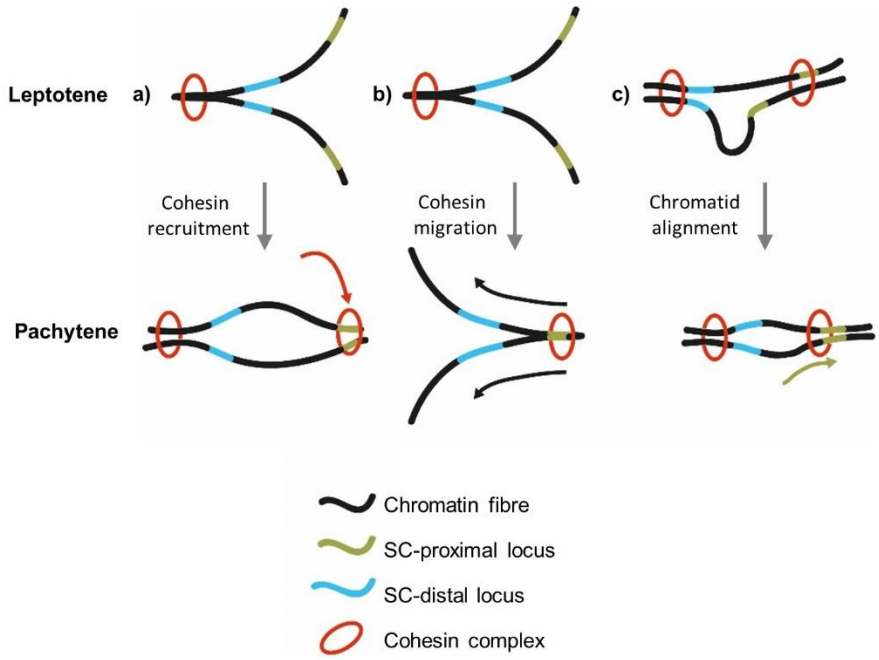

Figure 4-16. Models of cohesin-dependent modulation of sister chromatid organisation at a SC-proximal and a SC-distal locus between leptotene and pachytene. In leptotene **a)** and **b)**, the SC-distal locus is in greater proximity to the cohesin complex compared to the SC-proximal locus and in **c)**, SC-distal chromatids are in greater alignment than the SC-proximal chromatids. As a consequence of both arrangements sister chromatids appear more intimately juxtaposed at the SC-distal locus compared to the SC-proximal locus. In pachytene, a cohesin complex is recruited to the SC-proximal locus **(a)**, the chromatin undergoes extrusion as a cohesin complex migrates along a chromatin fibre **(b)** or chromatids become aligned **(c)**, causing the chromatids at SC-proximal locus to be positioned in greater physical proximity compared to at the SC-distal locus.

To conclusively ascertain whether inter-sister chromatid distances alter over time at autosomal loci, alternate FISH-based approaches could be employed, which enables the visible discrimination of homologous and sister chromatids. One means by which this might be achieved, is by crossing two genetically modified mouse lines, which each possess a specific non-homologous sequence at the same genomic region. This strategy would enable custom FISH probes specific to each sequence to differentiate homologous chromatids. During the design of such non-homologous sequences, it would be important to consider the length of the inserts to ensure they are sufficient to enable accurate discrimination of the homologous chromatids, while minimising the risk of disrupting the homology search or chromatin loop architecture. These analyses should assess the spatial organisation of chromatids between leptotene and

pachytene, as such temporal analyses would not only reveal novel aspects of chromatid organisation, but may also help to improve present understanding of a functional relationship between chromatid positioning and the progression of meiotic recombination during prophase I.

4.3.2 Transcription and Pachytene Chromatin Organisation

During pachytene, the distance of specific loci relative to the SC and inter-chromatid distances did not correlate with SC length and thus the progression of pachytene. This observation complements HiC data, which showed that the boundaries of large-scale chromatin structures mapped in pachytene, are relatively stable with high strength scores of ~75% (Vara *et al*., 2019). Taken together, these data point towards the presence of active or fixed structural machinery, responsible for maintaining chromatin organisation in pachytene spermatocytes.

A historic EM study has previously shown that global inhibition of RNA polymerase causes meiotic autosomes to appear amorphous in mice, as chromatin extensions from the SC were reduced in length and visualisation of the SC was obscured (Handel, Caldwell and Wiltshire, 1995). In agreement with the EM study, inhibition of transcription initiation and elongation corresponded with a reduction in the area which chromatin covers on a chromosomal and nuclear scale as the physical distance chromatin extends from its respective SC declines. Furthermore, SC length measurements showed that transcription inhibition had no significant impact on basic SC topology, thus changes in chromatin morphology occurred independently of cytologically evident changes in SC organisation. The relative positioning of SC-distal and SC-proximal regions to the pachytene SC was maintained on transcription inhibition, inferring that no drastic change in the patterning of axis-association sites occurs. However, this assay was conducted at a relatively low-resolution, with BAC FISH probes spanning ~200 kb, meaning that I cannot discount the possibility that the apparent reduction in the physical length of chromatin extensions on transcription inhibition results due to an increase in the number or length of axis-association sites below the current resolution limitations. It is important to mention, conversely to prior and present cytological analyses, one study has previously demonstrated that HiC-defined structures remained unchanged after transcription inhibition (Wang *et al.,* 2019). This may be explained by the distinct nature of cytological and HiC readouts,

as spatial configurations of chromatin are altered, without significant implications on the likelihood of contact frequencies between specific loci being affected. However, it is presently not clear whether the transcription-dependent change in chromatin extensions results from an increase in chromatin compaction/chromatid clustering and/or the positioning of axis-association sites, as has been observed in interphase cells and yeast meiocytes (Figure 4-17; Björkegren and Baranello, 2018; Davidson *et al*., 2017; Stigler *et al.*, 2016; Sun *et al.*, 2015). To investigate this uncertainty, the resolution of the IF-FISH assay should be heightened by employing shorter FISH probes, such as a fosmids, to track potential changes in axis-associated sites and chromatin compaction on transcription inhibition.

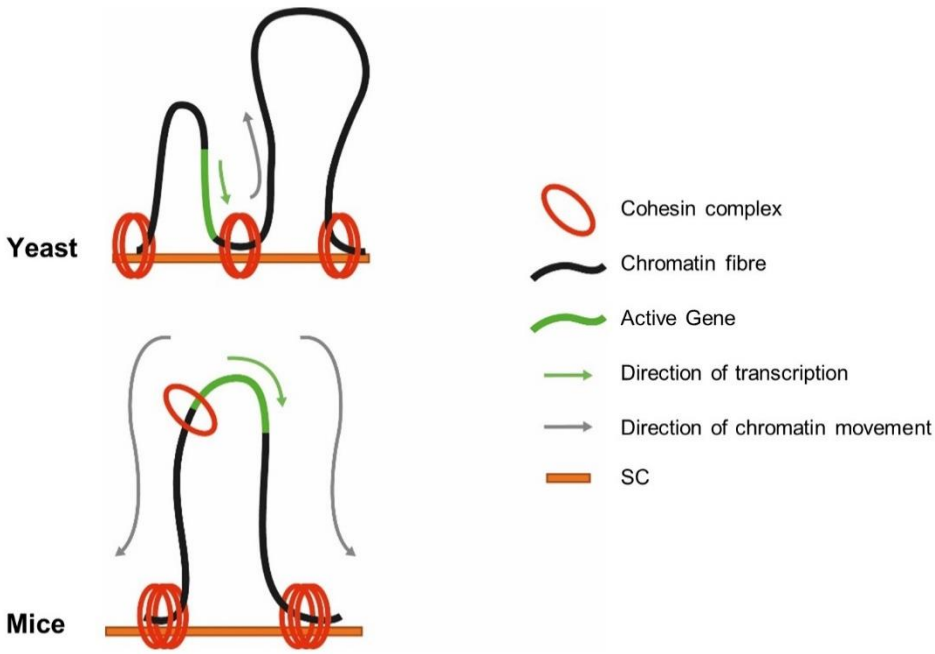

Figure 4-17. Model of transcription- and cohesin-dependent chromatin loop extension relative to the meiotic chromosome axis in yeast and murine meiocytes. Cohesin forms a topological link between the chromosome axis and meiotic chromatin. In yeast on the activation of transcription, the elongating RNA polymerase II drives the cohesin along the chromatin fibre, presumably as it is unable to bypass the cohesin ring. Corresponding changes in chromatin loop length are dependent on the dynamics of the opposing axis-association site/convergent transcription and the directionality of transcription. In mice, cohesin co-localises at the 5' end of the gene and a presently uncharacterised transcription-dependent mechanism promotes chromatin loop extension causing transcriptionally active genes to appear distal from the pachytene SC.

Intriguingly, the transcription-dependent refocusing of axis-associated sites, as observed by Sun *et al.* in *S. cerevisiae* (Figure 4-17), is reliant on the redistribution of cohesin, which topologically entraps chromatin at the chromosome axis. However, in mice >80% of cohesin binding sites, defined by REC8/RAD21L ChIP-seq, binds within 2 kb of transcriptional start sites in mouse prophase I (Vara *et al*., 2019). This distance is considerably shorter than the length of chromatin loops predicted by my IF-FISH (Figure 3-3 and Figure 3-4) and published HiC data (Patel *et al*., 2019). A plausible explanation for this is that only a subset of cohesin enrichment sites are exploited to create the cohesin-defined loops at the chromosome axis, whilst additional cohesin looping may occur within the axis-defined loop boundaries. However, these data also point to the possibility that cohesin is not involved in the manipulation of transcription-dependent chromatin loop topology in mammalian meiocytes and alternate factors, such as condensin may be involved. Indeed, the deletion of cohesin in mammalian spermatocytes does not conform to the complex acting as an loop extrusion factor, since chromatin loops become longer in the absence of cohesin (Novak *et al*., 2008; Revenkova *et al*., 2004). In addition, transcriptionally active genes were enriched in SC-distal regions, unlike in yeast meiocytes where axis-association sites were positioned within ~150 bp of the 3' untranscribed region of genes (Sun *et al*., 2015). This indicates that, if transcription-dependent refocusing of axis-association sites occurs in mammalian meiocytes, it is unlikely to be due to RNA polymerase II directly driving an axis-associated factor along a chromatin fibre. Instead, such redistributing forces may act indirectly through transcription-dependent alterations in DNA supercoiling, or the continued migration of the mobile axis-association factors passively along the chromatin fibre, until an obstacle is met.

Based on cytological analyses a correlative link between the maintenance of pachytene morphology and a transcriptional component has become evident. However, these transcription inhibition experiments were reliant on non-discriminatory transcriptional inhibitors, with nucleus-wide effects. Although the inhibition of RNA polymerase had a substantially greater effect on nuclear compaction than RNA degradation, suggesting that the initiation and/or elongation of transcription is involved in structurally manipulating pachytene chromatin organisation, a significant caveat of such global treatments is that alterations in chromatin structure may result as a by-product of the perturbed expression of one or multiple essential structural proteins. To address this drawback, I suggest a more refined experiment is conducted, in which the promoter of a transcriptionally active, non-essential gene is deleted through

CRISPR-Cas9 editing, whereupon transcription-dependent changes to chromatin architecture can be assessed. Such an approach would reduce the risk of misexpression of genes encoding fundamental, structural components.

In addition, it is interesting to note that marks of active transcription are enriched within loop-associated sequences in wildtype spermatocytes. This finding is consistent with super-resolution imaging of epigenetic marks, indicative of active and repressive transcription, which demonstrated that open, active chromatin emanates into chromatin loop, while closed, silent chromatin clusters in proximity to the SC (Prakash *et al*., 2015). Several HiC studies have reported that strong pairwise contacts tend to colocalise with sites of transcriptional activity (Alavattam *et al*., 2019; Patel *et al*., 2019; Wang *et al.,* 2019). Thus, in combination, the IF-FISH maps generated presently and the HiC data suggest that inter-loop contacts create transcriptional 'hubs' (Patel *et al*., 2019), which could feasibly improve the efficiency of gene expression regulation and therefore encourage the evolutionary drive for chromatin loop formation and maintenance in meiocytes.

4.3.3 RNA and Pachytene Chromatin Organisation

Although RNA degradation does not have as significant an impact on nuclear compaction as the inhibition of RNA polymerase, RNase was found to reduce the nuclear area of spermatocytes, suggesting that an RNA component is involved in the manipulation of meiotic chromatin architecture, in addition to the activity of RNA polymerase. This observation appears compliant with emerging evidence in interphase cells, in which negatively charged chromatin associated RNA (caRNA) works cooperatively with heterogeneous nuclear ribonucleoproteins (hnRNPs) to form a dynamic nuclear mesh. This mesh has been likened to water, that prevents the chromatin 'sponge' from shrinking, overcoming the natural tendency of chromatin to self-associate (Hall and Lawrence, 2016; Nozawa and Gilbert, 2019). Furthermore, the structural influence of RNA is not necessarily constrained to the local vicinity of its associated gene. This proposition may help to explain why the grossly silent sex chromosomes underwent compaction on transcription inhibition, since the reduction in RNA synthesis reduced the strength of the nuclear mesh throughout the entire nucleus. To determine the exact structural role of RNA in meiocytes, further

characterisation of the range and turnover of caRNA species in the meiotic nucleus, as well as the proteins which interact with them, will be necessary.

It is sensible to acknowledge that the RNase experiment conducted presently is relatively crude, therefore it will be important in future investigations to refine the experimental procedure: firstly, RNA degradation was confirmed through quantifying RNA abundance following RNA extraction. Resultantly, I cannot exclude the possibility that RNA degradation occurred subsequent to cell lysis and RNA extraction. One alternate strategy to quantify the global RNA abundance *in vivo* is through pulse-labelling with 5-ethynyl uridine (5EU), which rapidly permeates cells, incorporates into nascent RNA and can be detected with a click reaction, using a fluorescent azide. Attempts to conduct such analyses were made, but spermatocyte uptake of uridine analogs was poor, compared to cultured NIH3T3 cells, thus further optimisation is required. And secondly, similarly to the transcription inhibition experiments, nuclear compaction on RNase treatments may result as a primary effect of RNA degradation, or a secondary effect of genetic misexpression. To discriminate between these two possibilities the natural RNase activity of the *Neisseria meningitidis* Cas9 (Rousseau *et al.*, 2018) could be exploited to target specific RNA sequences of interest for degradation, ensuring that only a specific RNA variant or family were targeted.

Chapter 5:

Chromatid Organisation and Meiotic Recombination in Mouse Meiocytes

Chapter 5 Chromatid Organisation and Meiotic Recombination in Mouse Meiocytes

5.1 Introduction

Across the mouse genome, only a small subset of meiotic DSBs mature into crossovers (COs; Baudat and de Massy, 2007). An increasingly complex picture of the regulatory pathways linking meiotic DSBs to COs is evolving, describing the balance between multiple reparative strategies, including homolog- and sister chromatid-mediated recombination, synthesis-dependent strand annealing and non-homologous end joining. As well as the processes of CO designation and maturation, dictated by phenomena such as CO interference (COI).

Several studies have highlighted a strong correlative relationship between large-scale chromatin organisation and CO generation in mammalian meiocytes; as CO frequency commonly rises with SC length and is inversely related to the length of chromatin extensions (Baier *et al.*, 2014; Froenick *et al.*, 2002; Gruhn *et al.*, 2013; Kauppi *et al.*, 2011; Lynn *et al.*, 2002; Tease and Hultén, 2004). Some of the earliest findings to establish a relationship between chromosome organisation and CO abundance were made through comparative analyses between human males and females, where female SC length and chiasmata number were double that observed in males (Bojko, 1985; Petkov *et al.*, 2007; Rasmussen and Holm, 1978; Tease, Hartshorne, and Hultén, 2002). More recently, immunofluorescence-fluorescent *in situ* hybridisation (IF-FISH)-based analyses also demonstrated that the width of chromosomal territories is ~25% less in human females, relative to males (Gruhn *et al*., 2013). A similar pattern has been observed in mice, where SC length is ~2-fold greater in females, compared to males, again showing these features vary co-ordinately with an elevated CO frequency in females (Lynn, 2005). Additionally, the width of the SC is sexually dimorphic, as a significantly narrower SC is present in females compared to males (Agostinho *et al*., 2018). These findings point to a mechanistic link between the control of CO formation and specific features of chromosome morphology. However, although a clear correlation between these features is evident, it is not presently known how they inter-relate to dictate the fate of meiotic DSBs. Importantly, such analyses are yet to directly elucidate the relationship between CO formation and chromosome organisation, at the level of individual chromatin loops. Therefore, the principle aim of this chapter was to conduct

comparative analyses of chromatin loop organisation, between mouse meiocytes and loci of differing recombinogenic activities.

5.2 Results

5.2.1 Comparing Chromosome Loop Morphology in Male and Female Pachytene Meiocytes

Previous studies in mice and humans, suggest an association between SC length and CO frequency (Lynn *et al*., 2002; Tease and Hultén, 2004). To verify this relationship, total autosomal SC lengths (anti-SYCP3 IF) were compared between males and females (Figure 5-1b), as oocytes are known to generate ~2-fold more COs relative to spermatocytes (Petkov *et al*., 2007). Consistently with prior IF and EM studies, total SC length was ~2-fold greater in females, relative to males (Figure 5-1b). Chromatin morphology was also compared at the chromosomal level, where the length of chromosome 6 SC was found to be ~1.6-fold greater in females than males, extending an average of 13.21 ± 0.47 µm, compared to 8.40 ± 0.13 µm in males (Figure 5-1c). Whole chromosome morphology has yet to be compared between male and female mice, therefore the size of chromosome territories was next compared between the sexes. By measuring the territory area, highlighted by a chromosome 6 specific FISH probe, male chromatin was found to cover an ~1.2-fold greater area (76.83 ± 0.2.97 μm^2) than in females (62.86 ± 0.2.86 μm^2; Figure 5-1d). Taken together, these results show a marked difference in both SC organisation and chromatin morphology between sexes; chromosomes appear longer and thinner in oocytes, relative to spermatocytes. Moreover, these observations complement prior investigations, which proposed an inverse correlation between the length of the SC and chromatin extensions (Revenkova *et al*. 2004; Kolas *et al*. 2004).

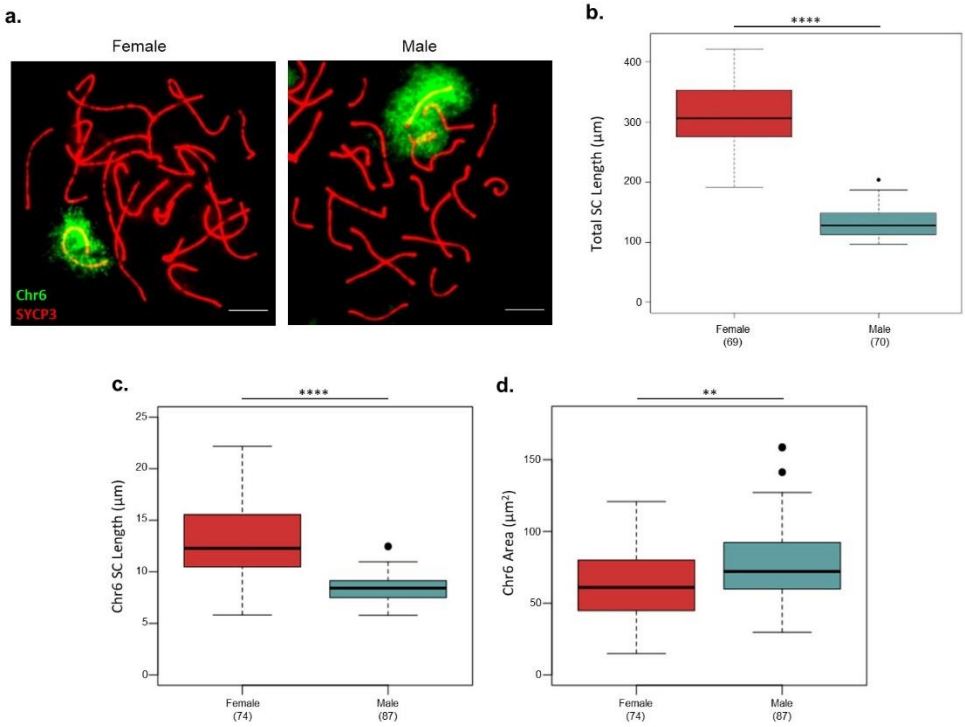

Figure 5-1. Differences in pachytene chromosome morphology between males and females. a. Representative images of chromosome 6 SC length and chromatin area in male and female meiocytes. Chr6 paint, green. Anti-SYCP3 IF, red. 5 µm scale bar. **b.** Boxplots of total SC length (µm) in male and female meiocytes. **c.** Boxplots of chromosome 6 SC length (µm) in male and female meiocytes. **d.** Boxplots of chromosome 6 paint territory area (μm^2) in male and female meiocytes. 3 mice analysed per sex. Bracketed values, number of nuclei scored. ****, $p<0.0001$; **, $p<0.01$ (Mann Whitney U test).

Following characterisation of the sex-specific differences in chromosome-wide chromatin morphology, IF-FISH analysis was refined by comparing chromatin organisation at the level of a single chromatin loop, which I had previously defined in spermatocytes, across the *HoxA* cluster at 6qB3 (Figure 3-2). Initially, three BAC FISH probes were selected to determine whether the positioning of an SC-distal region and two flanking SC-proximal regions were conserved between spermatocytes and oocytes (Figure 5-2). The relative positioning of the three chromatin regions to the SC was determined by measuring the frequency at which the associated BAC probe visibly overlapped with the anti-SYCP3 IF signal; a greater frequency of overlap is indicative of a greater physical proximity to the SC. No significant difference was seen in the frequency of SC overlap by the two BAC probes, defined as SC-proximal in males between males and females (Figure 5-2d; BAC-B p=0.59; BAC-I p=1, Fisher's exact test). However, the relative positioning of the SC-distal region to the SC observed in males was not conserved in females, with a 49% rise to 91% in the likelihood of overlap with the SC (Figure 5-2d; p=0.0001, Fisher's exact test). These results support chromosome-wide FISH paint probe analysis (Figure 5-1), which indicated that both male-defined SC-proximal and SC-distal regions are in proximity to the longer pachytene SC in females. It is important to highlight, the proximity of chromatin to the female SC prevents the BAC-SC overlap assay from accurately defining chromatin loops, according to the positioning of SC-distal and SC-proximal regions.

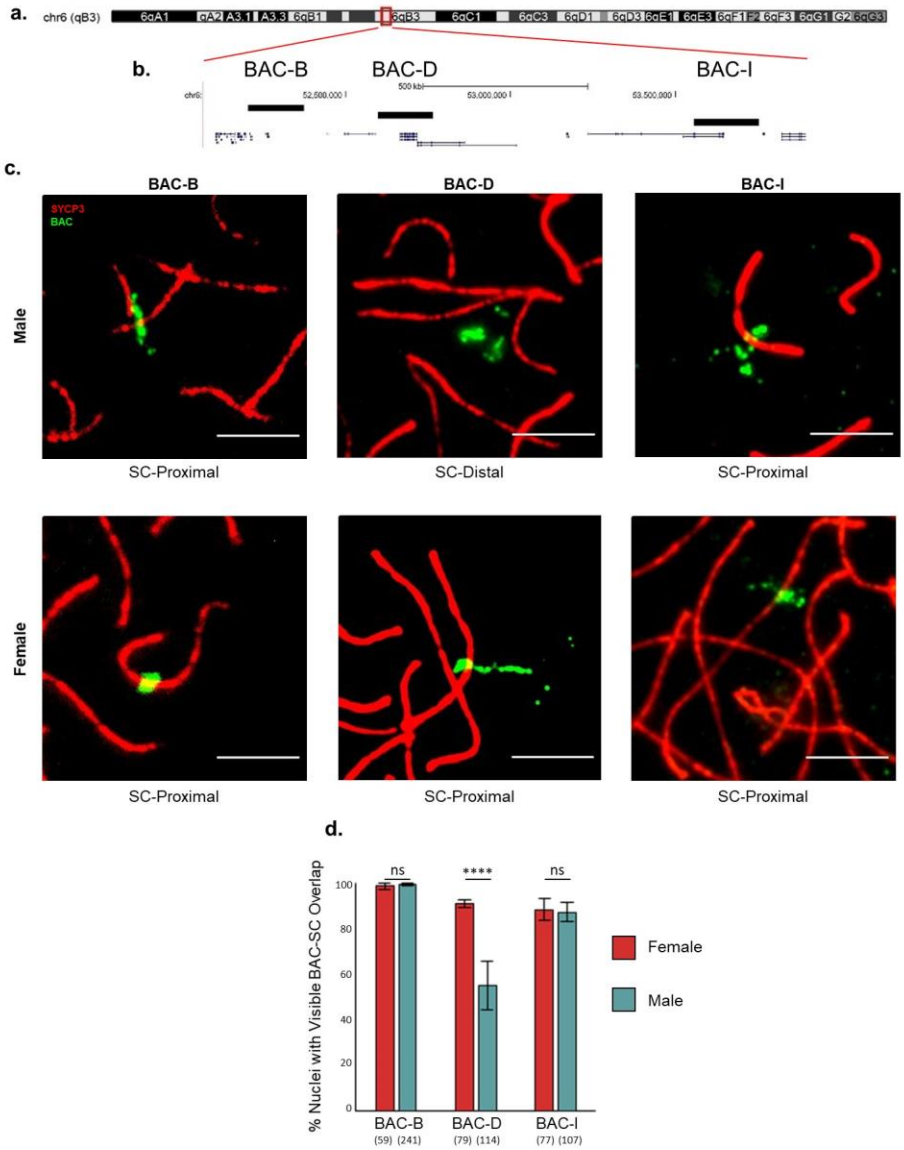

Figure 5-2. Differences in the positioning of SC-proximal and SC-distal regions in male and female pachytene meiocytes. a. Chromosome 6 ideogram. Red box and lines, location of BAC FISH probes. **b.** Schematic of the genomic location of BAC FISH probes (mm9 assembly). RefSeq genes shown. **c.** Representative images in male and female meiocytes of the visible BAC-SC overlap of three BAC probes defined as SC-proximal (BAC-B and BAC-I) and SC-distal (BAC-D) in wildtype spermatocytes. BAC probe, green. Anti-SYCP3 IF, red. 5 µm scale bar. **d.** Bar chart showing percent of pachytene meiocytes where each BAC probe visibly overlaps with the SC (Anti-SYCP3 IF) in male and female meiocytes. 3 mice analysed per sex and per probe. Error bars, standard error. Bracketed values, number of nuclei scored. ****, $p<0.0001$; ns, $p>0.05$ (Fisher's exact test).

5.2.2 Comparing Local Chromatin Condensation in Male and Female Pachytene Meiocytes

The sexually dimorphic proximity of specific chromatin regions to the pachytene SC may be explained by differences in chromatin condensation, presently defined as the combination of chromatin compaction and chromatid clustering, between males and females. The area of two chromatin regions (BAC FISH probe signal), within the *HoxA* chromatin loop, were compared to assess the extent to which chromatin condensation differs between males and females (Figure 5-3). One BAC was representative of a common SC-proximal region (BAC-B; 169 kb) and the second a male-defined SC-distal region (BAC-D; 167 kb). The area of neither BAC probe significantly differed between males and females (BAC-B, p=0.29; BAC-D, p=0.15, Mann Whitney U test); demonstrating that the sex-specific differences in the positioning of chromatin regions, relative to the SC at this specific chromatin loop, are unlikely to be determined by a change in chromatin compaction, or chromatid clustering.

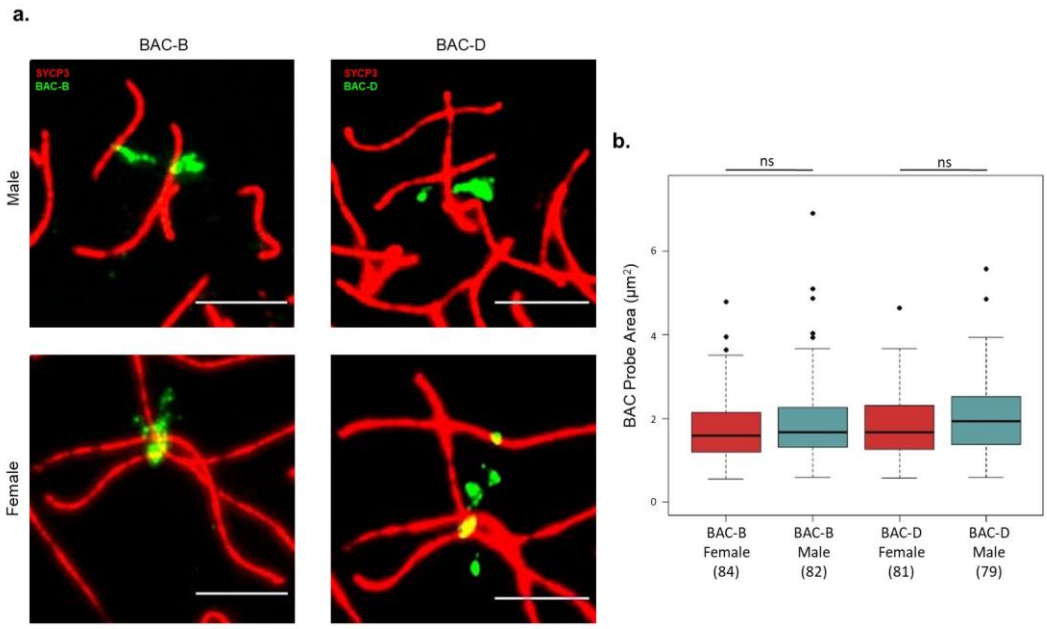

Figure 5-3. Autosomal chromatin compaction in male and female pachytene meiocytes. **a.** Representative images of two autosomal BAC probes BAC-B (SC-proximal in males) and BAC-D (SC-distal in males) in male and female meiocytes. BAC probes, green. Anti-SYCP3 IF, red. 5 µm scale bar. **b.** Boxplots of the area (µm^2) of BAC-B and BAC-D in male and female meiocytes. 3 mice analysed per sex and per probe. Bracketed values, number of nuclei scored. ns, p>0.05 (Mann Whitney U test).

The chromatin within the pseudoautosomal region (PAR), a ~700 kb region of homology between the male sex chromosomes (Rouyer *et al*., 1986; Soriano *et al*., 1987), is known to be distinctly organised, relative to the rest of genome in spermatocytes (Kauppi *et al*., 2011). Subsequently, chromatin condensation was compared between males and females at the PAR, to ascertain whether chromatin compaction and/or chromatid clustering was sexually dimorphic at this highly specialised genomic region. Similarly to autosomal loci, no significant difference in BAC probe area was observed at the PAR between pachytene spermatocytes (1.49 ± 0.07 μm^2) and oocytes (1.54 ± 0.08 μm^2; p=0.7435, Mann Whitney U test; Figure 5-4); suggesting that the extent of chromatin compaction and the relatively arrangement of chromatids, does not differ between males and females at a PAR locus, as well as at autosomal loci.

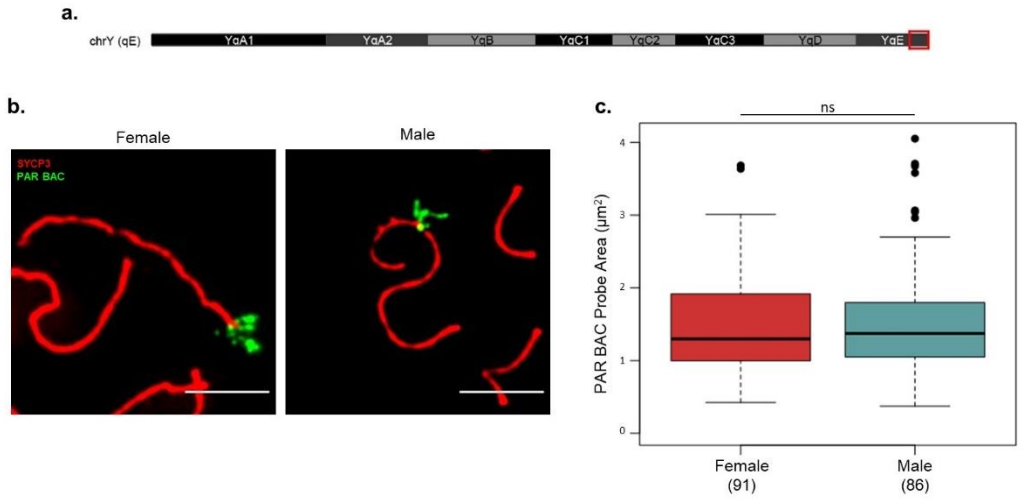

Figure 5-4. Sex chromosome chromatin compaction in male and female pachytene meiocytes. a. Chromosome Y ideogram. Red box, location of the PAR (mm9 assembly). **b.** Representative images of a BAC probe positioned at the PAR (PAR BAC, 146 kb) in male and female meiocytes. Anti-SYCP3 IF, red. PAR BAC, green. 5 µm scale bar. **c.** Boxplots of the area (μm^2) of the PAR BAC probe in male and female meiocytes. 3 mice analysed per sex. Bracketed values, number of nuclei scored. ns, p>0.05 (Mann Whitney U test).

5.2.3 Comparing Chromatin Loop Axis-Association in Male and Female Pachytene Meiocytes

Since the sexually dimorphic appearance of meiotic chromosomes is unlikely to be explained by differences in chromatin compaction, the path of an individual chromatin loop was compared between males and females, using IF-FISH, to determine whether alterations in axis- and loop-associated chromatin sequences are involved (Figure 5-5). Seven fosmids were selected to compare the distance between the SC and specific loci along the male-defined chromatin loop, between males and females. A tether-to-fosmid assay was performed by combining a BAC FISH probe, which acted as a proxy for the SC 'tether' point, due to its high incidence of visible SC-overlap in males and females (BAC-B, Figure 5-2d), with one of the selected fosmid FISH probes and anti-SYCP3 IF, to highlight the pachytene SC. The mean tether-to-fosmid distances per nucleus were calculated by measuring the distance between the point at which the 'tether' BAC probe overlapped with the SC and the four fosmid probe signals, created by each chromatid, and then determining the mean of all four distances. The majority of fosmid probes were positioned significantly closer to the pachytene SC in females, relative to males, with a maximum increase in SC-proximity of ~0.84 µm (Figure 5-5d). These data therefore conform to observations made on a chromosome-wide level, which presumed that the physical length of individual chromatin loops is significantly shorter in females, compare to males. Interestingly, no significant difference in average tether-to-fosmid distance was observed between males and females at the two fosmids with the lowest average tether-to-fosmid distance in males (Figure 5-5d; F-A and F-F). This indicates that the basic conformation of the chromatin loops is comparable between the sexes. Notably, it is possible that the axis-associated points may not be precisely conserved between males and females, as the minimal average tether-to-fosmid distance shifts by ~170 kb, from fosmid F-F in males to fosmid F-E in females (Figure 5-5d). However, it would be necessary to conduct higher-resolution mapping of axis-associated sites to determine whether such sites differ between the sexes.

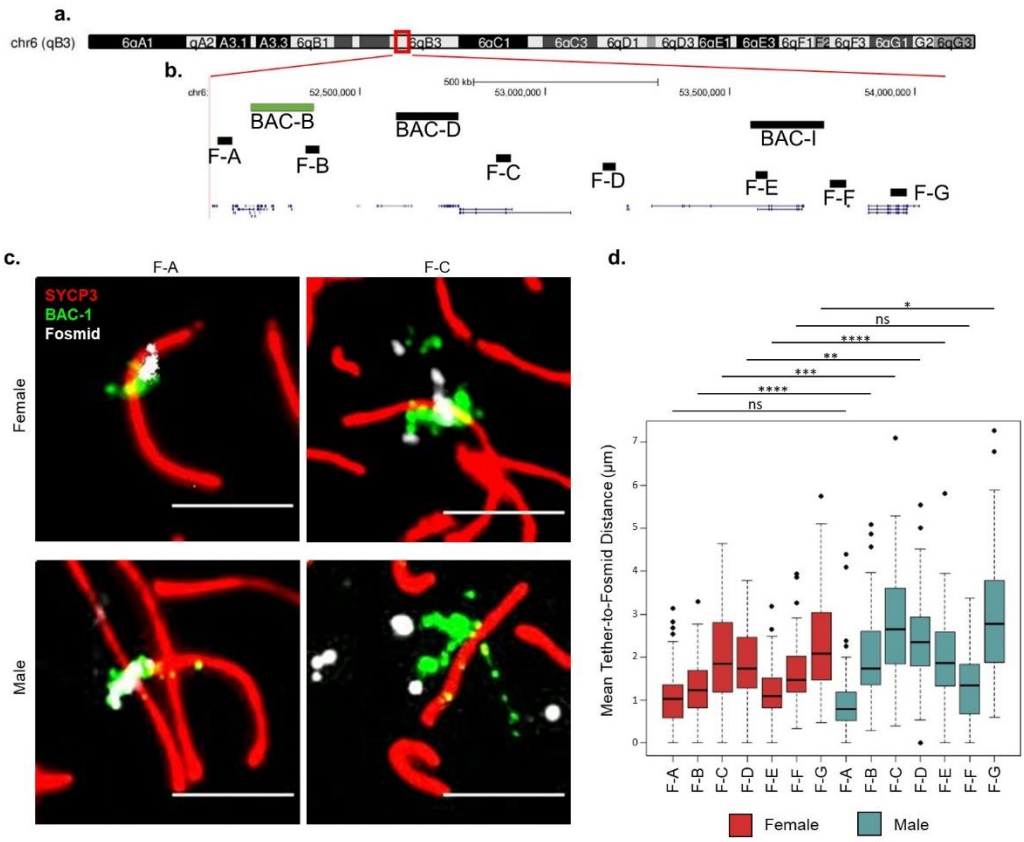

Figure 5-5. Differences in the organisation of a single chromatin loop in male and female pachytene meiocytes. a. Chromosome 6 ideogram. Red box, location of FISH probes. **b.** Schematic of the genomic location of BAC and fosmid FISH probes (mm9 assembly). 'Tether' BAC probe, green. RefSeq genes shown. **c.** Representative images of chromatid separation from the SC for F-A (SC-proximal) and F-C (SC-distal) in male and female meiocytes. 'Tether' BAC probe (BAC-B), green. Fosmid, white. Anti-SYCP3 IF, red. 5 µm scale bar. **d.** Boxplots of the average tether-to-fosmid distance per nucleus (µm) for fosmids F-A to F-G in male and female meiocytes. 3 mice analysed per sex and per probe. Female F-A to F-G nuclei scored: 56, 62, 45, 72, 76, 45 and 72. Male F-A to F-G nuclei scored: 73, 93, 72, 50, 61, 75 and 69. ****, p<0.0001; ***, p<0.001; **, p<0.01; *, p<0.05; ns, p >0.05 (Mann Whitney U test).

5.2.4 Comparing Chromatid Organisation in Male and Female Pachytene Meiocytes

To gain further insight into the relationship between chromatin architecture and sex-specific differences in CO abundance, chromatid separation was compared between males and females (Figure 5-6). Chromatid separation was measured by calculating the average inter-chromatid distance per nucleus, using fosmid FISH probes to highlight each of the four chromatids. Average inter-chromatid distances were compared between males and females at seven distinct loci throughout the *HoxA* chromatin loop (Fosmids F-A to F-G; Figure 5-6). At five of the seven loci, chromatids were significantly further apart in males relative to females (Figure 5-6b; F-A, $p=4.32x10^{-5}$; F-B, $p=1.42x10^{-8}$; F-D, $p=1.37x10^{-3}$; F-E, $p=3.44x10^{-3}$; F-F, $p=1.97x10^{-3}$, Mann Whitney U test). However, no significant difference in average inter-chromatid distance was observed at the two loci with the highest maximal inter-chromatid distance (F-C, p=0.27; F-G, p=0.07, Mann Whitney U test), between males and females (Figure 5-6). Similarly to what was previously observed in males (Figure 3-4e), inter-chromatid distance exhibited a strong positive correlation, with tether-to-fosmid distance in females (0.46-0.57; Linear regression model), confirming that chromatid separation consistently increases with distance from the SC (Figure 5-6c). Together, these data demonstrate that basic chromatid organisation is comparable between males and females, but average-inter chromatid distance is typically greater in males, relative to females, and thus coincides with sex-specific differences in SC length and chromatin loop length.

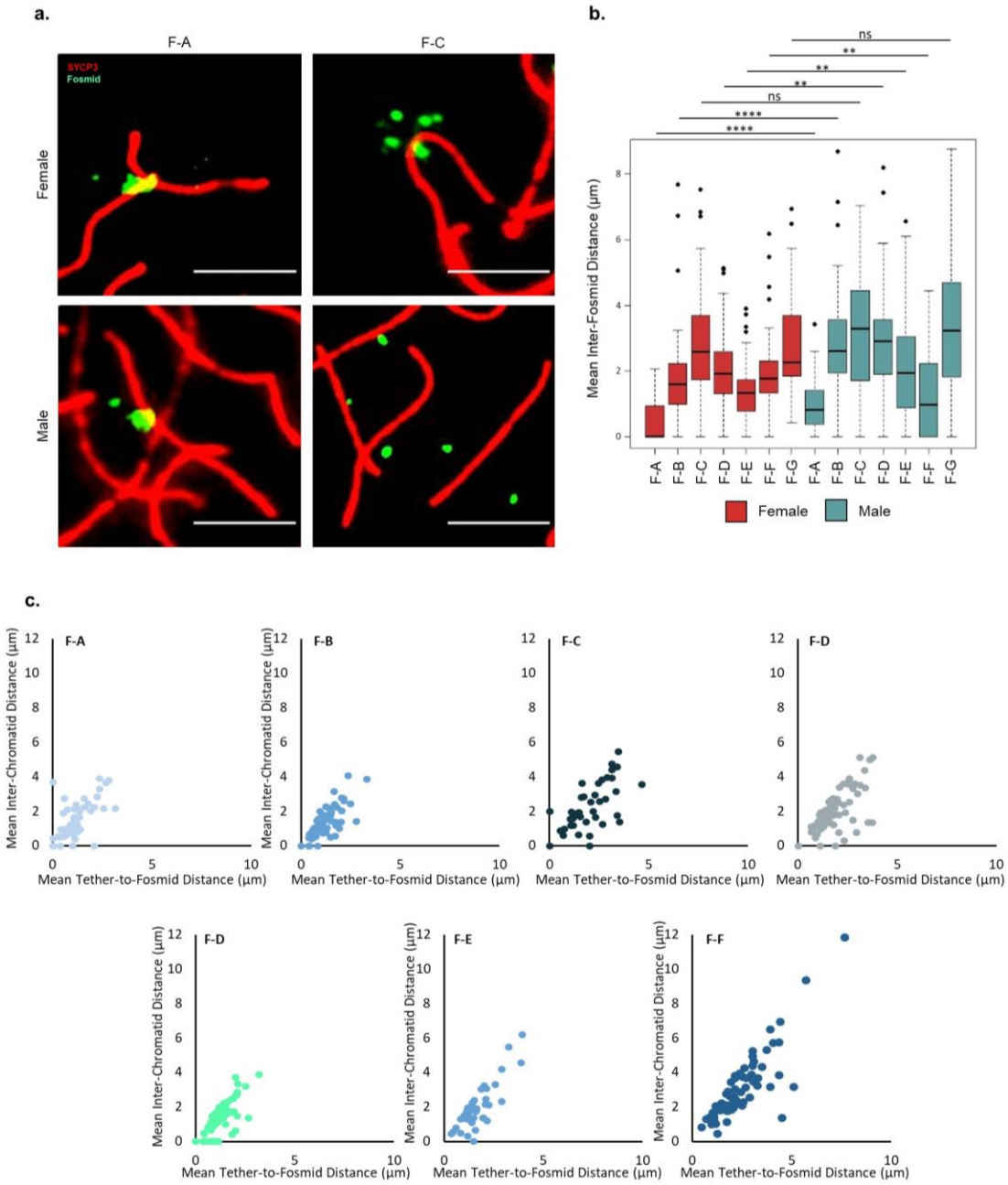
a.
F-A
F-C
SYCP3
Fosmid
Female
Male
b.
ns
**
**
**
ns
****
****
Mean Inter-Fosmid Distance (µm)
F-A F-B F-C F-D F-E F-F F-G F-A F-B F-C F-D F-E F-F F-G
Female
Male
c.
F-A
F-B
F-C
F-D
F-D
F-E
F-F
Mean Inter-Chromatid Distance (µm)
Mean Tether-to-Fosmid Distance (µm)

Figure 5-6. Inter-chromatid distances along a single chromatin loop in male and female pachytene meiocytes. a. Representative images of inter-chromatid distance for F-A (SC-proximal) and F-C (SC-distal) in male and female meiocytes. Fosmid, green. Anti-SYCP3 IF, red. Scale bar, 5 µm. **b.** Boxplots of average inter-fosmid distance (µm) per nucleus at fosmids F-A to F-G in male and female meiocytes. 3 mice analysed per sex and per probe. Female F-A to F-G nuclei scored: 67, 60, 58, 72, 75, 45 and 73. Male F-A to F-G nuclei scored: 74, 73, 74, 50, 61, 75 and 69. ****, $p<0.0001$; **, $p<0.01$; ns, $p>0.05$ (Mann Whitney U test). **c.** Scatterplots of average tether-to-fosmid distance (µm) per nucleus against average inter-chromatid distance (µm) for fosmids F-A to F-G in oocytes (A, 0.46; B, 0.53; C, 0.51; D, 0.47; E, 0.48; F, 0.52; G, 0.57; $p<0.0001$, Linear regression model). 3 mice analysed per sex and per probe. Nuclei scored: F-A to F-G, 63, 61, 52, 72, 76, 45, 73; M-A to M-G: 73, 93, 72, 50, 61, 75, 69.

5.2.5 Chromatid Organisation at Meiotic Hotspots

It is evident that sex-based differences in CO abundance positively correlate with SC length and inversely with loop length and chromatid separation. However, it is not clear whether the sexually dimorphic organisation of large-scale chromatin structures mediates differences in DSB formation and early processing. To examine the relationship between chromatin organisation and early DSB processing, I sought to establish whether chromatid separation differs according to DMC1-defined hotspot usage, in males (Brick *et al*., 2018). Mean nuclear inter-chromatid distances in pachytene were compared between eight loci, representative of coldspots and hotspots common to males and females and representative of female-biased hotspots and male-biased hotspots (Figure 5-7; Brick *et al*., 2018). No consistently significant difference in inter-chromatid distance was observed between both representatives of any of the hotspot/coldspot groups (Figure 5-7b). This indicates that chromatid organisation does not relate to hotspot usage on a local level. Furthermore, since chromatid separation and axis proximity are positively correlated (Figure 3-4e), these data infer that the positioning of loci relative to the pachytene SC does not relate to the extent of DMC1 binding.

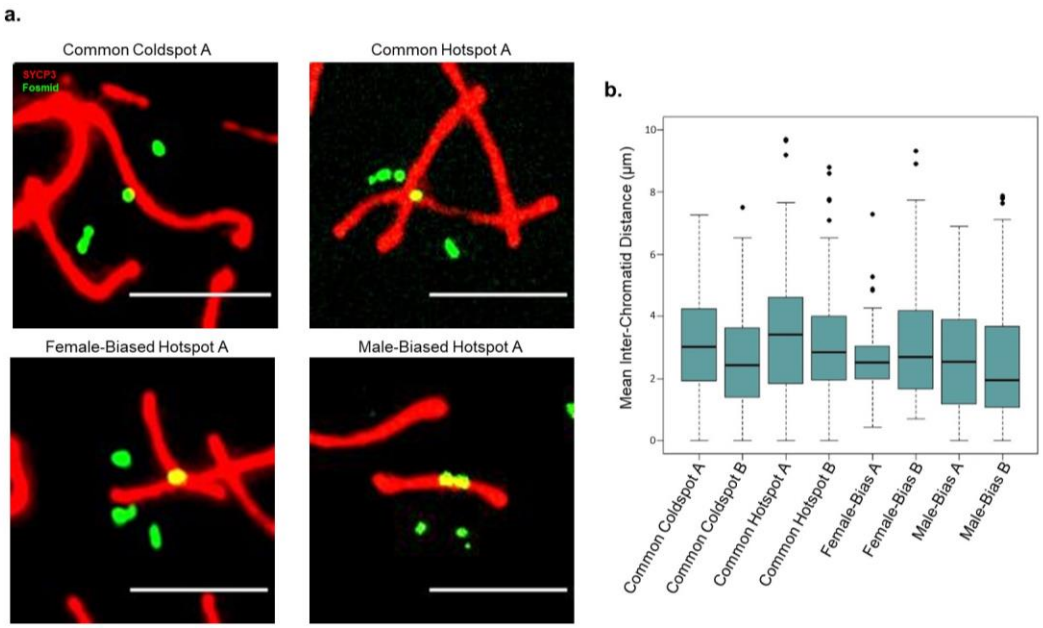

Figure 5-7. Chromatid organisation at meiotic hotspots in pachytene spermatocytes. a. Representative images of inter-chromatid distance at a common coldspot (A), common hotspot (A), female-biased hotspot (A) and male-biased hotspot (A) in spermatocytes. Fosmid, green. Anti-SYCP3 IF, red. Scale bar, 5 µm. **b.** Boxplots of the mean inter-chromatid distance (µm) per pachytene nucleus at two common coldspots (A and B), two common hotspots (A and B), two female-biased hotspots (A and B) and two male-biased hotspots (A and B) in spermatocytes. 3 mice analysed per probe. Nuclei scored: Coldspot A, 63; Coldspot B, 70; Hotspot A, 62; Hotspot B, 91; Female-Bias A, 83; Female-Bias B, 76; Male-Bias A, 79; Male-Bias B, 75.

The strategy utilised to differentiate the different cold/hotspot groups, defined by Brick *et al.*, was reliant on the genome-wide mapping of DMC1-DNA interactions, which occur during leptotene/zygotene (Brick *et al*., 2018). To ensure that hotspot mapping was temporally comparable with the inter-chromatid analyses, the inter-chromatid organisation during leptotene was examined (Figure 5-8). During leptotene, homologous chromosomes are yet to physically pair and synapse, as sister chromatids are in greater proximity to one another, compared to homologous chromatids, causing the sister chromatids to appear as pairs of fosmid FISH probe signals. Therefore, the assumption was made that the two shortest inter-chromatid distances, if 2-fold less than the average of the remaining four inter-chromatid distance, were representative of the two inter-sister chromatid distances. The nuclear

mean of presumptive inter-sister chromatid distances were compared between the same common coldspots, common hotspots, male-biased hotspots and female-biased hotspots, previously used in the pachytene analysis (Figure 5-7). The mean presumptive inter-sister chromatid distance was determined at each locus by measuring all six inter-chromatid distances and calculating the mean of the two shortest inter-chromatid distances per nucleus. No significant difference in mean presumptive inter-sister chromatid distances was consistently observed between any of the coldspot/hotspot groups in leptotene (Figure 5-8). Therefore, similarly to inter-chromatid distances in pachytene (Figure 5-7), inter-sister chromatid distance in leptotene did not correlate with DMC1 binding at a local level.

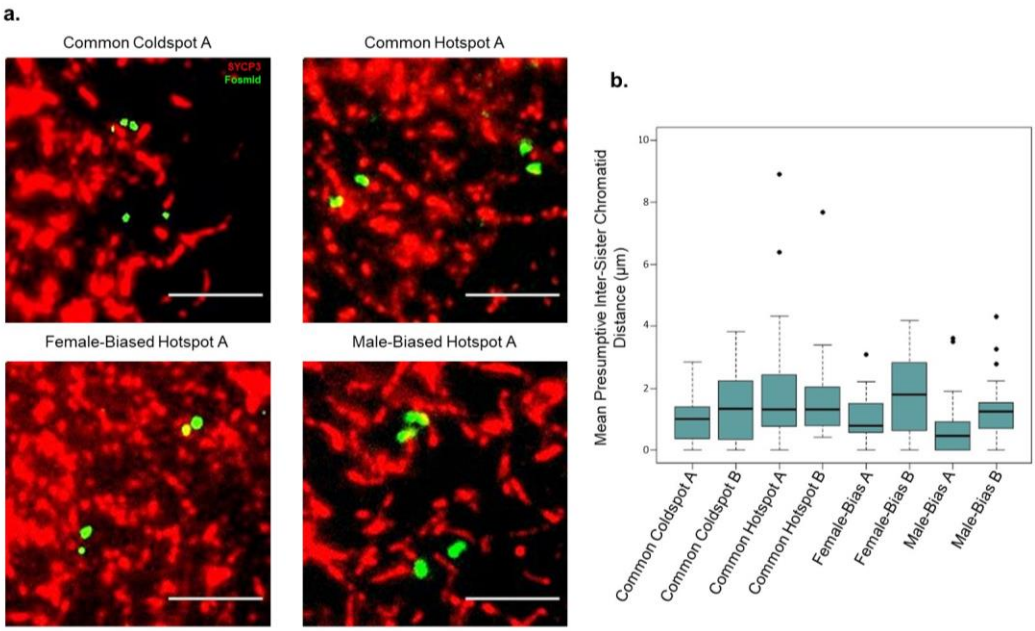

Figure 5-8. Chromatid organisation at meiotic hotspots in leptotene spermatocytes. a. Representative images of inter-chromatid distance at a common coldspot (A), common hotspot (A), female-biased hotspot (A) and male-biased hotspot (A) in leptotene spermatocytes. Fosmid, green. Anti-SYCP3 IF, red. Scale bar, 5 µm. **b.** Boxplots of the mean presumptive inter-sister chromatid distance (µm) per leptotene nucleus at two common coldspots (A and B), two common hotspots (A and B), two female-biased hotspots (A and B) and two male-biased hotspots (A and B) in leptotene spermatocytes. 3 mice analysed per probe. Nuclei scored: Coldspot A, 32; Coldspot B, 30; Hotspot A, 20; Hotspot B, 22; Female-Bias A, 83; Female-Bias B, 76; Male-Bias A, 79; Male-Bias B, 75.

5.2.6 Chromosome Morphology in Juvenile Spermatocytes

The above data indicates that sex-specific CO levels correlate with changes in SC length, the length of chromatin extensions from the SC and the extent of chromatid separation. CO abundance is theoretically reliant on several aspects of recombination, including DSB formation, repair template choice and the balance between homologous recombination pathways. Previous studies have highlighted that although juvenile (16 dpp) spermatocytes exhibit comparable levels of the early recombination markers RAD51 and DMC1 to their adult counterparts. However, the abundance of RPA2 foci in pachytene, which are thought to mark inter-homolog interactions, declines by ~40% in younger males (Vrooman *et al.*, 2014; Zelazowski *et al.*, 2017). Initially, a basic comparison of chromosome morphology was conducted between juvenile and adult spermatocytes, to determine whether differences in chromosome organisation could be observed between the two age cohorts and thus correlate with changes in inter-homolog interactions (Figure 5-9). In accordance with prior comparisons of total SC length, no change in the length of the chromosome 6 SC (anti-SYCP3 IF) was observed between juvenile (7.32 ± 0.14 µm) and adult (7.05 ± 0.14 µm) spermatocytes (p=0.212, Mann Whitney U test; Figure 5-9b). In addition, the size of the chromosome 6 territory, as highlighted by a chromosome 6-specific FISH paint, did not differ between adult and juvenile spermatocytes, each covering ~60 μm^2 (p=0.9502, Mann Whitney U test; Figure 5-9c). These data demonstrate that the decline in predicted inter-homolog interactions between juvenile and adult mice, does not correlate with a change in SC length, or the extent to which the chromatin extends from the SC.

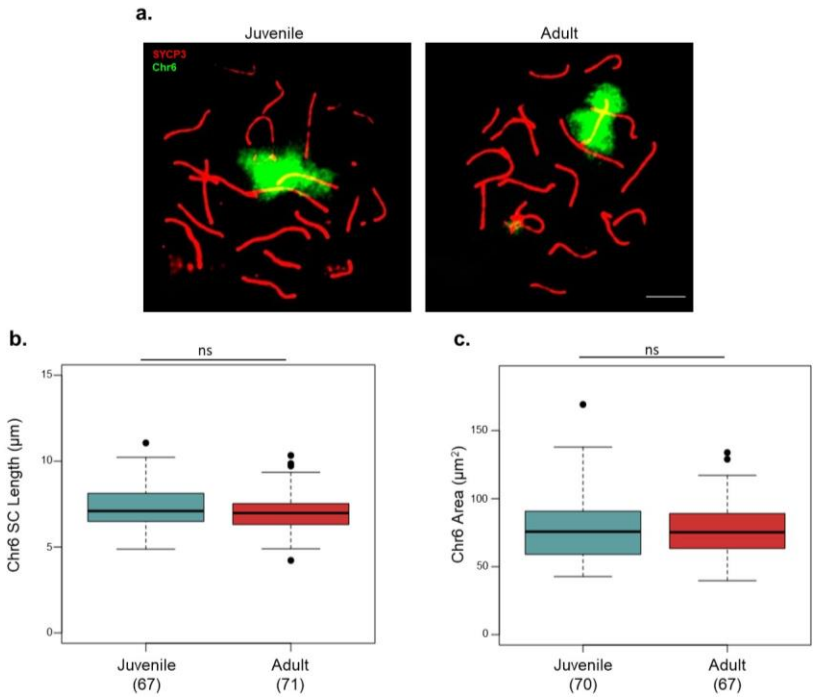

Figure 5-9. Differences in chromosome morphology in juvenile and adult pachytene spermatocytes. a. Representative images of chromosome 6 (Chr6) SC length (anti-SYCP3 IF, red) and chromatin area (Chr6 paint, green) in juvenile and adult spermatocytes. 5 µm scale bar. **b.** Boxplots of the Chr6 SC length (µm) in juvenile and adult spermatocytes. **c.** Boxplots of the chromosome 6 paint territory area (µm^2) in juvenile and adult spermatocytes. 3 mice analysed per age cohort. Bracketed values, number of nuclei scored. ns, p>0.05 (Mann Whitney U test).

5.2.7 Chromatid Organisation in Juvenile Spermatocytes

Since striking changes in SC length and the length of chromosome-wide chromatin extensions did not appear to correlate with age-dependent differences in inter-homolog interactions, mean inter-chromatid distance was next compared between juvenile and adult spermatocytes. Inter-chromatid distances were compared at two hotspots, A3 and 59.5, which have previously been reported to experience a 1.2- and a 1.3-fold reduction in CO formation in juveniles relative to adults, respectively. In addition, although A3 experiences no change in NCO formation, NCOs are reduced by ~1.7-fold at 59.5 (Zelazowski *et al*., 2017). This published data can be interpreted to suggest that overall homolog-mediated repair is lower, during the first round of spermatogenesis, in juvenile spermatocytes at 16 dpp. The nuclear mean of inter-chromatid distances was significantly greater at the two hotspots in juvenile mice, compared to adult mice, with a ~1.5-fold increase at A3 and a ~1.3-fold increase at 59.5 (Figure 5-10b). In summary, these data suggest that a greater inter-chromatid distance correlates with a decline in inter-homolog interactions. Yet, the change in chromatid organisation observed between juvenile and adult mice, occurs largely independently of changes in SC length and gross chromosome morphology.

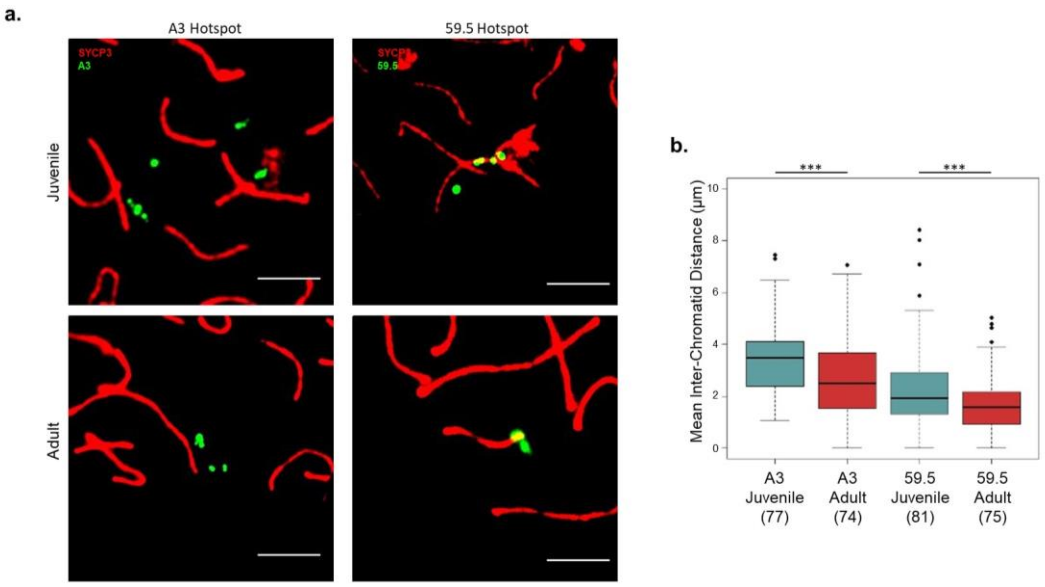

Figure 5-10. Differences in chromatid organisation at meiotic hotspots in juvenile and adult pachytene spermatocytes. a. Representative images of inter-chromatid distance at the A3 (green-left) and 59.5 (green-right) hotspots in juvenile and adult spermatocytes. Anti-SYCP3 IF, red. Scale bar, 5 µm. **b.** Boxplots of the average inter-chromatid distance (µm) per nucleus at the A3 and 59.5 hotspots in juvenile and adult spermatocytes. 3 mice analysed per age cohort and per probe. Bracketed values, nuclei scored. ***, p<0.001 (Mann Whitney U test).

I next investigated how the above findings inter-relate with the organisation of specifically sister chromatids and whether the effects of chromatid organisation in juvenile animals were specific to meiotic hotspots, or might represent a more general phenomenon on meiotic chromosomes. Since sister chromatids cannot be definitively distinguished from homologous chromatids in the isogenic C57BL/6 mice using FISH-based approaches, inter-sister chromatid organisation was assessed by using fosmid FISH probes at two loci on the non-homologous region of the X chromosome (Figure 5-11). Inter-sister chromatid distance was measured by determining the centroid coordinates of the two foci generated by a single fosmid FISH probe and calculating the inter-centroid distance. Similarly to the autosomal hotspots, inter-sister chromatid distance on the X chromosome increased ~1.6-fold at both loci, from 1.88 ± 0.23 µm to 1.05 ± 0.10 µm at fosmid A and from 1.75 ± 0.18 µm to 1.12 ± 0.15 µm at fosmid B in juvenile mice, compared to adults (Figure 5-11b). These data demonstrate that an increase in inter-sister chromatid distance corresponds with the establishment of

fewer inter-homolog interactions in juvenile spermatocytes, compared to adult spermatocytes. In addition, these data indicate that the increase in chromatid separation may be a nucleus-wide phenomenon in juvenile mice, since this pattern was observed at two meiotic coldspots, as well as the two hotspots assessed in Figure 5-10.

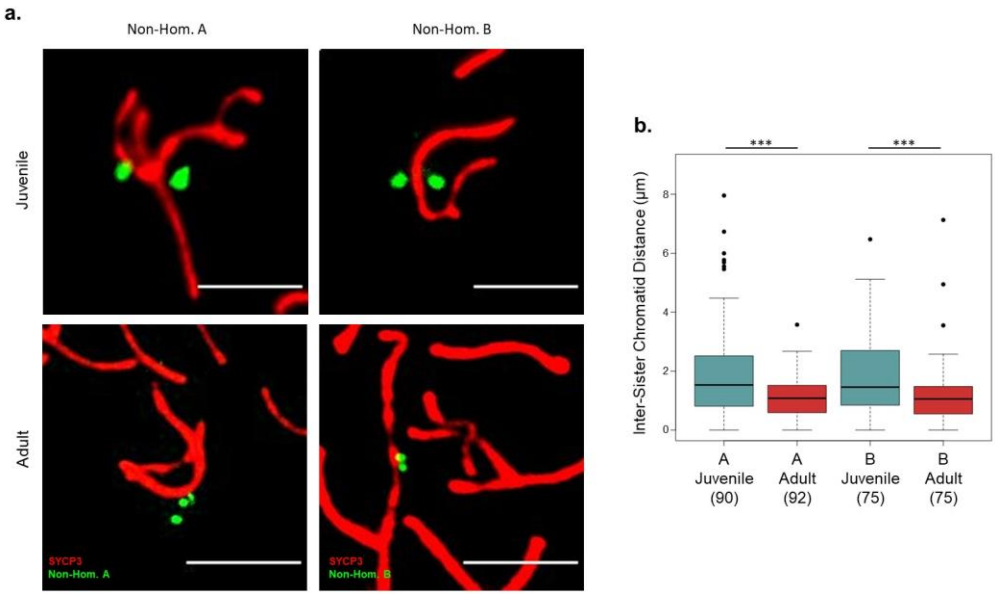

Figure 5-11. Differences in sister chromatid organisation in juvenile and adult pachytene spermatocytes. a. Representative images of inter-sister chromatid distance at two loci on the non-homologous X chromosome (Non-Hom. A and Non-Hom. B) in juvenile and adult spermatocytes. Non-Hom. A, green-left. Non-Hom. B, green-right. Anti-SYCP3 IF, red. 5 µm scale bar. **b.** Boxplots of inter-sister chromatid distances (µm) for fosmids A and B in juvenile and adult spermatocytes. 3 mice analysed per age cohort and per probe. Bracketed values, number of nuclei score. ***, $p<0.001$ (Mann Whitney U test).

To ascertain whether differences in chromatid organisation between juvenile and adult mice are evident in early prophase I, at which point meiotic recombination is initiated, inter-sister chromatid distance was compared between juvenile and adult spermatocytes in leptotene (Figure 5-12). Mean inter-sister chromatid distances in leptotene were measured as described in Section 5.2.5. The relative positioning of sister chromatids were examined at the A3 and 59.5 hotspots used in Figure 5-10, as well as the same two non-homologous loci used in Figure 5-11. Interestingly, no significant difference was observed between juvenile and adult presumptive inter-sister chromatid distances at the A3 (~1.06 µm) and 59.5 (~0.97 µm) hotspots (Figure 5-12b; A3, p=0.94; 59.5, p=0.95, Mann Whitney U test) or the two non-homologous loci during leptotene (Figure 5-12c; A, p=0.89; B, p=0.36, Mann Whitney U test). These data are consistent with the lack of correlation between DMC1-binding and chromatid organisation in leptotene, previously described in Figure 5-7 and Figure 5-8. Thus, together these findings indicate that the extent of chromatid separation has the potential to influence CO levels, after the initial formation and processing of meiotic DSBs.

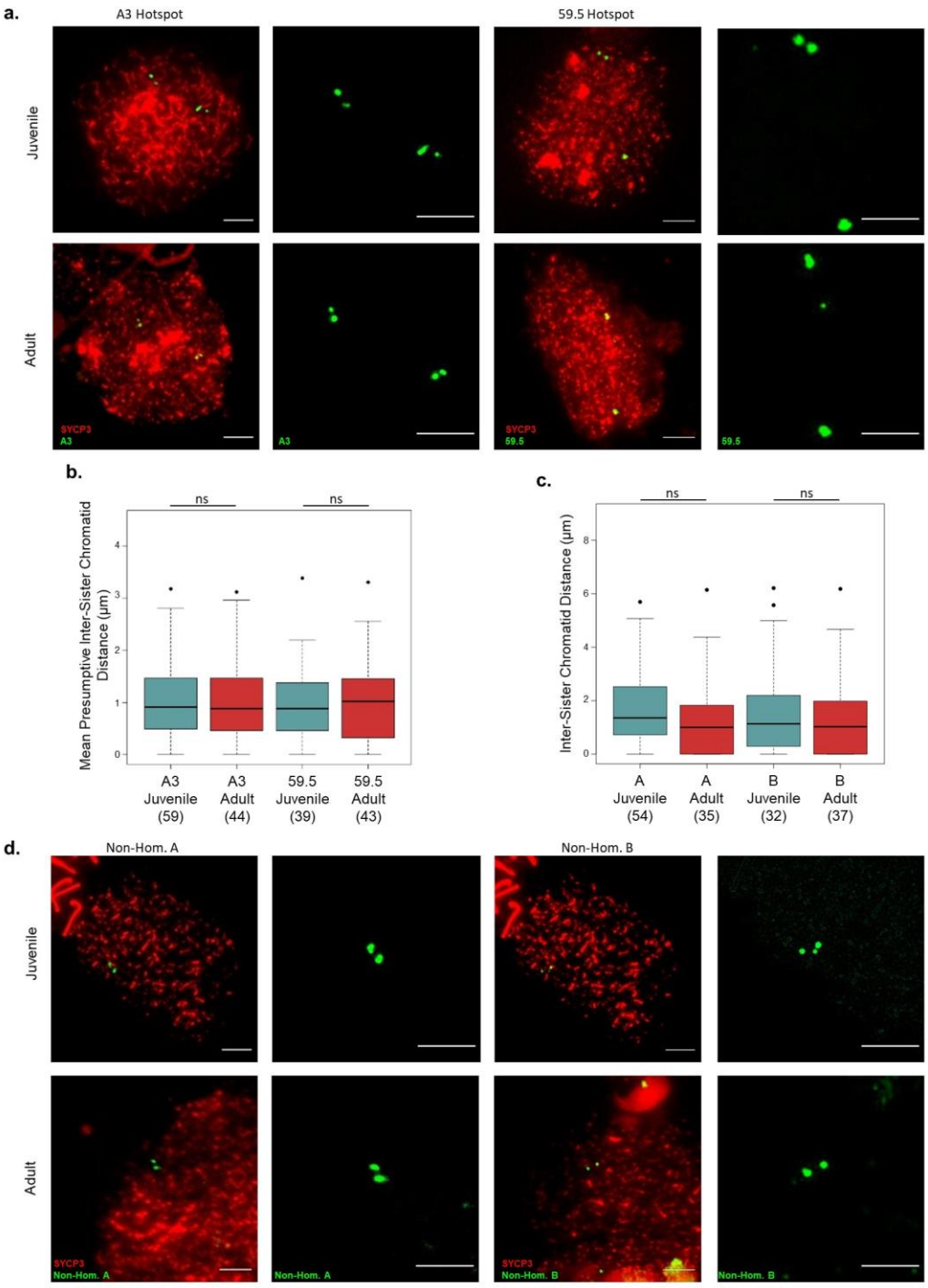
a.
A3 Hotspot
59.5 Hotspot
Juvenile
Adult
SYCP3
A3
A3
SYCP3
59.5
59.5
b.
Mean Presumptive Inter-Sister Chromatid Distance (µm)
ns
ns
A3 Juvenile (59)
A3 Adult (44)
59.5 Juvenile (39)
59.5 Adult (43)
c.
Inter-Sister Chromatid Distance (µm)
ns
ns
A Juvenile (54)
A Adult (35)
B Juvenile (32)
B Adult (37)
d.
Non-Hom. A
Non-Hom. B
Juvenile
Adult
SYCP3
Non-Hom. A
Non-Hom. A
SYCP3
Non-Hom. B
Non-Hom. B

Figure 5-12. Differences in chromatid organisation in juvenile and adult leptotene spermatocytes. a. Representative images of inter-chromatid distance at the A3 (green-left) and 59.5 (green-right) hotspots in juvenile and adult leptotene spermatocytes. Anti-SYCP3 IF, red. Scale bar, 5 µm. **b.** Boxplots of the mean presumptive inter-sister chromatid distance (µm) per nucleus at the A3 and 59.5 hotspots in juvenile and adult leptotene spermatocytes. ns, p>0.05 (Mann Whitney U test). **c.** Boxplots of inter-sister chromatid distances (µm) for fosmids A and B in juvenile and adult leptotene spermatocytes. ns, p>0.05 (Mann Whitney U test). **d.** Representative images of inter-sister chromatid distance at two loci on the non-homologous X chromosome (Non-Hom. A and Non-Hom. B) in juvenile and adult leptotene spermatocytes. Anti-SYCP3 IF, red. Fosmid FISH probes, green. 5 µm scale bar. 3 mice analysed per age cohort and per probe. Bracketed values, number of nuclei scored.

5.3 Discussion

5.3.1 Regulating Inter-Homolog versus Inter-Sister Interactions

The present comparative analyses of chromatin architecture in male and female mouse meiocytes have verified that the sex-specific difference in CO abundance corresponds with significant changes in chromosome morphology, as the increase in CO frequency in females was shown to positively correlate with SC length and inversely correlate with the length of chromatin extensions on a chromosome-wide level (Bojko, 1985; Gruhn *et al*., 2013; Lynn *et al*., 2005; Petkov *et al*., 2007; Rasmussen and Holm, 1978; Tease *et al*., 2002). Excitingly, a novel correlative relationship between CO abundance and chromatin separation was also observed, as an increase CO abundance in females occurred coincidently with a fall in chromatid separation. However, a causal link is yet to be substantiated between chromatid separation and CO abundance.

The abundance of meiotic COs is theoretically dependent on several factors, including the frequency of DSB formation, the balance between inter-sister and inter-homolog interactions and the ratio of CO and NCO events. Therefore, in order to account for the apparent sexually dimorphic organisation, chromatid separation must be involved in the manipulation of at least one of these events, if CO abundance and chromatid separation are indeed mechanistically related. Cytological analyses in juvenile and adult spermatocytes have previously demonstrated that juvenile spermatocytes are predicted to establish significantly fewer inter-homolog interactions, following the formation of an equivalent number of early recombination intermediates, marked by RAD51 and DMC1 (Vrooman *et al.*, 2014; Zelazowski *et al.*, 2017). If there was no specialised meiotic chromosome structure, DSBs would repair primarily from the sister chromatid, due to their closer proximity, and the homolog search would be considerably less efficient. Thus highlighting, a specialised aspect of meiotic chromosome structure must exist to manipulate the age-specific ratio of homolog to sister interactions, either through promotive or suppressive mechanisms. I chose to exploit this age-specific disparity in apparent template choice, to explore what structural feature of chromosome organisation corresponds to a decline in inter-homolog interactions in juvenile spermatocytes, relative to their adult counterparts.

IF-FISH analyses revealed that the bias towards inter-homolog interactions in adult spermatocytes, inversely correlates with the extent of chromatid separation, while no change in SC length or gross chromosome morphology was observed between juvenile and adult spermatocytes. Taken together, these observations indicate that inter-chromatid distance in pachytene might be more directly related to repair template choice, than other aspects of chromosome morphology. Therefore, any parameter of chromosome structure that affects chromatid separation, such as SC length or chromatin loop length, could alter the ratio of inter-homolog and inter-sister interactions.

In *S. cerevisiae*, homolog bias is governed by a plethora of factors residing at chromosome axes, including the meiotic kinase Mek1 and Rec8-mediated sister chromatid cohesion (Kim *et al*., 2010; Wu *et al*., 2010), resulting in striking abnormalities in the inter-homolog to inter-sister interaction ratios on axial disruption (Hong *et al*., 2013; Schwacha and Kleckner, 1997). Since a direct assay to quantify template choice is yet to be applied in mammals, it is not clear what molecular mechanisms are at play, to determine repair template biases. Determining whether the sister or homologous chromatid is exploited as a reparative template is dependent on the ability to reliably distinguish sister and homologous chromatids. In isogenic animals, such as the C57BL/6 mice employed presently, chromatid differentiation cannot occur at the DNA level. Instead, it is possible that repair template choice is determined according to chromatid organisation, where a decline in chromatid separation promotes a bias towards homolog-mediated repair. I propose a model (Figure 5-13) in which axis-association may govern the extent of inter-homolog versus inter-sister interactions in mammalian meiocytes: In mice, SPO11 cleaves DNA to form DSBs in leptotene, immunostaining of the SPO11 accessory protein MEI4 has demonstrated the factor is enriched at the chromosome axis (Kumar *et al*., 2015), indicating that prior to, or following, DSB formation, the targeted DNA duplex is recruited to the chromosome axis. I propose that inter-sister chromatid proximity helps mediate chromatid differentiation, by promoting the simultaneous recruitment of both the broken and intact sister chromatids to the chromosome axis. Consequently, the likelihood that the intact sister chromatid is utilised as a repair template is reduced, leaving the homologous chromatids more amenable to the homology search. This preferential homology search could occur in tandem with chromatin loop formation and extension during late leptotene and zygotene (Kauppi *et al*., 2011; Patel *et al*., 2019), which would promote the separation of chromatids and aid the homology

search. Notably, although elegant IF-FISH data has demonstrated that the cleaved hotspot sequence is restricted to the chromosome axis throughout its repair (Grey *et al*., 2009), the coincidental recruitment of sister chromatids to the chromosome axis is likely to be dynamic, since the preference towards inter-homolog interactions is a bias rather than an absolute. This model could be initially verified in fixed spermatocytes, by conducting an IF-FISH experiment comparable to that developed by Grey *et al.*, to establish the relative positioning of chromatids on DSB repair and axis recruitment (Grey *et al*., 2009).

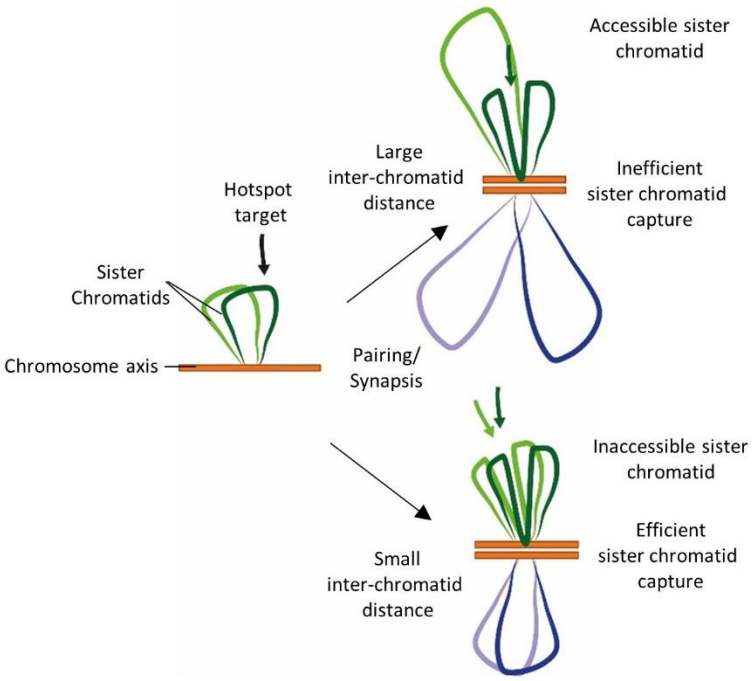

Figure 5-13. Sister chromatid capture model. A hotspot is designated for DSB formation and is recruited to the chromosome axis. Hotspots affiliated with a greater inter-sister chromatid distance experience less efficient recruitment (‘capture’) of the intact sister chromatid to the chromosome axis concomitantly with the sister chromatid targeted by SPO11 and recombination machinery. The tandem capture of intact sister chromatid reduces its availability for the homology search and consequently promotes an inter-homolog bias in recombinogenic repair.

The dynamic dissociation and re-association of the intact sister chromatid with the chromosome axis might cause the inter-homolog to inter-sister bias to behave differently at SC-proximal and SC-distal loci. Efficient recombination sites might need to strike a balance between being located close enough to the SC to allow some sister chromatid capture to take place and repress sister chromatid-mediated repair, but a sufficient distance from the chromosome axis that the homologous sequence can efficiently undergo the homology search. Furthermore, according to the above model the greater inter-chromatid distance observed in juveniles would suggest that sister chromatid capture is less efficient in juveniles, leaving the intact sister chromatid more susceptible to the homology search. Interestingly, of the two hotspots examined, A3 and 59.5, both reported a decline in COs in juvenile compared to adult spermatocytes. However, NCO levels were disparately regulated between A3 and 59.5, as NCO abundance declined at 59.5, while no change occurred at A3 (Zelazowski *et al*., 2017). At this point it is intriguing to consider that the position-dependent effect on homolog versus sister interactions might explain the disparity in the repair of the two hotspots examined A3 and 59.5. According to the model presented above I would predict that chromatids at 59.5 are in relatively greater proximity than at A3 in late leptotene/ zygotene, which increases the likelihood that the sister chromatid is captured and inter-homolog repair, causing the significant decline in both COs and NCOs at 59.5 in juveniles as inter-chromatid distance increases. To further substantiate this proposition, it would prove useful to consider chromatid separation at additional hotspots with differing efficiencies of homolog versus sister chromatid interactions and examine not only chromatid separation, but also their relative positioning of loci to the chromosome axis.

Sister and homologous chromatids are thought to be differentiated for recombinogenic repair during late leptotene/zygotene (Moens *et al*., 2002). Therefore, according to the above model, I predict that inter-sister chromatid distance is greater at these stages in juvenile, compared to adult spermatocytes, resulting in the sister chromatid being more frequently available as a repair template in the younger mice. The increase in rates of inter-sister repair result in the lower RPA frequencies, reported by Zelazowski *et al.*, as inter-sister repair occurs more rapidly than inter-homolog repair (Zelazowski *et al*., 2017). Importantly, these differences in chromatid organisation were not observed in leptotene analyses. Thus, the mechanisms driving the disparity are likely to be activated during the leptotene-zygotene transition. Furthermore, such structural mechanisms are not constricted to meiotic hotspots, or

regions bearing homology, since a greater inter-chromatid distance was also observed at meiotic coldspots, positioned on the non-homologous X chromosome in juvenile spermatocytes. The absence of a significant difference in SC length and gross chromosome morphology between juvenile and adult pachytene spermatocytes could be explained by the fact that these differences in chromatin organisation are of functional relevance and under more stringent structural regulation, during earlier stages of prophase I, prior to the completion of SC and loop array assembly in pachytene. Thus, the increase in inter-chromatid distance observed in pachytene, occurs as a by-product of earlier inter-sister versus inter-homolog choices made, in late leptotene/early zygotene. To verify this model, it will be necessary to characterise the temporal kinetics of chromatid organisation, in relation to the advances of meiotic recombination, during the intervening stages between leptotene and pachytene, with the expectation that chromatid dynamics would conform to (Figure 5-13), if the proposed model is indeed correct. However, such analyses are restricted, by the fact that IF-FISH cannot definitively discriminate between homologous and sister chromatids. One could consider utilising mice of a mixed-genetic background, enabling short oligo FISH probes to visibly differentiate homolog-specific SNPs of each homolog, or through the insertion of homolog-specific FISH probe targeting sites. It is important to note, even in highly polymorphic strains there may be insufficient variation for FISH probes to discriminate homolog, while artificial manipulation of sequences could disrupt chromatin loop formation and the behaviour of individual chromatids. Due to such limitations, it may not be feasible to visibly differentiate chromatids through sequence alone.

It is important to note, the model proposed to justify the apparent decline in inter-homolog interactions, in juvenile mice, might not directly translate between the age-specific and sex-specific comparative analyses. Particularly since at present no comparison of inter-homolog versus inter-sister interactions has been conducted between males and females meiocytes. In addition, although both sex- and age-based comparisons reported differences in inter-chromatid distance, they were also found to exhibit structural disparities, since the decline in inter-chromatid distances observed in females was also accompanied by a rise in SC length and a decline in the length of chromatin extensions, which was not seen in adult spermatocytes, relative to juvenile spermatocytes.

5.3.2 Chromatid Organisation at DMC1-Defined Hotspots and Coldspots

No difference in chromatid separation was consistently observed between discrete families of hotspots and coldspots, defined by DMC1 binding (Brick *et al*., 2018). This data complements the model proposed above (Figure 5-13), since relative chromatid positioning corresponds to repair template choice, rather than recombinase loading in leptotene. However, it is important to mention that hotspots and coldspots cannot be discriminated solely by the extent of DMC1 binding. It may therefore be of value to assess relative chromatid positioning utilising alternate markers of early recombination, such as at PRDM9 binding or SPO11-oligos, in order to further substantiate the claim that meiotic hotspots and coldspots do not differ in the relative organisation of chromatids in pachytene.

By utilising the pachytene inter-chromatid distance as a proxy of distance from the SC, all the coldspots and hotspots examined are positioned at a comparable distance to SC-distal loci identified. It is therefore plausible that chromatid organisation behaves differently at SC-proximal loci, in relation to recombinogenic activity. Additionally, the presence of both meiotic hotspots and coldspots in SC-distal regions, suggests that the position of loci within chromatin loops does not absolutely discriminate the two sites. Although it remains possible that meiotic hotspots are excluded from axis-associated sites. Accordingly, the relative positioning to the SC could influence whether the frequency at which specific hotspots are utilised.

5.3.3 Sexually Dimorphic Chromatin Loop Topology

The sexual dimorphism in meiotic chromosome morphology has been recognised for several decades. Excitingly, the results described within this chapter are the first to examine sex-specific chromatin organisation at the level of a chromatin loop. The reduction in the length of the examined chromatin loop and loss of visibly distinct SC-distal regions in female mice, compared to male mice, is highly complementary to previous mammalian EM and IF studies performed on a chromosomal level (e.g. Gruhn *et al*., 2013; Tease and Hultén, 2004; Zickler and Kleckner, 1999). Novel insight was gained by enhancing the resolution of these structural assessments. No change in chromatin compaction and/or chromatid clustering was observed at the mapped

chromatin loop, or at the PAR between sexes. These findings indicate that chromatin compaction does not account for sex-specific differences in chromatin loop organisation, at least at the positions examined. This therefore infers that chromatin extensions reduce in length from the chromosome axis in females, due to an increase in axis-association; this may result from either more chromatin being constrained at axis-association sites, causing shallower loops to form or, an increase in axis association sites creating more, shorter loops. At the present resolution of IF-FISH utilised, these two possibilities cannot be definitively discriminated, since although the profile of the tether-to-fosmid distances appears to shift between sexes it will be necessary to identify the exact loop anchor sequences in each sex to verify this claim. One means by which this may be achieved, is through heightening the resolution at which the IF-FISH mapping strategy is performed, for instance utilising shorter oligonucleotide FISH probes and high-resolution microscopy strategies. In addition, an increase in resolution may also enable the length of chromatin axis-associated sites to be determined.

Chapter 6:

Conclusion

Chapter 6 Conclusion

6.1 Summary

6.1.1 Mapping Meiotic Chromatin Loops in Mice

The overarching purpose of the research undertaken in this thesis was to gain further insight into the fundamental features of meiotic chromatin architecture, at the level of individual chromatin loops in murine meiocytes. Extensive cytological data has confirmed the basic architecture of large-scale chromatin organisation in meiotic prophase I is highly conserved across taxa, as chromatin is folded into sequential loop arrays emanating from a central proteinaceous axis (Zickler and Kleckner, 1999). In yeast, comprehensive molecular studies, including ChIP-seq and HiC analyses, have revealed the sequence-specificity of axis-association sites, enabling large-scale chromatin looping to be mapped across the genome (Blat *et al.*, 2002; Schalbetter *et al.*, 2018). However, it has proven challenging in mammalian meiocytes to identify axis-association sites at the base of chromatin loops, through molecular analyses, including HiC (Alavattam *et al*., 2019; Patel *et al*., 2019; Vara *et al*., 2019; Wang *et al*., 2019), ChIP-seq (Johnson *et al*., 2013; Vara *et al*., 2019) and the mechanical isolation of chromatin in association with the chromosome axis (Heng, Tsui, and Moens, 1994; Kolas *et al*., 2004), leading to the proposition that the position of chromatin loops varies from cell to cell. However, such analyses are presently hindered by the incomplete understanding of how axis-association sites are defined in mammals and whether such sites are fixed in individual cells. Furthermore, conducting molecular mapping approaches can also be complicated by the inherent challenges of working with mammalian meiocytes, such as isolating highly synchronous cellular populations. Rather than perform a genome-wide molecular mapping approach, I chose to conduct IF-FISH to characterise meiotic chromatin looping in mouse spermatocytes. Importantly, this approach permits the positioning of specific chromatin regions, relative to the chromosome axis, to be determined, without being obscured by inter-cellular heterogeneity, or having to define the precise protein composition, or chromatin configuration at axis-association sites.

My findings are the first to demonstrate that the organisation of chromatin, relative to the mammalian chromosome axis, is consistent between individual pachytene meiocytes and animals. Multiplexing of FISH probes enabled specific chromatin regions to be visualised extending from the chromosome axis in a loop-like manner

which, in combination with the mapping of sequential SC-proximal and SC-distal regions, helps to confirm the arrangement of meiotic chromatin in loop arrays in mouse meiocytes. The visualisation of entire chromosome loop arrays, through EM imaging and chromosome paint analysis, had previously pointed toward the presumption that the length of individual chromatin loops is relatively uniform along a chromosome axis (Novak *et al*., 2008; Zickler and Kleckner, 1999). However, chromatin mapping across a ~7 Mb on chromosome demonstrated that the length of adjacent SC-distal and SC-proximal is highly variable.

Notably, the IF-FISH assays described in this project, measure the relative positioning of genomic regions at least 40 kb in length and cannot determine exact axis-association sites. Therefore, it remains possible that precise axis-association sites are variable between individual meiocytes, but the extent of such variation is below the limit of resolution of the IF-FISH assays conducted. Importantly, it is not yet clear whether the distribution of axis-association sites is governed by specific *cis* features of the sites themselves, for instance their underlying genetic sequences, or the positioning of alternate genetic features, such as transcriptional activity, acting in *trans* to determine the positioning of SC-proximal regions. If the former model is true, specific axis-association sites may be conserved between mammalian species, this proposition could be relatively simply examined, by conducting comparable IF-FISH assessments in alternate species, such as human or dog spermatocytes. The latter model, for genetic factors working in *trans* to dictate the distribution of axis-association sites, would suggest that inside a single nucleus all four chromatids would need to be modulated comparably to maintain common axis- and loop-associated patterning. Such structural synchrony between chromatids may prove important for key events during prophase I, including the efficiency of the homology search and synapsis. This hypothesis may be tested through altering putative *trans* acting factors, such as transcription, on a single homolog to assess the coordination of axis-association sites between chromatids. In this respect, it may also prove interesting to assess how the epigenetic phenomenon of imprinting may influence the orchestration of axis-association sites between homologs (Sasaki and Matsui, 2008).

On several occasions, EM imaging has reported evidence of ‘doubleness’ between chromatin fibres, highlighting that it is possible to cytologically distinguish individual chromatids (Zickler and Kleckner, 1999). However, to date, the extent of chromatid separation during prophase I had not been thoroughly characterised. Intriguingly, IF-

FISH employing short fosmid FISH probes (~40 kb), revealed that chromatids tend to cluster at a common sequence, when in proximity to the pachytene SC and separate from one another, as they extend away from the axis, causing chromatid separation to positively correlate with distance from SC to reach a mean inter-chromatid distance of ~3.4 µm. A second striking observation made in testes sections, was that although chromatid pairing was evident at a SC-proximal locus, sister and homologous chromatids appeared to be similar distances apart at a SC-distal locus, with no obvious pairing of chromatids. Presumably, the spatial distinction of chromatid pairing occurs because of the positioning of specific genomic regions, relative to the chromosome axis, where cohesin is known to be significantly enriched.

6.1.2 The Regulation of Meiotic Chromatin Loops

The initial characterisation of the chromatin loop surrounding the chromosome 6 *HoxA* cluster in pachytene, not only provided a fundamental insight into basic chromatin organisation, relative to the chromosome axis, but also provided the opportunity to directly assess the regulatory mechanisms which maintain it. The influence of the SMC1 variants, SMC1α and SMC1β, on whole chromosome organisation is well characterised in mammalian meiocytes (Biswas, Stevense, and Jessberger, 2018; Novak, Wang, Revenkova, 2008; Revenkova *et al*., 2004); as studies have described the ability of both variants to modulate the compaction of the chromosome axis, while *Smc1β-/-* spermatocytes have also been shown to experience a rise in the average length of chromatin extensions (Revenkova *et al*., 2004). This prior knowledge was firstly exploited to verify the mapping of the *HoxA* chromatin loop, as changes in the length of the chromatin loop in *Smc1β-/-* and *Smc1β-/-,1α* spermatocytes appeared to comply with predictions made from chromosome-wide FISH analysis (Biswas, Stevense, and Jessberger, 2018; Novak, Wang, Revenkova, 2008; Revenkova *et al*., 2004). Furthermore, it was not clear in prior research, how individual chromatin loops responded to changes in the abundance of the SMC1 variants. A previous study suggested that *Smc1β-/-* oocytes exhibit heterogeneity in chromatin loop length, following the observation that chromosome paint morphology became irregular along the length of the chromosome axis (Novak *et al*., 2008). This finding led to the proposition that a subset of specific axis-association sites is SMC1β-dependent, therefore in *Smc1β-/-* oocytes these sites are lost and released from the axis, while SMC1β-independent sites are maintained. My IF-FISH-based mapping approach

revealed, although the positioning of large chromatin regions (~200 kb), relative to the chromosome axis, are unchanged in *Smc1β-/-* spermatocytes, each of the three loci examined within a chromatin loop increased in distance from the pachytene SC. These data indicate that, at least at the loop examined, significantly more chromatin is 'released' from axis-association regions, or that novel axis-association sites are acquired through extrusion in the mutant. Furthermore, the up-regulation of *Smc1α* expression induced a partial rescue, suggesting that SMC1α only bears partial redundancy with SMC1β, causing a fraction of 'released' chromatin to return to axis-associated regions, or intermediate axis-association sites to be established in *Smc1β-/-,1α* spermatocytes. Furthermore, it also remains feasible that changes specifically in chromatin compaction, alter chromatin loop length in *Smc1β-/-* and *Smc1β-/-,1α* spermatocytes, which were not detected at the present resolution of the IF-FISH assay conducted. In addition to determining whether novel axis-association sites are acquired, future investigations could also begin to exploit chromatin loop maps, generated through IF-FISH, and genetically manipulate the distribution of structural factors, such as cohesin, SYCP3 and CTCF, at specific positions in relation to the chromosome axis. For instance, by deleting or mutating specific binding/enrichment motifs, to determine how the recruitment of such factors influence individual chromatin loop topology, without significantly perturbing the organisation of the entire genome and the progression of meiocytes through prophase I.

EM imaging has also previously revealed that transcription inhibition triggers condensation of meiotic autosomes, indicating that a transcriptional component influences large-scale chromatin organisation (Handel, Caldwell, and Wiltshire, 1995). I chose to interrogate this relationship in more detail and established the change in length of chromatin extensions observed in EM, occurs independently of alterations to SC length. Coincidently with gross and local chromosomal condensation, inter-chromatid distance significantly declines, as chromatin is drawn into greater proximity to the SC. RNA depletion triggered a similar, yet less substantial, change in nuclear condensation to transcription inhibition, indicating that a portion of chromosomal condensation could be reliant on RNA polymerase activity, whilst the remainder is dependent on the synthesis of RNA. Despite the possibility that meiotic RNA could act as a structural component involved in large-scale chromatin decompaction (Nozawa and Gilbert, 2019), this role cannot presently be discriminated from the effect of integral structural genes becoming misexpressed. Consequently, future investigations examining the inter-relationship between transcription and pachytene

chromatin loop organisation will require refinement, to differentiate the primary and secondary effects of altering gene expression. As discussed in Section 4.3, I suggest that the role of active transcription and chromatin loop formation could be interrogated by comparing chromatin loop organisation between meiocytes in which a loop-associated, non-essential promoter is deleted and a mutant in which only gene function is perturbed. This experiment would verify, whether the length of pachytene loop extensions and the preferential enrichment of transcriptionally active regions at SC-distal loci, occurs as a direct consequence of transcription and therefore, is actively maintained.

6.1.3 The Functional Significance of Meiotic Chromatin Loop Arrays

The elaborate genetics and inducible synchronisation of *S. cerevisiae* have allowed an increasingly comprehensive picture of the regulatory mechanisms, behind meiotic chromatin loop dynamics and the distribution of key meiotic events, within the context of the sequential loop arrays, to evolve. For instance, the spatially disparate arrangement of axis-associated recombination machinery and loop-associated meiotic hotspots in *S. cerevisiae*, led to the proposition of the tethered loop-axis complex (TLAC) model, in which hotspot sequences are physically recruited to the axis, in order to undergo recombination (Blat *et al*., 2002; Panizza *et al*., 2011). Crucially, the model could not be reliably translated between yeast and mammalian systems, without a map in which axis- and loop-associated sequenced were differentiated in mammals. I demonstrate that markers of early recombinogenic activity (SPO11-oligonucleotide mapping and DMC1 SSDS) are enriched in the pachytene chromatin SC-distal region of a chromatin loop, at the *HoxA* cluster on chromosome 6. It is not presently known whether SPO11 and DMC1 are recruited actively to these targeted hotspots prior to and/or after chromatin loop formation. Thus, preventing complete elucidation of the structural relationship between recombination machinery and establishment of chromatin loop. It is important to note however, that an individual hotspot is targeted relatively infrequently across a population of spermatocytes, despite chromatin loops appearing consistently between cells. This indicates that chromatin loop formation is unlikely to be dependent on the recruitment of early recombination machinery to each individual chromatin loop. Additionally, according to comparisons of chromatid behaviour between leptotene and

pachytene, the same chromatin loop, defined in pachytene, is unlikely to be conserved between the two stages and thus, influence SPO11-oligo formation and DMC1 activity.

These data, in combination with prior IF-FISH experiments that showed the co-localisation of the CO marker, MLH1, and meiotic hotspots at the chromosome axis (Grey *et al*., 2009), highlight similarities in the spatial distribution of meiotic hotspots and recombination between mouse and yeast meiocytes. Importantly however, whether the spatial discrimination of meiotic hotspots and recombination machinery is of functional relevance, for instance in hotspot designation, is presently unknown, particularly in mammals, such as mice, which are known to be reliant on PRDM9 to determine the distribution of recombination events (Brick *et al*., 2012; Mihola *et al*., 2019). It is also interesting to consider the possibility that recombination and chromatin loop positioning may be related in a cyclical evolutionary relationship, where the positioning of chromatin loops dictates the distribution of meiotic hotspots, making SC-distal loci more susceptible to successful inter-homolog recombination, which consequently alters the genetic environment that distally regulates axis-association sites. Conversely, hotspot sites may be specifically enriched in SC-distal sites, to reduce the likelihood of such recombination events disrupting axis-association sites. To assess the validity of these two propositions, it may prove valuable to assess whether the distribution axis-association sites has altered over evolutionary time.

Diverse evidences in mammalian meiocytes have demonstrated that CO abundance covaries with the length of the SC and chromatin extensions, as CO abundance increases proportionally with SC length and inversely with the length of chromatin extensions (Baier *et al*., 2014; Gruhn *et al*., 2013; Kauppi *et al*., 2013; Kleckner, 2006). My investigations also demonstrate that inter-chromatid distance, in comparative analyses between spermatocyte and oocytes, inversely correlates with CO abundance. However, from such descriptive analyses it is not clear whether chromatid organisation functionally relates to CO abundance, or simply occurs as a by-product of changes to chromosome axis assembly and the enrichment of cohesin at the chromosome axis.

One key event during meiotic recombination, is the discrimination between the sister and homologous chromatids, during repair template choice, in order to promote CO

formation, a preferential inter-homolog bias should be established. Juvenile spermatocytes are thought to establish significantly more inter-sister chromatid interactions than their adult counterparts, which was presently found to correspond to a rise in inter-chromatid distances. Thus, raising the possibility that chromatid separation might be a specialised aspect of meiotic chromosome structure, that favours inter-sister repair. I propose a model in which differences in inter-chromatid distance observed in pachytene are residual from late leptotene/early zygotene when the relative positioning of individual chromatids influences repair template choice, as an increase in inter-chromatid distance correlates with a decline in inter-homolog interactions. However, more research is now required to substantiate the relationship between chromatid separation and the balance between inter-homolog and inter-sister interactions. These future investigations could include comparing inter-chromatid distances between sites of distinct preferential rates of homolog- and sister-mediated repair and examining chromatid separation in the intervening stages of prophase I between leptotene and pachytene.

It is interesting to note that pachytene-defined SC-distal sites exhibit shorter presumptive inter-sister chromatid distances compared to pachytene-defined SC-proximal sites in leptotene and are also enriched for markers of early recombination. A reduction in inter-sister chromatid distance may prove advantageous during early recombination at meiotic hotspots by increasing the likelihood of tandem sister chromatid 'capture' and the suppression of inter-sister chromatid interactions during the homology search (Figure 6-1). Intriguingly, evidence from prior studies have shown that over-time chromatin loops extend (Kauppi *et al*., 2011; Patel *et al*., 2019; Vara *et al*., 2019), which may occur as a consequence of changes to the distribution and extent of cohesin binding and/or transcriptional activity. The resultant increase in chromatin loop length over time could help to manipulate the balance of inter-homolog versus inter-sister interactions, as initially inter-homolog interactions are preferential to encourage synapsis and the formation of obligate COs. An increasing demand for inter-sister interactions can develop as prophase I progresses due to the need to resolve delayed, persistent or non-homologous associated DSBs. Thus, as chromatin loops become longer, sister chromatid capture becomes less efficient and repair template bias shifts towards inter-sister interactions (Figure 6-1). Moreover, it is interesting to consider that the rates of inter-sister versus inter-homolog rates could be affiliated with the evolutionary drive behind sexually dimorphic chromatin loop topology, as a rise in chromatid separation and chromatin loop length might increase

the relative amount of sister chromatid-mediated repair in males compared to females, ensuring the resolution of DSBs on the non-homologous sex chromosomes. In order to test this hypothesis, the abundance of DSBs would need to be compared with the abundance of NCOs and COs, between males and females, genome wide.

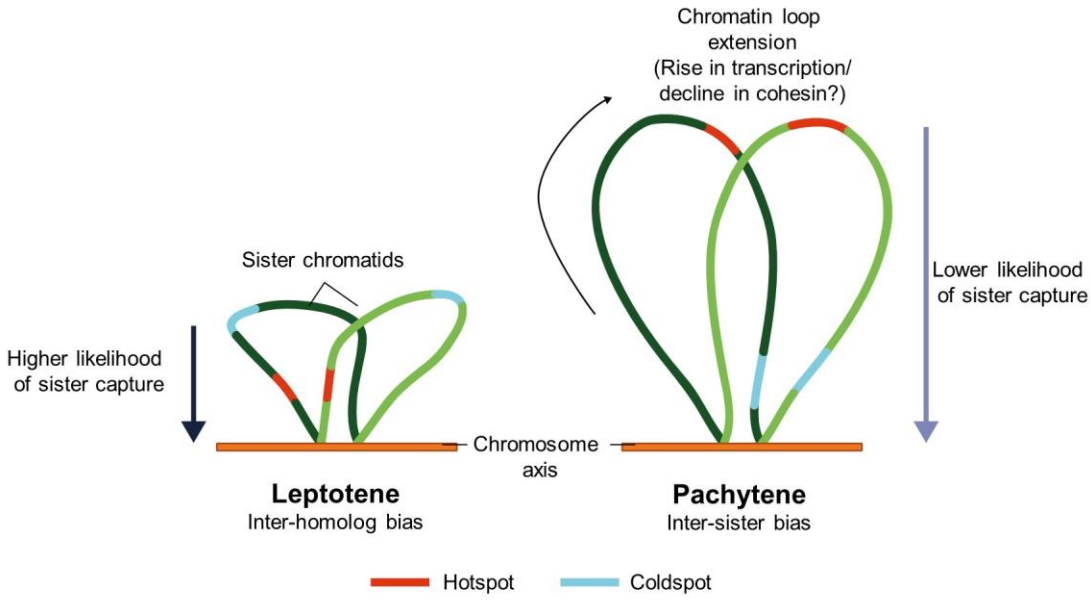

Figure 6-1. Chromatin loop organisation and repair template choice overtime in murine spermatocytes. Schematic depicts two sister chromatids (light and dark green lines), attached to the chromosome axis (orange bar) to form individual loops. Between leptotene and pachytene, chromatin loops increase in length through a presently uncharacterised mechanism, that may relate to transcription and/or the abundance/distribution of cohesin. In leptotene, an inter-homolog bias is established, as chromatin loops are shorter and inter-chromatid distances are reduced causing the efficiency of sister chromatid capture to increase. However, by pachytene, the increase in loop length may reduce sister chromatid capture efficiency, promoting a shift towards sister chromatid-mediated repair.

6.1.4 Extending IF-FISH Analyses Temporally and Spatially

To date, the characterisation of large-scale chromatin organisation in meiotic prophase I has primarily focussed on pachytene, as homologous chromatids coalesce at a common SC to form cytologically distinct morphological units, that can be analysed relatively accurately and efficiently. The cytological identification of the chromosome axis, corresponding to a specific chromatin region, is significantly more demanding in leptotene, zygotene and diplotene, as it can be complicated by the extent of chromosome pairing, LE assembly and synapsis. EM images have revealed chromatin loop arrays are established during leptotene (Zickler and Kleckner, 1999). Yet, recent HiC analyses have shown that large-scale chromatin interactions in leptotene/zygotene are visually distinct from pachytene and represent an intermediary state, between the loss of interphase-associated long-range contacts, and conventional compartments and TADs, and the formation of loop arrays characteristic of pachytene (Patel *et al*., 2019; Wang *et al.,* 2019). In combination, these approaches have provided an insight into the dynamics of the relative positioning of chromatin regions. However, how such structures spatially relate to the developing chromosome axis is not known. Therefore, alternate approaches should be explored to map meiotic chromatin loop throughout prophase I, in order to answer crucial questions regarding chromatin loop dynamics, such as determining whether loop-axis attachment points are fixed, or mobile. Analysis of individual chromatids in leptotene and pachytene indicate this effect is likely to be dependent on the position of loci, within the chromatin loop. The development of novel mapping strategies might stem from a greater appreciation of the structural aspects, which define loop-axis association in pachytene. Importantly, the presumption cannot be made that such features are conserved throughout prophase I. For instance, there is presently no evidence to suggest chromatin-axis association is fixed or conserved between individual chromatids, during leptotene/zygotene.

The extent of chromatin loop mapping conducted in this project was restricted by the inherently time-consuming and labour-intensive nature of the traditional FISH protocol employed. Several prior studies have highlighted regional differences exist in chromatin organisation, for instance at the PAR and autosomal telomeres (Heng *et al*., 1996; Kauppi *et al*., 2011). Accordingly, the findings presented are not necessarily representative of the entire genome but are instead snapshots of what could occur. Yet it was reassuring to note, that the most highly characterised chromatin loop in this

project, the *HoxA* loop, behaved in a comparable manner to the bulk loop population in cohesin mutants and in comparative analyses between females and males. Indicating that the loop is likely to be a good representation of the bulk loop population, but it will remain important to verify key findings generated from the *HoxA* loop at additional loci. Excitingly, recent developments in high-throughput FISH could significantly improve the efficiency at which the FISH performed presently are conducted, enabling chromatin organisation to be assessed over large genetic distances or indeed genome-wide (eg. Beliveau *et al*., 2015; Finn *et al*., 2019). However, despite such approaches being highly automated, the subsequent analysis and interpretation of the generated data will remain highly demanding.

6.2 Wider Perspectives

This project has provided a greater appreciation of the 3D meiotic genome, the regulatory mechanisms which underlie it and its correlative relationship with meiotic recombination. Although my findings are largely descriptive, they will contribute towards forming the basis from which further investigations can examine key meiotic events and the nuclear environment in which they take place. In addition, the successful orchestration of appropriate chromosomal interactions during meiosis is critical from both a medical and an evolutionary perspective; by ensuring the faithful division of homologous chromosomes during the first meiotic division and the reciprocal exchange of genetic information between homologous chromosomes. My findings may therefore have implications both evolutionarily and clinically; for instance, the conservation of axis-association regions between chromatids could be integral for optimising the efficiency of the homology search. Consequently, if the structural coordination of chromatids, relative to the chromosome axis, is perturbed there may be significant ramifications for chromosome synapsis and the exchange of genetic information between homologous chromosomes. In addition, if the distribution of meiotic hotspots is dependent on loop- and axis-association patterns, it is possible that the dimensions and positioning of chromatin loops could influence the number and distribution of genetic sites which undergo recombination. Thus, ultimately impacting on the evolutionary rates of specific haplotypes, as well as whether chromosomes can successfully synapse and form mature COs. With these propositions in mind, it is important to note that aberrant mutations effecting the expression of genes encoding meiosis-specific structural factors, which are known to manipulate large-scale chromatin structure, such as *Smc1β* and *Sycp3*, may contribute towards disruptions, not only in the direction of evolution (Webster and Hurst, 2012), but also an elevated risk of aneuploidy associated conditions, including infertility, spontaneous miscarriage and developmental disorders (discussed in Handel and Schimenti, 2010). Thus, research, such as my own, not only provides greater appreciation of fundamental biological processes, but also creates a platform to encourage further questioning of affiliated evolutionary concepts and medical conditions in mammalian populations.

Chapter 7 Bibliography

Aboussekhra, A., Chanet, R., Adjiri, A., and Fabre, F. (2015). Semidominant suppressors of Srs2 helicase mutations of Saccharomyces cerevisiae map in the RAD51 gene, whose sequence predicts a protein with similarities to procaryotic RecA proteins. *Mol. Cell. Biol. 12*(7), 3224–3234.

Acquaviva, L., Székvölgyi, L., Dichtl, B., Dichtl, B.S., de La Roche Saint André, C., and Géli, V. (2013). The COMPASS subunit Spp1 links histone methylation to initiation of meiotic Recombination. *Science*, *339*(6), 215–218.

Agostinho, A., Kouznetsova, A., Hernández-Hernández, A., Bernhem, K., Blom, H., Brismar, H., and Höög, C. (2018). Sexual dimorphism in the width of the mouse synaptonemal complex. *J. Cell Sci.*, *131*(5), jcs.212548.

Alavattam, K.G., Maezawa, S., Sakashita, A., Khoury, H., Barski, A., Kaplan, N., and Namekawa, S.H. (2019). Attenuated chromatin compartmentalization in meiosis and its maturation in sperm development. *Nat. Struct. Mol. Biol., 26*(March), 175–184.

Alberts, B., Johnson, A., Lewis, J., Raff, M., Roberts, K., and Walter, P. (2002). *Mol. Biol. Cell* (4th ed.). New York: Garland Science.

Alipour, E., and Marko, J.F. (2012). Self-organization of domain structures by DNA-loop-extruding enzymes. *Nucleic Acids Res.*, *40*(22), 11202–11212.

Allers, T., and Lichten, M. (2001). Differential timing and control of noncrossover and crossover recombination during meiosis. *Cell*, *106*(1), 47–57.

Altemose, N., Noor, N., Bitoun, E., Tumian, A., Imbeault, M., Chapman, J.R., Aricescu, A.R., and Myers, S.R. (2017). A map of human PRDM9 binding provides evidence for novel behaviors of PRDM9 and other zinc-finger proteins in meiosis. *ELife*, *6*, e28383.

Anderson, D.E., Losada, A., Erickson, H.P., and Hirano, T. (2002). Condensin and cohesin display different arm conformations with characteristic hinge angles. *J. Cell Biol*, *218*(1), 419–424.

Anderson, L.K., Reeves, A., Webb, L.M., and Ashley, T. (1999). Distribution of crossing over on mouse synaptonemal complexes using immunofluorescent localization of MLH1 protein. *Genetics*, *151*, 1569–1579.

Aragon, L. (2018). The Smc5/6 Complex: New and old functions of the enigmatic long-distance relative. *Annu. Rev. Genet*, *52*, 89–107.

Azuara, V., Brown, K.E., Williams, R.R.E., Webb, N., Dillon, N., Festenstein, R., Buckle, V., Merkenschlager, M., and Fisher, A.G. (2003). Heritable gene silencing in lymphocytes delays chromatid resolution without affecting the timing of DNA replication. *Nat. Cell Biology*, *5*(7), 668–674.

Baier, A., Alsheimer, M., and Benavente, R. (2007). Synaptonemal complex protein SYCP3: Conserved polymerization properties among vertebrates. *Biochim. Biophys. Acta.*, *1774*(5), 595–602.

Baier, B, Hunt, P., Broman, K.W., and Hassold, T. (2014). Variation in genome-wide levels of meiotic recombination is established at the onset of prophase in mammalian males. *PLoS Genet.*, *10*(1), 1004125.

Baker, C.L., Walker, M., Kajita, S., Petkov, P.M., and Paigen, K. (2014). PRDM9 binding organizes hotspot nucleosomes and limits Holliday junction migration. *Genome Res.*, *24*(5), 724–732.

Baker, S.M., Plug, A.W., Prolla, T.A., Bronner, C.E., Harris, A.C., Yao, X., Christie, D.M., Monell, C., Arnheim, N., Bradley, A., Ashley, T., and Hughes, H. (1996). Involvement of mouse mlh1 in DNA mismatch repair and meiotic crossing over. *Nat. Genet.*, *13*(3), 336–342.

Bannister, L.A., Reinholdt, L.G., Munroe, R.J., and Schimenti, J.C. (2004). Positional cloning and characterization of mouse mei8, a disrupted allele of the meiotic cohesin Rec8. *Genesis*, *40*(3), 184–194.

Barchi, M., Mahadevaiah, S., Di Giacomo, M., Baudat, F., de Rooij, D.G., Burgoyne, P.S., Jasin, M., and Keeney, S. (2005). Surveillance of different recombination defects in mouse spermatocytes yields distinct responses despite elimination at an identical developmental stage. *Mol. Cell. Biol.*, *25*(16), 7203–7215.

Barlow, A.L., Benson, F.E., West, S.C., and Hultén, M.A. (1997). Distribution of the Rad51 recombinase in human and mouse spermatocytes. *EMBO J.*, *16*(17), 5207–5215.

Baudat, F, Buard, J., Grey, C., Fledel-Alon, A., Ober, C., Przeworski, M., Coop, G., and de Massy, B. (2010). PRDM9 is a major determinant of meiotic recombination hotspots in humans and mice. *Science*, *327*(5967), 836–840.

Baudat, F., and de Massy, B. (2007). Regulating double-stranded DNA break repair towards crossover or non-crossover during mammalian meiosis. *Chromosome Res.*, *15*(5), 565–577.

Baudat, F., Imai, Y., and de Massy, B. (2013). Meiotic recombination in mammals: localization and regulation. *Nature*, *14*(11), 764-806.

Baudat, F., Manova, K., Yuen, J.P., Jasin, M., and Keeney, S. (2000). Chromosome synapsis defects and sexually dimorphic meiotic progression in mice lacking Spo11. *Mol. Cell*, *6*(5), 989–998.

Beliveau, B.J., Boettiger, A.N., Avendaño, M.S., Jungmann, R., McCole, R.B., Joyce, E.F., Kim-Kiselak, C., Bantignies, F., Fonseka, C.Y., Erceg, J., Hannan, M.A., Hoang, H.G., Colognori, D., Lee, J.T., Shih, W.M., Yin, P. Zhuang, X., and Wu, C. (2015). Single-molecule super-resolution imaging of chromosomes and in situ haplotype visualization using Oligopaint FISH probes. *Nat. Commun.*, *6*, 7147.

Bell, L., and Byers, B. (1983). Separation of branched from linear DNA by gel electrophoresis. *Anal. Biochem.*, *130*(2), 527–535.

Bellani, M.A., Romanienko, P.J., Cairatti, D.A., and Camerini-Otero, R.D. (2005). SPO11 is required for sex-body formation, and Spo11 heterozygosity rescues the prophase arrest of Atm-/- spermatocytes. *J. Cell Sci*., *118*(15), 3233-3245.

Bensaude, O. (2011). Inhibiting eukaryotic transcription: Which compound to choose? How to evaluate its activity? *Transcription*, *2*(3), 103–108.

Berchowitz, L.E., Hanlon, S.E., Lieb, J.D., and Copenhaver, G.P. (2009). A positive but complex association between meiotic double-strand break hotspots and open chromatin in Saccharomyces cerevisiae. *Genome Res.*, *19*(12), 2245–2257.

Bergerat, A., de Massy, B., Gadelle, D., Varoutas, P.C., Nicolas, A., and Forterre, P. (1997). An atypical topoisomerase II from Archaea with implications for meiotic recombination. *Nature*, *386*(6623), 414–417.

Bhargava, R., Onyango, D.O., and Stark, J.M. (2016). Regulation of single strand annealing and its role in genome maintenance. *Trends Genet.*, *32*(9), 566–575.

Bhattacharyya, T., Walker, M., Powers, N.R., Brunton, C., Fine, A.D., Petkov, P.M., and Handel, M.A. (2019). Prdm9 and meiotic cohesin proteins cooperatively promote DNA double-strand break formation in mammalian spermatocytes. *Curr. Biol*, *29*(6), 1002-1018.e7.

Bickmore, W.A., and Van Steensel, B. (2013). Genome architecture: Domain organization of interphase chromosomes. *Cell*, *152*, 1270–1284.

Bishop, D.K., Park, D., Xu, L., and Kleckner, N. (1992). DMC1: A meiosis-specific yeast homolog of E. coli recA required for recombination, synaptonemal complex formation, and cell cycle progression. *Cell*, *69*(3), 439–456.

Bishop, D.K., and Zickler, D. (2004). Early decision: Meiotic crossover interference prior to stable strand exchange and synapsis. *Cell*, *117*(1), 9–15.

Biswas, U., Hempel, K., Llano, E., Pendas, A., and Jessberger, R. (2016). Distinct roles of meiosis-specific cohesin complexes in mammalian spermatogenesis. *PLoS Genet.*, *12*(10), 1–24.

Biswas, U., Stevense, M., and Jessberger, R. (2018). SMC1α substitutes for many meiotic functions of SMC1β but cannot protect telomeres from damage. *Curr. Biol.*, *28*(2), 249-261.e4.

Biswas, U., Wetzker, C., Lange, J., Christodoulou, E.G., Seifert, M., Beyer, A., and Jessberger, R. (2013). Meiotic cohesin SMC1β provides prophase I centromeric cohesion and is required for multiple synapsis-associated functions. *PLoS Genet.*, *9*(12), e1003985.

Björkegren, C., and Baranello, L. (2018). DNA supercoiling, topoisomerases, and cohesin: Partners in regulating chromatin architecture? *Int. J. Mol. Sci.*, *19*(3), E884.

Blat, Y., and Kleckner, N. (1999). Cohesins bind to preferential sites along yeast chromosome III, with differential regulation along arms versus the centric region. *Cell*, *98*, 249–259.

Blat, Y., Protacio, R.U., Hunter, N., and Kleckner, N. (2002). Physical and functional interactions among basic chromosome organizational features govern early steps of meiotic chiasma formation. *Cell*, *111*(6), 791–802.

Boateng, K.A., Bellani, M.A., Gregoretti, I.V., Pratto, F., and Camerini-otero, R.D. (2013). Homologous pairing preceding SPO11-mediated double-strand breaks in mice. *Dev. Cell*, *24*(2), 196–205.

Boddy, M.N., Gaillard, P.H.L., McDonald, W.H., Shanahan, P., Yates, J.R., and Russell, P. (2001). Mus81-Eme1 are essential components of a Holliday junction resolvase. *Cell*, *107*(4), 537–548.

Bojko, M. (1985). Human meiosis IX. Crossing over and chiasma formation in oocytes. *Carlsberg Research Communications*, *50*(2), 43–72.

Bolcun-Filas, E., Costa, Y., Speed, R., Taggart, M., Benavente, R., De Rooij, D.G., and Cooke, H.J. (2007). SYCE2 is required for synaptonemal complex assembly, double strand break repair, and homologous recombination. *J. Cell Biol.*, *176*(6), 741–747.

Bolcun-Filas, E., Speed, R., Taggart, M., Grey, C., de Massy, B., Benavente, R., and Cooke, H.J. (2009). Mutation of the mouse Syce1 gene disrupts synapsis and suggests a link between synaptonemal complex structural components and DNA repair. *PLoS Genet.*, *5*(2), e1000393.

Bollschweiler, D., Radu, L., and Pellegrini, L. (2018). Cryo-electron tomography of SYCP3 fibers under native conditions. *Methods Cell Biol.*, *145*, 347-371.

Bonev, B., Mendelson Cohen, N., Szabo, Q., Fritsch, L., Papadopoulos, G.L., Lubling, Y., Xu, X., Lv, X., Hugnot, J.P., Tanay, A., and Cavalli, G. (2017). Multiscale 3D genome rewiring during mouse neural development. *Cell*, *171*(3), 557-572.e24.

Borde, V., Wu, T.C., and Lichten, M. (1999). Use of a recombination reporter insert to define meiotic recombination domains on chromosome III of Saccharomyces cerevisiae. *Mol. Cell. Biol.*, *19*(7), 4832–4842.

Brick, K., Smagulova, F., Khil, P., Camerini-Otero, R.D., and Petukhova, G.V. (2012). Genetic recombination is directed away from functional genomic elements in mice. *Nature*, *485*(7400), 642–645.

Brick, K., Thibault-Sennett, S., Smagulova, F., Lam, K.W., Pu, Y., Pratto, F., Camerini-Otero, R.D., and Petukhova, G. V. (2018). Extensive sex differences at the initiation of genetic recombination. *Nature*, *561*(7723), 338–342.

Buis, J., Wu, Y., Deng, Y., Leddon, J., Westfield, G., Eckersdorff, M., Sekiguchi, J.M., Chang, S., and Ferguson, D.O. (2008). Mre11 nuclease activity has essential roles in DNA repair and genomic stability distinct from ATM activation. *Cell*, *135*(1), 85–96.

Cahoon, C.K., Yu, Z., Wang, Y., Guo, F., Unruh, J.R., Slaughter, B.D., and Hawley, R.S. (2017). Superresolution expansion microscopy reveals the three-dimensional organization of the Drosophila synaptonemal complex. *Proc. Natl. Acad. Sci.*, *114*(33), E6857–E6866.

Cai, S., Böck, D., Pilhofer, M., and Gan, L. (2018). The in situ structures of mono-, di-, and trinucleosomes in human heterochromatin. *Mol. Biol. Cell*, *29*(20), 2450–2457.

Cannavo, E., and Cejka, P. (2014). Sae2 promotes dsDNA endonuclease activity within Mre11-Rad50-Xrs2 to resect DNA breaks. *Nature*, *514*(7520), 122–125.

Cao, L., Alani, E., and Kleckner, N. (1990). A pathway for generation and processing of double-strand breaks during meiotic recombination in S. cerevisiae. *Cell*, *61*(6), 1089–1101.

Carpenter, A.T.C. (1981). EM autoradiographic evidence that DNA synthesis occurs at recombination nodules during meiosis in Drosophila melanogaster females. *Chromosoma*, *83*(1), 59–80.

Celeste, A., Petersen, S., Romanienko, P. J., Fernandez-Capetillo, O., Chen, H.T., Sedelnikova, O.A., Reina-San-Martin, B., Coppola, V., Meffre, E., Difilippantonio, M.J., Redon, C., Pilch, D.R., Olaru, A., Eckhaus, M., Camerinin-Otero, R.D., Tessarollo, L., Livak, F., Manova, K., Bonner, W.M., Nussenzweig, M.C., and Nussenzweig, A. (2002). Genomic instability in mice lacking histone H2AX. *Science*, *296*(5569), 922–927.

Chan, R.C., Severson, A.F., and Meyer, B.J. (2004). Condensin restructures chromosomes in preparation for meiotic divisions. *J. Cell Biol.*, *167*(4), 613–625.

Chang, H.H.Y., Pannunzio, N.R., Adachi, N., and Lieber, M.R. (2017). Non-homologous DNA end joining and alternative pathways to double-strand break repair. *Nat. Rev. Mol. Cell Biol.*, *18*(8), 495–506.

Chen, H., Lisby, M., and Symington, L.S. (2013). RPA coordinates DNA end resection and prevents formation of DNA hairpins. *Mol. Cell*, *50*(4), 589–600.

Chicano, A., Crosas, E., Otón, J., Daban, J., Melero, R., and Engel, B.D. (2019). Frozen-hydrated chromatin from metaphase chromosomes has an interdigitated multilayer structure. *EMBO J.*, *38*(7), e99769.

Clermont, Y. (1972). Kinetics of spermatogenesis in mammals: seminiferous epithelium cycle and spermatogonial renewal. *Physiological Reviews*, *52*(1), 198–236.

Cohen, P.E., Pollack, S.E., and Pollard, J.W. (2006). Genetic analysis of chromosome pairing, recombination, and cell cycle control during first meiotic prophase in mammals. *Endocr. Rev.*, *27*(4), 398–426.

Cole, F., Kauppi, L., Lange, J., Roig, I., Wang, R., Keeney, S., and Jasin, M. (2012). Homeostatic control of recombination is implemented progressively in mouse meiosis. *Nat. Cell Biol.*, *14*(4), 424–430.

Costa, Y., Speed, R., Ollinger, R., Alsheimer, M., Semple, C.A., Gautier, P., Maratou, K., Novak, I., Höög, C., Benavente, R., and Cooke, H.J. (2005). Two novel proteins recruited by synaptonemal complex protein 1 (SYCP1) are at the centre of meiosis. *J. Cell Sci, 118*(12), 2755-2762.

Covo, S., Westmoreland, J.W., Gordenin, D.A., and Resnick, M.A. (2010). Cohesin is limiting for the suppression of DNA damage-induced recombination between homologous chromosomes. *PLoS Genet.*, *6*(7), 1001006.

Cremer, T., and Cremer, M. (2010). Chromosome Territories. *Cold Spring Harb. Perspect. Biol*, *2*(3), a003889.

Crickard, J.B., Kaniecki, K., Kwon, Y., Sung, P., Lisby, M., and Greene, E.C. (2018). Regulation of Hed1 and Rad54 binding during maturation of the meiosis-specific presynaptic complex. *The EMBO J.*, *37*(7), e98728.

Cromie, G.A., Hyppa, R.W., Taylor, A.F., Zakharyevich, K., and Smith, G.R. (2006). Single holliday junctions are intermediates of meiotic recombination. *Cell*, *127*(6), 1167–1178.

Cuylen, S., Metz, J., and Haering, C.H. (2011). Condensin structures chromosomal DNA through topological links. *Nat. Struct. Mol. Biol.*, *18*(8), 894–901.

da Cruz, I., Rodríguez-Casuriaga, R., Santiñaque, F.F., Farías, J., Curti, G., Capoano, C.A., Folle, G.A., Benavente, R., Sotelo-Silveira, J.R., and Geisinger, A. (2016). Transcriptome analysis of highly purified mouse spermatogenic cell populations: Gene expression signatures switch from meiotic-to postmeiotic-related processes at pachytene stage. *BMC Genomics*, *17*, 294.

Daban, J. (2003). High concentration of DNA in condensed chromatin. *Biochem. Cell Biol.*, *81*(3), 91–99.

Dai, J., Voloshin, O., Potapova, S., and Camerini-Otero, R.D. (2017). Meiotic knockdown and complementation reveals essential role of RAD51 in mouse spermatogenesis. *Cell Reports*, *18*(6), 1383–1394.

Daniel, K., Lange, J., Hached, K., Fu, J., Anastassiadis, K., Roig, I., Cooke, H.J., Stewart, A.F., Wassmann, K., Jasin, M., and Tóth, A. (2011). Meiotic homologous chromosome alignment and its surveillance are controlled by mouse HORMAD1. *Nat Cell Biol*, *13*(5), 599–610.

Davidson, I.F., Goetz, D., Zaczek, M.P., Molodtsov, M.I., Huis, P.J., Weissmann, F., Litos, G., Cisneros, D.A., Ocampo-Hafalla, M., Ladurner, R., Ulhmann, F., Vaziri, A., and Peters, J. (2017). Rapid movement and transcriptional re-localization of human cohesin on DNA. *EMBO J*, *35*(24), 2671–2685.

Davies, O.R., Maman, J.D., and Pellegrini, L. (2012). Structural analysis of the human SYCE2-TEX12 complex provides molecular insights into synaptonemal complex assembly. *Open Biology*, *2*(7), 120099.

de Massy, B. (2013). Initiation of meiotic recombination: How and where? Conservation and specificities among eukaryotes. *Annu. Rev. Genet*, *47*, 563–599.

de Muyt, A., Jessop, L., Kolar, E., Sourirajan, A., Chen, J., Dayani, Y., and Lichten, M. (2012). BLM helicase ortholog Sgs1 is a central regulator of meiotic recombination intermediate metabolism. *Mol. Cell*, *46*(1), 43–53.

de Vries, F., de Boer, E., van den Bosch, M., Baarends, W.M., Ooms, M., Yuan, L., Liu, J.G., van Zeeland, A.A., Heyting, C., and Pastink, A. (2005). Mouse Sycp1 functions in synaptonemal complex assembly, meiotic recombination, and XY body formation. *Genes Dev*, *19*(11), 1376–1389.

de Vries, S.S., Baart, E.B., Dekker, M., Siezen, A., de Rooij, D.G., de Boer, P., and Riele, H. (1999). Mouse MutS-like protein Msh5 is required for proper chromosome synapsis in male and female meiosis. *Genes Dev.*, *13*(5), 523–531.

de Wit, E., Vos, E.S.M., Holwerda, S.J., Valdes-Quezada, C., Verstegen, M.J., Teunissen, H., Splinter, E., Wijchers, P.J., Krijger, P.H., and de Laat, W. (2015). CTCF binding polarity determines chromatin looping. *Mol. Cell*, *60*(4), 676–684.

Diebold-Durand, M.L., Lee, H., Ruiz Avila, L.B., Noh, H., Shin, H.C., Im, H., Bock, F.P., Bürmann, F., Durand, A., Basfeld, A., Ham, S., Basquin, J., Oh, B.H., and Gruber, S. (2017). Structure of full-length SMC and rearrangements required for chromosome organization. *Mol. Cell*, *67*(2), 334-347.e5.

Dixon, J.R., Selvaraj, S., Yue, F., Kim, A., Li, Y., Shen, Y., Hu, M. Liu, J.S., and Ren, B. (2012). Topological domains in mammalian genomes identified by analysis of chromatin interactions. *Nature*, *485*(7398), 376–380.

Dobson, M. J., Pearlman, R.E., Karaiskakis, A., Spyropoulos, B., and Moens, P.B. (1994). Synaptonemal complex proteins: occurrence, epitope mapping and chromosome disjunction. *J. Cell Sci.*, *107 (*Pt 10*)*, 2749–2760.

Dunce, J.M., Dunne, O.M., Ratcliff, M., Millán, C., Madgwick, S., Usón, I., and Davies, O. R. (2018). Structural basis of meiotic chromosome synapsis through SYCP1 self-assembly. *Nat. Struct. Mol. Biol.*, *25*(7), 557–569.

Dunne, O.M., and Davies, O.R. (2019a). A molecular model for self-assembly of the synaptonemal complex protein SYCE3. *J Biol Chem*, *294*(23), 9260-9675.

Dunne, O.M., and Davies, O.R. (2019b). Molecular structure of human synaptonemal complex protein SYCE1. *Chromosoma*, doi:10.1007/s00412-018-00688-z.

Edelmann, W., Cohen, P.E., Kneitz, B., Winand, N., Lia, M., Heyer, J., Koloder, R., Pollard, J.W., and Kucherlapati, R. (1999). Mammalian MutS homologue 5 is required for chromosome pairing in meiosis. *Nat Genet*, *21*(1), 123–127.

Eijpe, M, Heyting, C., Gross, B., and Jessberger, R. (2000). Association of mammalian SMC1 and SMC3 proteins with meiotic chromosomes and synaptonemal complexes. *J. Cell Sci.*, *113*(4), 673–682.

Eijpe, M., Offenberg, H., Jessberger, R., Revenkova, E., and Heyting, C. (2003). Meiotic cohesin REC8 marks the axial elements of rat synaptonemal complexes before cohesins SMC1β and SMC3. *J. Cell Biol.*, *160*(5), 657–670.

Eltsov, M., MacLellan, K.M., Maeshima, K., Frangakis, A.S., and Dubochet, J. (2008). Analysis of cryo-electron microscopy images does not support the existence of 30-nm chromatin fibers in mitotic chromosomes in situ. *Proc. Natl. Acad. Sci.*, *105*(50), 19732–19737.

Enguita-marruedo, A., Martın-Ruiz, M., Garcia, E., Gil-Fernandez, A., Parra, M. T., Viera, A., Rufas, J.S., and Page, J. (2019). Transition from a meiotic to a somatic-like DNA damage response during the pachytene stage in mouse meiosis. *PLoS Genet.*, *15*(1), e1007439.

Enguita-marruedo, A., Van Cappellen, W.A., Hoogerbrugge, J.W., Carofiglio, F., Wassenaar, E., Slotman, J.A., Houstmuller, A., and Baarends, W.M. (2018). Live cell analyses of synaptonemal complex dynamics and chromosome movements in cultured mouse testis tubules and embryonic ovaries. *Chromosoma*, *127*(3), 341–359.

Fallahi, M., Getun, I.V., Wu, Z.K., and Bois, P.R.J. (2010). A global expression switch marks pachytene initiation during mouse male meiosis. *Genes*, *1*(3), 469–483.

Feinauer, C.J., Hofmann, A., Goldt, S., Liu, L., Máté, G., and Heermann, D.W. (2013). Zinc finger proteins and the 3D organization of chromosomes. *Adv. Protein Chem. Struct. Biol.*, *90*, 67–117.

Finn, E.H., Pegoraro, G., Dekker, J., Mirny, L., Misteli, T., Valton, A., Oomen, M.E., Dekker, J., Mirny, L.A., and Misteli, T. (2019). Extensive heterogeneity and intrinsic variation in spatial genome organization. *Cell*, *176*(6), 1502-1515.e10.

Flyamer, I.M., Gassler, J., Imakaev, M., Brandão, H.B., Ulianov, S.V., Abdennur, N., Razin, S.V., Mirny, L.A., and Tachibana-Konwalski, K. (2017). Single-nucleus Hi-C reveals unique chromatin reorganization at oocyte-to-zygote transition. *Nature*, *544*(7648), 110–114.

Forget, A.L., and Kowalczykowski, S.C. (2012). Single-molecule imaging of DNA pairing by RecA reveals a 3-dimensional homology search. *Nature*, *482*(7385), 423–427.

Fraune, J., Schramm, S., Alsheimer, M., and Benavente, R. (2012). The mammalian synaptonemal complex: Protein components, assembly and role in meiotic recombination. *Exp. Cell Res.*, *318*(12), 1340–1346.

Froenicke, L., Anderson, L.K., Wienberg, J., and Ashley, T. (2002). Male mouse recombination maps for each autosome identified by chromosome painting. *Am. J. Hum. Genet.*, *71*(6), 1353–1368.

Fudenberg, G., and Imakaev, M. (2017). FISH-ing for captured contacts: towards reconciling FISH and 3C. *Nature Methods*, *14*(7), 673–678.

Fudenberg, G., Imakaev, M., Lu, C., Goloborodko, A., Abdennur, N., and Mirny, L.A. (2016). Formation of chromosomal domains by loop extrusion. *Cell Rep*, *15*(9), 2038–2049.

Fukuda, T., Fukuda, N., Agostinho, A., Hernández-Hernández, A., Kouznetsova, A., and Christer Höög, and. (2014). STAG3-mediated stabilization of REC8 cohesin complexes promotes chromosome synapsis during meiosis. *EMBO J., 33*, 1243–1255.

Ganji, M., Shaltiel, I.A., Bisht, S., Kim, E., Kalichava, A., Haering, C.H., and Dekker, C. (2018). Real-time imaging of DNA loop extrusion by condensin. *Science*, *360*(6384), 102–105.

Garcia, V., Phelps, S.E.L., Gray, S., and Neale, M.J. (2011). Bidirectional resection of DNA double-strand breaks by Mre11 and Exo1. *Nature*, *479*(7372), 241–244.

Gaysinskaya, V., Soh, I.Y., van der Heijden, G.W., and Bortvin, A. (2014). Optimized flow cytometry isolation of murine spermatocytes. *Cytometry A*, *85*(6), 556–565.

Geisinger, A., and Benavente, R. (2017). Mutations in genes coding for synaptonemal complex proteins and their impact on human fertility. *Cytogenet. Genome Res.*, *150*(2), 77–85.

Ghosh, S.K., and Jost, D. (2018). How epigenome drives chromatin folding and dynamics, insights from efficient coarse-grained models of chromosomes. *PLoS Comput. Biol., 14*(5), 1–26.

Gibcus, J.H., and Dekker, J. (2014). Connecting the genome: dynamics and stochasticity in a new hierarchy for chromosome conformation. *Mol. Cell*, *49*(5), 773–782.

Gibcus, J.H., Samejima, K., Goloborodko, A., Samejima, I., Nuebler, J., Kanemaki, M., Xie, L., Paulson, J.R., Earnshaw, W.C., Mirny, L.A., and Dekker, J. (2018). A pathway for mitotic chromosome formation. *Science*, *359*(6376), 1–29.

Goedecke, W., Eijpe, M., Offenberg, H.H., Van Aalderen, M., and Heyting, C. (1999). Mre11 and Ku70 interact in somatic cells, but are differentially expressed in early meiosis. *Nat. Genet.*, *23*(2), 194–198.

Goetz, P., Chandley, A., and Speed, R. (1984). Morphological and temporal sequence of meiotic prophase development at puberty in the male mouse. *J. Cell Sci*, *65*, 249–263.

Goldfarb, T., and Lichten, M. (2010). Frequent and efficient use of the sister chromatid for DNA double-strand break repair during budding yeast meiosis. *PLoS Biol.*, *8*(10), e1000520.

Golub, E.I., Gupta, R.C., Haaf, T., Wold, M.S., and Radding, C. M. (1998). Interaction of human Rad51 recombination protein with single-stranded DNA binding protein, RPA. *Nucleic Acids Res.*, *26*(23), 5388–5393.

Gómez-H, L., Felipe-Medina, N., Sánchez-Martín, M., Davies, O. R., Ramos, I., García-Tuñón, I., de Rooij, D.G., Dereli, I., Tóth, A., Barbero., J.L., Benavente, R., Llano, E., and Pendas, A.M. (2016). C14ORF39/SIX6OS1 is a constituent of the synaptonemal complex and is essential for mouse fertility. *Nat. Commun.*, *7*, 13298.

Grey, C., Barthès, P., Friec, G., Langa, F., Baudat, F., and de Massy, B. (2011). Mouse Prdm9 DNA-binding specificity determines sites of histone H3 lysine 4 trimethylation for initiation of meiotic recombination. *PLoS Biol.*, *9*(10), 1–9.

Grey, C., Baudat, F., and de Massy, B. (2009). Genome-wide control of the distribution of meiotic recombination. *PLoS Biol.*, *7*(2), 0327–0339.

Grey, C., Clément, J.A.J., Buard, J., Leblanc, B., Gut, I., Gut, M., Duret, L., and de Massy, B. (2017). In vivo binding of PRDM9 reveals interactions with noncanonical genomic sites. *Genome Res.*, *27*(4), 580–590.

Gruber, S., Haering, C.H., and Nasmyth, K. (2003). Chromosomal cohesin forms a ring. *Cell*, *112*(6), 765–777.

Gruhn, J.R., Rubio, C., Broman, K.W., Hunt, P.A., and Hassold, T. (2013). Cytological studies of human meiosis: Sex-specific differences in recombination originate at, or prior to, establishment of double-strand breaks. *PLoS ONE*, *8*(12), e85075.

Guacci, V., Koshland, D., and Strunnikov, A. (1997). A direct link between sister chromatid cohesion and chromosome condensation revealed through the analysis of MCD1 in S. cerevisiae. *Cell*, *91*(1), 47–57.

Guillon, H., Baudat, F., Grey, C., Liskay, R.M., and de Massy, B. (2005). Crossover and noncrossover pathways in mouse meiosis. *Mol. Cell*, *20*(4), 563–573.

Guo, Y., Xu, Q., Canzio, D., Shou, J., Li, J., Gorkin, D.U., Jung, I., Wu, H., Zhai, Y., Tang, Y., Lu, Y., Wu, Y., Jia, Z., Li, W., Zhang, M.Q., Ren, B., Krainer, A.R., Maniatis, T., and Wu, Q. (2015). CRISPR inversion of CTCF sites alters genome topology and enhancer/promoter function. *Cell*, *162*(4), 900–910.

Haarhuis, J.H.I., van der Weide, R.H., Blomen, V.A., Yáñez-Cuna, J.O., Amendola, M., van Ruiten, M.S., Krijger, P.H.L., Teunissen, H., Medema, R.H., van Steensel, B., Brummelkamp, T.R., de Wit, E., and Rowland, B.D. (2017). The cohesin release factor WAPL restricts chromatin loop extension. *Cell*, *169*(4), 693–707.

Haering, C.H., Farcas, A.M., Arumugam, P., Metson, J., and Nasmyth, K. (2008). The cohesin ring concatenates sister DNA molecules. *Nature*, *454*(7202), 297–301.

Haering, C.H., Löwe, J., Hochwagen, A., and Nasmyth, K. (2002). Molecular architecture of SMC proteins and the yeast cohesin complex C-terminal domains forming a head would be part of. *Mol. Cell*, *9*, 773–788.

Haldane, J.B.S. (1922). Sex ratio and unisexual sterility in hybdrid animals. *J. Genet*, *7*(2), 101–109.

Hall, L.L., and Lawrence, J.B. (2016). RNA as a fundamental component of interphase chromosomes: Could repeats prove key? *Curr Opin Genet Dev*, *37*, 137–147.

Hamer, G. (2006). Characterization of a novel meiosis-specific protein within the central element of the synaptonemal complex. *J. Cell Sci., 119*(19), 4025-4032.

Hamer, G., Wang, H., Bolcun-Filas, E., Cooke, H.J., Benavente, R., and Hoog, C. (2008). Progression of meiotic recombination requires structural maturation of the central element of the synaptonemal complex. *J. Cell Sci.*, *121*(15), 2445–2451.

Handel, M.A., Caldwell, K.A., and Wiltshire, T. (1995). Culture of pachytene spermatocytes for analysis of meiosis. *Dev. Genet.*, *16*(2), 128–139.

Handel, M.A. (2004). The XY body: A specialized meiotic chromatin domain. *Exp. Cell Res.*, *296*(1), 57–63.

Handel, M.A., and Schimenti, J.C. (2010). Genetics of mammalian meiosis: Regulation, dynamics and impact on fertility. *Nat. Rev. Genet.*, *11*(2), 124–136.

Heger, P., Marin, B., Bartkuhn, M., Schierenberg, E., and Wiehe, T. (2012). The chromatin insulator CTCF and the emergence of metazoan diversity. *Proc. Natl. Acad. Sci.*, *109*(43), 17507–17512.

Heger, P., Marin, B., and Schierenberg, E. (2009). Loss of the insulator protein CTCF during nematode evolution. *BMC Mol. Biol.*, *10*, 84.

Heng, H.H.Q, Chamberlain, J.W., Shi, X.M., Spyropoulos, B., Tsui, L.C., and Moens, P.B. (1996). Regulation of meiotic chromatin loop size by chromosomal position. *Proc. Natl. Acad. Sci.*, *93*, 2795–2800.

Heng, H.H.Q, Tsui, L.C., and Moens, P.B. (1994). Organization of heterologous DNA inserts on the mouse meiotic chromosome core. *Chromosoma*, *103*(6), 401–407.

Hernández-Hernández, A., Lilienthal, I., Fukuda, N., Galjart, N., and Höög, C. (2016). CTCF contributes in a critical way to spermatogenesis and male fertility. *Sci. Rep.*, *6*, 28355.

Hernández-Hernández, A., Masich, S., Fukuda, T., Kouznetsova, A., Sandin, S., Daneholt, B., and Höög, C. (2016). The central element of the synaptonemal complex in mice is organized as a bilayered junction structure. *J. Cell Sci.*, *129*(11), 2239–2249.

Herrán, Y., Gutiérrez-Caballero, C., Sánchez-Martín, M., Hernández, T., Viera, A., Barbero, J.L., de Álava, E., de Rooji, D.G., Suja, Á.J., and Pendás, A.M. (2011). The cohesin subunit RAD21L functions in meiotic synapsis and exhibits sexual dimorphism in fertility. *EMBO J.*, *30*(15), 3091–3105.

Heyting, C., Dietrich, A.J.J., Redeker, E.J.W., and Vink, A.C.G. (1985). Structure and composition of synaptonemal complexes, isolated from rat spermatocytes. *Eur J Cell Biol*, *36*(2), 307–314.

Hirano, T, Kobayashi, R., and Hirano, M. (1997). Condensins, chromosome condensation protein complexes containing XCAP-C, XCAP-E and a Xenopus homolog of the Drosophila barren protein. *Cell*, *89*, 511–521.

Hirano, T. (2012). Condensins: Universal organizers of chromosomes with diverse functions. *Genes Dev.*, *26*(15), 1659–1678.

Hirano, T., and Mitchison, T.J. (1994). A heterodimeric coiled-coil protein required for mitotic chromosome condensation in vitro. *Cell*, *79*(3), 449–458.

Holloway, J.K., Booth, J., Edelmann, W., Mcgowan, C.H., and Cohen, P.E. (2008). MUS81 generates a subset of MLH1-MLH3–independent crossovers in mammalian meiosis. *PLoS Genet.*, *4*(9), e1000186.

Holloway, J.K., Morelli, M.A., Borst, P.L., and Cohen, P.E. (2010). Mammalian BLM helicase is critical for integrating multiple pathways of meiotic recombination. *J. Cell Biol.*, *188*(6), 779–789.

Hong, S., Sung, Y., Yu, M., Lee, M., Kleckner, N.E., and Kim, K.P. (2013). The logic and mechanism of homologous recombination partner choice. *Mol. Cell*, *51*(4), 440–453.

Hopkins, J., Hwang, G., Jacob, J., Sapp, N., Bedigian, R., Oka, K., Overbeek, P., Murray, S., and Jordan, P.W. (2014). Meiosis-specific cohesin component, Stag3 is essential for maintaining centromere chromatid cohesion, and required for DNA repair and synapsis between homologous chromosomes. *PLoS Genet.*, *10*(7), e1004413.

Houlard, M., Godwin, J., Metson, J., Lee, J., Hirano, T., and Nasmyth, K. (2015). Condensin confers the longitudinal rigidity of chromosomes. *Nat. Cell Biol.*, *17*(6), 771–781.

Huis in 't Veld, P.J., Herzog, F., Ladurner, R., Davidson, I., Piric, S., Kreidl, E., Bhaskara, V., Aebersold, R., Peters, J. (2014). Characterization of a DNA exit gate in the human cohesin ring. *Science*, *346*(6212), 968–972.

Hunter, N., and Kleckner, N. (2001). The single-end invasion: An asymmetric intermediate at the double-strand break to double-holliday junction transition of meiotic recombination. *Cell*, *106*(1), 59-70.

Imai, Y., Baudat, F., Taillepierre, M., Stanzione, M., Toth, A., and de Massy, B. (2017). The PRDM9 KRAB domain is required for meiosis and involved in protein interactions. *Chromosoma*, *126*(6), 681–695.

Ira, G., Malkova, A., Liberi, G., Foiani, M., and James, E. (2003). Srs2 and Sg1-Top3 suppress crossovers during double-strand break repair in yeast. *Cell*, *115*(4), 401–411.

Ishiguro, K.I., Kim, J., Fujiyama-Nakamura, S., Kato, S., and Watanabe, Y. (2011). A new meiosis-specific cohesin complex implicated in the cohesin code for homologous pairing. *EMBO Rep.*, *12*, 267–275.

Ishiguro, K. (2018). The cohesin complex in mammalian meiosis. *Genes Cells*, *24*, 6-30.

Ishiguro, K. I., Kim, J., Shibuya, H., Hernández-Hernández, A., Suzuki, A., Fukagawa, T., Shioi, G., Kiyonari, H., Li, X.C., Schimenti, J., Höög, C., and Watanabe, Y.(2014). Meiosis-specific cohesin mediates homolog recognition in mouse spermatocytes. *Genes Dev.*, *28*(6), 594–607.

Ito, M., Kugou, K., Fawcett, J.A., Mura, S., Ikeda, S., Innan, H., and Ohta, K. (2014). Meiotic recombination cold spots in chromosomal cohesion sites. *Genes Cells, 19*(5), 359-373.

Jabbari, K., Heger, P., Sharma, R., and Wiehe, T. (2018). The diverging routes of BORIS and CTCF: An interactomic and phylogenomic analysis. *Life*, *8*(1), 4.

Johnson, M.E., Rowsey, R.A., Shirley, S., Vandevoort, C., Bailey, J., and Hassold, T. (2013). A specific family of interspersed repeats (SINEs) facilitates meiotic synapsis in mammals. *Mol. Cytogenet.*, *6*(1), 1.

Kauppi, L., Barchi, M., Baudat, F., Romanienko, P.J., Keeney, S., and Jasin, M. (2011). Distinct properties of the XY pseudoautosomal region crucial for male meiosis. *Science*, *331*, 916–920.

Kauppi, L., Barchi, M., Lange, J., Baudat, F., Jasin, M., and Keeney, S. (2013). Numerical constraints and feedback control of double-strand breaks in mouse meiosis. *Genes Dev.*, *27*(8), 873–886.

Kaur, H., de Muyt, A., and Lichten, M. (2015). Top3-Rmi1 DNA single-strand decatenase is integral to the formation and resolution of meiotic recombination intermediates. *Mol. Cell*, *57*(4), 583–594.

Keelagher, R.E., Cotton, V.E., Goldman, A.S.H., and Borts, R.H. (2011). Separable roles for Exonuclease I in meiotic DNA double-strand break repair. *DNA Repair*, *10*(2), 126–137.

Keeney, S. (2008). Spo11 and the formation of DNA double-strand breaks in meiosis. *Genome Dyn. Stab., 2*, 81–123.

Keeney, S., Baudat, F., Angeles, M., Zhou, Z.H., Copeland, N.G., Jenkins, N.A., Manova, J., and Jasin, M. (1999). A mouse homolog of the Saccharomyces cerevisiae meiotic recombination DNA transesterase Spo11p. *Genomics*, *61*(2), 170–182.

Keeney, S., Giroux, C.N., and Kleckner, N. (1997). Meiosis-specific DNA double-strand breaks are catalyzed by Spo11, a member of a widely conserved protein family. *Cell*, *88*(3), 375–384.

Khil, P.P., Smagulova, F., Brick, K.M., Camerini-Otero, R.D., and Petukhova, G.V. (2012). Sensitive mapping of recombination hotspots using sequencing-based detection of ssDNA. *Genome Res.*, *22*(5), 957–965.

Kim, E., Kerssemakers, J., Shaltiel, I.A., Haering, C.H., and Dekker, C. (2019). DNA-loop extruding condensin complexes can traverse one another. *BioRxiv*, doi.org/10.1101/682864.

Kim, K.P., Weiner, B.M., Zhang, L., Jordan, A., Dekker, J., and Kleckner, N. (2010). Sister cohesion and structural axis components mediate homolog bias of meiotic recombination. *Cell*, *143*(6), 924–937.

Kleckner, N. (2006). Chiasma formation: Chromatin/axis interplay and the role(s) of the synaptonemal complex. *Chromosoma*, *115*, 175–194.

Kleckner, N., Zhang, L., Weiner, B., and Zickler, D. (2011). Meiotic chromosome dynamics. *Genome organization and function in the cell nucleus* (pp. 487–583).

Kleckner, N., Zickler, D., Jones, G.H., Dekker, J., Padmore, R., Henle, J., and Hutchinson, J. (2004). A mechanical basis for chromosome function. *Proc. Natl. Acad. Sci.*, *101*(34), 12592–12597.

Kneitz, B., Cohen, P.E., Avdievich, E., Zhu, L., Kane, M. F., Hou, H., Kolodner, R.D., Kucherlapati, R., Pollard, J.W., and Edelmann, W. (2000). MutS homolog 4 localization to meiotic chromosomes is required for chromosome pairing during meiosis in male and female mice. *Genes Dev.*, *14*(9), 1085–1097.

Kogo, H., Tsutsumi, M., Inagaki, H., Ohye, T., Kiyonari, H., and Kurahashi, H. (2012). HORMAD2 is essential for synapsis surveillance during meiotic prophase via the recruitment of ATR activity. *Genes Cells*, *17*(11), 897–912.

Kogo, H., Tsutsumi, M., Ohye, T., Inagaki, H., Abe, T., and Kurahashi, H. (2012). HORMAD1-dependent checkpoint/surveillance mechanism eliminates asynaptic oocytes. *Genes Cells*, *17*(6), 439–454.

Kolas, N.K., Yuan, L., Höög, C., Heng, H.H.Q., Marcon, E., and Moens, P.B. (2004). Male mouse meiotic chromosome cores deficient in structural proteins SYCP3 and SYCP2 align by homology but fail to synapse and have possible impaired specificity of chromatin loop attachment. *Cytogenet. Genome Res.*, *105*(2–4), 182–188.

Kolas, N.K, Svetlanov, A., Lenzi, M.L., Macaluso, F.P., Lipkin, S.M., Liskay, R. M., Greally, J., Edelmann, W., and Cohen, P.E. (2005). Localization of MMR proteins on meiotic chromosomes in mice indicates distinct functions during prophase I. *J. Cell Biol.*, *171*, 447–458.

Kouznetsova, A., Benavente, R., Pastink, A., and Höög, C. (2011). Meiosis in mice without a synaptonemal complex. *PLoS ONE*, *6*(12), e28255.

Kubo, N., Ishii, H., Gorkin, D., Meitinger, F., Xiong, X., Fang, R., Liu, T., Ye, Z., Li, B., Dixon, J.R., Desai, A., Zhao, H., and Ren, B. (2017). Preservation of chromatin organization after acute loss of CTCF in mouse embryonic stem cells. *BioRxiv*, doi.org/10.1101/118737/

Kumar, R., Ghyselinck, N., Ishiguro, K.I., Watanabe, Y., Kouznetsova, A., Höög, C., Strong, E., Schimenti, J., Daniel, K., Tóth, A. and de Massy, B. (2015). MEI4 - a central player in the regulation of meiotic DNA double-strand break formation in the mouse. *J. Cell Sci.*, *128*(9), 1800–1811.

Kumar, R., Bourbon, H.M., and de Massy, B. (2010). Functional conservation of Mei4 for meiotic DNA double-strand break formation from yeasts to mice. *Genes Dev.*, *24*(12), 1266–1280.

Lam, I., and Keeney, S. (2014). Mechanism and regulation of meiotic recombination initiation. *Cold Spring Harb. Perspect. Biol.*, *7*(1), a016634.

Lange, J., Yamada, S., Tischfield, S.E., Pan, J., Kim, S., Zhu, X., Socci, N.D., Jasin, M., and Keeney, S. (2016). The landscape of mouse meiotic double-strand break formation, processing, and repair. *Cell*, *167*(3), 695-698.e16.

Lao, J.P., and Hunter, N. (2010). Trying to avoid your sister. *PLoS Biol.*, *8*(10), e1000519.

Lawrimore, J., Friedman, B., Doshi, A., and Bloom, K. (2017). RotoStep: A chromosome dynamics simulator reveals mechanisms of loop extrusion. *Cold Spring Harb. Symp. Quant. Biol.*, *82*, 101–109.

Lee, C.Y., Conrad, M.N., and Dresser, M.E. (2012). Meiotic chromosome pairing is promoted by telomere-led chromosome movements independent of bouquet formation. *PLoS Genet.*, *8*(5), e1002730.

Lee, J., Iwai, T., Yokota, T., and Yamashita, M. (2003). Temporally and spatially selective loss of Rec8 protein from meiotic chromosomes during mammalian meiosis. *J. Cell Sci.*, *116*(13), 2781–2790.

Lee, J.Y., Steinfeld, J.B., Qi, Z., Kwon, Y., Sung, P., and Greene, E.C. (2017). Sequence imperfections and base triplet recognition by the Rad51 / RecA family of recombinases. *J. Biol. Chem.*, *292*, 11125–11135.

Lee, J., and Hirano, T. (2011). RAD21L, a novel cohesin subunit implicated in linking homologous chromosomes in mammalian meiosis. *J. Cell Biol. 192*(2), 263-276.

Li, S., Meistrich, M.L., Brock, W.A., Hsu, T.C., and Kuoip, M.T. (1983). Isolation and preliminary characterization of the synaptonemal complex from rat pachytene spermatocytes. *Exp. Cell Res., 144*(1), 63–12.

Lichten, M., and Goldman, A.S.H. (1995). Meiotic recombination hotspots. *Annu. Rev. Genet., 29*, 423-444.

Liebe, B., Alsheimer, M., Höög, C., Benavente, R., and Scherthan, H. (2004). Telomere attachment, meiotic chromosome condensation, pairing, and bouquet stage duration are modified in spermatocytes lacking axial elements. *Mol. Biol. Cell*, *15*(2), 827–837.

Lieberman-Aiden, E., van Berkum, N. L., Williams, L., Imakaev, M., Ragoczy, T., Telling, A., Amit, I., Lejoie, B.R., Sabo, P.J., Dorschner, M.O., Sandstrom, R., Bernsteins, B., Bender, M.A., Groudine, M., Gnirke, A., Stamatoyannopoulos, J., Mirny, L.A., Lander, E.S., and Dekker, J. (2009). Comprehensive mapping of long-range interactions reveals folding principles of the human genome. *Science*, *326*(5950), 289–293.

Lipkin, S.M., Moens, P.B., Wang, V., Lenzi, M., Shanmugarajah, D., Thomas, J., Cheng, J., Touchman, J.W., Green, E.D., Schwartzberg, P., Collins, F.S., and Cohen, P.E. (2002). Meiotic arrest and aneuploidy in MLH3-deficient mice. *Nat. Genet.*, *31*, 385–390.

Liu, E.Y., Morgan, A.P., Chesler, E.J., Wang, W., Churchill, G.A., and de Villena, F.P.M. (2014). High-resolution sex-specific linkage maps of the mouse reveal polarized distribution of crossovers in male germline. *Genetics*, *197*(1), 91–106.

Liu, H., Huang, T., Li, M., Li, M., Zhang, C., Jiang, J., Yu, X., Yin, Y., Lu, G., Luo, M.C., Zhang, L.R., Li, J., Liu, K., and Chen, Z.J. (2019). SCRE serves as a unique synaptonemal complex fastener and is essential for progression of meiosis prophase I in mice. *Nucleic Acids Res.*, *47*(11), 5670-5683.

Liu, Y., Gaines, W.A., Callender, T., Busygina, V., Oke, A., Sung, P., Fung, J.C., and Hollingsworth, N.M. (2014). Down-regulation of Rad51 activity during meiosis in yeast prevents competition with Dmc1 for repair of double-strand breaks. *PLoS Genet.*, *10*(1), e1004005.

Llano, E., Gomez-H, L., García-Tuñón, I., Sánchez-Martín, M., Caburet, S., Barbero, J. L., Schimenti, J.C., Veitia, R.A., and Pendas, A.M. (2014). STAG3 is a strong candidate gene for male infertility. *Hum. Mol. Genet.*, *23*(13), 3421–3431.

Llano, E., Herrán, Y., García-Tuñón, I., Gutiérrez-Caballero, C., de Álava, E., Barbero, J. L., Schimenti, J., de Rooij, D.G., Sánchez-Martín, M., and Pendás, A.M. (2012). Meiotic cohesin complexes are essential for the formation of the axial element in mice. *J. Cell Biol., 197*(7), 877–885.

Loidl, J., Scherthan, H., Den Dunnen, J.T., and Klein, F. (1995). Morphology of a human-derived YAC in yeast meiosis. *Chromosoma*, *104*(3), 183–188.

Loukinov, D.I., Pugacheva, E., Vatolin, S., Pack, S. D., Moon, H., Chernukhin, I., Mannan, P., Larsson, E., Kanduri, C., Vostrov, A.A., Cui, H., Niemitz, E.L., Rasko, J.E., Docquier, F.M., Kistler, M., Breen, J.J., Zhuang, Z., Quischke, W.W., Renkawitz, R., Klenova, E.M., Feinberg, A.P., Ohlsson, R., Morse, H.C. 3rd, and Lobanenkov, V.V. (2002). BORIS, a novel male germ-line-specific protein associated with epigenetic reprogramming events, shares the same 11-zinc-finger domain with CTCF, the insulator protein involved in reading imprinting marks in the soma. *Proc. Natl. Acad. Sci. USA*, *99*(10), 6806–6811.

Lu, J., Gu, Y., Feng, J., Zhou, W., Yang, X., and Shen, Y. (2014). Structural insight into the central element assembly of the synaptonemal complex. *Scientific Reports*, *4*, 7059.

Luo, M., Yang, F., Leu, N.A., Landaiche, J., Handel, M.A., Benavente, R., La Salle, S., and Wang, P. J. (2013). MEIOB exhibits single-stranded DNA-binding and exonuclease activities and is essential for meiotic recombination. *Nat. Commun.*, *4*, 1–12.

Lupiáñez, D.G., Kraft, K., Heinrich, V., Krawitz, P., Brancati, F., Klopocki, E., Horn, D., Kayserili, H., Opitz, J.M., Laxova, R., Santos-Simarro, F., Gilbert-Dussardier, B., Wittler, L., Borschiwer, M., Haas, S.A., Osterwalder, M., Franke, M., Timmermann, B., Hecht, J., Spielmann, M., Visel, A., and Mundlos, S. (2015). Disruptions of topological chromatin domains cause pathogenic rewiring of gene-enhancer interactions. *Cell*, *161*(5), 1012–1025.

Lynn, A., Koehler, K.E., Judis, L., Chan, ER., Cherry, J.P., Schwartz, S., Seftel, A., Hunt, P.A., and Hassold, T.J. (2002). Covariation of synaptonemal complex rates meiotic exchange. *Science*, *296*(5576), 2222–2225.

Lynn, A., Schrump, S., Cherry, J., Hassold, T., and Hunt, P. (2005). Report Sex, Not Genotype, Determines Recombination Levels in Mice. *Am. J. Hum. Genet*, *77*, 670–675.

Maeshima, K., Ide, S., and Babokhov, M. (2019). Dynamic chromatin organization without the 30-nm fiber. *Curr. Opin. Cell Biol.*, *58*(30), 95–104.

Mahadevaiah, S.K., Bourc'his, D., de Rooij, D.G., Bestor, T.H., Turner, J.M.A., and Burgoyne, P.S. (2008). Extensive meiotic asynapsis in mice antagonises meiotic silencing of unsynapsed chromatin and consequently disrupts meiotic sex chromosome inactivation. *J. Cell Biol.*, *182*(2), 263–276.

Mahy, N.L., Perry, PE., Gilchrist, S., Baldock, R.A., and Bickmore, W.A. (2002). Spatial organization of active and inactive genes and noncoding DNA within chromosome territories. *J. Cell Biol.*, *157*(4), 579–589.

Maison, C., Bailly, D., Peters, A.H., Quivy, J. P., Roche, D., Taddei, A., Lachner, M., Jenuwein, T., and Almouzni, G. (2002). Higher-order structure in pericentric heterochromatin involves a distinct pattern of histone modification and an RNA component. *Nat. Genet.*, *30*(3), 329–334.

McDowall, A.W., Smith, J.M., and Dubochet, J. (1986). Cryo-electron microscopy of vitrified chromosomes in situ. *EMBO J.*, *5*(6), 1395–1402.

McKee, B.D., and Handel, M.A. (1993). Sex chromosomes, recombination, and chromatin conformation. *Chromosoma*, *102*(2), 71–80.

Meijering, E., Jacob, M., Sarria, J.C.F., Steiner, P., Hirling, H., and Unser, M. (2004). Design and validation of a tool for neurite tracing and analysis in fluorescence microscopy images. *Cytometry A, 58*(2), 167–176.

Merkenschlager, M., and Nora, E.P. (2016). CTCF and Cohesin in genome folding and transcriptional gene regulation. *Annu. Rev. Genomics Hum. Genet.*, *17*(1), 17–43.

Mets, D.G., and Meyer, B.J. (2009). Condensins regulate meiotic DNA break distribution, thus crossover frequency, by controlling chromosome structure. *Cell*, *139*(1), 73–86.

Metzler-Guillemain, C., and de Massy, B. (2000). Identification and characterization of an SPO11 homolog in the mouse. *Chromosoma*, *109*(1–2), 133–138.

Mihola, O., Pratto, F., Brick, K., Linhartova, E., Kobets, T., Flachs, P., Baker, C.L., Sedlacek, R., Paigen, K., Petkov, P.M., Camerini-Otero, R.D., and Trachtulec, Z. (2019). Histone methyltransferase PRDM9 is not essential for meiosis in male mice. *Genome Res.*, doi:10.1101/gr.244426.118.

Milano, C.R., Holloway, J. K., Zhang, Y., Jin, B., Smith, C., Bergman, A., Edelmann, W.A., and Cohen, P. E. (2019). Mutation of the ATPase domain of MutS Homolog-5 (MSH5) reveals a requirement for a functional MutSγ complex for all crossovers in mammalian meiosis. *G3 (Bethesda, Md.)*, *9*(6), 1839–1850.

Mimitou, E.P., Yamada, S., and Keeney, S. (2017). A global view of meiotic double-strand break end resection. *Science*, *355*(6320), 4757–4763.

Mlynarczyk-Evans, S., Royce-Tolland, M., Alexander, M.K., Andersen, A.A., Kalantry, S., Gribnau, J., and Panning, B. (2006). X chromosomes alternate between two states prior to random X-inactivation. *PLoS Biol.*, *4*(6), 0906–0916.

Moens, P.B., Marcon, E., Shore, J.S., Kochakpour, N., and Spyropoulos, B. (2007). Initiation and resolution of interhomolog connections: Crossover and non-crossover sites along mouse synaptonemal complexes. *J. Cell Sci.*, *120*(6), 1017–1027.

Moens, P.B., and Pearlman, R.E. (1988). Chromatin organization at meiosis. *BioEssays*, *9*(5), 151–153.

Moens, P., Kolas, N., Tarsounas, M., Marcon, R., Cohen, P.E., and Spyropoulos, B. (2002). The time course and chromosomal localization of recombination-related proteins at meiosis in the mouse are compatible with models that can resolve the early DNA-DNA interactions without reciprocal recombination. *J. Cell Sci.*, *115*(8), 1611–1622.

Monesi, V. (1964). Ribonucleuic acid synthesis during mitosis and meiosis in the mouse testis. *J. Cell Biol*, *22*, 521–523.

Montavon, T., and Duboule, D. (2013). Chromatin organization and global regulation of Hox gene clusters. *Phil. Trans. R. Soc. B.*, *368*(1620), 20120367.

Moses, M.J. (1968). Synaptonemal complex. *Annu. Rev. Genet*, *2*, 363–412.

Muller, H.J. (1916). The mechanism of crossing-over. *The American Naturalist*, *50*(592), 193–221.

Muñoz-Fuentes, V., Rienzo, A., and Vilà, C. (2011). Prdm9, a major determinant of meiotic recombination hotspots, is not functional in dogs and their wild relatives, wolves and coyotes. *PLoS ONE*, *6*(11), 1–7.

Murdoch, B., Owen, N., Stevense, M., Smith, H., Nagaoka, S., Hassold, T., McKay, M., Xu, H., Fu, J., Revenkova, E., Jessberger, R., and Hunt, P. (2013). Altered cohesin gene dosage affects mammalian meiotic chromosome structure and behavior. *PLoS Genet.*, *9*(2), e1003241.

Myers, S., Bowden, R., Tumian, A., Bontrop, R.E., Freeman, C., MacFie, T.S., McVean, G., and Donnelly, P. (2010). Drive against hotspot motifs in primates implicates the PRDM9 gene in meiotic recombination meiotic recombination. *Science*, *327*(5967), 876–879.

Nakahashi, H., Kwon, K.K., Resch, W., Vian, L., Stavreva, D., Hakim, O., Pruett, N., Nelson, S., Yamane, A., Qian, J., Dubois, W., Walsh, S., Phair, R.D., Pugh, B.G., Lobanenkov, V, Hager, G.L., and Casellas, R. (2013). A genome-wide map of CTCF multivalency redefines the CTCF code. *Cell Rep.*, *3*(5), 1678–1689.

Narendra, V., Rocha, P.P., An, D., Raviram, R., Skok, J.A., Mazzoni, E.O., and Reinberg, D. (2015). CTCF establishes discrete functional chromatin domains at the Hox clusters during differentiation. *Science*, *347*(6225), 1017–1021.

Nasmyth, K. (2001). Disseminating the genome: Joining, resolving, and separating sister chromatids during mitosis and meiosis. *Annu. Rev. Genet*, *35*, 673–745.

Nasmyth, K. (2011). Cohesin: A catenase with separate entry and exit gates? *Nature*, *13*(10), 1170–1177.

Nasmyth, K., and Haering, C.H. (2009). Cohesin: Its roles and mechanisms. *Annu. Rev. Genet.*, *43*, 525–558.

Naumova, N., Imakaev, M., Fudenberg, G., Zhan, Y., Lajoie, B.R., Mirny, L.A., and Dekker, J. (2013). Organization of the mitotic chromosome. *Science*, *342*(6161), 948–953.

Neale, M.J., Pan, J., and Keeney, S. (2005). Endonucleolytic processing of covalent protein-linked DNA double-strand breaks. *Nature*, *436*(7053), 1053–1057.

Nichols, M.D., DeAngelis, K., and Berger, J.M. (1999). Structure and function of an archaeal topoisomerase VI subunit with homology. *EMBO J.*, *18*(21), 6177.

Nishiyama, T. (2019). Cohesion and cohesin-dependent chromatin organization. *Curr. Opin. Cell Biol.*, *58*, 8–14.

Niu, H., Wan, L., Baumgartner, B., Schaefer, D., Loidl, J., and Hollingsworth, N.M. (2005). Partner choice during meiosis Is regulated by Hop1-promoted dimerization of Mek1. *Mol. Biol. Cell*, *16*, 5804–5818.

Niu, H., Wan, L., Busygina, V., Kwon, Y., Jasmina, A., Li, X., Kunz, R.C., Kubota, K., Wang, B., Sung, P., Shokat, K.M., Gygi, S.P., and Hollingsworth, N. M. (2009). Regulation of meiotic recombination via Mek1-mediated Rad54 phosphorylation. *Mol. Cell*, *36*(3), 393–404.

Nora, E.P., Goloborodko, A., Valton, A.L., Gibcus, J.H., Uebersohn, A., Abdennur, N., Dekker, J., Mirny, L.A., and Bruneau, B.G. (2017). Targeted degradation of CTCF decouples local onsulation of chromosome domains from genomic compartmentalization. *Cell*, *169*(5), 930-944.e22.

Nora, E.P., Lajoie, B.R., Schulz, E.G., Giorgetti, L., Okamoto, I., Servant, N., Piolot, T., van Berkum, N.L., Meisig, J., Sedat, J., Gribnau, J., Barrilot, E., Blüthgen, N, Dekker, J., and Heard, E. (2012). Spatial partitioning of the regulatory landscape of the X-inactivation center. *Nature*, *485*(7398), 381–385.

Novak I, Wang H, Revenkova E, Jessberger, R., Scherthan, H. and Höög, C. (2008). Cohesin Smc1B determines meiotic chromatin axis loop organization. *J. Cell Biol*, *180*(1), 83–90.

Nozawa, R.S., and Gilbert, N. (2019). RNA: Nuclear glue for folding the genome. *Trends Cell Biol.*, *29*(3), 201–211.

Offenberg, H.H., Schalk, J.A.C., Meuwissen, R.L.J., Van Aalderen, M., Kester, H.A., Dietrich, A.J.J., and Heyting, C. (1998). SCP2: A major protein component of the axial elements of synaptonemal complexes of the rat. *Nucleic Acids Res.*, *26*(11), 2572–2579.

Ollinger, R., Alsheimer, M., and Benavente, R. (2005). Mammalian protein SCP1 forms synaptonemal complex-like structures in the absence of meiotic chromosomes. *Mol. Biol. Cell*, *16*, 1223–1231.

Ollinger, R., Childs, A., Burgess, H., Speed, R., Lundegaard, P., Reynolds, N., Gray, N.K., Cooke, H.J., and Adams, I. (2008). Deletion of the pluripotency-associated Tex19.1 gene causes activation of endogenous retroviruses and defective spermatogenesis in mice. *PLoS Genet.*, *4*(9), e1000199.

Oomen, M.E., Hansen, A.S., Liu, Y., Darzacq, X., Dekker, J., and Chase, C. (2019). CTCF sites display cell cycle – dependent dynamics in factor binding and nucleosome positioning. *Genome Res.*, *29*, 1–14.

Ou, H., Phan, S., Deerinck, T., Thor, A., Ellisman, M., and O'Shea, C. (2017). ChromEMT: Visualizing 3D chromatin structure and compaction in interphase and mitotic cells. *Science*, *357*(6349), eaag0025.

Pacheco, S., Maldonado-Linares, A., Marcet-Ortega, M., Rojas, C., Martínez-Marchal, A., Fuentes-Lazaro, J., Lange, J., Jasin, M., Keenye, S., Fernández-Capetillo, O., Garcia-Caldés, M., and Roig, I. (2018). ATR is required to complete meiotic recombination in mice. *Nat. Commun.*, *9*(1), 2622.

Page, J., de la Fuente, R., Manterola, M., Teresa Parra, M., Viera, A., Berríos, S., Fernández-Donoso, R., and Rufas, J.S. (2012). Inactivation or non-reactivation: what accounts better for the silence of sex chromosomes during mammalian male meiosis? *Chromosoma*, *121*(3), 307–326.

Page, S.L., and Hawley, R.S. (2003). Chromosome choreography: the meiotic ballet. *Science*, *301*, 785–789.

Pan, J., Sasaki, M., Kniewel, R., Murakami, H., Blitzblau, H.G., Tischfield, S. E., Zhu, X., Neale, M.J., Jasin, M., Socci, N.D., Hochwagen, A., and Keeney, S. (2011). A hierarchical combination of factors shapes the genome-wide topography of yeast meiotic recombination initiation. *Cell*, *144*(5), 719–731.

Panizza, S., Mendoza, M.A., Berlinger, M., Huang, L., Nicolas, A., Shirahige, K., and Klein, F. (2011). Spo11-accessory proteins link double-strand break sites to the chromosome axis in early meiotic recombination. *Cell*, *146*(3), 372-283.

Parvanov, E.D., Petkov, P.M., and Paigen, K. (2010). Prdm9 controls activation of mammalian recombination hotspots. *Science*, *327*(5967), 835.

Patel, L., Kang, R., Rosenberg, S.C., Qiu, Y., Raviram, R., Chee, S., Hu, R., Ren, B., Cole, F., and Corbett, K.D. (2019). Dynamic reorganization of the genome shapes the recombination landscape in meiotic prophase. *Nat.Struct. Mol. Biol.*, *26*(3), 164-174.

Pattabiraman, D., Roelens, B., Woglar, A., and Villeneuve, A.M. (2017). Meiotic recombination modulates the structure and dynamics of the synaptonemal complex during C. elegans meiosis. *PLoS Genet., 24*(30), e1006670.

Paulson, J.F., and Laemmli, U.K. (1977). Chromosomes of histone-depleted metaphase. *Cell*, *12*, 817–828.

Pearlman, R.E., Tsao, N., and Moens, P.B. (1992). Synaptonemal complexes from DNase-treated rat pachytene chromosomes contain (GT)(n) and LINE/SINE sequences. *Genetics*, *130*(4), 865–872.

Pelttari, J., Hoja, M., Yuan, L.I., Liu, J., Brundell, E.V.A., Moens, P., Santucci-Darmanin, S., Jessberger, R., Barbero, J.L., Heyting, C., and Höög, C. (2001). A meiotic chromosomal core consisting of cohesin complex proteins recruits DNA recombination proteins and promotes synapsis in the absence of an axial element in mammalian meiotic cells. *Mol. Cell Biol.*, *21*(16), 5667–5677.

Perry, J., Palmer, S., Gabriel, A., and Ashworth, A. (2001). A short pseudoautosomal region in laboratory mice. *Genome Res.*, *11*(11), 1826–1832.

Peters, A.H., Plug, A.W., van Vugt, M.J., and de Boer, P. (1997). A drying-down technique for the spreading of mammalian meiocytes from the male and female germline. *Chromosome Res.*, *5*(1), 66–71.

Petkov, P.M., Broman, K.W., Szatkiewicz, J.P., and Paigen, K. (2007). Crossover interferences underlies sex differences in recombination rates. *Trends in Genet.*, *23*(11), 539–542.

Petronczki, M., Siomos, M.F., and Nasmyth, K. (2003). The molecular biology of chromosome segregation in meiosis. *Cell*, *112*(4), 423–440.

Pezzi, N., Prieto, I., Kremer, L., Pérez Jurado, L.A., Valero, C., Del Mazo, J., Martínez-A, C., and Barbero, J.L. (2000). STAG3, a novel gene encoding a protein involved in meiotic chromosome pairing and location of STAG3-related genes flanking the Williams-Beuren syndrome deletion. *FASEB J.*, *14*(3), 581–592.

Pittman, D.L., Cobb, J., Schimenti, K.J., Wilson, L.A., Cooper, D.M., Brignull, E., Handel, M.A., and Harbor, B. (1998). Meiotic prophase arrest with failure of chromosome synapsis in mice deficient for Dmc1 , a germline-specific RecA homolog. *Mol. Cell*, *1*(5), 697–705.

Poirier, M.G., and Marko, J.F. (2002). Mitotic chromosomes are chromatin networks without a mechanically contiguous protein scaffold. *Proc. Natl. Acad. Sci. USA*, *99*(24), 15393–15397.

Powers, N.R., Parvanov, E.D., Baker, C.L., Walker, M., Petkov, P.M., and Paigen, K. (2016). The meiotic recombination activator PRDM9 trimethylates both H3K36 and H3K4 at recombination hotspots in vivo. *PLoS Genet.*, *12*(6), 1–24.

Prakash, K., Fournier, D., Redl, S., Best, G., Borsos, M., and Tiwari, V.K. (2015). Superresolution imaging reveals structurally distinct periodic patterns of chromatin along pachytene chromosomes. *Proc. Natl. Acad. Sci.*, *112*(47), 14635–14640.

Pratto, F., Brick, K., Khil, P., Smagulova, F., Petukhova, G.V, and Camerini-Otero, R.D. (2014). Recombination initiation maps of individual human genomes. *Science*, *346*(6211), e1256442.

Prieto, I., Suja, J.A., Pezzi, N., Kremer, L., Martínez-A., C., Rufas, J.S., and Barbero, J.L. (2001). Mammalian STAG3 is a cohesin specific to sister chromatid arms in meiosis I. *Nat. Cell Biol.*, *3*(8), 761–766.

Rankin, S. (2015). Complex elaboration: making sense of meiotic cohesin dynamics. *FEBS J.*, *282*(13), 2413–2430.

Rao, S.S.P., Huang, S.C., Glenn St Hilaire, B., Engreitz, J.M., Perez, E.M., Kieffer-Kwon, K.R., Sanborn, A.L., Johnstone, S.E., Bascom, G.D., Bochkov, I.D., Huang, X., Shamim, M.S., Shin, J., Turner, D., Ye, Z., Omer, A.D., Robinson, J.T., Schlick, T., Bernstein, B.E., Casellas, R., Lander, E.S., and Aiden, E.L. (2017). Cohesin loss eliminates all loop domains. *Cell*, *171*(2), 305-320.e24.

Rao, S.S.P., Huntley, M.H., Durand, N.C., Stamenova, E.K., Bochkov, I.D., Robinson, J.T., Sanborn, A.L., Machol, I., Omer, A.D., Lander, E.S., and Aiden, E.L. (2014). A 3D map of the human genome at kilobase resolution reveals principles of chromatin looping. *Cell*, *159*(7), 1665–1680.

Rasmussen, S.W., and Holm, P.B. (1978). Human meiosis II. Chromosome pairing and recombination nodules in human spermatocytes. *Carlsberg Research Communications*, *43*(5), 275–327.

Rattner, J.B., Goldsmith, M.R., and Hamkalo, B.A. (1981). Chromosome organization and during male meiosis in Bomby mori. *Chromosoma*, *82*, 341-351.

Revenkova, E., Eijpe, M., Heyting, C., and Gross, B. (2001). Novel meiosis-specific isoform of mammalian SMC1. *Mol. Cell. Biol.*, *21*(20), 6984–6998.

Revenkova, E., Eijpe, M., Heyting, C., Hodges, C. A., Hunt, P.A., Liebe, B., Scherthan, H., and Jessberger, R. (2004). Cohesin SMC1 beta is required for meiotic chromosome dynamics, sister chromatid cohesion and DNA recombination. *Nat. Cell Biol.*, *6*(6), 555–562.

Rinaldi, V.D., Bolcun-Filas, E., Kogo, H., Kurahashi, H., and Schimenti, J. C. (2017). The DNA damage checkpoint eliminates mouse eocytes with chromosome synapsis failure. *Mol. Cell*, *67*(6), 1026-1036.e2.

Robine, N., Uematsu, N., Amiot, F., Gidrol, X., Barillot, E., Nicolas, A., and Borde, V. (2007). Genome-wide redistribution of meiotic double-strand breaks in Saccharomyces cerevisiae. *Mol. Cell. Biol.*, *27*(5), 1868–1880.

Rodríguez-Carballo, E., Lopez-Delisle, L., Zhan, Y., Fabre, P.J., Beccari, L., El-Idrissi, I., Huynh, T.H.N., Ozadam, H., Dekker, J., and Duboule, D. (2017). The HoxD cluster is a dynamic and resilient TAD boundary controlling the segregation of antagonistic regulatory landscapes. *Genes Dev.*, *31*(22), 2264–2281.

Rog, O., Köhler, S., and Dernburg, A.F. (2017). The synaptonemal complex has liquid crystalline properties and spatially regulates meiotic recombination factors. *ELife*, *6*, e21455.

Rogacheva, M.V., Manhart, C.M., Chen, G., Guarne, A., Surtees, J., and Alani, E. (2014). Mlh1-Mlh3, a meiotic crossover and DNA mismatch repair factor,is a Msh2-Msh3-stimulated endonuclease. *J. Biol. Chem.*, *289*(9), 5664–5673.

Rogakou, E.P., Boon, C., Redon, C., and Bonner, W.M. (1999). Megabase chromatin domains involved in DNA double-strand breaks in vivo. *J. Cell Biol.*, *146*(5), 905–915.

Romanienko, P.J., and Camerini-Otero, R.D. (2000). The mouse Spo11 gene is required for meiotic chromosome synapsis. *Mol. Cell*, *6*(5), 975–987.

Rong, M., Matsuda, A., Hiraoka, Y., and Lee, J. (2016). Meiotic cohesin subunits RAD21L and REC8 are positioned at distinct regions between lateral elements and transverse filaments in the synaptonemal complex of mouse spermatocytes. *J. Reprod. Dev., 62*(6), 623-630.

Rousseau, B.A., Hou, Z., Gramelspacher, M.J., and Zhang, Y. (2018). Programmable RNA cleavage and recognition by a natural CRISPR-Cas9 system from Neisseria meningitidis. *Mol. Cell*, *69*(5), 906-914.e4.

Rouyer, F., Simmler, M., Johnsson, C., Vergnaud, G., Cooke, H.J., and Weissenbach, J. (1986). A gradient of sex linkage in the pseudoautosomal region of the human sex chromosomes. *Nature*, *319*, 291–295.

Sakai, Y., Mochizuki, A., Kinoshita, K., Hirano, T., and Tachikawa, M. (2018). Modeling the functions of condensin in chromosome shaping and segregation. *PLoS Comput. Biol.*, *14*(6), 1–19.

Saldaña-Meyer, R., González-Buendía, E., Guerrero, G., Narendra, V., Bonasio, R., Recillas-Targa, F., and Reinberg, D. (2014). CTCF regulates the human p53 gene through direct interaction with its natural antisense transcript, Wrap53. *Genes Dev.*, *28*(7), 723–734.

La Salle, S., Palmer, K., O'Brien, M., Schimenti, J.C., Eppig, J., and Handel, M.A. (2012). Spata22, a Novel Vertebrate-Specific Gene, Is Required for Meiotic Progress in Mouse. *Biol. Reprod.*, *86 (2)*(45), 1–12.

Sanborn, A.L., Rao, S.S.P., Huang, S.C., Durand, N.C., Huntley, M.H., Jewett, A.I., Bochkov, I.D., Chinnappan, D., Cutkosky, A., Li, J., Geeting, K.P., Gnirke, A., Melnikov, D., Stamenova, E.K., Lander, E.S., and Aiden, E.L. (2015). Chromatin extrusion explains key features of loop and domain formation in wild-type and engineered genomes. *Proc. Natl. Acad. Sci.*, *112*(47), 201518552.

Santucci-Darmanin, S., Walpita, D., Lespinasse, F., Desnuelle, C., Ashley, T., and Paquis-Flucklinger, V. (2000). MSH4 acts in conjunction with MLH1 during mammalian meiosis. *FASEB J.*, *14*(11), 1539–1547.

Sasaki, H., and Matsui, Y. (2008). Epigenetic events in mammalian germ-cell development: reprogramming and beyond. *Nat. Rev. Genet.*, *9*(2), 129–140.

Schaetzlein, S., Chahwan, R., Avdievich, E., Roa, S., Wei, K., Eoff, R.L., Sellers, R.S., Clark, A.B., Kunkel, T.A., Scharff, M.D., and Edelmann, W. (2013). Mammalian Exo1 encodes both structural and catalytic functions that play distinct roles in essential biological processes. *Proc. Natl. Acad. Sci.*, *110*(27), E2470–E2479.

Schalbetter, S.A., Fudenberg, G., Baxter, J., and Pollard, K.S. (2018). Principles of Meiotic Chromosome Assembly. *bioRxiv,* dio.org/10.1101/442038.

Scherthan, H. (2001). A bouquet makes ends meet. *Nat. Rev. Mol. Cell Biol.*, *2*(8), 621–627.

Schmekel, K., Skoglund, U., and Daneholt, B. (1993). The three-dimensional structure of the central region in a synaptonemal complex: a comparison between rat and two insect species, *Drosophila melanogaster* and *Blap cribrosa*. *Chromosoma, 102*, 682-692.

Schramm, S., Fraune, J., Naumann, R., Hernandez-Hernandez, A., Höög, C., Cooke, H.J., Alsheimer, M., and Benavente, R. (2011). A novel mouse synaptonemal complex protein is essential for loading ofc entral element proteins, recombination, and fertility a novel mouse synaptonemal complex protein is essential for loading of central element proteins. *PLoS Genet.*, *7*(5), e1002088.

Schücker, K., Holm, T., Franke, C., Sauer, M., and Benavente, R. (2015). Elucidation of synaptonemal complex organization by super-resolution imaging with isotropic resolution. *Proc. Natl. Acad. Sci.*, *112*(7), 2029–2033.

Schwacha, A., and Kleckner, N. (1994). Identification of joint molecules that form frequently between homologs but rarely between sister chromatids during yeast meiosis. *Cell*, *76*(1), 51–63.

Schwacha, A., and Kleckner, N. (1995). Identification of double Holliday junctions as intermediates in meiotic recombination. *Cell*, *83*(5), 783–791.

Schwacha, A., and Kleckner, N. (1997). Interhomolog bias during meiotic recombination: Meiotic functions promote a highly differentiated interhomolog-only pathway. *Cell*, *90*(6), 1123–1135.

Sears, D.D., Hegemann, J.H., and Hieter, P. (1992). Meiotic recombination and segregation of human-derived artificial chromosomes in Saccharomyces cerevisiae. *Proc. Natl. Acad. Sci.*, *89*, 5296–5300.

Shenkar, R., Shen, M., and Arnheim, N. (1991). DNase I-hypersensitive sites. *Mol. Cell. Biol.*, *11*(4), 1813–1819.

Shi, B., Xue, J., Yin, H., Guo, R., Luo, M., Ye, L., Shi, Q., Huang, X., Liu, M., Sha, J. and Wang, P.J. (2019). Dual functions for the ssDNA-binding protein RPA in meiotic recombination. *PLoS Genet.*, *15*(2), e1007952.

Shin, Y.H., McGuire, M.M., and Rajkovic, A. (2013). Mouse HORMAD1 is a meiosis I checkpoint protein that modulates DNA double-strand break repair during female meiosis. *Biol. Reprod.*, *89*(2), 1–12.

Shin, Y.H., Choi, Y., Erdin, S.U., Yatsenko, S.A., Kloc, M., Yang, F., Wang, P.J., Meistrich, M.L., and Rajkovic, A. (2010). Hormad1 mutation disrupts synaptonemal complex formation, recombination, and chromosome segregation in mammalian meiosis. *PLoS Genet.*, *6*(11), e1001190.

Shintomi, K., Takahashi, T.S., and Hirano, T. (2015). Reconstitution of mitotic chromatids with a minimum set of purified factors. *Nat. Cell Biol.*, *17*(8), 1014–1023.

Skibbens, R.V. (2016). Of rings and rods: Regulating cohesin entrapment of DNA to generate intra- and intermolecular tethers. *PLoS Genet.*, *12*(10), 1–12.

Sleutels, F., Soochit, W., Bartkuhn, M., Heath, H., Dienstbach, S., Bergmaier, P., Franke, V., Rosa-Garrido, M., van de Nobelen, S., Caesar, L., van der Reijden, M., Bryne, J.C., van ljcken, W., Grootegoed, J.A., Delgado, M.D., Lenhard, B., Renkawitz, F., and Galjart, N. (2012). The male germ cell gene regulator CTCFL is functionally different from CTCF and binds CTCF-like consensus sites in a nucleosome composition-dependent manner. *Epigenetics and Chromatin*, *5*(1), 8.

Smagulova, F., Gregoretti, I.V., Brick, K.M., Khil, P., Camerini-Otero, R.D., and Petukhova, G.V. (2011). Genome-wide analysis reveals novel molecular features of mouse recombination hotspots. *Nature*, *472*, 375–378.

Solari, A. (1974). The behavior of the XY pair in mammals. *Int. Rev. Cytol.*, *38*(0), 273–317.

Sommermeyer, V., Béneut, C., Chaplais, E., Serrentino, M.E., and Borde, V. (2013). Spp1, a member of the Set1 complex, promotes meiotic DSB formation in promoters by tethering histone H3K4 methylation sites to chromosome axes. *Mol. Cell*, *49*(1), 43-54.

Song, R., Ro, S., Michaels, J., Park, C., McCarrey, J., and Yan, W. (2009). Many X-linked microRNAs escape meiotic sex chromosome inactivation. *Nat. Genet.*, *41*(4), 488–493.

Soriano, P, Keitges, E.A., Schorderet, D.F., Harbers, K., Gartler, S.M., and Jaenisch, R. (1987). High rate of recombination and double crossovers in the mouse pseudoautosomal region during male meiosis. *Proc. Natl. Acad. Sci.*, *84*(20), 7218–7220.

Soriano, P., Keitgest, E.A., Schorderett, D.F., Harbers, K., Gartlert, S.M., and Jaenisch, R. (1987). High rate of recombination and double crossovers in the mouse pseudoautosomal region during male meiosis. *Proc. Natl. Acad. Sci.*, *84*, 7218–7220.

Souquet, B., Abby, E., Herve, R., Finsterbusch, F., Tourpin, S., Le Bouffant, R., Duquenne, C., Messiaen, S., Martini, E., Bernardino-Sgherri, J., Tóth, A., and Livera, G. (2013). MEIOB targets single-stranded DNA and is necessary for meiotic recombination. *PLoS Genet.*, *9*(9), e1003784.

Speed, R.M. (1982). Meiosis in the foetal mouse ovary - I. An analysis at the light microscope level using surface-spreading. *Chromosoma*, *85*(3), 427–437.

Stanyte, R., Nuebler, J., Blaukopf, C., Hoefler, R., Stocsits, R., Peters, J.M., and Gerlich, D.W. (2018). Dynamics of sister chromatid resolution during cell cycle progression. *J. Cell Biol.*, *217*(6), 1985–2004.

Stanzione, M., Baumann, M., Papanikos, F., Dereli, I., Lange, J., Ramlal, A., Tränkner, D., Shibuya, H., de Massy, B., Watanabe, Y., Jasin, M., Keeny, S., and Tóth, A. (2016). Meiotic DNA break formation requires the unsynapsed chromosome axis-binding protein IHO1 (CCDC36) in mice. *Nat. Cell Biol.*, *18*(11), 1208–1220.

Stevens, T.J., Lando, D., Basu, S., Atkinson, L.P., Cao, Y., and Steven, F. (2017). 3D structure of individual mammalian genomes studied by single cell Hi-C. *Nature*, *544*(7648), 59–64.

Stigler, J., Çamdere, G.Ö., Koshland, D.E., and Greene, E.C. (2016). Single-molecule imaging reveals a collapsed conformational state for DNA-bound cohesin. *Cell Rep.*, *15*(5), 988–998.

Sturtevant, H. (1914). *The Behavior of the Chromosome as Studied through Linkage.* Berlin, Gerb. Bortraeger, 1915.

Sun, F., and Handel, M.A. (2008). Regulation of the meiotic prophase I to metaphase I in mouse spermatocytes. *Chromosoma*, *117*(5), 471–485.

Sun, X., Huang, L., Markowitz, T.E., Blitzblau, H.G., Chen, D., Klein, F., and Hochwagen, A. (2015). Transcription dynamically patterns the meiotic chromosome-axis interface. *ELife*, *4*, e07424.

Suzuki, T., Kosaka-Suzuki, N., Pack, S., Shin, D.-M., Yoon, J., Abdullaev, Z., Pugacheva, E., Morse H.C. 3rd, Loukinov, D., and Lobanenkov, V. (2010). Expression of a testis-specific form of Gal3st1 (CST), a gene essential for spermatogenesis, is regulated by the CTCF paralogous gene BORIS. *Mol. Cell. Biol., 30*(10), 2473–2484.

Svetlanov, A., Baudat, F., Cohen, P.E., and de Massy, B. (2008). Distinct functions of MLH3 at recombination hot spots in the mouse. *Genetics*, *178*(4), 1937–1945.

Syrjänen, J.L, Heller, I., Candelli, A., Davies, O.R., Peterman, E.J.G., Wuite, G.J., and Pellegrini, L. (2017). Single-molecule observation of DNA compaction by meiotic protein SYCP3. *Elife*, *6*, e22582.

Syrjänen, J.L., Pellegrini, L., and Davies, O.R. (2014). A molecular model for the role of SYCP3 in meiotic chromosome organisation. *Elife*, *3*, doi: 10.7554/eLife.02963.

Szostak, J.W., Orr-Weaver, T.L., Rothstein, R.J., and Stahl, F.W. (1983). The double-strand-break repair model for recombination. *Cell*, *33*(1), 25–35.

Tease, C., and Hultén, M.A. (2004). Inter-sex variation in synaptonemal complex lengths largely determine the different recombination rates in male and female germ cells. *Cytogenet. Genome Res.*, *107*(3–4), 208–215.

Tease, C., Hartshorne, G.M., and Hultén, M.A. (2002). Patterns of meiotic recombination in human fetal oocytes. *Am. J. Hum. Genet.*, *70*(6), 1469–1479.

Terakawa, T., Bisht, S., Eeftens, J.M., Dekker, C., Haering, C.H., and Greene, E.C. (2017). The condensin complex is a mechanochemical motor that translocates along DNA. *Science*, *358*(6363), 672-676.

Theunissen, J.W.F., Kaplan, M.I., Hunt, P.A., Williams, B.R., Ferguson, D.O., Alt, F.W., and Petrini, J.H.J. (2003). Checkpoint failure and chromosomal instability without lymphomagenesis in Mre11ATLD1/ATLD1 mice. *Mol. Cell*, *12*(6), 1511–1523.

Toledo, M., Sun, X., Brieño-Enríquez, M.A., Raghavan, V., Gray, S., Pea, J., Milano, C.R., Venkatesh, A., Patel, L., Borst, P.L., Alani, E., and Cohen, P. E. (2019). A mutation in the endonuclease domain of mouse MLH3 reveals novel roles for MutLγ during crossover formation in meiotic prophase I. *PLOS Genet.*, *15*(6), e1008177.

Turner, J.M.A. (2007). Meiotic sex chromosome inactivation. *Development (Cambridge, England)*, *134*(10), 1823–1831.

Turner, J.M.A., Aprelikova, O., Xu, X., Wang, R., Kim, S., Chandramouly, G., Barrett, J.C., Burgoyne, P.S. and Deng, C.X. (2004). BRCA1, histone H2AX phosphorylation and male meiotic sex chromosome inactivation. *Curr. Biol.*, *14*, 2135–2142.

Turner, J.M.A., Mahadevaiah, S.K., Fernandez-Capetillo, O., Nussenzweig, A., Xu, X., Deng, C.X., and Burgoyne, P.S. (2005). Silencing of unsynapsed meiotic chromosomes in the mouse. *Nat. Genet.*, *37*(1), 41–47.

Uhlmann, F, and Nasmyth, K. (1998). Cohesion between sister chromatids must be established during DNA replication. *Curr. Biol.*, *8*, 1095–1101.

Uhlmann, F. (2016). SMC complexes: from DNA to chromosomes. *Nat.Rev. Mol. Cell Biol.*, *17*(7), 399–412.

Uhlmann, F., Lottspeich, F., and Nasmyth, K. (1999). Sister-chromatid separation at anaphase onset is promoted by cleavage of the cohesin subunit Scc1. *Nature,* 400(6739), 37–42.

Vara, C., Paytuví-Gallart, A., Cuartero, Y., Le Dily, F., Garcia, F., Salvà-Castro, J., Gómez-H, L., Julià, E., Moutinho, C., Aiese Cigliano, R., Sanseverino, W., Fonas, O., Pendás, A.M., Heyn, H., Waters, P.D., Marti-Renom, M.A., and Ruiz-Herrera, A. (2019). Three-dimensional genomic structure and cohesin occupancy correlate with transcriptional activity during spermatogenesis. *Cell Rep.*, *28*(2), 352-367.e9.

Volpi, E.V, Chevret, E., Jones, T., Vatcheva, R., Williamson, J., Beck, S., Campbell, R.D., Goldsworthy, M., Powis, S.H., Ragoussis, J., Trowsdale, J., and Sheer, D. (2000). Large-scale chromatin organization of the major histocompatibility complex and other regions of human chromosome 6 and its response to interferon in interphase nuclei. *J. Cell Sci.*, *113*, 1565–1576.

Vranis, N.M., van der Heijden, G.W., Malki, S., and Bortvin, A. (2010). Synaptonemal complex length variation in wild-type male mice. *Genes*, *1*(3), 505–520.

Vrielynck, N., Chambon, A., Vezon, D., Pereira, L., Chelysheva, L., de Muyt, A., Mézard, C., Mayer, C., and Grelon, M. (2016). A DNA topoisomerase VI–like complex initiates meiotic recombination. *Science*, *351*(6276), 939–943.

Vrooman, L.A., Nagaoka, S.I., Hassold, T.J., and Hunt, P.A. (2014). Evidence for paternal age-related alterations in meiotic chromosome dynamics in the mouse. *Genetics*, *196*(2), 385–396.

Walker, M., Billings, T., Baker, C.L., Powers, N., Tian, H., Saxl, R.L., Choi, K., Hibbs, M.A., Carter, G.W., Handel, M.A., Paigen, K., and Petkov, P. M. (2015). Affinity-seq detects genome-wide PRDM9 binding sites and reveals the impact of prior chromatin modifications on mammalian recombination hotspot usage. *Epigenetics Chromatin*, *8*, 31.

Wang, Y., Wang, H., Zhang, Y., Du, Z, Si, W., Fan, S., Qin, D., Wang, M., Duan, Y., Li, L., Jiao, Y., Li, Y., Wang, Q., Shi, Q., Wu, X., and Xie, W. (2019). Reprogramming of meiotic chromatin architecture during spermatogenesis. *Mol. Cell*, *73*, 547-561.e6.

Ward, A., Hopkins, J., Mckay, M., Murray, S., and Jordan, P. W. (2016). Genetic interactions between the meiosis-specific cohesin components, STAG3, REC8, and RAD21L. *G3 (Bethesda, Md.)*, *6*(6), 1713–1724.

Webster, M.T., and Hurst, L.D. (2012). Direct and indirect consequences of meiotic recombination: Implications for genome evolution. *Trends Genet.*, *28*(3), 101–109.

Wei, K., Clark, A.B., Wong, E., Kane, M.F., Mazur, D.J., Parris, T., Kolas, N.K., Russel, R., Jou, H.Jr., Kneitz, B., Yang, G., Kunkel, T.A., Kolodner, R.D., Cohen, P.E., and Edelmann, W. (2003). Inactivation of Exonuclease 1 in mice results in DNA mismatch repair defects, increased cancer susceptibility, and male and female sterility. *Genes Dev.*, *17*(5), 603–614.

Wells, J.N., Gligoris, T.G., Nasmyth, K.A., and Marsh, J.A. (2017). Evolution of condensin and cohesin complexes driven by replacement of Kite by Hawk proteins. *Curr. Biol.*, *27*(1), R17–R18.

Wendt, K. S., Yoshida, K., Itoh, T., Bando, M., Koch, B., Schirghuber, E., Tsutsumi, S., Nagae, G., Ishihara, K., Mishiro, T., Yahata, K., Imamoto, F., Aburanti, H., Nakao, M., Imamoto, N., Naeshima, K., Shirahige, K., and Peters, J.M. (2008). Cohesin mediates transcriptional insulation by CCCTC-binding factor. *Nature, 451*(7180), 769-801.

West, A.M., Rosenberg, S.C., Ur, S.N., Lehmer, M.K., Ye, Q., Hagemann, G., Caballero, I., Usón, I., MacQueen, A.J., Herzog, F., and Corbett, K.D. (2019). A conserved filamentous assembly underlies the structure of the meiotic chromosome axis. *Elife*, *8,* e40372.

Westergaard, M., and von Wettstein, D. (1972). Synaptinemal complex. *Annu. Rev. Genet*, *6*, 71–110.

Williamson, I., Berlivet, S., Eskeland, R., Boyle, S., Illingworth, R.S., Paquette, D., and Bickmore, W.A. (2014). Spatial genome organization : contrasting views from chromosome conformation capture and fluorescence in situ hybridization. *Genes Dev.*, *28*(24), 2778–2791.

Williamson, I., Kane, L., Devenney, P.S., Anderson, E., Kilanowski, F., Hill, R.E., Bickmore, W.A., and Lettice, L. A. (2019). Developmentally regulated Shh expression is robust to TAD perturbations. *BioRxiv*, doi.org/10.1101/609941.

Winkel, K., Alsheimer, M., Öllinger, R., and Benavente, R. (2009). Protein SYCP2 provides a link between transverse filaments and lateral elements of mammalian synaptonemal complexes. *Chromosoma*, *118*(2), 259–267.

Winters, T., Mcnicoll, F., and Jessberger, R. (2014). Meiotic cohesin STAG3 is required for chromosome axis formation and sister chromatid cohesion. *EMBO J.*, *33*, 1256–1270.

Wojtasz, L., Cloutier, J.M., Baumann, M., Daniel, K., Varga, J., Fu, J., Anastassiadis, K., Stewart, A.F., Reményi, A., Turner, J.M.A., and Tóth, A. (2012). Meiotic DNA double-strand breaks and chromosome asynapsis in mice are monitored by distinct HORMAD2-independent and -dependent mechanisms. *Genes Dev.*, *26*(9), 958–973.

Wojtasz, L., Daniel, K., Roig, I., Bolcun-Filas, E., Xu, H., Boonsanay, V., Eckmann, C.R., Cooke, H.J., Jasin, M., Keeney, S., McKay, M.J., and Tóth, A. (2009). Mouse HORMAD1 and HORMAD2, two conserved meiotic chromosomal proteins, are depleted from synapsed chromosome axes with the help of TRIP13 AAA-ATPase. *PLoS Genet.*, *5*(10), e1000702.

Wold, M. S. (1997). Replication Protein A : A Heterotrimeric , Single-Stranded DNA-Binding Protein Required for Eukaryotic DNA Metabolism. *Ann. Rev. Genet*, *66*, 61–92.

Wu, H., Ho, H., Burgess, S.M., Hsin-Yen, W., Hsuan-Chung, H., and Burgess, S.M. (2010). Modulating MEK1 kinase alters outcomes of meiotic recombination and the stringency of the recombination checkpoint response. *Curr. Biol.*, *20*(19), 1707–1716.

Xu, H., Beasley, M.D., Warren, W.D., van der Horst, G.T.J., McKay, M.J. (2005). Absence of mouse REC8 cohesin promotes synapsis of sister chromatids in meiosis. *Dev. Cell*, *8*, 949–961.

Xu, Y., Greenberg, R.A., Schonbrunn, E., and Wang, J. (2017). Meiosis-specific proteins MEIOB and SPATA22 cooperatively associate with the single-stranded DNA-binding replication protein A complex and DNA double-strand breaks. *Biol. Reprod.*, *96*, 1096–1104.

Yamada, S., Kim, S., Tischfield, S.E., Lange, J., Jasin, M., and Keeney, S. (2017). Genomic and chromatin features shaping meiotic double-strand break formation and repair in mice. *Cell Cycle*, *16*(20), 1870–1884.

Yang, F., De La Fuente, R., Leu, N.A., Baumann, C., McLaughlin, K.J., and Wang, P. J. (2006). Mouse SYCP2 is required for synaptonemal complex assembly and chromosomal synapsis during male meiosis. *J. Cell Biol.*, *173*(4), 497–507.

Yang, F., Eckardt, S., Leu, N.A., McLaughlin, K.J., and Wang, P. J. (2008). Mouse TEX15 is essential for DNA double-strand break repair and chromosomal synapsis during male meiosis. *J. Cell Biol.*, *180*(4), 673–679.

Yoshida, K., Kondoh, G., Matsuda, Y., Habu, T., Nishimune, Y., and Morita, T. (1998). The mouse RecA-like gene Dmc1 is required for homologous chromosome synapsis during meiosis. *Mol. Cell*, *1*(5), 707–718.

Yu, H.G., and Koshland, D.E. (2003). Meiotic condensin is required for proper chromosome compaction, SC assembly, and resolution of recombination-dependent chromosome linkages. *J. Cell Biol.*, *163*(5), 937–947.

Yuan, L., Liu, J.G., Hoja, M.R., Wilbertz, J., Nordqvist, K., and Höög, C. (2002). Female germ cell aneuploidy and embryo death in mice the meiosis-specific protein SCP3. *Science*, 296, 1115–1118.

Yuan, L., Liu, J.G., Zhao, J., Brundell, E., Daneholt, B., and Höög, C. (2000). The murine SCP3 gene is required for synaptonemal complex assembly, chromosome synapsis, and male fertility. *Mol. Cell*, *5*(1), 73–83.

Yuan, L., Pelttari, J., Brundell, E., Björkroth, B., Zhao, J., Liu, J.G., Brismar, H., Daneholt, B., and Höög, C. (1998). The synaptonemal complex protein SCP3 can form multistranded, cross-striated fibers in vivo. *J Cell Biol.*, *142*(2), 331–339.

Zakharyevich, K., Ma, Y., Tang, S., Hwang, P.Y.H., Boiteux, S., and Hunter, N. (2010). Temporally and Biochemically Distinct Activities of Exo1 during Meiosis: Double-Strand Break Resection and Resolution of Double Holliday Junctions. *Mol. Cell*, *40*(6), 1001–1015.

Zelazowski, M.J., Sandoval, M., Paniker, L., Hamilton, H.M., Han, J., Gribbell, M.A., Kang, R., and Cole, F. (2017). Age-dependent alterations in meiotic recombination cause chromosome segregation errors in spermatocytes. *Cell*, *171*(3), 601-614.e13.

Zhang, L., Espagne, E., Muyt, A. De, Zickler, D., and Kleckner, N.E. (2014). Interference-mediated synaptonemal complex formation with embedded crossover designation. *Proc. Natl. Acad. Sci.*, *111*(47), E5059-68.

Zickler, D., and Kleckner, N. (1999). Meiotic Chromosomes: Integrating Structure and Function. *Annu. Rev. Genet.*, *33*, 603–754.

Zickler, D., and Kleckner, N. (2015). Recombination, pairing, and synapsis of homologs during meiosis. *Cold Spring Harb. Persp. Biol.*, *7*(6), a016626.

Zuin, J., Dixon, J.R., van der Reijden, M.I.J.A., Ye, Z., Kolovos, P., Brouwer, R.W.W., van der Corput, M.P., van de Werken, H.J., Knoch, T.A., van IJcken, W.F., Grosveld, F.G., Ren, B., and Wendt, K. S. (2014). Cohesin and CTCF differentially affect chromatin architecture and gene expression in human cells. *Proc. Natl. Acad. Sci.*, *111*(3), 996–1001.